



University
of Glasgow

Trchalik, Josef (2009) *Aeroelastic modelling of gyroplane rotors*. PhD thesis.

<http://theses.gla.ac.uk/1232/>

Copyright and moral rights for this thesis are retained by the author

A copy can be downloaded for personal non-commercial research or study, without prior permission or charge

This thesis cannot be reproduced or quoted extensively from without first obtaining permission in writing from the Author

The content must not be changed in any way or sold commercially in any format or medium without the formal permission of the Author

When referring to this work, full bibliographic details including the author, title, awarding institution and date of the thesis must be given

Aeroelastic Modelling of Gyroplane Rotors

Josef Trchalík, Dipl.Ing.

Ph. D. Thesis



Department of Aerospace Engineering

University of Glasgow

July 2009

Thesis submitted to the Faculty of Engineering
in fulfillment of the requirements for
the degree of Doctor of Philosophy

© J. Trchalík, 2009

Abstract

The gyroplane represents the first successful rotorcraft design and it paved the way for the development of the helicopter during the 1940s. Gyroplane rotors are not powered in flight and work in autorotative regime and hence the characteristics of a helicopter rotor during powered flight and a rotor in autorotation differ significantly. Gyroplanes in the UK have been involved in number of fatal accidents during the last two decades. Despite several research projects focused on gyroplane flight dynamics, the cause of some of gyroplane accidents still remains unclear. The aeroelastic behaviour of autorotating rotors is a relatively unexplored problem and it has not yet been investigated as possible cause of the accidents.

A mathematical model was created to simulate aeroelastic behaviour of rotors in autorotation. The model can investigate couplings between blade teeter, bending, torsion and rotor speed using a finite element model combined with a blade element method and a dynamic inflow model. A set of 'McCUTCHEON' rotor blades was subjected to a series of experiments, yielding baseline input parameters for the model. The model was validated against published results of modal analysis of helicopter rotor blades, experimental flight measurements and other data published in open literature.

Effect of selected rotor design parameters on performance and stability of autorotating rotors was analyzed. Results of the model suggest that steady autorotative flight is not possible for excessive values of blade fixed incidence angle or geometric twist of the blade, leading to an aeromechanical instability. Negative values of these parameters lead to rotor over-speed, loss of rotor thrust and increase in vehicle speed of descent. The simulations have shown that moderate values of blade geometric twist applied to the inboard region of the blade together with blade tip mass can improve stability of a rotor in autorotation.

A significant part of the research was focused on investigation of the effect of different values of torsional and flexural stiffness, and the relative chord-wise positions of blade elastic axis and centre of mass on rotor stability during autorotation. The results obtained from the model demonstrate an interesting and unique characteristic of the autorotative regime. Coupled flap-twist-rotor speed oscillations of the rotor occur if the torsional stiffness of the blade is lower than a critical value and if the blade centre of mass is aft of the blade elastic axis. The new type of aeroelastic instability is *specific* to autorotating rotors and differs from both helicopter rotor flutter and fixed-wing flutter. An extra degree of freedom in rotor speed does not alter flutter onset point significantly and hence this instability can be classified as pitch-flap flutter, with the stability boundary of a hyperbolic shape. However, variation of rotor speed in response to coupled flexural and torsional dynamics of the rotor blades changes behaviour of the rotor *during* the instability. The coupling of rotor teeter, blade torsion and rotor speed with vehicle speed of descent results in a combined flutter and divergence instability.

The investigation aeroelastic behaviour of rotors in autorotation has shown that although autorotation has strong autostabilizing character, catastrophic aeroelastic instability can occur. Aeroelastic instability of this type has not been previously described in open literature. The instability can be initiated by incorrect mass balance of the rotor blades together with their insufficient torsional stiffness. Alternatively, unsuitable rotor geometry causing excessive blade incidence can prevent the rotor from entering steady autorotation. Hence a rotor in autorotation with unsuitable design of rotor blades can encounter an aeroelastic instability even if it is correctly mass balanced.

Notation and Nomenclature

Roman Symbols

a Offset of the pitch axis from half-chord, in half-chords, $a = \frac{y_{EA} - b}{b}$; Vector of additional forcing terms

a_0 Area of blade cross-section [m^2]

a_x Horizontal acceleration of the rotor hub [ms^{-2}]

a_y Lateral acceleration of the rotor hub [ms^{-2}]

a_z Vertical acceleration of the rotor hub [ms^{-2}]

A Rotor disc area, $A = \pi R^2$ [m^2]

$[A_G]$ Generalized aerodynamic forcing matrix

\bar{A}_i i -th coefficient of the characteristic equation

b Half-chord, $b = \frac{c}{2}$ [m]

c Local value of rotor blade chord length [m]; Damping coefficient

c_{crit} Critical damping coefficient

c_D Local blade drag coefficient

c_L Local blade lift coefficient

$c_{L\alpha}$ Lift curve slope, $c_{L\alpha} \approx 2\pi$ [1/rad]

c_T Rotor thrust coefficient, $c_T = \frac{T}{\rho\pi\Omega^2 R^4}$

c_β	Flap damping coefficient [Nms/rad]
c_θ	Torsional damping coefficient [Nms/rad]
c_ξ	Chord-wise bending damping coefficient [Nms/rad]
C_0	Apparent mass factor, $C_0 = 1$ or 0.64 for Pitt-Peters dynamic inflow model, depending on blade twist
$[C]$	Damping matrix
D	Rotor blade drag [N]; Dissipation function of the blade [J]
EI	Blade flexural stiffness [Nm^2]
f	Rotor thrust coefficient based on descending velocity
$\{f\}$	Forcing vector
F	Rotor thrust coefficient based on resultant velocity
F_G	Lagrange's generalized forcing [N or N.m]
GJ	Blade torsional stiffness [Nm^2/rad]
h	International Standard Atmosphere (ISA) altitude [m]; Rotor blade plunge [m]
\dot{h}	Plunge velocity [m/s]
H	Rotor in-plane force (H-force) [N]
H_i	i-th blade flexural (Hamiltonian) shape function
i_x	Polar mass radius of gyration around span-wise axis (x-axis), $i_x = \sqrt{\frac{Q_x}{m}}$
I_x	Mass moment of inertia about pitch axis [kgm^2]
J_y	Second (or area) moment of inertia about flapping axis [m^4]
J_z	Moment of inertia about axis of rotation [m^4]

k	Reduced frequency
k_x	Induced velocity longitudinal weighting factor
k_x	Polar area radius of gyration around span-wise axis (x-axis), $k_x = \sqrt{\frac{P_x}{a_0}}$
k_y	Induced velocity lateral weighting factor
k_β	Equivalent flexural stiffness, $k_\beta = \frac{EI_f}{r}$ [Nm/rad]
k_θ	Equivalent torsional stiffness, $k_\theta = \frac{GJ}{r}$ [Nm/rad]
k_ξ	Equivalent chord-wise bending stiffness, $k_\xi = \frac{EI_c}{r}$ [Nm/rad]
[K]	Stiffness matrix
l_i	Length of i-th rotor blade element, $l_i = r_{i+1} - r_i$ [m]
L	Rotor blade lift [N]
m	Mass [kg]
M	Mach number; Total blade mass [kg]
[M]	Mass matrix
$M_{\bar{y}}$	Rotor blade pitching moment at chord-wise station \bar{y} [Nm]
$M_{\beta,A}$	Aerodynamic forcing moment of blade flapping motion (flat-wise bending) [Nm]
$M_{\theta,A}$	Aerodynamic forcing moment of blade torsion (induced twist) [Nm]
$M_{\Omega,A}$	Aerodynamic forcing moment of blade rotation [Nm]
$M_{\xi,A}$	Aerodynamic forcing moment of blade lag-wise (edge-wise) bending [Nm]
N_b	Number of rotor blades
N_{elem}	Number of blade span-wise elements

P_x	Polar area moment of inertia around span-wise axis (x-axis), $P_x = \int y^2 + z^2 da_0$
q	Torsional loading per length [N]
\bar{q}	Dynamic pressure, $\bar{q} = \frac{\rho V^2}{2}$ [Pa]
q_G	Lagrange's generalized coordinate [m or rad]
Q	Rotor torque [Nm]
Q_x	Polar mass moment of inertia around span-wise axis (x-axis), $Q_x = \int y^2 + z^2 dm$
r	Blade radial (span-wise) coordinate [m]; Position vector of a blade
r_i	Span-wise coordinate of i-th rotor blade node, $l_i = r_{i+1} - r_i$ [m]
R	Blade span (rotor radius) [m]
R_u	Universal gas constant, $R = 287.053 [Jkg^{-1}K^{-1}]$
Re	Reynolds number
S_i	i-th blade torsional shape function
t	Time [s]; Blade thrust per length [N/m]
T	Rotor thrust [N]; Kinetic energy [J]; Temperature ISA, $T = 288.15(1 - 0.0065h)$ [K]
$[T]$	Transformation matrix relating rotating and non-rotating systems of coordinates
u_m	Mass flow parameter
U	Inflow speed [m/s]; Strain and potential energy of the blade [J]
U_p	Vertical component of inflow speed [m/s]
U_r	Radial component of inflow speed [m/s]

U_t	Tangential component of inflow speed [m/s]
v_h	Mean induced velocity at hover, $v_h = \sqrt{\frac{T}{2\rho A}} = \Omega R \sqrt{\frac{c_T}{2}}$ [m/s]
v_i	Inflow speed [m/s]
v_{i0}	Induced velocity at the rotor disc centre, $v_{i0} = \frac{\Omega R c_T}{2\sqrt{\mu^2 + \lambda^2}}$ [m/s]
v_{ic}	Longitudinal component of induced velocity [m/s]
v_{is}	Lateral component of induced velocity [m/s]
v_t	Total velocity at the rotor disc centre [m/s]
V	Free-stream velocity [m/s]
V_d	Speed of descent [m/s]
V_h	Horizontal speed [m/s]
V_x	Component of free-stream velocity parallel to rotor disc longitudinal axis, $V_x = V_h \cos \iota - V_d \sin \iota$ [m/s]
V_y	Component of free-stream velocity parallel to rotor disc lateral axis [m/s]
V_z	Component of free-stream velocity perpendicular to the rotor disc plane, $V_z = V_h \sin \iota + V_d \cos \iota$ [m/s]
w	Flexural displacement of a blade span-wise element in direction perpendicular to its longitudinal axis [m]
\hat{w}	Weighting (test) function
w_P	Flexural displacement of a blade span-wise element in direction z-axis of the global rotating system of coordinates [m]
x	Dimensionless span-wise coordinate, $x = \frac{r}{R}$
y	Chord-wise coordinate [m]
\bar{y}	Dimensionless chord-wise coordinate, $\bar{y} = \frac{y}{c}$

y_{CG}	Chord-wise position of blade centre of gravity [m]
y_{EA}	Local chord-wise position of elastic axis [m]
y_g	Offset of elastic axis from centre of gravity [m]

Greek Symbols

α	Steady angle of attack [rad]
$\dot{\alpha}$	Rate of change of angle of attack [rad/s]
$\hat{\alpha}$	Parameter of mass matrix of blade bending FEM
α_{div}	Angle of attack corresponding to first signs of drag divergence [rad]
α_D	Angle of attack of the rotor disc [rad]
α_L	Angle of attack corresponding to first signs of stall [rad]
α_q	Quasi-steady angle of attack [rad]
α_x	Parameter of exponential shape function
β	Rotor blade flapping angle [rad]
ϵ_A	Blade aerodynamic twist, $\epsilon_A = \alpha_{0T} - \alpha_{0R}$ [rad]
ϵ_G	Blade geometric twist [rad]
ϕ	Inflow angle [rad]
Φ	Rotor blade eigenvector (mode shape)
γ	Angle of climb/descent of the vehicle [rad]
ι	Rotor disc longitudinal tilt [rad]
ι_L	Rotor disc lateral tilt [rad]
κ	Poisson ratio, $\kappa = 1.4$ for air

λ	Inflow ratio, $\lambda = \frac{V_d - v_i}{\Omega R}$
λ_i	Induced inflow ratio, $\lambda_i = \frac{v_i}{\Omega R}$
$[\Lambda]$	Dynamic inflow static gain matrix
$\hat{\mu}$	Blade weight per length [kg/m]
μ	Advance ratio, $\mu = \frac{V_H}{\Omega R}$
μ_v	Dynamic viscosity, $\mu_v = (17.06 + 0.0484(T - 273.15)) 10^{-6} [kgm^{-1}s^{-1}]$
μ_x	Advance ratio defined parallel to rotor disc plane, $\mu_x = \frac{\sqrt{V_x + V_y}}{\Omega R}$
μ_z	Advance ratio defined perpendicular to rotor disc plane, $\mu_z = \frac{V_z}{\Omega R} = \lambda - \lambda_i$
ω	Rotor blade eigenfrequency [rad/s]
$\dot{\theta}$	Angular velocity of blade torsion (induced twist) [rad/s]
θ	Rotor blade torsional angle (induced twist) [rad]
ϑ	Slope of rotor blade longitudinal axis [rad]
ρ	Air density, $\rho_0 = 1.225 (1 + 2,25577 \cdot 10^{-5} h)^{4.25577} [kgm^{-3}]$
$[\tau]$	Time constant matrix
Ω	Rotor speed [rad/s]
χ	Wake skew angle, $\chi \approx \arctan \frac{\mu_x}{\lambda}$ [rad]
ξ	Rotor blade lag angle (chord-wise bending) [rad]
ψ	Azimuth [rad]
ζ	Damping ratio, $\zeta = \frac{c}{c_{crit}}$

Superscripts

BX X-th term of differential equation of blade bending (flapping)

RX X-th term of differential equation of blade rotation

TX X-th term of differential equation of blade torsion

Subscripts

$1rav$ Value averaged over one revolution

R A matrix reduced using modal orthogonality

tot Total value for whole rotor

Other Symbols

\cdot First time derivative

$\ddot{}$ Second time derivative

Acronyms

BEM Blade element method

CAA UK Civil Aviation Authority UK

CFD Computational fluid dynamics

DE Differential equation

DoF Degree(s) of Freedom

FEA Finite element analysis

FEM Finite element method

ISA International Standard Atmosphere

NACA National Advisory Committee for Aeronautics

NASA National Aeronautics and Space Administration

R.A.E. Royal aircraft establishment

RASCAL Rotorcraft Aeromechanic Simulation for Control Analysis

SAR Search and Rescue

UAV Unmanned Aerial Vehicle

VTM Vorticity transport model

Contents

1	Introduction	1
1.1	Background	1
1.2	Aims and Objectives	12
1.3	Modelling Techniques	16
1.4	Structure of the Thesis	18
2	Literature Review	20
2.1	Review of Relevant Research on Helicopter Rotor Aerodynamics and Dynamics	21
2.1.1	Aerodynamics of Helicopter Rotors	21
2.1.2	Dynamics of Helicopter Rotors	26
2.2	Review of Research on Aerodynamics and Dynamics of Rotors in Autorotation	31
2.2.1	Aerodynamics of Rotors in Autorotation	31
2.2.2	Dynamics of Rotors in Autorotation	35
2.2.3	Experimental Measurements of Rotors in Autorotation	37
2.2.4	Summary	44
3	Mathematical Modelling of Rotors in Autorotation	46
3.1	Modelling of Aerodynamics of Rotors in Autorotation	48
3.1.1	Modified Prouty’s Polynomial Approximation of an Airfoil Lift Curve	56
3.1.2	Modified Prouty’s Polynomial Approximation of an Airfoil Drag Curve	59

3.1.3	Polynomial Approximation of an Airfoil Moment Curve	60
3.1.4	Aerodynamic Forcing of an Autorotating Rotor Blade	61
3.2	Modelling of the Inflow of a Rotor in Autorotation	63
3.3	Modelling of Rotor Blade Structural Dynamics	66
3.3.1	Derivation of Full, Non-Linear Blade Equations of Motion	67
3.3.2	Linearization of Equations of Motion of Autorotating Rotor Blade	72
3.3.3	Eigenvalue Analysis of Linearized Equations of Motion of Au- torotating Rigid Rotor Blade	75
3.3.4	Eigenvalue Analysis of Linearized Blade Equations Using FEM Formulation	76
3.3.5	Solution of Differential Equations of Blade Motion with the Aid of Finite Element Method	77
3.3.6	Capabilities of the <i>AMRA</i> Model	85
4	Estimation and Experimental Measurements of Blade Physical Prop- erties	88
4.1	Experimental Measurements of the Physical Properties of McCutcheon Rotor Blades	88
4.2	Numerical Estimation of Moments of Inertia of McCutcheon Rotor Blade	94
5	Verification and Validation of the <i>AMRA</i> Model	96
5.1	Validation of the BEM Aerodynamic Model	96
5.2	Verification of the FEM Model of Blade Torsion	100
5.3	Verification of the FEM Model of Blade Bending	105
5.4	Validation of Model of Rotor Teeter	107
5.5	Verification of <i>AMRA</i> Predictions of Gyroplane Flight Mechanics and Performance	110
5.6	The Effect of Level of Complexity of the Blade Dynamic Model	116
5.7	Summary	122

6	The Influence of Basic Design Parameters on the Stability of Rotors in Autorotation	125
6.1	Blade Fixed Incidence Angle	127
6.2	Blade Geometric Twist	134
6.3	The Critical Rotor Speed and Blade Tip Mass	139
6.4	Concluding Remarks	143
7	Aeroelastic Stability of Rotors in Autorotation	145
7.1	Torsional Aeroelastic Stability Boundary of an Autorotating Rotor . .	147
7.2	The Effect of Blade Fixed Angle of Incidence on Rotor Aeroelastic Stability	158
7.3	The Effect of Chord-Wise Position of Blade Elastic Axis on Rotor Aeroelastic Stability	161
7.4	The Effect of the Value of Blade Zero-Lift Pitching Moment Coeffi- cient on Rotor Aeroelastic Stability	162
7.5	The Effect of Rotor Disc Tilt Hinge Offset on Rotor Aeroelastic Stability	165
7.6	The Effect of Flexural Stiffness on Rotor Aeroelastic Stability	168
7.7	Summary	170
8	Conclusions	173
	Appendices	192

List of Figures

1.1	Cierva C.30A, most successful Cierva’s design (left), compared with an example of a modern light gyroplane design, VPM M16. Reproduced from [1] and [2], respectively.	3
1.2	Typical rotor layout of a modern light gyroplane.	3
1.3	Fairey Rotodyne. Reproduced from [3]	5
1.4	CarterCopter technology demonstrator built by Carter Aviation Technologies, Inc., USA. Reproduced from [4]	6
1.5	Groen Brothers Aviation Hawk 4 gyroplane is powered by a turboprop engine. Reproduced from [5]	7
1.6	MMIST CQ-10A Snow Goose UAV in a gyroplane configuration. Reproduced from [6]	8
1.7	Wing Commander Ken Wallis and one of his gyroplanes.	8
1.8	A comparison of accident rates of different types of aircraft. Reproduced from CAP 735 CAA Aviation Safety review.	9
1.9	Time history of the number of gyroplane accidents within UK. Reproduced from CAP 735 CAA Aviation Safety review.	9
1.10	University of Glasgow Montgomerie-Parsons gyroplane (G-UNIV)	10
1.11	Snapshots of blade deflections during aeroelastic instability of a gyroplane rotor. Reproduced from a footage of the Australian Civil Aviation Safety Authority (CASA).	11
1.12	Comparison of different rotorcraft hub designs. Reproduced from Leishman [7].	17

2.1	Change of NACA 0012 lift and drag curve with Mach number. Reprinted from Prouty [8].	23
2.2	Change of lift curve slope of NACA 0012 with Mach number; reprinted from Prouty [8]	23
2.3	Relation of induced velocity and speed of descent as predicted by momentum theory. Reproduced from Gessow [9]	32
2.4	Vimperis diagram; reproduced from Leishman [7]	34
2.5	Span-wise distribution of blade torque that occurs during steady descent in autorotation; reproduced from Leishman [7]	38
2.6	Dependence of c_R on rotor disc angle of attack; reproduced from Leishman [7]	39
2.7	Dependence of dimensionless speed of descent on dimensionless forward speed; reproduced from Leishman [7]	40
2.8	Comparison of aerodynamic efficiencies of gyroplane rotors and two versions of a helicopter rotor; reproduced from Leishman [7]	42
3.1	Comparison of inflow of a helicopter rotor and gyroplane rotor. Reproduced from Leishman [7]	47
3.2	The layout and orientation of the system of coordinates of a rotor in autorotation used in the <i>AMRA</i> model	49
3.3	Calculation of inflow angle with the aid of components of inflow velocity	51
3.4	A sketch of aerodynamics of a rotor blade in autorotation	52
3.5	Range of Mach numbers and angles of attack that occur at the root region, three quarter radius and the tip region of a typical gyroplane rotor blade. Computed by <i>AMRA</i> for advance ratio of 0.1.	54
3.6	Range of Mach numbers and angles of attack that occur at three quarter radius and the tip region of a typical gyroplane rotor blade. Computed by <i>AMRA</i> for advance ratio of 0.1.	55
3.7	Comparison of Prouty's approximation of α_L with wind tunnel data .	57
3.8	Dependence of coefficient C_5 on the value of Mach number	58
3.9	Dependence of coefficient C_6 on the value of Mach number	59

3.10	A comparison of the values of induced velocity obtained with the aid of full modified Peters-HaQuang dynamic inflow model and its simplified (1 DoF) version.	65
3.11	Distribution of induced velocity over the rotor disc during one revolution as predicted by full (3DoF) Peters-HaQuang model	66
3.12	Centrifugal forces acting on a rotating slender beam	68
3.13	Positions of centre of gravity (CG), blade elastic axis (EA) and blade aerodynamic centre (AC) along the chord of a typical rotorcraft blade	69
3.14	Comparison of different types of shape functions for FEM modeling of rotor blade torsion	82
3.15	Hamiltonian shape functions for FEM modeling of blade bending	83
4.1	Span-wise distribution of mass of McCutcheon rotor blade	89
4.2	Layout of the experiment aimed at measurements of blade stiffness and EA position	90
4.3	A sketch showing determination of blade stiffness from experimental data	91
4.4	Span-wise distributions of EA, CG and AC of McCutcheon rotor blade	92
4.5	Span-wise distributions of torsional and flexural stiffness of McCutcheon rotor blade	93
4.6	Experimental measurement of first natural frequency in torsion of McCutcheon rotor blade	93
4.7	Values of mass moment of inertia in torsion of McCutcheon blade as estimated by several different methods	95
4.8	Comparison of a model of McCutcheon blade model with the real internal structure of the blade	95
5.1	Comparison of the enhanced Prouty's approximation of NACA 0012 lift curve with experimental data published by Carpenter [10] in the low angle-of-attack region	97

5.2	Comparison of the enhanced Prouty's approximation of NACA 0012 lift curve with experimental data published by Carpenter [10]	98
5.3	Comparison of the Prouty's approximation of NACA 0012 drag curve with experimental data published by Carpenter [10] in the low angle-of-attack region	98
5.4	Comparison of the enhanced Prouty's approximation of NACA 0012 drag curve with experimental data published by Carpenter [10]	99
5.5	Comparison of polynomial fit of NACA 0012 moment curve with experimental data published by Bielawa [11] and Leishman [12]	99
5.6	Comparison of newly formulated polynomial approximation of NACA 0012 moment curve with experimental data published by Carpenter [10] and [13]	100
5.7	Comparison of estimations of torsional deformation of slender beam under static load of the FEM model of blade torsion with analytical results	101
5.8	Comparison of the first torsional mode shape computed by <i>AMRA</i> and data from the open literature [11].	102
5.9	Comparison of the torsional mode shapes of McCutcheon blade computed by the <i>AMRA</i> and analytical results	102
5.10	A comparison of torsional natural frequencies predicted by the <i>AMRA</i> with analytical results	103
5.11	The Southwell plot of McCutcheon rotor blade showing the result of experimental measurements and predictions of <i>AMRA</i>	104
5.12	Southwell plot of the Aérospatiale SA330 Puma helicopter rotor blade	104
5.13	Comparison of the values of flexural vertical displacements and blade longitudinal gradients obtained from <i>AMRA</i> with corresponding analytical predictions	106
5.14	A comparison of bending mode shapes of McCutcheon blade computed by the <i>AMRA</i> with analytical results	107

5.15	A comparison of bending natural frequencies predicted by the <i>AMRA</i> with analytical results	108
5.16	Comparison of the first two flapping natural frequencies of Aérospatiale SA330 Puma helicopter rotor blade computed by <i>AMRA</i> and other mathematical models	108
5.17	Comparison of predictions of rotor teeter and G-UNIV experimental data - case A	109
5.18	Comparison of predictions of rotor teeter and G-UNIV experimental data - case B	110
5.19	Results of <i>AMRA</i> simulation of axial flight in autorotation	111
5.20	Span-wise distribution of rotor torque during autorotative vertical descent as predicted by <i>AMRA</i>	112
5.21	A qualitative comparison of distribution of torque generated by rotor blade over the rotor disc as predicted by the model and a qualitative sketch of torque distribution reproduced in open literature [12]	113
5.22	The effect of different initial values of rotor speed on the equilibrium value of rotor speed	114
5.23	The effect of blade fixed angle of incidence on the steady value of rotor speed of a gyroplane rotor during axial autorotative flight as predicted by <i>AMRA</i>	114
5.24	The effect of blade tip mass on the steady value of rotor speed of a gyroplane rotor during axial autorotative flight as predicted by <i>AMRA</i>	115
5.25	Comparison of values of dimensionless flight speed for a range of rotor disc angles of attack as determined during flight tests and predicted by <i>AMRA</i>	115
5.26	Comparison of values of resultant force coefficient for a range of rotor disc angles of attack as determined during flight tests and predicted by <i>AMRA</i>	116

5.27	Comparison of the relationship between speed of descent and horizontal speed of a gyroplane as determined during flight tests and predicted by <i>AMRA</i>	117
5.28	Results of <i>AMRA</i> simulation of axial flight in autorotation	118
5.29	Span-wise distribution of blade torque during autorotative forward flight for different values of blade azimuth.	119
5.30	Rotor blade motion in flap and torsion in autorotative forward flight during one revolution	120
5.31	Distribution of blade torsional deflection and vertical displacement in bending obtained with the aid of <i>AMRA</i>	121
5.32	Span-wise distribution of blade torsional deflection and vertical flexural displacement in bending at four azimuthal stations as obtained with the aid of <i>AMRA</i>	121
6.1	The effect of blade fixed angle of incidence on rotor speed of a rotor in autorotative flight as predicted by <i>AMRA</i>	128
6.2	The effect of blade fixed angle of incidence on rotor resultant force coefficient during autorotative flight	129
6.3	The effect of blade fixed angle of incidence on rotor induced velocity during autorotative flight	129
6.4	A comparison of distribution of aerodynamic torque over the rotor disc during forward flight in autorotation as predicted by the model for zero fixed angle of incidence (left) and fixed angle of incidence approaching the critical value	130
6.5	The effect of blade fixed angle of incidence on span-wise distribution of blade aerodynamic torque during axial autorotative flight	130
6.6	Example of an aeroelastic instability during flight in autorotation caused by high blade fixed incidence angle as predicted by <i>AMRA</i>	131
6.7	Values of aerodynamic torque and blade torsional deflections of a gyroplane blade estimated by <i>AMRA</i> for different values of fixed incidence angle	132

6.8	The effect of blade fixed angle of incidence on speed of descent during autorotative flight	133
6.9	The effect of blade fixed angle of incidence on span-wise thrust distribution during autorotative axial flight	133
6.10	Change of rotor blade span-wise distributions of angle of attack and lift coefficient	134
6.11	The effect of blade geometric twist at the tip region on rotor equilibrium rotor speed during autorotative flight	135
6.12	Change of speed of descent and rotor resultant force coefficient with the value of blade geometric twist at the tip	135
6.13	The effect of blade geometric twist at the root region on rotor equilibrium rotor speed during autorotative flight	136
6.14	Change of speed of descent and rotor resultant force coefficient with the value of blade geometric twist at the root	137
6.15	The effect of blade root geometric twist on rotor induced velocity during autorotative flight	138
6.16	The effect of blade geometric twist at the root region on blade span-wise distribution of aerodynamic angle of attack during autorotative flight	139
6.17	The shape of step increment of blade twist used to study the effect of step change of rotor blade torsional deflection	140
6.18	The effect of step increment of blade twist on rotor speed of a gyroplane rotor	141
6.19	The effect of blade tip mass on rotor speed of a rotor in autorotation	142
7.1	Comparison of aeroelastic stability boundaries obtained from two different frequency domain models of an autorotating rotor. Elastic axis of the rotor blades lies at 32% chord.	148
7.2	Aeroelastic instability during axial flight in autorotation	149
7.3	Catastrophic decrease of rotor speed during aeroelastic instability during autorotative vertical descent	150

7.4	Torsional stability boundary of an autorotating rotor in axial flight as predicted by the <i>AMRA</i> model	151
7.5	The effect of degree of freedom in rotation on the shape of blade torsional stability boundary.	152
7.6	A comparison of the values of equilibrium rotor speed during autorotative vertical descent; computed for different span-wise positions of blade CG and varying blade torsional stiffness	153
7.7	A comparison of the values of equilibrium blade torsional and flapping deflections during autorotative vertical descent; computed for different span-wise positions of blade CG and varying blade torsional stiffness	153
7.8	Comparison of an aeroelastic instability during axial flight in autorotation as predicted by the <i>AMRA</i> using equivalent spring stiffness (left) and coupled torsion-bending FEM model of blade dynamics. . .	154
7.9	Comparison of an aeroelastic instability during forward flight in autorotation as predicted by the <i>AMRA</i> using equivalent spring stiffness (left) and coupled torsion-bending FEM model of blade dynamics. . .	154
7.10	A comparison of the values of equilibrium rotor speed during autorotative forward flight; computed for different span-wise positions of blade CG and varying blade torsional stiffness	155
7.11	A comparison of the values of equilibrium blade torsional and flapping deflections during autorotative forward flight; computed for different span-wise positions of blade CG and varying blade torsional stiffness .	155
7.12	Torsional stability boundaries of gyroplane rotor in forward flight as predicted by different versions of <i>AMRA</i>	157
7.13	Stability boundary of a rotor in autorotation	157
7.14	A comparison of torsional stability boundaries for two different values of blade fixed angle of incidence.	158

7.15	A comparison of the values of equilibrium rotor speed for two different values of blade fixed angle of incidence, varying chord-wise positions of CG and typical values of torsional stiffness ($GJ=1500N.m/rad$) . . .	159
7.16	A comparison of the values of equilibrium blade torsional and flapping deflections for two different values of blade fixed angle of incidence, varying chord-wise positions of CG and typical values of torsional stiffness ($GJ=1500N.m/rad$)	160
7.17	The effect of elastic axis position on stability of a rotor in autorotative flight.	161
7.18	The effect of positive values of c_{m0} on the values of equilibrium rotor speed for different positions of blade CG.	163
7.19	The effect of negative values of c_{m0} on the values of equilibrium rotor speed for different positions of blade CG.	164
7.20	The effect of different values of c_{m0} on the shape of blade torsional stability boundary.	164
7.21	Rotor hinge offset in a typical modern light gyroplane rotor design . .	165
7.22	Change of CG-EA offset of a gyroplane rotor with non-zero hinge offset. In the figure on the left, the blades are assumed to pitch around the root attachment only. Linear change of elastic axis between root attachment at the root and natural elastic axis is assumed in the right-hand side figure.	166
7.23	The effect of rotor hinge offset on the values of equilibrium rotor speed for different positions of blade CG. Computed for $\Delta y_h = -0.1c$	167
7.24	The effect of rotor hinge offset on the shape of blade torsional stability boundary. Computed for $\Delta y_h = -0.1c$	167
7.25	Dependence of the value of equilibrium rotor speed and critical torsional stiffness upon blade flexural stiffness of an autorotating rotor. .	168
7.26	Single degree of freedom aeroelastic instability in torsion of a rotor in vertical descent in autorotation.	169

7.27	Single degree of freedom aeroelastic instability in torsion of a rotor in vertical descent in autorotation and autorotative forward flight. . . .	170
7.28	The change of the equilibrium rotor speed with blade torsional stiffness of a typical gyroplane rotor, a gyroplane rotor with infinitely high torsional stiffness and a gyroplane rotor with infinitely high flexural stiffness.	171
A2-1	The difference between linear lift-curve lift coefficient and measured non-linear lift coefficient plotted against $\alpha - \alpha_L$. The plot uses logarithmic scale.	196
A3-1	Different versions of the F-curve, graphical interpretation of the relationship between vertical component of inflow velocity and speed of descent	199
A4-1	An example of transformation of coordinates from rotating frame of reference to non-rotating one	203
A4-2	Potential energy of a rotor blade due to gravitational force	205

List of Tables

1.1	An overview of the main building blocks of <i>AMRA</i> model	14
3.1	Comparison of predictions of different versions of Peters-HaQuang dynamic inflow model	65
4.1	Results of experimental measurements of McCutcheon blade torsional stiffness and EA location	91
4.2	Results of experimental measurements of McCutcheon blade flexural natural frequency	92
5.1	A comparison of the values of non-rotating torsional natural frequency of McCutcheon rotor blades as estimated by <i>AMRA</i> with analytical results	103
5.2	A comparison of the values of non-rotating flexural natural frequency of McCutcheon rotor blades as estimated by <i>AMRA</i> with analytical results	107
5.3	Comparison of predictions of rotor blade teeter and G-UNIV experimental data	109
A2-1	Values of coefficients of polynomial approximation of NACA 0012 moment curve	198
A3-1	Comparison of outcomes of the semi-empirical inflow model for three different versions of the F-curve	201

Declaration

The author declares that this dissertation is a record of work carried out in the Department of Aerospace Engineering, Faculty of Engineering, University of Glasgow under CAA sponsored 'Aeroelastic Modelling of Gyroplane Rotors' research project. The research project started in March 2005 and was finished in October 2008. This work is original in content except where stated otherwise.

Josef Trchalik

July 2009

Acknowledgements

I would like to express my thanks to my supervisors, Dr Eric Gillies and Dr Douglas Thomson for great help and support they gave me throughout my studies in Glasgow. I also want to thank Dr Marat Bagiev for kind help with my research. Help of Dr Richard Green and the departmental team of technicians from Acre Road laboratories during the experimental measurements is greatly appreciated too. I would like to acknowledge the continued support for gyroplane research provided by the UK Civil Aviation Authority. This work was funded through a CAA Air Registration Board Fellowship And Research Grant Scheme, CAA Contract No.905. The support and advise from Steve Griffin, Jonathan Howes, Alistair Maxwell, Andrew Goudie and Joji Waites is highly appreciated.

Many thanks go also to academic staff of the Institute of Aerospace Engineering, Brno University of Technology for making last three years of my undergraduate studies special and for giving me the chance to spend one year of my course abroad. I want to thank Helen and her family, Morgyn, Trudy and Chris, for their kind support and friendship. Next thanks must go to all the lovely people I met in Glasgow - Ad, Lucy, Dave S., Pam, Przemek, Aleks, Giangi and Dave G. - for making me laugh and helping me to relax.

I would like to express my deep gratitude to my family, especially to my father Josef, my mother Edita and my sister Jana who have always supported me and respected all my decisions, no matter how hard for them it was. I would never be able to finish my studies without generous help of my closest family and therefore I would like to dedicate this work to them.

To my parents Josef and Edita and sister Jana

Chapter 1

Introduction

1.1 Background

Helicopters have always played special role in the world aviation - capable of unique flight regimes and manoeuvres, they can perform tasks that no other existing type of aircraft can fulfill. Helicopters evolved from gyroplanes, another type of rotorcraft, in 1920's. Helicopters represent the majority of all operational rotary wing aircraft today while gyroplanes are relatively rare to spot and virtually none are in commercial use.

Although they are outnumbered by helicopters today, gyroplanes were once very popular. Invented and tailored by pioneer Juan de la Cierva, gyroplanes were the only rotorcraft in operation during first few decades of the last century and hence became the first successful rotorcraft design. Juan de la Cierva developed gyroplane design in order to avoid poor low-speed handling qualities of fixed wing aircraft and catastrophic consequences of wing stall in low altitude [7]. Many technical features originally developed by designers of gyroplanes can be found in modern helicopters such as a flap hinge and a lead/lag hinge, leading to a fully articulated rotor hub [7]. Although modern gyroplanes are much smaller and lighter than Cierva's models, the basic features as developed by Cierva remain unchanged.

A gyroplane is an aircraft with a free rotating rotor that generates majority of the lifting force. Gyroplane rotors are working in autorotation (windmilling regime) when the rotor is driven by aerodynamic forces generated by the airflow passing through the rotor disc. The rotor is usually pre-rotated before take-off in order to shorten the take-off distance. A typical gyroplane rotor has fixed blade pitch, i.e. there is no collective or cyclic pitch control. Lateral and longitudinal tilt of the whole rotor hub is used instead, and it is applied by the pilot through mechanical linkages from the control stick. It is often the case that rotor tilt is sufficient for pitch and roll control of a gyroplane - some light gyroplane models have no horizontal stabilizers, however, a vertical stabilizer and a rudder are still necessary for vehicle yaw control. Deflections of the rudder are usually controlled with the aid of pedals.

Piston engines in combination with fixed-pitch propellers are used for the propulsion of the majority of gyroplanes. While tractor configurations prevailed in early gyroplane designs including all Cierva's models, modern light gyroplanes use pusher propulsion systems. Generally, a two-bladed teetering rotor is used in modern gyroplanes as it represents simple and effective main rotor configuration. Early gyroplanes were equipped with three or four-bladed main rotors and flapping hinges, first developed by Cierva for his gyroplane designs [12]. Figure 1.1 shows comparison of a typical modern gyroplane with Cierva's most successful design, the C.30.

Dynamics of a gyroplane rotor is relatively complex and some of features of the rotor can potentially reduce its aeroelastic stability. Gyroplane rotor blades are flexible in bending, although they are quite stiff in torsion. Centrifugal stiffening acting on the rotor blades is variable as rotor speed changes during maneuvers. Rotor blades of many modern gyroplanes are manufactured in modest conditions and often are not mass balanced. The gyroplane hub often includes an offset of its centre of rotation from the axis of longitudinal tilt of the rotor disc (see figure 1.2). This design feature was first introduced by Dr Igor Bensen in order to increase longi-



Figure 1.1: Cierva C.30A, most successful Cierva's design (left), compared with an example of a modern light gyroplane design, VPM M16. Reproduced from [1] and [2], respectively.

tudinal stability of the vehicle. Flexibility of long rotor control linkages can also affect aeroelastic behaviour of the rotor. Reflex camber airfoils that generate high values of the pitching moment coefficient are often used in gyroplane rotor design. Figure 1.2 shows rotor layout of a modern light gyroplane. Some of the features of the design could contribute to development of an aeroelastic instability of the rotor - e.g. variable rotor speed, flexible control linkages, use of reflex camber airfoils and offset of the rotor hub pitch hinge from rotor axis of rotation.

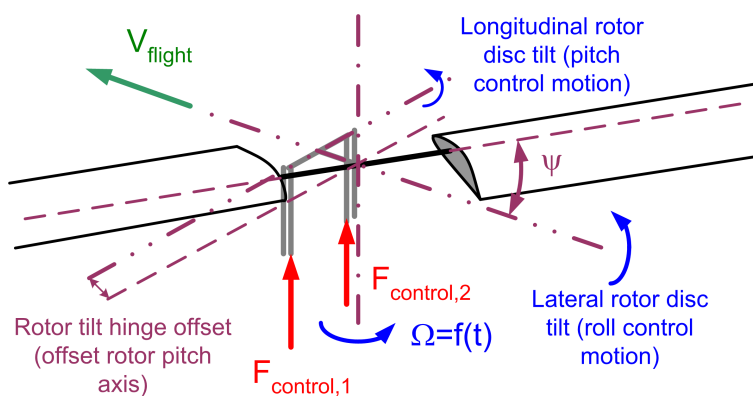


Figure 1.2: Typical rotor layout of a modern light gyroplane.

Early gyroplanes suffered of higher drag and lower flight speeds than conventional aircraft and were not capable of vertical take-off [12]. Later Cierva's designs as C.30 were able to perform a jump take-off, but Cierva did not manage to gather

the amount of money that was necessary for further development of his designs. He was the main driving force of the evolution of the gyroplane and this momentum disappeared when he died in an aircraft accident in 1936. Despite being proclaimed as the safest flying machines with best handling qualities, gyroplanes experienced sudden regression. Competition got much tougher due to arrival of first helicopter models. Enormous amounts of money were invested in development of a helicopter during Second World War, with the Sikorsky Co. awarded a grant to develop models V.S.300 and VS-316 that led to Sikorsky R-3, the first operational helicopter.

Domination of helicopters continued for the next sixty years despite several research projects focused on flight in autorotation. The main advantage of helicopters against gyroplanes was and still is their ability to hover. In the contrast to helicopters, the torque of gyroplane rotor does not come from an engine but from aerodynamic forces generated by airflow passing through the rotor disc. That is why hovering flight is an impossible task for gyroplane. Hovering flight is especially useful for search and rescue (SAR) operations and fast deployment of armed forces. Since military customers played a key role in aeronautical development during the major part of the second half of 20th century, gyroplanes were overshadowed by helicopters. There were only a few significant investments into gyroplane technology since then. A handful of experimental gyroplanes or compound rotorcraft (gyrocopters or gyrodynes) were partially successful (McDonnell XV-1, Fairey Rotodyne or Kamov Ka-22 and few others) but all efforts to re-introduce gyroplanes in large scale were unsuccessful. Many projects were ceased because technology required by the design was not mature enough at the time - this is especially true in case of Fairey Rotodyne (see Figure 1.3).

However, several limitations that are inherent to helicopters were identified during their evolution and operational use. The maximum speed of horizontal flight of a helicopter is restricted by compressibility effects on advancing side of the rotor disc and by reverse flow (and dynamic stall) on the retreating side of the disc. Since the



Figure 1.3: Fairey Rotodyne. Reproduced from [3]

main rotor represents the only source of forward thrust of conventional helicopters, they are less efficient in forward flight than fixed wing aircraft. Despite significant progress in rotor aerodynamics and structural dynamics, some of these problems remained unsolved.

Many of these shortcomings are not present in gyroplanes. Forward flight performance of a rotor in autorotation is less degraded by compressibility effects and dynamic stall since rotor speed and also rotor loading is lower. This is partly given by the fact that the rotor doesn't have to produce propulsive force during the flight and is used solely for the generation of lift. Gyroplanes also offer a flight performance that combines speed and efficiency of fixed-wing aircraft with the capability for extremely short take-off, vertical landing and low-speed flight similar to helicopters [7]. Gyroplanes are of much simpler design and therefore they are lighter, more reliable and require less maintenance than helicopters. Hence gyroplanes can be used as low-cost alternative of helicopters or VTOL replacement of conventional fixed-wing aircraft. The concept of a gyroplane may be especially suitable for a role of reconnaissance or combat UAVs.

The progress in aerospace technology that was achieved during past thirty years may indicate that it is the time for revival of gyroplane design. There is hope that application of new technologies can remove shortcomings of the concept and that gyroplanes can successfully compete with both helicopters and fixed wing aircraft. The need for higher speeds, better flight performance and rising cost of fuel have drawn the attention of several aerospace manufacturers back to gyroplanes. Carter Aviation Technologies (CAT), a US-based aerospace company has developed the CarterCopter, a demonstrator of an advanced gyroplane design (see Figure 1.4). CarterCopter became the first rotorcraft in aviation history to break the $\mu = 1$ barrier (i.e. achieved rotor advance ratio equal to one). This technology demonstrator was also recognized by US Army as a possible solution for its HeavyLift initiative [14]. Unfortunately, CarterCopter's only prototype suffered several accidents and was severely damaged in a crash in summer 2005 [15]. Test flights of the vehicle did not resume after this incident even though the CarterCopter was repairable. New technologies and knowledge gained during the programme are being used within new design projects at CAT.



Figure 1.4: CarterCopter technology demonstrator built by Carter Aviation Technologies, Inc., USA. Reproduced from [4]

Groen Brothers Aviation (GBA) is another American company that specialize in design and manufacturing of gyroplanes and are developers of the Hawk IV (see Figure 1.5), the only turboshaft-powered gyroplane. GBA Hawk IV was successfully

deployed as security monitoring aircraft during the Winter Olympic Games in Salt Lake City in 2002. GBA was awarded a contract with US Defence Advanced Research Project Agency (DARPA) and is working on a project of compound aircraft that will utilize some features of gyroplane design into a demonstrator of high-speed VTOL aircraft. Current interest in the concept suggests that gyroplanes are being seriously considered as candidates for the next generation of VTOL category aircraft.



Figure 1.5: Groen Brothers Aviation Hawk 4 gyroplane is powered by a turboprop engine. Reproduced from [5]

A self-launched version of the CQ-10A Snow Goose cargo UAV represents one of the first gyroplane UAVs. It uses a pre-rotated main rotor in combination with a pusher propeller and is capable of jump take-off. The vehicle is being used by the US special forces (see figure 1.6).

Although use of gyroplanes for commercial purposes was extremely limited ever after Second World War, they remained quite popular among amateur pilots. Interest in gyroplanes as recreational vehicles grew even stronger during last few decades. Availability of gyroplanes kits together with simplicity of the design and low operational costs helped to increase the number of gyroplanes in USA, Australia and also in Europe. Some of small manufacturers of light gyroplanes became quite successful - for example Wing Commander Ken Wallis [16], Dr. Igor Bensen and Vittorio Magni [17]. Many light gyroplanes were and still are manufactured by relatively small companies with only limited access to the latest technologies.



Figure 1.6: MMIST CQ-10A Snow Goose UAV in a gyroplane configuration. Reproduced from [6]



Figure 1.7: Wing Commander Ken Wallis and one of his gyroplanes.

Unfortunately, light gyroplanes in the UK were involved in a series of fatal accidents between 1989 and 1991 and the accident rate remained very high throughout 1990's [2; 18; 19] - see figure 1.8.

Between 1992 and 2001, number of accidents dropped (see figure 1.9) but the fact that there are less than 100 gyroplanes registered in the UK gave average rate

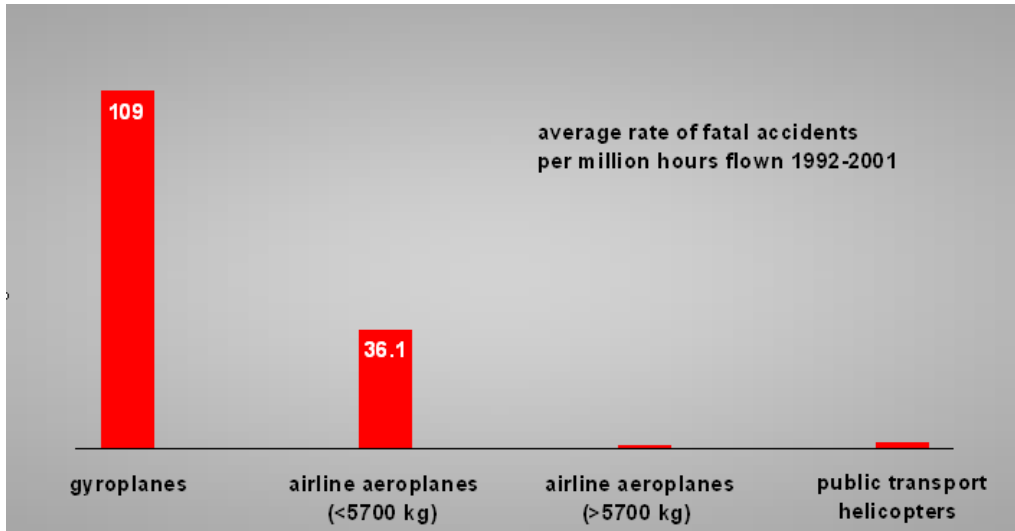


Figure 1.8: A comparison of accident rates of different types of aircraft. Reproduced from CAP 735 CAA Aviation Safety review.

of fatalities of 109 per million flight hours [2; 18].

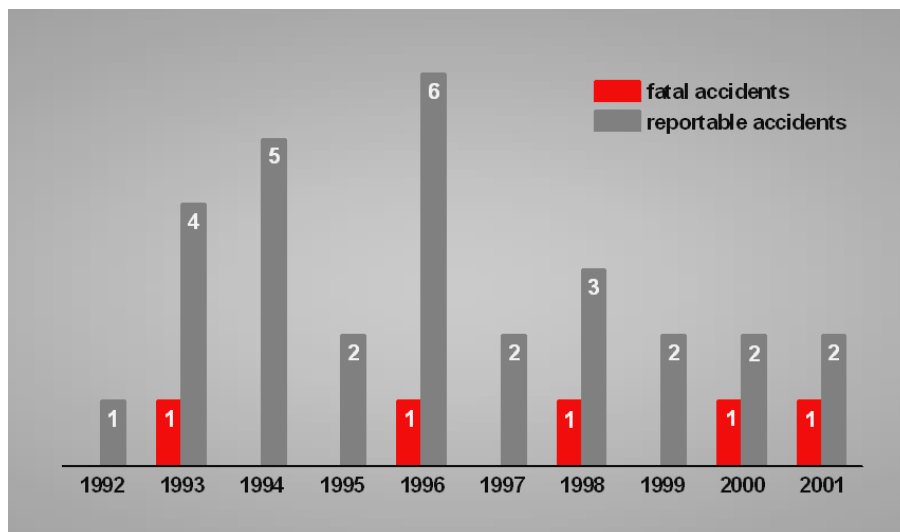


Figure 1.9: Time history of the number of gyroplane accidents within UK. Reproduced from CAP 735 CAA Aviation Safety review.

Following the conclusions of the Air Accidents Investigation Branch (AAIB), decision was made to review the British Civil Airworthiness Requirements for gyroplanes (BCAR Section T). Very little data on gyroplane flight mechanics and handling qualities were available in the literature at the time. UK Civil Aviation Authority (CAA UK) contracted the Department of Aerospace Engineering, University of Glasgow to investigate aerodynamics and flight mechanics of the gyroplane.

Several research projects were undertaken, most of them dealing with aerodynamics and flight handling qualities of gyroplanes. Wind tunnel measurements of a typical light gyroplane in several different configurations were performed and the data were used as an input into an advanced gyroplane flight dynamics simulator [20]. The generic rotorcraft mathematical model RASCAL was modified for this purpose [2; 21]. The resulting model was then verified with the aid of two sets of flight test data obtained during flight trials. Flight measurements were carried out with the aid of Montgomerie-Parson gyroplane (UK registration G-UNIV) that is owned by the Department of Aerospace Engineering, University of Glasgow. G-UNIV can be described as typical modern light gyroplane and thus it was well suited for the job. Results of the research project were recognized internationally and rebutted an argument that many of fatal accidents were caused by modifications of pod or tail plane of the gyroplane [2; 8; 18; 22].



Figure 1.10: University of Glasgow Montgomerie-Parsons gyroplane (G-UNIV)

This research work carried out at the University of Glasgow represented significant contribution in the field of gyroplane aerodynamics and flight mechanics. The causes of most of the accidents in the UK were determined, and mostly they were attributed to poor pilot handling or maintenance related component failure. Often, however, one of the features of the accidents reported by witnesses or revealed by

post-accident inspection was mechanical failure of the rotor blades (e.g. delamination of composite blade structure), which could be attributed to the occurrence of an aeroelastic instability [2; 18]. There is a suspicion that rotor speed dropped to zero or to a very low value during some of the fatal accidents. In some cases, investigation revealed the presence of large forces in controls that the pilot was not able to cope with [18; 19]. One of the main driving forces in undertaking this research is that virtually no research work investigating coupled bending-torsion-rotorspeed rotor dynamics or aeroelastic stability of rotors in autorotation was published to the date. Since rotor aeroelastic instability was identified as a possible cause of some of the accidents, decision was made to gain more knowledge on aeroelasticity of autorotating rotors. After all, Cierva had to deal with aeroelastic problems on his gyroplanes and aeroelasticity has caused troubles in rotorcraft design and development ever since then - see figure 1.11.

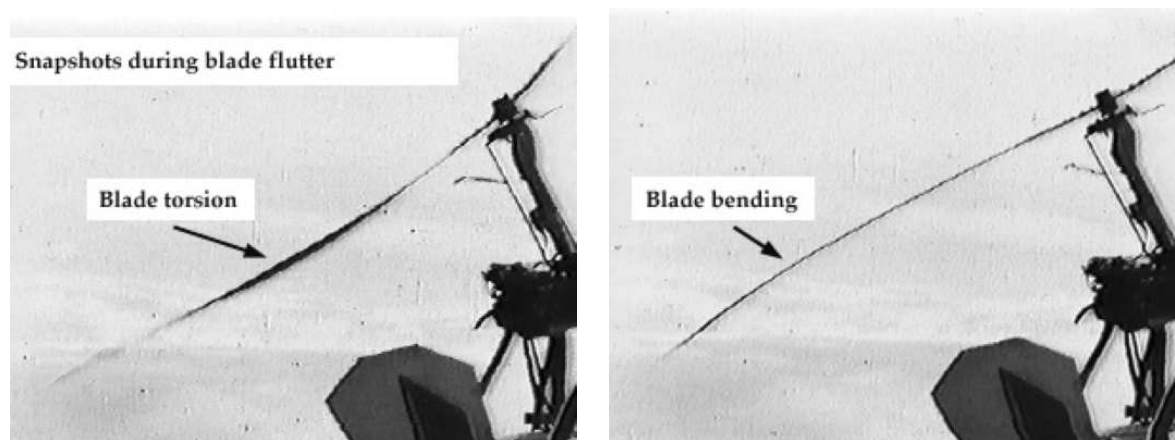


Figure 1.11: Snapshots of blade deflections during aeroelastic instability of a gyroplane rotor. Reproduced from a footage of the Australian Civil Aviation Safety Authority (CASA).

Cierva's problems with excessive torsion of rotor blades forced designers of the first modern helicopters to use symmetrical (uncambered) airfoils. Better understanding of helicopter rotor dynamics allowed use of cambered, high-performance airfoils in later generations of helicopter designs. Excessive torsion of rotor blades was avoided with the aid of stiffer rotor blades and amended arrangement of blade hinges (e.g. δ_3 kinematic coupling).

Since the speed of gyroplane rotors is not mechanically restricted, it depends on aerodynamic loading of the rotor. Reflex camber airfoils are used in the design of modern gyroplane rotors as they generate positive (nose-up) pitching moment that reduces rotor torque and hence decreases aerodynamic loading. This allows establishing of a balance between rotor speed and span-wise distribution of blade incidence.

Since both hub layout and the aerodynamic properties of modern autogyro rotors are different from those used in helicopters, aeromechanical behaviour of a gyroplane rotor and a helicopter rotor differ as well. Nevertheless, current British airworthiness requirements (BCAR Section T) for blade mass balance to avoid pitch-flap flutter are the same as for helicopters. This dissertation investigates unstable modes of rotors in autorotation with focus on gyroplane rotors. The author's thesis is that the gyroplanes display some unique aeroelastic behaviour due to different rotor design and its windmilling mode of operation. Since the aeroelastic instability that can occur in an autorotating rotor is essentially a pitch-flap flutter coupled with variable rotor speed, the current BCAR-T mass balance guidelines are satisfactory. However, similar aeroelastic instability can be initiated by stall of the rotor blades or reduction of rotor speed during an extreme maneuver. Hence BCAR-T might need to be expanded in order to include these new findings.

1.2 Aims and Objectives

The aim of this research work was to investigate aeroelastic behaviour of gyroplane rotors with focus on hazardous rotor configurations and flight regimes. The results of the work are also fully applicable to helicopter rotors in autorotation. A mathematical model had to be created during the research project since no suitable modelling tools were available. In order to fulfil the aim of the research project,

following objectives had to be met.

i) Literature survey was carried out at the very beginning of the research project in order to gain more knowledge on aeromechanics of autorotating rotors and find out how much research work was published to the date. Revision of available literature also provided summary of theoretical principles and modelling techniques that were suitable for the current research project that can be found in the Chapter 2 of this work.

ii) Development of a stand-alone mathematical model of the aeroelastic behaviour of a rotor in autorotation represented a major part of the research project. A simplified version of the model was developed during the initial phase of the project in order to test the proposed model structure and modelling techniques. The first generation of the 'Aeroelastic Model of a Rotor in Autorotation' code (*AMRA*) was developed in the SIMULINK computer package. Work on the first generation of the model helped to verify functionality of all model components and define convenient configurations for each of them. Development of the early versions of the model also clearly showed the need for more powerful and flexible computing environment.

Completion of the first generation of *AMRA* paved the way for evolution of a more comprehensive and detailed version of the model that would meet any future requirements of the project. The second generation of the model is coded in the MATLAB programming language (M) and uses a more sophisticated model of the rotor blade structural dynamics based on a finite element method approach. The model was gradually tailored to suit the needs of the research, which allowed study of the influence of the fidelity of individual components of the model on its overall performance. It consists of three main blocks - a model of the blade aerodynamics, a model of the blade structural dynamics and dynamic inflow model. Chapter 3 of this work contains a review of the analytical methods used in the model. The open architecture of the model made it easy to modify and to expand gradually during the

research project. *AMRA* was designed to be generic so that it is possible to switch between several different configurations of model blocks - see table 1.1. Hence the model could be easily used for prediction of stability of new or modified gyroplane rotor configurations as it is shown in the Chapter 6.

Table 1.1: An overview of the main building blocks of *AMRA* model

BLOCK	OUTPUT	DESCRIPTION
AERODYNAMICS	Aerodynamic forcing	Incompressible quasi-steady OR Unsteady Blade Element Method (incompressible); Enhanced polynomial fit of blade aerodynamic properties (compressibility and non-linear aerodynamics included)
INFLOW	Rotor induced velocity	Glauert's semi-empirical inflow model OR Modified Peters-HaQuang dynamic inflow model (1DoF OR 3DoF)
ROTOR DYNAMICS	Dynamic behaviour of rotor blades	Model of rotor blade dynamics using equivalent spring stiffness OR slender beam FEM (1D)

iii) The physical properties of a gyroplane rotor blade represent crucial input parameters of the model. The majority of light gyroplane rotor blades are manufactured in relatively modest conditions and hence their physical properties are not well documented. A pair of McCutcheon rotor blades was subjected to a series of experimental measurements in order to determine basic physical properties of typical gyroplane rotor blades. These experimental measurements played important role in the project since virtually no data on properties of the type of rotor blades had been published to the date. Thorough description of the experiments along with the measured data can be found in Chapter 4. The data were used as input parameters for the *AMRA* model and also played important role in validation of the model.

iv) To gain confidence about its accuracy, the aeroelastic model had to be verified before it was used for research purposes. As it can be seen in Chapter 5, functionality of all components of the *AMRA* mathematical model was tested throughout its development. The aerodynamic block and dynamic inflow model were verified with

the aid of data from flight measurements carried out by NACA (today's NASA) in 1950's and other data from open literature. Main part of model verification work was focused on the structural dynamics block of the model since it represents its most complex component. Predictions of static deflections in both torsion and bending were validated against analytical results. Predictions of blade dynamic behaviour were verified with the aid of both experimental data and predictions of similar, validated models. Results of the model of rotor blade teeter were compared against G-UNIV flight test data.

Once verified, the *AMRA* model was used for modelling of aeroelastic behavior and flight performance of rotors in autorotation.

v) A series of parametric studies was performed in order to investigate the effect of selected blade design parameters on performance and stability of a rotor in autorotation. Chapter 6 of this work summarizes the results of these parametric studies.

vi) The effect of complexity of the model of blade structural dynamics on fidelity of the whole aeroelastic model was also investigated. The study helped to identify necessary level of modelling required to achieve valid solutions. The outcomes of the study are described in Chapter 5 of this work.

vii) The major part of the research work was focused on determination of an aeroelastic stability boundary for autorotating rotors with focus on gyroplane rotors. Detailed analysis of aeroelastic behaviour of rotors in autorotation as predicted by the *AMRA* can be found in Chapter 7.

Results of the simulations helped to identify rotor configurations that might have catastrophic consequences. Hence it was possible to formulate basic design criteria for gyroplane blades. The gyroplane community will be advised on conclusions of

this work and safety issues closely connected with aeroelastic behaviour of gyroplane rotors by UK CAA, sponsors of the research.

1.3 Modelling Techniques

As the mathematical modelling efforts form a major part of this thesis, it is worthwhile giving some over-arching description of the background philosophy of the model development, and some detail of the modelling techniques used. The *AMRA* model allows investigation of rotor blade aeroelastic behaviour both in time-marching regime and in the frequency domain. *AMRA* can use several different integration schemes but classical rectangular or trapezoidal rules were found to be sufficient and relatively fast. The model has an open architecture and modular programming philosophy was used where possible, i.e. there is single data array that is shared and modified by individual model blocks. This configuration of the model allows easy modifications and expansion of the model and makes it relatively generic. Each rotor blade is modelled individually in the model and it is possible to choose either hingeless, teetering or bearingless rotor configuration. A comparison of different rotor hub designs can be found in figure 1.12.

The aerodynamic block of the model can use quasi-steady aerodynamics or Theodorsen theory of unsteady aerodynamics to compute aerodynamic loading of each rotor blade. Incorporation of Theodorsen's theory improves fidelity of the model for high values of reduced frequency. Aerodynamic coefficients of individual blade cross-sections are calculated with the aid of modified Prouty's polynomial approximation of aerofoil aerodynamic characteristics. This approach allows inclusion of both stall (non-linear aerodynamics) and compressibility effects. A simple form of the tip loss factor was employed to account for 3D flow effects at the tip of each rotor blade.

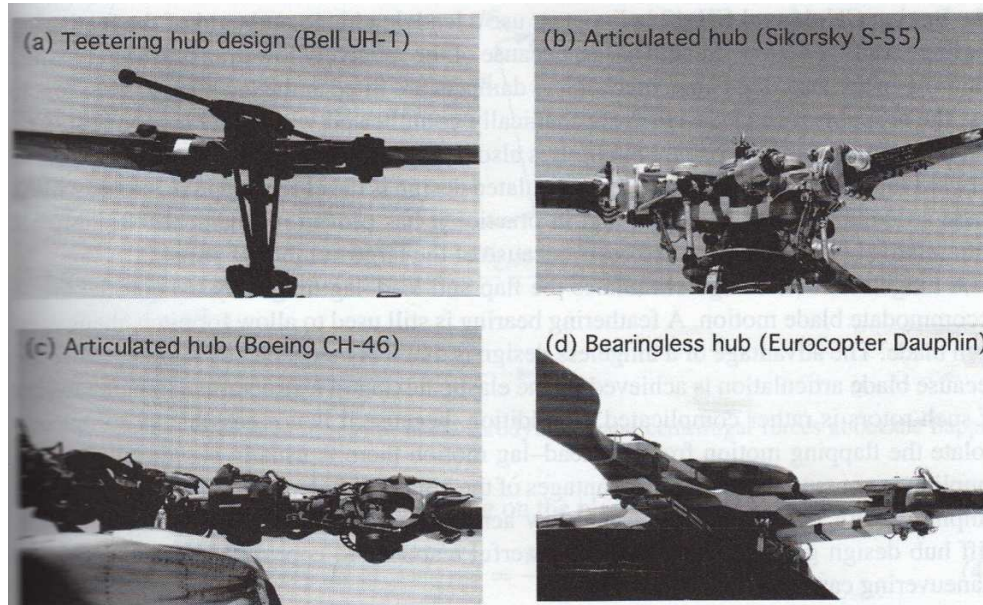


Figure 1.12: Comparison of different rotorcraft hub designs. Reproduced from Leishman [7].

Special care had to be taken when modelling structural dynamics of gyroplane blades. Flight trials of Cierva C.30 proved that gyroplane rotor blades have to cope with significant deflections in twist and bending [23]. Flexibility of gyroplane blades can affect rotor behaviour significantly since the rotor torque of a gyroplane rotor blade is generated solely by the aerodynamic forces. Consequently a gyroplane rotor may experience significant changes of rotor speed and corresponding centrifugal stiffening. Extensive elastic deformation of rotor blades can result in catastrophic decrement of rotor speed and loss of lift.

The Lagrange's equation is used for derivation of blade equations of motion and is solved with the help of two different methods. The first one uses equivalent spring stiffness approach (i.e. 'rigid' blade model) and it is especially useful for analysis of rotor blade teetering motion or blade rotation. The finite element method represents second modelling method used in the structural block of *AMRA*. FEM is significantly more complex but also much more accurate than 'rigid' rotor blade model using equivalent blade stiffness. The *AMRA* model gives an option to select which method is to be used so that the more complicated (and hence slower) FEM method can be used only where it is necessary. Since the rotor speed of a gyroplane

rotor can change dramatically, the method of assumed modes (modal approximation) that is widely used in helicopter aeroelastic models is not suitable. Hence the direct form of the finite element method had to be used instead. Slender beam theory is used for formulation of 1-D FEM model of blade coupled bending-torsion-rotation.

The Peters-HaQuang dynamic inflow model modified by Houston and Brown was used for calculation of induced velocity of the rotor. This method is well validated and several relevant publications can be found in open literature [24]. The *AMRA* model can also use semi-empirical inflow model based on results of experimental flight measurements of gyroplane flight mechanics [25]. However, this type of inflow model is of limited use and it is less refined than the dynamic inflow model.

1.4 Structure of the Thesis

The pattern of chapters of this work follows individual stages of the research project. A literature survey that can be found in the following chapter describes and analyses the research work done to date in the field of aerodynamics and aeroelasticity of gyroplane rotors and rotors in autorotation. Most relevant publications dealing with helicopter aerodynamics and aeroelasticity are included in the review also.

Chapter 3 outlines the modelling techniques used in the *AMRA* model and a separate section is dedicated to each of model blocks. A summary of the mathematical modelling of rotor blade aerodynamics is followed by description of model of blade structural dynamics and dynamic inflow model.

Experimental measurements of physical properties of a typical light gyroplane rotor blade are described in the fourth chapter. Span-wise distributions of blade mass, torsional stiffness, flexural stiffness, position of centre of gravity and position of elastic axis were determined during the experiments and the data are provided in

the chapter also.

The fifth chapter of this work shows how the model was verified and presents details on validation of individual blocks of the *AMRA* model. Although verification of the aerodynamic block of *AMRA* is presented, the main part of the chapter is focused on verification of the model of rotor blade structural dynamics. Experimental measurements, analytical results and predictions of other validated predictive tools are used for verifications of the *AMRA* model.

The next part of the thesis deals with actual results of *AMRA* simulations. Outcomes of the parametric studies are included in the sixth chapter and aeroelastic behaviour of different configurations of gyroplane rotors is discussed in the seventh chapter. Stability boundaries estimated by the model using time-marching approach are compared with results of eigenvalue analysis. Analysis of data obtained with the aid of the model yields basic design guidelines for light gyroplane rotor blades.

Outcomes of the research work are discussed in the concluding chapter. The goals achieved during the project are contrasted with initial aims and objectives of the work too. Rotor blade design parameters that have the strongest influence on the performance and aeroelastic stability of rotors in autorotation are reviewed. The shape of the aeroelastic stability boundary of a gyroplane rotor that was identified with the aid of *AMRA* is contrasted with a typical pitch-flap flutter stability boundary of helicopter rotors. Recommendations for rotor design and testing are given based on the results of the parametric studies and on the fact that the effect of the extra degree of freedom in rotation on flutter onset was found to be negligible. Brief overview of possible future work and further development of the model is also given in the final chapter.

Chapter 2

Literature Review

Although tremendous progress has been made in the field of aerodynamics and aeroelasticity of helicopter rotors during last sixty years, many problems remain to be solved. Thanks to the high complexity of the rotor flow field and the complicated dynamics of helicopter rotor blades, some problems could not be solved until recent times when the required computational tools were accessible.

Helicopter forward flight features harmonic variation of both inflow speed and inflow angles and high oscillatory loading [11; 12; 26; 27]. The value of the Mach number of the inflow is dependent on span-wise position and azimuth and can reach transonic values toward the tip at the advancing side of the rotor disc. Since rotor blade moves against direction of flight at the retreating side of the rotor disc, a reverse flow region is formed at the inboard part of rotor blades with the possibility of dynamic stall further outboard. The existence of at least two blade tip vortices and their interaction with the rotor blades results in complex rotor wake and high vibratory loads. Rotorcraft blades are subjected to harmonic loading and high centrifugal forces, and coupled pitch-flap-lag degrees of freedom of the rotor blades yield complex equations of motion. Rotor blades can suffer a whole range of aeroelastic and aeromechanic instabilities, from classical bending-torsion flutter and stall flutter to pitch-flap-lag instability and ground resonance. This makes rotorcraft engineering perhaps the most challenging discipline of aerospace engineering.

Since the gyroplane represents the first operational type of rotorcraft, some of the oldest research works on rotary wing aircraft are investigating physics of autorotating rotors. Some of the analytic methods developed specifically for gyroplanes were later used in helicopter design. Rotorcraft research has made remarkable progress since then and computational tools used by pioneers of rotorcraft engineering can't be compared with capabilities of modern computers. Hence it is remarkable that many of mathematical tools and theories that originated many decades ago are still broadly used and are still considered to be sufficiently accurate.

2.1 Review of Relevant Research on Helicopter Rotor Aerodynamics and Dynamics

2.1.1 Aerodynamics of Helicopter Rotors

Some of first research works dealing with rotorcraft aerodynamics used theories developed for analysis of aerodynamics of propellers or fixed wing aircraft such as the blade element method or momentum theory (also known as *actuator disc theory*).

Glauert [28] applied his expertise in propeller aerodynamics [29] in the modelling of gyroplane rotors. His work led to simple but powerful tools suitable for application in rotorcraft aerodynamics. Both momentum theory and blade element theory (BEM, sometimes also referred to as the *blade strip analysis*) are described in detail in this work. Although both BEM and momentum theory represent relatively simple tools, they proved to be efficient, fast and relatively accurate and are still very popular. The combination of blade element method and quasi-steady aerodynamics has been successfully used in many studies on rotorcraft aeromechanics since the early days of rotary wing aviation [9; 12; 27; 30; 31]. Rotor blade tip loss can be included in BEM with the aid of tip loss factors that were introduced by Prandtl and later

by Goldstein and Lock [12; 27]. Prandtl's tip loss function represents more complex representation of tip loss effect and it is dependent on rotor disc inflow angle [27].

Despite the possibility of the tip loss modelling, the ability of BEM to capture 3D aerodynamic effects is very limited. This together with the need to input detailed aerodynamic data of blade cross-sections, represents major drawbacks of BEM [12; 27]. Hence BEM is suitable for tasks that require short computational time and where detailed modelling of 3D flow is not necessary. The use of more comprehensive methods such as panel methods or finite volume methods for modelling of rotor blade aerodynamic loading results in more accurate predictions of the effects of 3D airflow but it significantly increases model complexity. This is especially true in case of rotorcraft aeroelastic models that deal with solutions of complex systems of blade equations of motion. That is why use of complicated CFD aerodynamic models in simulation of rotor blade aeroelastic behaviour is usually avoided if possible as it would cause dramatic increase in computational time. Simplified aerodynamic models as BEM or momentum theory are still used in many modern rotorcraft models as VTM [32], RASCAL [33] and many others.

Compressibility effects play important role in the aerodynamics of rotor blades as aerodynamic characteristics of blade sections change with Mach number and the airflow can become transonic in the blade tip region [12; 26; 27]. Airflow compressibility also has significant implications for rotor blade aeroelastic behaviour [26]. It can be seen from the work of Prouty [8], Carpenter [10] and Racisz [34] that Mach number influences lift curve slope of the linear part of the lift curve as well as the maximum lift coefficient and stall angle. Compressibility effects can not be neglected if Mach number exceeds value of 0.3. The effect of increasing Mach number on aerodynamic characteristics of an airfoil can be seen in figure 2.1.

Since blade sections may operate at very high angles of attack at the retreating side of rotor disc, effects of blade stall should be captured by an aerodynamic model

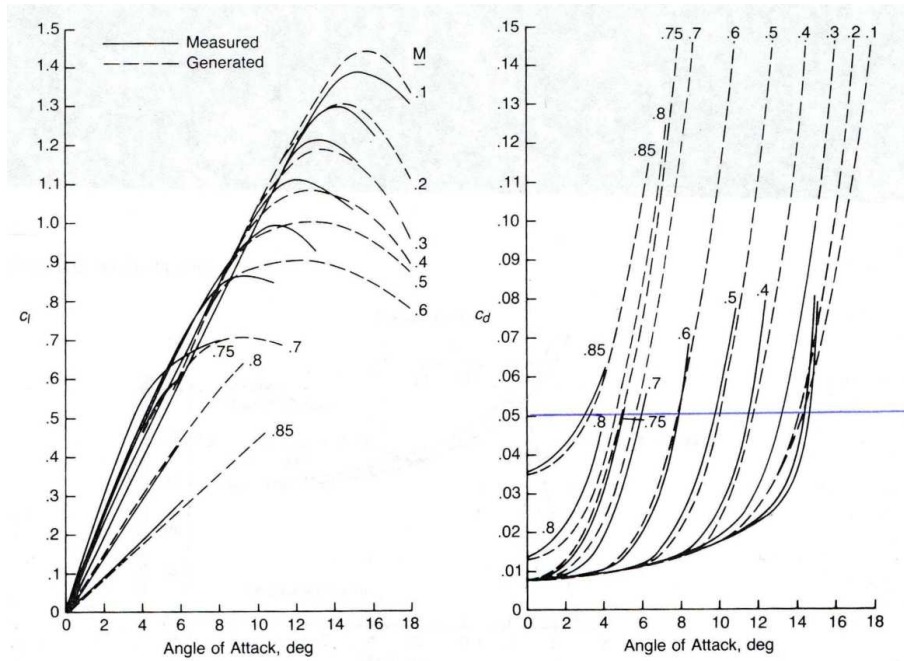


Figure 2.1: Change of NACA 0012 lift and drag curve with Mach number. Reprinted from Prouty [8].

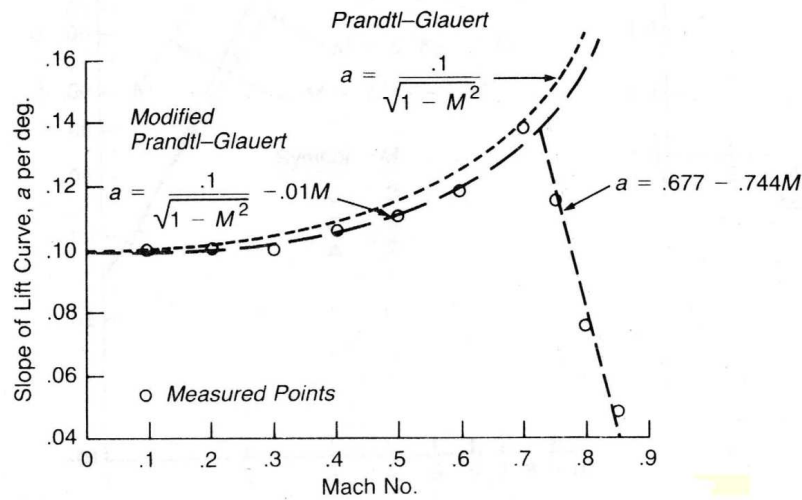


Figure 2.2: Change of lift curve slope of NACA 0012 with Mach number; reprinted from Prouty [8]

too. Hence use of linear aerodynamics (i.e. using assumption of linear lift-curve slope) is often not sufficient and may not result in correct predictions of blade aerodynamic loading. Look-up tables including non-linear aerodynamic data of blade sections for different Mach numbers represents the simplest way to incorporate stall and compressibility effects into a simplified aerodynamic model of rotor blades (e.g. BEM).

Polynomial fit of blade aerodynamic data can be used as a more elegant alternative to look-up tables [12]. Different forms of this method were developed by Prouty [8], Beddoes and others [12]. Approximation of lift, drag and moment curves of blade sections with the aid of polynomial or exponential functions of α and M allows to capture aerodynamic characteristics of the blade for the full range of angles of attack. However, experimental data from aerodynamic tunnel tests for the given airfoil and for sufficient range of angles of attack have to be obtained first. Unfortunately, such data are extremely scarce and only few works can be found in open literature [12; 35]. High angle of attack wind tunnel measurements of NACA0012 airfoil is the most commonly found experimental data [13; 36]. The amount of similar experimental data describing aerodynamic characteristics of cambered airfoils is extremely limited [37]. There are no open literature publications containing high angle of attack aerodynamic characteristics of reflex camber airfoils that are often used in modern gyroplanes. These airfoils are also widely used in tail-less aircraft design as reflex camber eliminates nose-down pitching moment that is present in any cambered airfoil. Although a comprehensive CFD evaluation of NACA 8-H-12 airfoil was performed in WHL (today's Augusta-Westland Helicopters) by A. Brocklehurst, only internal technical report was issued and no data were published in open literature.

Quasi-steady formulation of blade aerodynamics becomes insufficient if values of reduced frequency exceed a critical value ($k \geq 0.05$) [11; 12]. Theodorsen's theory [38] and other work based on his research became widely used for modelling of unsteady aerodynamics. Theodorsen included both non-circulatory effects from flow acceleration and circulatory effects in his equations of unsteady aerodynamics and introduced the so-called Theodorsen's function $C(k)$ [11; 12; 26]. Theodorsen's theory was later extended by Loewy, Sears, Wagner and others in order to include the effects of time history of unsteady airflow into the consideration [12; 26]. Theodorsen's theory is a frequency domain theory and hence it is less convenient for

analysis of rotor blade aeroelastic stability, these new time-domain methods soon became relatively popular [26].

Blade dynamic stall might occur on the border of the reverse flow region at the retreating side of a rotor disc. Dynamic stall causes excessive rotor loading and vibrations and represents a major limitation in performance of modern rotorcraft. Dynamic stall of rotor blades can result in blade stall flutter, a single degree of freedom instability in blade torsion that is characterised by limit cycle oscillations in blade angle of attack [12; 26]. A large number of studies were performed in order to investigate the phenomena of dynamic stall and several semi-empirical dynamic stall models were developed. Dynamic stall models such as the ONERA dynamic stall model and Leishman-Beddoes model were successfully used in many studies [26; 39]. Semi-empirical dynamic stall models require much shorter computational times than CFD and are also considerably simpler. However, since empirical coefficients derived from experimental wind tunnel data are used in these models, their use is limited to airfoil shapes for which the data are available. Hence, only advanced CFD models are capable of purely analytical modelling of stall flutter [12]. Since modern light gyroplanes are capable of relatively low flight speeds and their rotor blades are relatively stiff in torsion, occurrence of dynamic stall and stall flutter is unlikely. No publications dealing with modelling of stall flutter of gyroplane rotors can be found in open literature.

Values of rotor induced velocity have to be predicted correctly in order to obtain realistic span-wise distribution of the values of rotor blade inflow angle. Induced velocity is generated when the kinetic energy of rotor blades is transferred to air passing through the rotor disc and results in acceleration of the airflow. Higher speeds of the airflow lead to decrease of dynamic pressure downstream, and that in turn causes wake contraction [12; 27]. Leishman [12] and Bramwell [27] give concise overviews of rotorcraft inflow models developed to date. The majority of inflow models are based on the approximation of induced velocity distribution that was first proposed

by Glauert [28]. Classical estimation of induced velocity of hovering rotors based on momentum theory can be modified in order to capture inflow during forward flight [9; 25; 40]. Momentum theory uses a relation between velocity of descent and induced velocity based on the classical form of Bernoulli's equation [9; 12; 25]. Glauert [28] employed analytical prediction of the induced velocity of a rotor in hover in combination with weighting factors to account for the harmonic change of rotor blade aerodynamic loading during forward flight.

Great progress has been achieved in the field of inflow modelling since the early times of rotary wing aviation. Many different analytical models of helicopter rotor inflow emerged during the last sixty years. Many of them proved to be relatively accurate and were widely used for the modelling of helicopter aerodynamics. Refinement of the basic Glauert's inflow model resulted in several simple inflow models. Based on research of Coleman et al. [41], works of Drees [42], Payne [43] and Pitt and Peters [44] are considered to be most widely used. Mangler and Squire inflow model [12; 27] uses Fourier series to approximate the shape of induced velocity distribution over the rotor disc. Two types of loading, Type 1 (elliptic, high-speed loading) and Type 3 are combined with the aid of weighting factors by the method [12]. Inflow modelling was revolutionized in 1980's when first dynamic inflow models emerged. These models capture unsteady global wake effects that can be easily applied to entire rotor [12]. Dynamic inflow models developed by Pitt and Peters, Gaonkar and Peters, Peters and HaQuang and Peters and He represent the most up-to-date inflow models. Chen [40] provides a comprehensive survey of most modern dynamic inflow models (excluding 15-state Peters-He model [45; 46]).

2.1.2 Dynamics of Helicopter Rotors

Problems of structural dynamics and aeroelasticity of helicopter rotors are considered to be relatively well understood. Major progress in the field of helicopter rotor dynamics was achieved during last three decades of the 20th century thanks to

improvements in performance of modern computers and application of finite element analysis. Comprehensive summaries of up-to-date status of rotorcraft aeroelasticity is given by Friedmann [47] and Friedmann and Hodges [26]. The books of Bramwell [27] and Bielawa [11] also give detailed and extensive overview of the topic. Friedmann and Hodges [26] show that many different analytical methods have been developed in the field of rotor blade dynamics. Ranging from simple but elegant Lagrange's equations to computationally intensive but generic and powerful finite element analysis. The problem of rotor blade dynamics can be split into two major phases - formulation of blade equations of motion and their solution.

Compared to wings of conventional (fixed-wing) aircraft, rotorcraft blades are subjected to higher oscillatory loads and their dynamic characteristics are generally more complicated due to couplings of blade flexible deformations with blade rotation. While the offset of the elastic axis from the aerodynamic centre is often used as an important parameter in the aeroelastic analysis of fixed wing aircraft, offset of centre of gravity from the elastic axis plays the most important role in analysis of rotor blade aeroelastic stability [26]. Rotor blades are subjected to harmonic forcing caused by aerodynamic forces and centrifugal forces generated by blade rotation. Centrifugal forces are dependent upon rotor blade radius and cause additional blade stiffening. Coriolis forces are caused by combination of blade rotation and blade deformations and affect dynamic stability of rotor blades. Since rotational effects play important role in rotor blade dynamics and can not be neglected, extra terms have to be added into the equations of motion [27; 48; 49].

Blade degrees of freedom are mutually coupled, which has significant effects on blade dynamics. Hence equations of motion of a rotor blade have to be coupled too in order to describe blade behaviour correctly. Houbolt and Brooks [50] give derivations of combined equations of motion of bending and torsion of a rotor blade modelled as a slender beam. Aeroelastic equations of a helicopter rotor undergoing torsion and both flap-wise and chord-wise bending can be found in Kaza and

Kvaternik [39]. Ordering schemes can be applied to equations of motion to remove terms that are negligible [26]. Simplified and linearized forms of combined differential equations of blade bending and torsion can be found in open literature [11; 27].

Rotor blade dynamics can be described with the aid of the Newtonian approach which is, however, quite simplistic and can be quite problematic to apply to complex dynamics of rotor blades [11]. Equations of rotor blade dynamics can be obtained more conveniently via the extended form of Euler's equations of motion of a lumped mass [27]. However, so-called energy methods represent the most convenient way of derivation of equations of motion. Energy methods are based on the principle of virtual work and the principle of minimum potential energy [11; 27; 48]. Lagrange's equation is one of the most comprehensive and elegant examples of application of these principles. It can be applied even to complex dynamic systems and allows derivation of equations of motion via differentiation of expressions defining the kinetic and potential energy of a dynamic system. This can be done in an automated manner and hence Lagrange's equation is especially powerful in combination with modern mathematical software capable of symbolic expression manipulation, e.g. MATLAB, Mathematica or Maple.

Since aspect ratios of rotorcraft blades are high, they can be regarded as slender beams. Hence several simplifying assumptions can be made without significant effect on the predictive capabilities of the resulting analytical tools. Modelling of rotor blades as flexible, infinitely thin beams or a series of lumped masses is sufficient for many problems. Since the magnitude of blade loading due to rotation is dependent on span-wise position along the blade, rotor blades have to be discretized spatially. Discretization based on global or local (finite element) methods can be used, depending on method of solution of the equations of motion [26]. This yields a set of non-linear differential equations of motion.

Although it is possible to obtain an exact solution of the equations of motion

for a continuous system, applicability of this approach is extremely limited and in many cases solution is not possible at all [11; 48]. Simplifying assumptions have to be applied as approximate methods usually represent the only possible way of solving the blade equations of motion [48]. Global methods of solution of rotor blade equations of motion were widely used before the emergence of finite element analysis. These techniques solve blade equations of motion globally, i.e. over whole blade. But equations of motion of a rotor blade can become extremely complex, especially if more degrees of freedom are considered and appropriately coupled. As a result, use of global methods is limited only to relatively simple blade geometries and they still can be quite challenging to implement.

Simplified methods of solution of the blade equations of motion yield inaccurate predictions of blade dynamic behaviour. The assumption of perfectly rigid blades (i.e. blades with zero flexibility) results in significant simplification of the problem and perhaps represents the most primitive technique of modelling rotor blade motion. It is equivalent of using a single spring stiffness for each blade degree of freedom. Only one equation of motion has to be solved for each degree of freedom and blade geometry and physical properties can be integrated along blade span. This style of solution of the equations of motion is of limited use as it captures only zero-th (rigid) modes of blade motion [11; 27]. Hence accurate prediction of the blade dynamics is not possible and only rough estimates of blade deflections in torsion, flap-wise bending and chord-wise bending can be obtained. However, this approach can be conveniently used for problems where the assumption of a perfectly rigid blade is appropriate, e.g. modelling of blade rotation and teetering motion. It is also sufficient for fundamental flight dynamics modelling since the frequencies of vehicle body oscillations are much lower than natural frequencies of the rotor blades.

It can be presumed that the dynamics of a rotor blade can be described by a finite number of degrees of freedom and a finite number of modes. Although in reality infinite number of modes could be used to describe dynamics of a rotor blade,

sufficient approximation can be made with the aid of several dominant modes. *The method of assumed modes* belongs to the group of global methods and represents a fairly popular way of solving the DE of motion of rotor blades. A series of functions (mode shapes) are used for the first approximation of blade shape. Lagrange's method and the Raleigh-Ritz method are some of the most popular members of the family of methods of assumed modes. They allow estimation of modal shapes and corresponding modal frequencies. These methods are based on the fact that a function that satisfies both boundary conditions and differential equation of blade bending is a function that gives stationary value to Lagrangian of the blade [48]. A finite series of approximation functions (modal shapes) that also satisfy boundary conditions is assumed and substituted into the Lagrangian. The resulting system of equations is obtained using the condition of orthogonality of modes and it is essentially identical for both methods. Hence, mode shapes and modal frequencies can be calculated. Raleigh-Ritz method can be applied to broader range of problems than Lagrange's method (e.g. static equilibrium) [27; 48].

Galerkin's method is another method that is based on energy considerations and it represents perhaps most popular global method. It is widely used as it can be used in the case of non-linear or non-conservative problems that both Lagrange's and Raleigh-Ritz methods can not solve [27]. In Galerkin's method, an approximation function is substituted into the differential equation of blade motion. If n different mode shapes and frequencies are considered, it is transformed into a system of n differential equations [27].

Today the vast majority of practical problems are solved with the aid of local methods (i.e. finite element analysis). The finite element method (FEM) is a numerical method that gained high popularity during last few decades. It belongs to the group of so-called methods of lumped parameters and it originated in 1960's when world scientific community re-discovered a half-forgotten paper by Courant from 1943 [51–53]. FEM represents a powerful method of solution of differential

equations that, thanks to its universality, can be used for a wide range of applications. FEM also gave rise to Finite Volume Methods that are commonly used in Computational Fluid Dynamics (CFD) and other applications (e.g. thermodynamics etc.). In FEM, the rotor blade (or any other structure) is divided into a finite number of domains (i.e. elements) and a separate differential equation of motion is solved on each of these finite elements [27; 49]. Methods of weighed residuals are often used for solution of FEM problems. These methods use combination of trial functions and weighting (test) functions to approximate exact solution of differential equations. The collocation method, the least squares method and the Galerkin method are the most widely used types of methods of weighted residuals. These methods differ in the manner of definition of the weighting function [49].

Weak formulation of the methods of weighted residuals is used for FEM modelling. Piecewise continuous trial functions are defined at each domain (i.e. element) and blade equations of motion are solved simultaneously at each element [49]. This approach makes FEM a very robust and universal way of modelling structural dynamics. Modelling of blade torsional dynamics requires one degree of freedom (i.e. blade torsion) and linear or quadratic trial functions can be applied. Two degrees of freedom, blade local translation and blade slope together with cubic (Hamiltonian) trial functions are needed for modelling of both flap-wise and chord-wise bending of the blade [26; 49].

2.2 Review of Research on Aerodynamics and Dynamics of Rotors in Autorotation

2.2.1 Aerodynamics of Rotors in Autorotation

A review of research work that has been done on gyroplanes to date is given by Leishman [12]. The paper gives comprehensive overview of both theoretical and experimental research on gyroplanes from the very origins of rotary wing aviation

until recent days. It shows clearly that research on gyroplanes virtually ceased after helicopters came into the service. Hence certain aspects of gyroplane aeromechanics still remain relatively unexplored. In contrast to gyroplanes, the physics of helicopter rotors is relatively well understood and large number of publications can be found in the open literature. The need to use up-to-date analytical methods used in helicopter aerodynamics for modelling of gyroplane rotors emerged recently due to increased interest in this type of vehicle. If appropriately modified, modern analytical methods of helicopter aerodynamics and aeroelasticity can be used for analysis of gyroplane rotors.

A series of experimental flight measurements of gyroplane rotors and helicopter rotors in autorotation were carried out by NACA in USA and R.A.E. in the UK before Second World War [7; 9; 30; 54]. Data obtained during these measurements helped in the understanding of the physics of autorotation and validation of theoretical analysis of aerodynamics and flight mechanics of rotors in autorotation. Unfortunately, experimental measurements have shown that classical momentum theory is invalid for the windmilling regime of rotor operation (see Fig.2.3) [9; 12; 25].

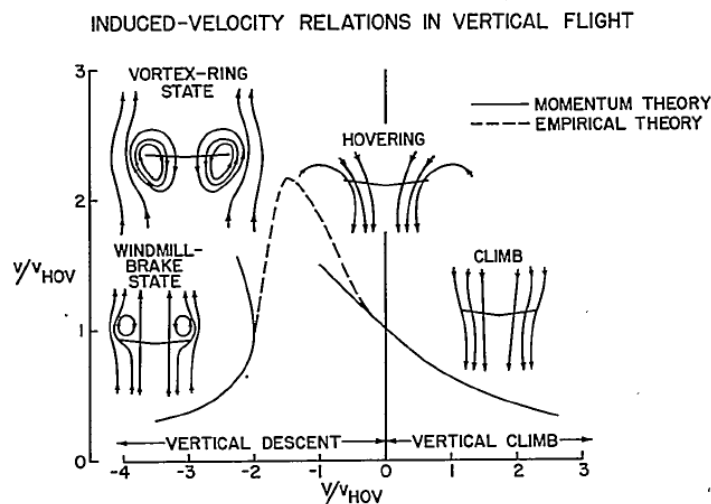


Figure 2.3: Relation of induced velocity and speed of descent as predicted by momentum theory. Reproduced from Gessow [9]

Hence the classical form of the momentum theory can not be used to describe the aerodynamics of autorotation. It is possible to assume that during autorotation, induced velocity is equal to speed of descent. This is known as *ideal autorotation* [27] and it can be used for estimation of basic parameters of autorotative regime of a rotor. However, it is of limited use and can not be coupled with BEM as the resulting vertical component of inflow velocity ($V_d - v_i$) is always zero. A few specialized inflow models were developed for rotors flying in autorotative regime. Glauert [28] showed that the combination of momentum theory, blade element theory and an empirical method of induced velocity calculation can be used. The relationship between vertical component of inflow velocity and speed of descent is captured with the aid of data from experimental flight measurements and wind tunnel data. Glauert's semi-empirical inflow model was later used and improved with the aid of new experimental data in NACA [31; 55].

Wheatley [56] showed that a combination of the blade element method with Glauert's semi-empirical inflow model can yield satisfactory predictions of performance of a rotor in autorotation. This type of simplified aerodynamic model of a rotor in autorotation was commonly used in NACA before and after the Second World War. Wheatley and Bioletti [30] describe in detail coupling of this type of aerodynamic model with a simple model of blade flapping dynamics. Nikolsky and Seckel [31] employed essentially identical methods to estimate the performance of a helicopter rotor in axial autorotative descent. The effects of blade twist and inclusion of blade section stall are studied also. Another research work of Wheatley [55] uses the same principles of rotorcraft aerodynamics to investigate dynamics of blade feathering in autorotation. This research report is of great significance as it investigates the effects of blade pitch angle and sectional drag coefficients on overall rotor performance.

Since rotor torque is generated purely by aerodynamic forces during autorotation, stable autorotative flight is not possible if aerodynamic angles of attack along

the blade are too high. Hence blade fixed incidence and induced twist (i.e. torsional deflections) are of great importance in autorotating rotors. A graphical method that allows estimation of the critical value of rotor blade pitch was first introduced by Vimperis [7]. Vimperis diagram is shown in figure 2.4.

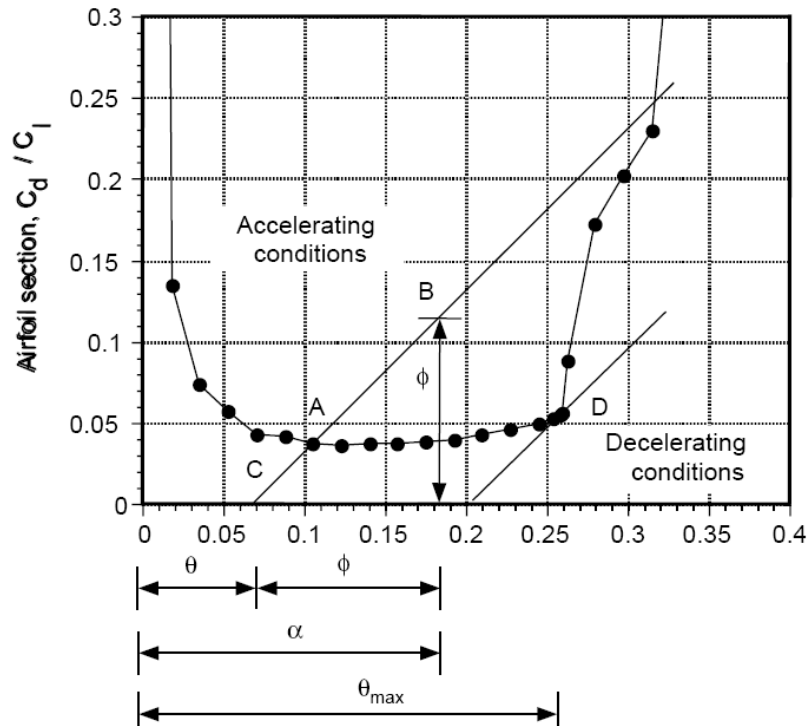


Figure 2.4: Vimperis diagram; reproduced from Leishman [7]

Sissingh [57] investigates blade flapping motion as well as the effect of different blade planform shapes on rotor performance. Quasi-steady aerodynamics using both rate of induced twist and flapping rate is applied to estimate rotor blade inflow angles and inflow velocities. Hufton et al. [23] applied a very similar approach to study the aeroelastic behaviour of a gyroplane rotor. Agreement of the author's predictions with experimental measurements clearly shows that relatively accurate predictions can be obtained with the aid of simplified models of blade aerodynamics and dynamics.

The majority of recent research work on aerodynamics of gyroplane rotors has been done at the Department of Aerospace Engineering, University of Glasgow un-

der CAA UK research contracts. Wind tunnel measurements of scaled model of a light gyroplane were carried out for several different flight configurations. More details on the research programme and results of the experimental measurements were published by Coton et al. [22]. Aerodynamic characteristics and stability derivatives obtained during the measurements were used for modelling of gyroplane flight dynamics. Houston [20] describes validation of modified advanced model of rotorcraft flight dynamics *RASCAL* [21] and the outcomes of subsequent simulations are presented in Houston [33]. A CFD model of rotorcraft aerodynamics based on vorticity transport model (VTM, see [32]) was coupled with *RASCAL* model in order to include the effect of rotor wake. Peters-HaQuang dynamic inflow model was also modified by Houston and Brown to allow modelling of inflow of a rotor in autorotative flight regime [24]. This type of inflow model is more suitable for modelling of gyroplane rotor inflow than semi-empirical inflow models as it is more generic and it can capture a perturbational inflow (unsteady wake effects) [26]. More details on the research work can be found in Houston and Brown [24]. Studies of gyroplane flight dynamics carried out at the University of Glasgow were summarized by Thomson et al. [18]. Investigation of gyroplane flight dynamics revealed that gyroplanes are rather less sensitive to changes in configuration of horizontal stabilizer or the vehicle pod. However, the position of centre of gravity above the engine thrust line was found to be destabilizing, causing unstable phugoid mode with relatively high period of oscillation. Results of simulations of gyroplane flight dynamics also showed that dynamic stability characteristics of gyroplanes resemble a mix of stability characteristics of fixed wing aircraft and helicopters.

2.2.2 Dynamics of Rotors in Autorotation

The development of early gyroplane designs revealed that their rotors can suffer of high torsional and flexural deformations thanks to variable centrifugal stiffening. Despite these problems very little work was done in the field of aeroelastic modelling of rotors in autorotation as Leishman [12] shows in his paper. This is especially true

if considering the modelling of coupled bending-torsion of rotor blades (e.g. modelling of classical flutter). Again, the aeroelastic behaviour of helicopter rotor blades is much better understood and documented than in case of gyroplanes. In contrast to helicopter rotors, rotor speed represents additional degree of freedom of a gyroplane rotor. Gyroplane rotor blades can experience large changes of rotorspeed in relatively short time and their dynamic behaviour can be significantly different from behaviour of helicopter rotor due to varying centrifugal stiffening.

Several research works on the dynamics of flapping and bending motion of rotor blades during autorotation were published since the early days of rotary wing aviation. Cierva's technical works on rotor blade dynamics led to development of flapping and lead/lag hinges that were later adopted by many helicopter designs [12]. In contrast to a typical articulated helicopter rotor, early Cierva's rotor blades had a very small flap hinge offset in order to minimize bending moments transferred to the rotor hub. The work of Hufton et al. [23] represents one of the few research works dealing with dynamics of coupled bending-torsion of autorotating rotors. Simple thin beam theory is used for development of dynamic equations of motion of Cierva C.30 rotor blades. Predictions obtained from the mathematical model are compared with experimental flight measurements carried out by R.A.E. Estimated values of blade deflections in torsion and bending were in good agreement with experimental data from flight trials of a C.30 gyroplane. However, this work merely shows the development of a simple aeroelastic model of a C.30 rotor and its validation and it does not investigate aeroelastic behaviour and stability of the rotor any further.

More recently, Somov and Polyntsev [58] published a paper on the modelling of bending and flapping motion of an A-002 gyroplane rotor. The blade dynamics are modelled with the aid of blade bending modes obtained from a commercial FEA computer package. This approach to the problem is questionable as the method of assumed modes is not suitable for the modelling of the stability of a gyroplane rotor. Direct solution of the differential equations of blade motion with the aid of the finite

element method would probably be more suitable. Only blade degrees of freedom in rotation and flapping/bending are modelled, which severely limits capabilities of the model. Blade torsion and its coupling with rotor bending significantly affects the aerodynamics and dynamics of rotor blades as it plays key role in rotor classical flutter (bending-torsion flutter) [11; 27]. Since stall flutter is essentially a single degree of freedom instability in blade torsion, it requires a model of blade torsion too. It can be shown that rotor aeroelastic stability analysis can yield misleading results if blade torsional dynamics is not captured by the model [26].

Rezgui et al. [59] present a study of aeromechanic stability of a teetering rotor in autorotation. Rezgui uses bifurcation analysis to predict the rotor stability boundary. Bifurcation methods are a powerful tool for stability analysis of complex dynamic systems. However, bifurcation requires a set of linearized blade equations of motion and hence does not allow use of more than two coupled degrees of freedom. Rezgui considers degrees of freedom in teeter and rotation and therefore his model can not capture coupled bending-torsion of rotor blades.

2.2.3 Experimental Measurements of Rotors in Autorotation

As already mentioned in this chapter, an extensive programme of flight tests was performed by the Royal Aeronautical Establishment (RAE) in the 1920's that led to formulation of basics of rotorcraft analytical tools. A similar series of research projects was undertaken by NACA one decade later. These experimental measurements were aimed at investigating the aerodynamics and performance of gyroplanes and later (after Second World War), attention was drawn to the behaviour of helicopters in the autorotative flight regime.

Characteristic span-wise distribution of blade torque is established during steady vertical descent in autorotation (see Fig. 2.5). It can be seen from Fig. 2.5 that outboard part of a blade in autorotation generates negative torque during torque

equilibrium. This negative torque is cancelled out by positive torque produced by the inboard part of the blade.

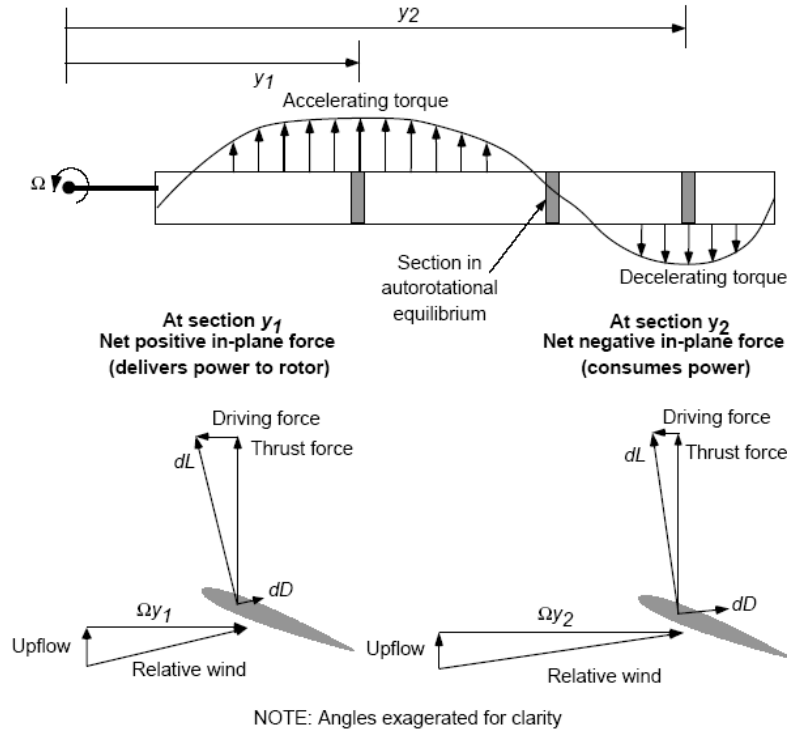


Figure 2.5: Span-wise distribution of blade torque that occurs during steady descent in autorotation; reproduced from Leishman [7]

Flight tests of gyroplanes also showed that the speed of descent and coefficient of resultant force in autorotation depend on the angle of attack of the rotor disc. Empirical formula was derived from flight test data giving an estimation of the value of speed of descent in axial autorotative flight [7; 12].

$$V_d \approx 1.212 \sqrt{\frac{T}{A}} \quad (2.1)$$

The formula shown in equation 2.1 applies for zero or very small values of blade fixed angle of incidence. Rotor aerodynamic efficiency can be significantly lower for higher fixed angles of blade incidence and steady autorotation is not possible for values of fixed incidence higher than the critical value. Speed of descent during steady axial flight in autorotation is between 10m/s and 12 m/s for rotors with small fixed

incidence [7; 12]. The maximum possible fixed angle of incidence of a rotor blade in autorotation can be estimated with the help of the Vimperis diagram that was developed with the aid of experimental data and is shown in figure 2.4 [7; 12].

Flight tests of gyroplanes revealed that the resultant force coefficient (c_R) represents an important aerodynamic characteristic of autorotating rotors. The resultant force of a rotor can be understood as *drag force generated by the rotor disc*. Experimental data show that resultant force coefficient is strongly dependent on rotor disc angle of incidence and that its value lies around 1.2 for rotor angle of incidence higher than 30 degrees [12]. This value of c_R is nearly identical to the drag coefficient of a circular disc or closed hemisphere. During axial autorotative flight a rotor acts like a bluff body with the attendant turbulent downstream wake and resultant force produced by the rotor is equivalent to resultant force of a parachute of similar size [7; 12].

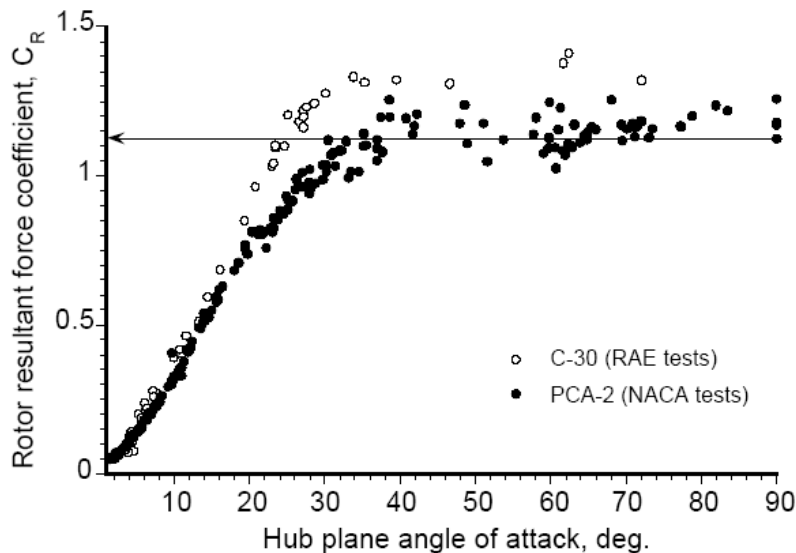


Figure 2.6: Dependence of c_R on rotor disc angle of attack; reproduced from Leishman [7]

As mentioned earlier, experimental flight measurements showed that there is a strong relationship between speed of descent and rotor disc incidence angle. Figure 2.7 shows relationship between forward speed and speed of descent during flight

in autorotation as obtained from flight trials of two different gyroplane models [7; 12]. The value of induced velocity in hover can be estimated using momentum theory.

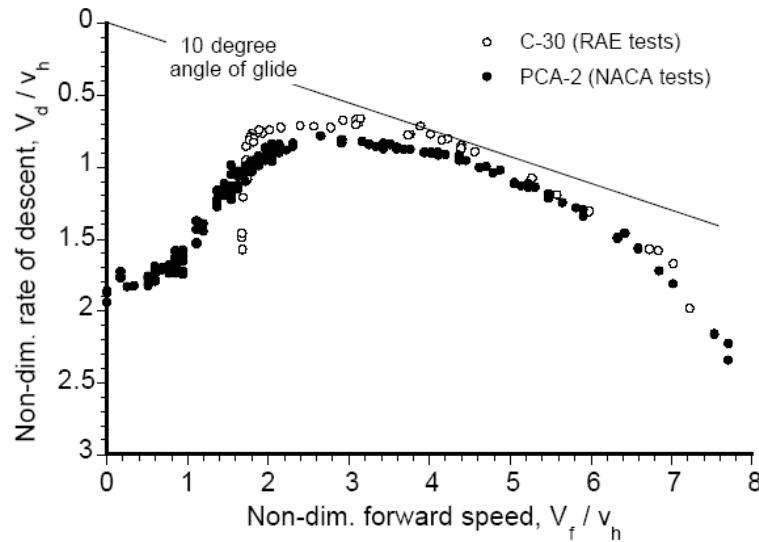


Figure 2.7: Dependence of dimensionless speed of descent on dimensionless forward speed; reproduced from Leishman [7]

During forward flight, the rotor blades are subjected to significant harmonic forcing that is dependent on blade azimuth. This causes a large amount of vibration which is transmitted to the fuselage via the rotor hub. The main purpose of flap and lag hinges used in helicopter design is to reduce vibration levels during forward flight. The majority of modern gyroplanes use two-bladed teetering rotors that are much simpler.

Following a series of aeroelastic problems involving a C.30 gyroplane that was fitted with cambered airfoils, several research projects were started to obtain experimental measurements of the aerodynamic behaviour of gyroplane blades. Experimental flight measurements and wind tunnel experiments, focused on determination of blade motion and blade loading, were carried out in R.A.E. and NACA before Second World War. The data were compared with theoretical results and hence helped to validate modelling tools used by NASA and R.A.E. [7; 23; 60–67]. Data from flight trials of a Cierva C.30 gyroplane describing flapping, torsion and in-plane

motion of rotor blades can be found in Hufton et al. [23]. This work also compares measured blade motion with analytical predictions and contains experimental data on aerodynamics and flight mechanics of the gyroplane. Wheatley [60] compares analytical predictions of gyroplane rotor induced twist with experimental measurements. He concludes that the assumption of linear variation of torsional deflection along the blade span is sufficient for accurate modelling of blade induced twist. Another publication of Wheatley [68] deals with in-plane (chord-wise) vibrations of a gyroplane rotor. Both theoretical and experimental investigations of the problem were carried out and revealed that chord-wise vibrations of the gyroplane rotor (i.e. variation of rotor speed) were predominantly caused by rotor flapping motion. Blade flapping motion changes angular moment of inertia of rotor blades, which results in rotor speed oscillations. The effect of aerodynamic loads and blade chord-wise flexibility on rotor in-plane vibrations were found to be negligible.

Bailey Jr. and Gustafson [62] investigate the region of stalled flow that occurs on gyroplane blades during forward flight. Comparison of experimental observations with predictions of blade stall made with the aid of the blade element method is given in the paper. The authors conclude that the simplified aerodynamic model of a gyroplane rotor predicts shape and location of the stalled region well, although it underpredicts its area. Experimental data also showed that the stalled region is large enough to affect rotor aerodynamic efficiency and rotor blade dynamics if the tip-speed ratio is high enough. Wheatley published the results of several flight tests and wind tunnel measurements of KD-1, PAA-1 and Pitcairn PCA-2 gyroplanes in Wheatley and Bioletti [30]; Wheatley [56, 60, 61, 68]; Wheatley and Hood [69]; Wheatley and Bioletti [70]; Wheatley [71]. Apart from many other parameters, gyroplane lift-to-drag ratios, glide angles and pressure distributions along the blade span were measured. Some of these experimental measurements were performed to compare aerodynamic characteristics of gyroplane rotors with and without the influence of the fuselage [7; 30; 56]. Several remarkable conclusions are made in these technical reports. Although the aerodynamic efficiency of the complete gyroplane

was found to be poor ($\frac{L}{D} \leq 4.5$), values of lift-to-drag ratio of the rotor alone were equivalent to aerodynamic efficiency of modern helicopter rotors [12]. Wheatley and Bioletti [30] conclude that this is caused by the excessive size of the hub used in the rotor wind tunnel model. As it can be seen from Figure 2.8, values of aerodynamic efficiency of gyroplane rotors remain relatively high even for very high advance ratios while $\frac{L}{D}$ of helicopter rotors decrease rapidly due to compressibility effects and retreating blade stall [7; 12]. Experimental measurements carried out by Wheatley and Bioletti [30] also showed that the pitch settings are the critical parameter that determines rotor characteristics. The same authors suggest in [69] that cambered rotor blades cause reduction of rotor blade induced twist due to their negative pitching moment coefficient. The study also surprisingly reveals that reduction of blade area in the root region decreases rotor aerodynamic efficiency significantly. A NACA Technical Report of Wheatley and Bioletti [70] describes full-scale wind tunnel tests of a Pitcairn PCA-2 gyroplane. It concludes that the change of aerodynamic characteristics of the rotor with rotor speed and thrust is caused by blade twist proportional to rotor thrust.

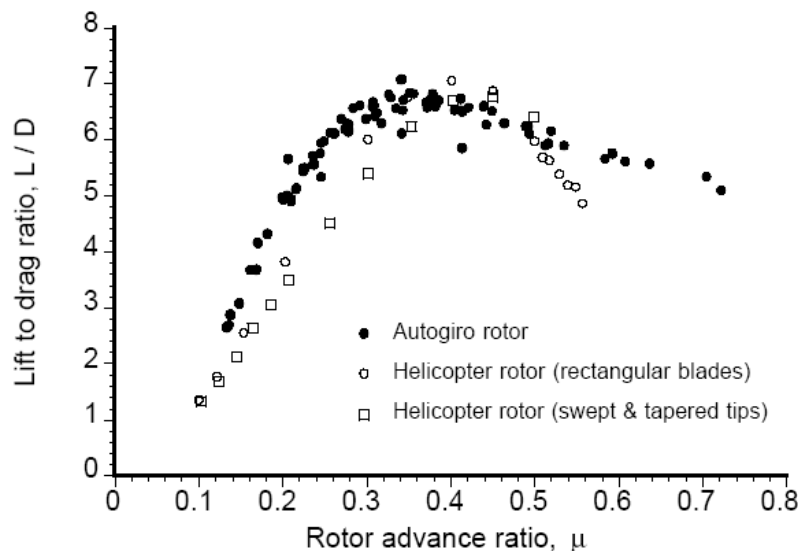


Figure 2.8: Comparison of aerodynamic efficiencies of gyroplane rotors and two versions of a helicopter rotor; reproduced from Leishman [7]

Experimental measurements of control stick vibrations of a YG-1B gyroplane

can be found in Bailey Jr. [72]. Since the YG-1B is equipped with a three-bladed rotor, the most important component of control stick force had frequency of 3Ω . It was also discovered that control stick vibrations are negligible for lower advance ratios (below $\mu = 0.2$). Bennett published technical memoranda [63] and [64] on high-speed flight and vertical descent of a gyroplane. Blade element theory in conjunction with Glauert's semi-empirical inflow model is used in these research works.

Problems caused by cambered airfoil sections and insufficient performance of reflex-camber airfoils forced manufactures of rotary wing aircraft to switch back to symmetrical airfoil sections. It took some time before high-performance, cambered airfoils were used in helicopter rotor blades again [7]. Further development of reflex-camber airfoils led to their wider use in gyroplane blade design. Aerodynamic characteristics of modern reflex-camber airfoils for low angles of attack can be found in Stivers and Rice [37]. A comparison of the aerodynamic characteristics of a NASA 8-H-12 reflex-camber airfoil, NACA 0012 airfoil and a derivative of 8-H-12 airfoil as used in modern light gyroplanes have shown that both NASA 8-H-12 and the modern gyroplane airfoil have positive pitching moment coefficient for low angles of attack. The main function of reflex camber was to eliminate the nose-down pitching moment of classical cambered airfoils in order to avoid blade torsion and loss of lift.

However, reflex camber airfoils do not produce very small pitching moments as one would expect - some airfoils from NACA reflex-camber 'H' family generate relatively high values of c_M . Stivers concludes that NACA 8-H-12 is perhaps the most suitable for helicopter blade design since it produces lower values of pitching moment than majority of other reflex camber airfoils. Results of CFD computations also indicate that reflex camber airfoils have worse high Mach number performance than similar symmetrical airfoils (e.g. NACA 0012). A conclusion can be made that it is more than desirable to investigate the aeroelastic behaviour of gyroplane rotors equipped with reflex camber airfoils, especially during high speed flight as

they might encounter high aerodynamic torsional moment. However, present lack of high angle of attack aerodynamic data severely limits capabilities of the resulting aeroelastic model.

A number of research works containing experimental data on aeromechanical behaviour of gyroplanes have been published recently. Wind tunnel tests of scaled model of a gyroplane performed during CAA UK funded research were carried out for several different configurations of the model, e.g. tail-on/tail-off, pod-on/pod-off etc [22]. A series of flight tests of University of Glasgow Montgomerie-Parsons gyroplane (G-UNIV) were also funded by CAA UK and resulted in several sets of data, including values of rotorspeed, blade teeter angle, blade azimuth, airspeed and altitude. Some of the results of the flight trials were published by Thomson et al. [18] and Bagiev et al. [73].

2.2.4 Summary

Although helicopter aeroelasticity is considered to be well understood, aeroelastic behaviour of rotors in autorotation is very much unexplored. Several open literature references dealing with the topic can be found but they study either steady-state deformations of the rotor blades or consider insufficient number of degrees of freedom for pitch-flap flutter to occur. However, publications focused on aerodynamics and flight performance of rotors in autorotation are available and can prove to be useful during development and verification of an aeroelastic model. A high number of technical reports on aeroelastics and structural dynamics of helicopter rotors can be found in open literature and can be used for design and verification of a model of blade structural dynamics.

A conclusion can be made that an investigation of coupled pitch-flap-rotation of rotors of autorotation would represent a new contribution in the field of rotorcraft aeroelasticity. Predictive tools developed for aeroelastic modelling of helicopter rotors are mature and well validated. Modification of these tools for modelling of

autorotating rotors should be relatively straightforward.

Chapter 3

Mathematical Modelling of Rotors in Autorotation

Predictive tools used in rotorcraft aeroelasticity contain an aerodynamic model of the rotor coupled with a model of blade structural dynamics. This chapter gives details of the modelling tools that were used in the *AMRA* model. First of all, description of unsteady model of gyroplane rotor aerodynamics is presented. The model is based on blade element theory and captures both compressibility effects and non-linear aerodynamic characteristics of a typical rotorcraft blade section. Improvements of Prouty's polynomial description of aerodynamic characteristics of NACA 0012 airfoil properties are shown, along with a new approximation of NACA 0012 $c_M - \alpha$ curve. The section dealing with gyroplane rotor aerodynamics is concluded with brief description of the rotor aerodynamic forcing and modified Peters-HaQuang dynamic inflow model used in *AMRA*.

The following section is focused on the modelling of rotor blade structural dynamics and it shows a derivation of the full nonlinear equations of motion of coupled bending-torsion-rotation of gyroplane rotor blades. Both the finite element model of coupled torsion-bending, and the modelling of blade structural dynamics with the aid of equivalent spring stiffness are described.

There are several substantial differences between the aeromechanical behaviour of a helicopter rotor and a rotor in autorotation. Contrary to the helicopter rotor in powered flight, an autorotating rotor works in the wind-milling regime, and kinetic energy from the airflow is transformed into aerodynamic forcing of the rotor. Hence, the direction of the airflow through the rotor disc in autorotation is opposite to the direction of inflow during typical flight regimes of helicopter rotors (see Figure 3.1).

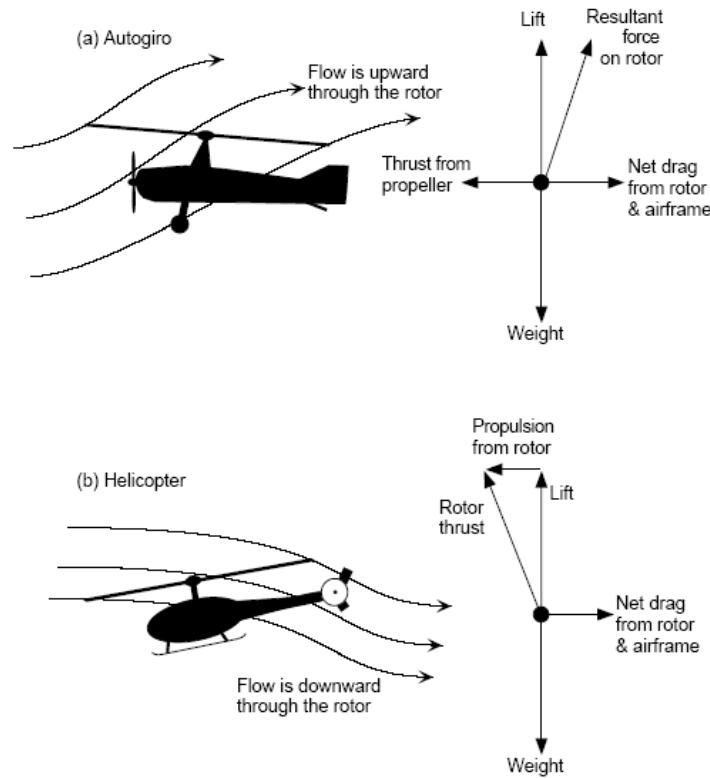


Figure 3.1: Comparison of inflow of a helicopter rotor and gyroplane rotor. Reproduced from Leishman [7]

Torque and thrust of the rotor are generated exclusively by the flow through the rotor disc during autorotation, which means that the value of rotor speed is dependent on the aerodynamic properties of the rotor blades. This also makes rotor speed directly dependent on the free-stream velocity of the vehicle, since the distribution of inflow speed over the rotor disc is dependent on values of the free-stream velocity and the rotor speed. Helicopter rotors work rather differently as constant rotational speed is maintained with the aid of the engine torque. Hence rotor speed does not depend upon free-stream velocity, and change of forward speed or rate of descent

have less significant influence on rotor performance.

3.1 Modelling of Aerodynamics of Rotors in Autorotation

In general, analytical methods required for modelling of the aerodynamics of autorotating rotors are similar to those developed for helicopter rotors in powered flight. However, several modifications have to be made in the blade element aerodynamic model of a helicopter rotor in order to reflect different character of the aerodynamics of a rotor in autorotation.

As with helicopter rotor blades, rotor blades in autorotation are subjected to high vibratory loading for most of the time. The blades are also highly flexible. Structural loading can reach even higher values than in the case of helicopters since the blades can experience significant fluctuation of centrifugal stiffening due to decrease of rotor speed. Additional components of aerodynamic angle of attack that are caused by blade oscillatory motion have to be considered. This can be done with the aid of the quasi-steady or the unsteady (Theodorsen's) aerodynamic theory. The airflow around a rotor blade can be considered quasi-steady if the reduced frequency of blade motion is lower than 0.05 [11; 12; 38]. Reduced frequency is defined as follows [11; 12; 38]

$$k = \frac{\omega c}{2V} \quad (3.1)$$

Classical formulations of quasi-steady lift and pitching moment coefficients of oscillating wing section are shown in Appendix A1 [11; 12].

Vertical displacement of local blade sections w_P is more consistent with the rotor coordinate system and rotor blade dynamics that were used in this work and in the

AMRA model (see equation 3.2).

$$\dot{w}_P = -\dot{h} = \dot{w} \cos \vartheta \quad (3.2)$$

The coordinate system used in the AMRA model is shown in figure 3.2.

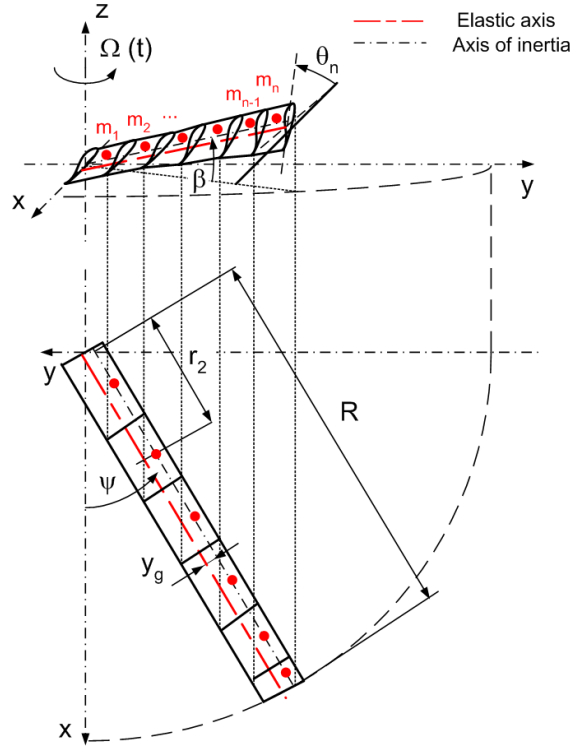


Figure 3.2: The layout and orientation of the system of coordinates of a rotor in autorotation used in the AMRA model

Hence the classical formulations of quasi-steady lift and moment coefficients generated by a blade section (see equation A1-1) has to be rewritten in order to be consistent with the coordinate system orientation of the model (shown in figure 3.2).

$$\begin{aligned} c_L &= c_{L\alpha} \left(\alpha + \frac{1}{\Omega r} \left(-\dot{w}_P + \left(\frac{3c}{4} - y_{EA} \right) \dot{\theta} \right) \right) \\ c_{M, \frac{c}{4}} &= -\frac{\pi}{8} \frac{\dot{\theta} c}{\Omega r} \end{aligned} \quad (3.3)$$

The terms on the right-hand side of equation 3.3 represent sum of steady angle of

attack and quasi-steady angle of attack caused by airfoil motion. Hence the equation can be written in a simpler form

$$c_L = c_{L\alpha} (\alpha + \alpha_q) \quad (3.4)$$

Corresponding forms of Theodorsen's equations of unsteady aerodynamics are

$$c_L = c_{L\alpha} C(k) (\alpha + \alpha_q) + \frac{cc_{L\alpha}}{4\Omega r} \left[\dot{\theta} - \frac{\ddot{w}_P}{\Omega r} - \frac{\left(y_{EA} - \frac{c}{2}\right) \ddot{\theta}}{\Omega r} \right] \quad (3.5)$$

$$\begin{aligned} c_{M, \frac{c}{2}} = & \frac{c_{L\alpha}}{2} C(k) \left(\frac{3}{2} - \frac{2y_{EA}}{c} \right) (\alpha + \alpha_q) - \frac{c_{L\alpha}}{4\Omega^2 r^2} \left[\left(y_{EA} - \frac{c}{2} \right) \ddot{w}_P + \left(\frac{9}{c^2} + y_{EA} (y_{EA} - c) \right) \ddot{\theta} \right] \\ & - \frac{c_{L\alpha}}{4} \left(\frac{3c}{4} - y_{EA} \right) \frac{\dot{\theta}}{\Omega r} \end{aligned} \quad (3.6)$$

Local values of vertical and horizontal components of the inflow velocity (U) have to be calculated in order to determine aerodynamic angle of attack of any blade section. The inflow velocity can be resolved into three components (U_p , U_t , U_r). Vertical component of inflow velocity U_p describes air speed of the flow in direction perpendicular to the rotor disc, U_t is parallel with the rotor disc plane and perpendicular to the longitudinal axis of the blade and U_r is parallel with both rotor disc plane and the blade axis.

Aerodynamic angle of attack of a blade section in autorotation is

$$\alpha = \theta + \phi = \theta + \arctan \left(\frac{U_p}{U_t} \right) \quad (3.7)$$

In forward flight, however, value of U_t can be negative in the reverse flow region of the rotor disc. In order to capture the reverse flow, the definition of inflow angle

has to be modified (see Fig. 3.3). This can be easily achieved in the manner shown in Bielawa [11] and Wheatley [56]. Alternatively, the value of the inflow velocity can be calculated as

$$\phi_{RF} = \begin{cases} \phi & \text{if } U_t \geq 0 \\ \phi + \pi & \text{if } U_t < 0 \end{cases} \quad (3.8)$$

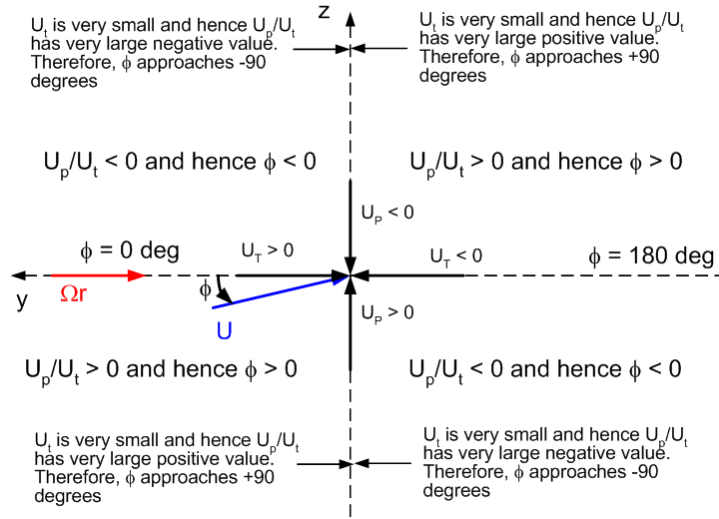


Figure 3.3: Calculation of inflow angle with the aid of components of inflow velocity

The inflow velocity is a function of angle of attack of the rotor disc that is given by a sum of incidence angle of the rotor disc ι (i.e. angle between the rotor disc plane and the horizontal plane) and pitch angle of the vehicle (see equation 3.9).

$$\begin{aligned} \alpha_D &= \iota + \gamma \\ \gamma &= \arctan\left(\frac{V_D}{V_H}\right) \end{aligned} \quad (3.9)$$

Referring to figure 3.4, analytical expressions of individual components of the inflow velocity of a gyroplane rotor can be formulated, including the effect of longi-

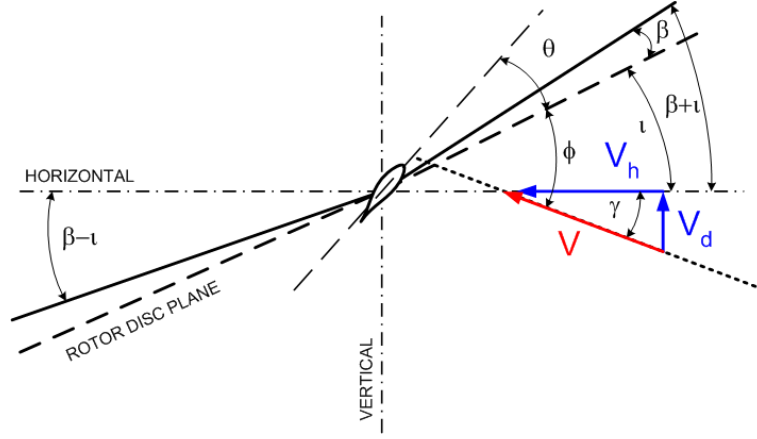


Figure 3.4: A sketch of aerodynamics of a rotor blade in autorotation

tudinal and lateral rotor disc tilt (ι and ι_L)

$$\begin{aligned}
 U_p = & -v_i + V_d \cos(\beta - \iota \cos \psi) - V_h (\sin(\beta - \iota \cos \psi) \cos \psi - \sin \iota \sin^2 \psi) \\
 & - V_s \left(\sin\left(\beta - \iota_L \cos\left(\psi + \frac{\pi}{2}\right)\right) \cos\left(\psi + \frac{\pi}{2}\right) - \sin \iota_L \sin^2\left(\psi + \frac{\pi}{2}\right) \right) \quad (3.10) \\
 & + \left(\frac{3c}{4} - y_{EA} \right) \dot{\theta} - \dot{\beta} r
 \end{aligned}$$

Horizontal (or tangential) component of the inflow velocity is then

$$U_t = \Omega r \cos \beta + (V_h \cos \iota - V_d \sin \iota) \sin \psi + V_s \cos \iota_L \sin\left(\psi + \frac{\pi}{2}\right) \quad (3.11)$$

The radial component of the inflow velocity is often neglected since it does not contribute to inflow angle that is defined as perpendicular to the leading edge of a blade. However, it is useful for calculation of rotor disc drag [12].

$$\begin{aligned}
 U_r = & V_h \cos(\beta - \iota \cos \psi) \cos \psi + V_d \sin(\beta - \iota \cos \psi) \\
 & + V_s \cos\left(\beta - \iota_L \cos\left(\psi + \frac{\pi}{2}\right)\right) \cos\left(\psi + \frac{\pi}{2}\right) \quad (3.12)
 \end{aligned}$$

Equations 3.10, 3.11 and 3.12 can be used to model the aerodynamics of a gyroplane rotor in both axial and forward flight as long as the coordinate system of the model of blade structural dynamics is equivalent to that shown in figure 3.2. This system of equations represents modified form of inflow equations of a helicopter rotor. Note that if the rotor disc incidence angle is zero, the flapping angle is assumed to be very small and some modifications are made, these three equations are reduced to

$$\begin{aligned}
 U_p &= \Omega R \left(\lambda - \mu \beta \cos \psi - \frac{x}{\Omega} \dot{\beta} + \frac{\frac{3c}{4} - y_{EA}}{\Omega} \dot{\theta} \right) \\
 U_t &= \Omega R (x + \mu \sin \psi) \\
 U_r &= \Omega R (\mu \cos \psi - \lambda \beta)
 \end{aligned}
 \tag{3.13}$$

The equations above represent the classical form of rotor inflow equations that have been broadly used for aerodynamic analysis of helicopter rotors in autorotation [12; 27; 55–57].

Once aerodynamic angles of attack of each blade element are calculated, they can be used for estimation of the aerodynamic loading of the rotor blades. In order to achieve this, relationships between the aerodynamic angle of attack of blade sections and lift, drag and pitching moment coefficients have to be defined. This can be done in several possible ways, depending on desired accuracy of estimation of blade aerodynamic loading.

Lift curve slope in equation 3.3 can be assumed to be constant in order to simplify the calculations and to save some computational time. However, the assumption of linear lift curve does not allow capturing of both blade stall and the compressibility effects.

Mach number and Reynolds number determine aerodynamic characteristics of

rotor blades. It can be seen from the work of Prouty [8], Carpenter [10] and Racisz [34] that Mach number influences slope of the linear part of lift curve, maximum lift coefficient and stall angle of an aerofoil.

Although typical value of rotor speed of a rotor in steady autorotation is around 40rad/s, values of up to 100rad/s have to be captured by the model in order to study aeroelastic stability of a rotor in autorotation [31; 74]. Both angle of attack and Mach number of the flow vary widely along a rotorcraft blade due to the change of tangential component of the inflow speed. The angle of attack reaches values of up to π rad both in autorotative forward flight and axial descent. Despite these facts, many studies of aerodynamics of autorotating rotors published in open literature use the assumption of linear lift curve and compressibility effects are neglected by some authors also. The range of flow Mach numbers and angles of attack that are common in gyroplane rotors are shown in figures 3.5 and 3.6.

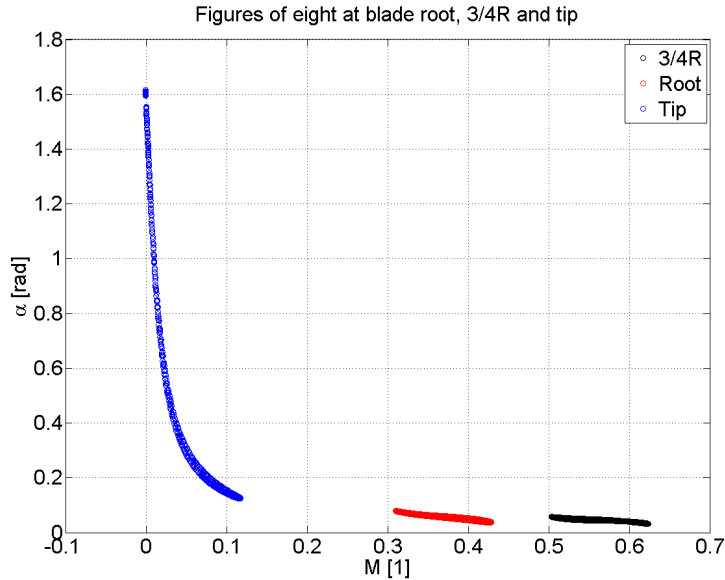


Figure 3.5: Range of Mach numbers and angles of attack that occur at the root region, three quarter radius and the tip region of a typical gyroplane rotor blade. Computed by *AMRA* for advance ratio of 0.1.

In order to make sure that predictions of the model will be accurate, compressibility effects and nonlinear aerodynamics of rotor cross-sections were included in

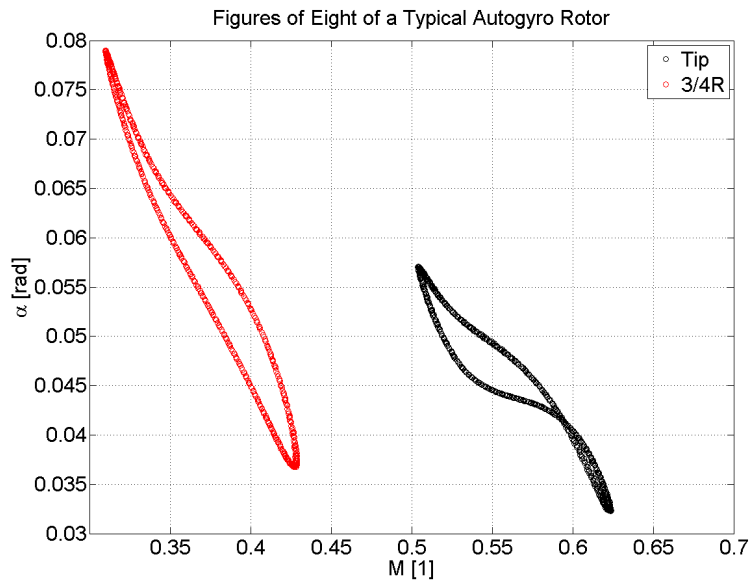


Figure 3.6: Range of Mach numbers and angles of attack that occur at three quarter radius and the tip region of a typical gyroplane rotor blade. Computed by *AMRA* for advance ratio of 0.1.

AMRA model.

It can be shown that the values of Reynolds number and Mach number are related. Hence it is convenient to express aerodynamic characteristics of a rotor blade as functions of angle of attack and Mach number of the inflow rather than angle of attack and Reynolds number [12]. This can be done by tabulating of the data and incorporation of look-up tables in the calculation which also allows incorporation of compressibility effects into the calculation as lift, drag and moment coefficients can be tabulated for several values of Mach number.

It is more convenient to express the aerodynamic characteristics of the blade airfoil as polynomial functions of angle of attack and Mach number. At least two different polynomials have to be used; the first polynomial is used for the area of angles of attack between $\alpha = -25\text{deg}$ and $\alpha = 25\text{deg}$. The outboard sections of rotor blades (which generate a major part of the rotor forcing) operate in this range of angles of attack most of the time, and hence an approximation of this part of the lift and drag curves should be more accurate. The trend of both lift and drag

curves outside this region can be approximated with the aid of simple trigonometric functions.

3.1.1 Modified Prouty's Polynomial Approximation of an Airfoil Lift Curve

It was shown by Prouty [8] that it is possible to obtain the full-range angle of attack aerodynamic data of an airfoil with the aid of numerical approximation. Prouty uses NACA 0012 airfoil in his book [8] as an example. This type of airfoil was widely used in the field of rotorcraft aerodynamics and an ample amount of experimental data are available for this airfoil. Prouty's empirical equations were derived from the data published by Carpenter [10]. The full-range AOA aerodynamic data for the same airfoil are also available at [13].

Unfortunately, aerodynamic characteristics of reflex camber airfoils that are typically used in gyroplane rotor blade design are not available. Since wind tunnel measurements of NACA 8-H-12 airfoil would require excessive amount of funding, well documented NACA 0012 airfoil was used instead. When available, aerodynamic data of a reflex camber airfoil can be easily added to *AMRA* thanks to open architecture of the model.

In general, the change of slope of lift-curve linear region is governed by Prandtl-Glauert's correction [8]. Prouty [8] showed that better results are obtained if a semi-empirical form of compressibility correction is used (see equation A2-1).

As it can be seen in the figure 2.2, the trend of the relation between lift-curve slope and Mach number changes radically for Mach numbers higher than $M = 0.7$. This area is not beyond the region of operation of gyroplane rotors (see figures 3.5 and 2.2). Prouty [8] defines the angle of attack α_L that represents the upper limit of the linear part of lift curve, i.e. airfoil shows first signs of stall at $\alpha \approx \alpha_L$. This

parameter represents an aerodynamic characteristic of an airfoil and it can be estimated with the help of the equation A2-2. Comparison of Prouty's predictions of values of α_L with the wind tunnel data of NACA 0012 airfoil published by Carpenter [10] are shown in figure 3.7.

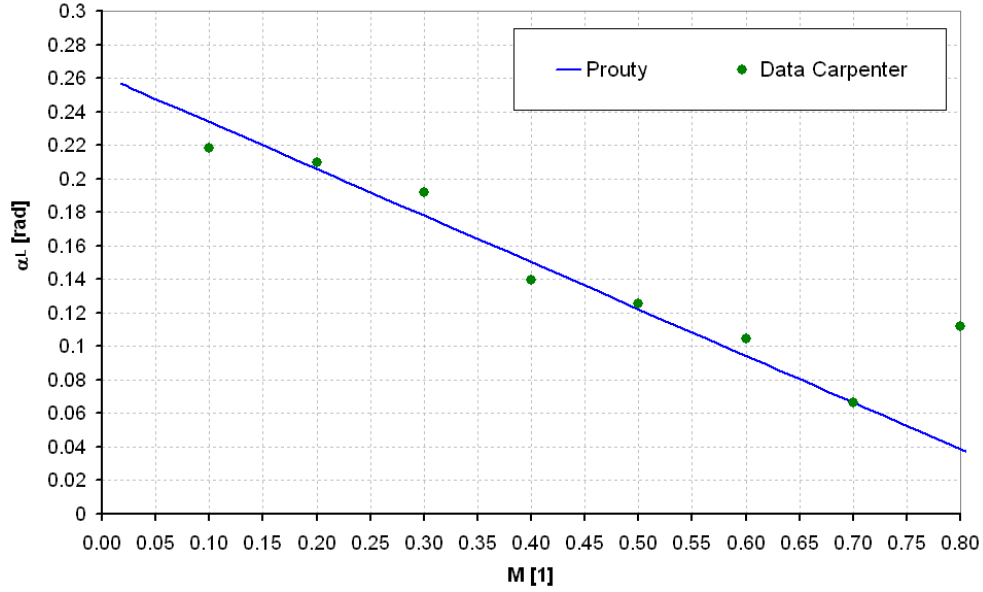


Figure 3.7: Comparison of Prouty's approximation of α_L with wind tunnel data

The original form of Prouty's polynomial approximation is shown in greater detail in Appendix A2. Due to the use of simple approximations, Prouty's polynomial fit of NACA 0012 lift curve is not accurate, especially for $M < 0.75$, which is the range of Mach numbers that mainly occurs in gyroplane rotors (see figure 2.1). This might be also partly caused by the fact that the validation of the method is done only for three different values of Mach number [8].

Prouty uses coefficients C_5 and C_6 to capture non-linear character of lift curve slope for $\alpha > \alpha_L$. More information on the use of these coefficients can be found in Appendix A2.

$$C_5 = \frac{c_{L\alpha} \alpha_{cLmax} - c_{Lmax}}{(\alpha_{cLmax} - \alpha_L)^{C_6}} \quad (3.14)$$

$$C_6 = C_7 + C_8 M \quad (3.15)$$

The results of Prouty's approach were enhanced by modification of equations 3.14 and 3.15. In the contrast to Prouty's method, constants C_5 and C_6 were treated as independent variables. Analysis of a polynomial approximation of NACA 0012 lift curve showed that it is more convenient to use a non-linear dependence of the parameters C_5 and C_6 on Mach number. As it can be seen from the figures 3.8 and 3.9, trends of these approximations are consistent with experimental data published by Prouty [8], Carpenter [10] and in [13]. Equation 3.16 shows the amended expressions of the coefficients C_5 and C_6 .

$$C_5 = -0.4375M^5 + 3.492M^4 - 5.3304M^3 + 3.4269M^2 - 1.0074M + 0.12334$$

$$C_6 = 67.0833M^5 - 152.8561M^4 + 143.6822M^3 - 72.3092M^2 + 18.6842M + 0.2004 \quad (3.16)$$

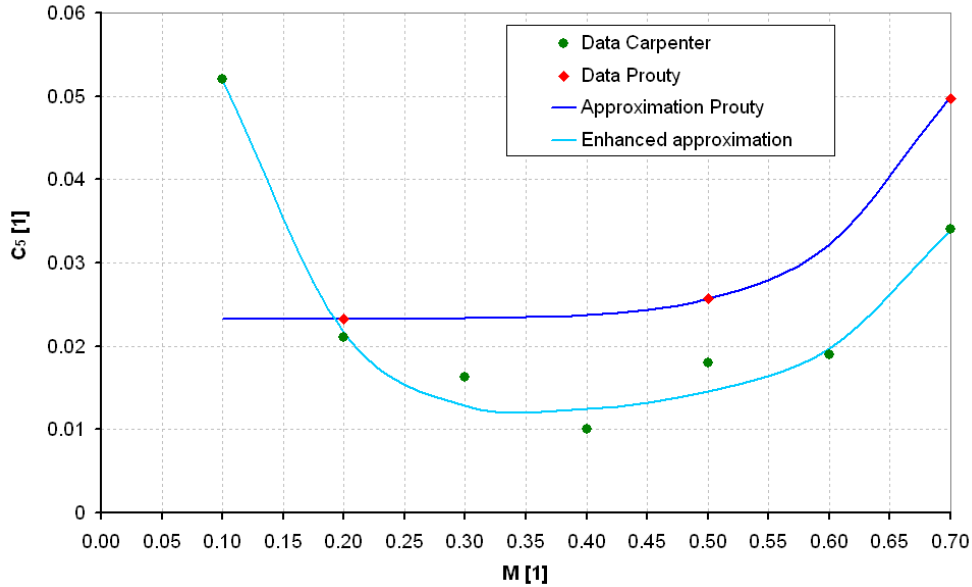


Figure 3.8: Dependence of coefficient C_5 on the value of Mach number

The improvements of Prouty's polynomial fit of lift curve of NACA 0012 airfoil result in a better agreement with the lift curves obtained during wind tunnel measurements of rotor lift [10]. Comparison of data published by Carpenter [10]

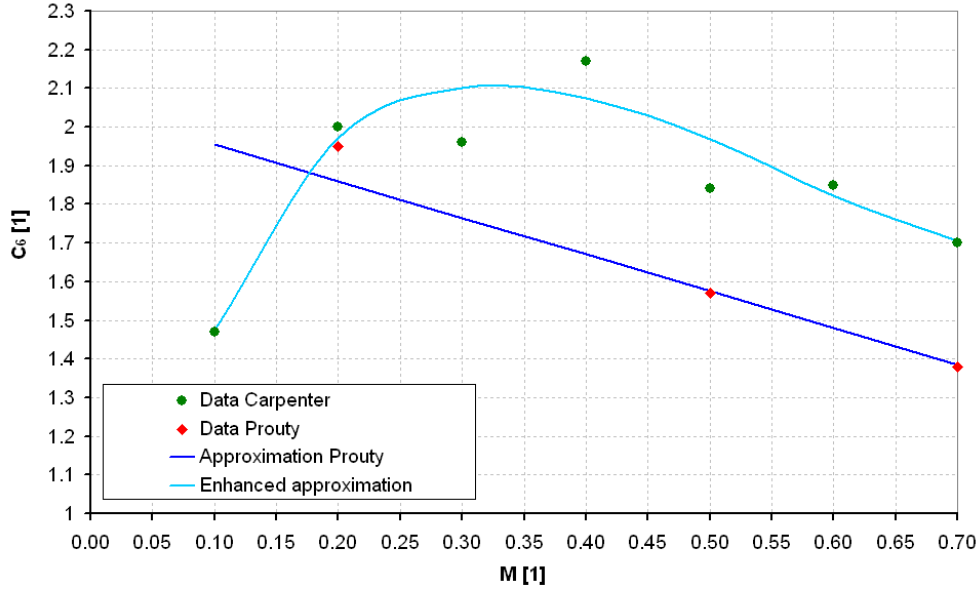


Figure 3.9: Dependence of coefficient C_6 on the value of Mach number

with results of the original and the enhanced Prouty’s approximation method are shown in Chapter 5 of this work (see figures 5.1 - 5.2). A comparison of the same experimental data with outcomes the original Prouty’s polynomial fit can be also found in Fig. 2.1.

It is also shown in Chapter 5 that agreement between the original Prouty’s method and the experimental data is sufficient for the rest of the range of angles of attack. Hence Prouty’s method was used in the *AMRA* model without any modifications for this region of the lift curve slope.

3.1.2 Modified Prouty’s Polynomial Approximation of an Airfoil Drag Curve

The polynomial fit of a drag curve described by Prouty [8] is based on piece-wise approximation of the curve with the aid of several types of mathematical functions. For values of angle of attack below the drag divergence (i.e. $\alpha < \alpha_{div}$), the drag curve of a typical airfoil can be approximated with the aid of a simple polynomial.

Wind tunnel measurements showed that the drag coefficient during the reverse flow ($\alpha \approx 180\text{deg}$) is considerably higher than for zero angle of attack and that the drag divergence is more severe too [12]. Prouty's method of polynomial fit of airfoil drag curve was enhanced in order to capture the effect of reverse flow. Again, the experimental data from [13] and Carpenter [10] were used.

$$\begin{aligned}
 c_{D1} &= 1.03 - 1.02 \cos 2\alpha \\
 c_{D2} &= 5.0885 - 1.7192 \cdot 10^3 \alpha + 2.4138 \cdot 10^1 \alpha^2 - 1.8027 \cdot 10^{-1} \alpha^3 + 7.5522 \cdot 10^{-4} \alpha^4 - 1.6828 \cdot 10^{-6} \alpha^5 + 1.5582 \cdot 10^{-9} \alpha^6 \\
 c_{D,revf} &= \begin{cases} c_{D1} & \text{if } c_{D2} \geq c_{D1} \\ c_{D2} & \text{if } c_{D1} \geq c_{D2} \end{cases}
 \end{aligned} \tag{3.17}$$

In contrast to the polynomial fit of NACA 0012 lift curve, Prouty's method gives relatively accurate approximation of drag curve of NACA 0012 airfoil for a wide range of Mach numbers and the full range of angles of attack. Hence the improvement of the polynomial fit in the reverse flow region of the drag curve represents the only modification of the method. A more detailed description of the original Prouty's approach is provided in Appendix A2.

Verification of the values of drag coefficient obtained by the method for both low and high angles of attack is given in Chapter 5 (figures 5.3 and 5.4).

3.1.3 Polynomial Approximation of an Airfoil Moment Curve

Since Prouty [8] describes only a polynomial fit of the moment curves of cambered airfoils, a polynomial approximation of moment curve of NACA 0012 airfoil was developed with the aid of wind tunnel data published in [13], Bielawa [11] and Leishman [12]. For angles of attack below the stall, moment curve of NACA 0012 can be expressed in the following way

$$c_{M,\alpha < 20deg}(\alpha, M) = M_0 + M_1\alpha + M_2\alpha^2 + M_3\alpha^3 + M_4\alpha^4 + M_5\alpha^5 \quad (3.18)$$

Coefficients of the polynomial M_0, \dots, M_5 are functions of Mach number and they can be generated with the aid of look-up tables. Values of these coefficients are shown in Appendix A2.

In a similar way to the approximation of lift and drag curves, the effect of Mach number on moment curve of NACA 0012 can be neglected for angles of attack above stall [7; 8]. The wind tunnel data available from [13] were used for development of appropriate polynomials that provide sufficient fit. Approximation of moment curve of NACA 0012 that was used in the *AMRA* model is

$$c_{M,\alpha > 20deg} = \begin{cases} 0.08 + 0.4 \sin(0.4\alpha^{1.8}) & \text{if } 20deg \leq \alpha \leq 166deg \\ 0.4 \sin(0.898\alpha^{2.5}) & \text{if } 166deg < \alpha \leq 180deg \end{cases} \quad (3.19)$$

Again, verification of the values of moment coefficient obtained by the method for both low and high angles of attack is given in Chapter 5 (figures 5.5 and 5.4).

3.1.4 Aerodynamic Forcing of an Autorotating Rotor Blade

Once aerodynamic coefficients at all span-wise stations are obtained, the aerodynamic forces and moments generated by the blade elements can be calculated. Lift and drag force and pitching moment at quarter-chord generated by an arbitrary element of the rotor blade of width dr are shown in their standard formulations [7; 11; 27].

$$\begin{aligned}
 dL &= \frac{1}{2} c_L \rho c U^2 dr \\
 dD &= \frac{1}{2} c_D \rho c U^2 dr \\
 dM_{\frac{\varepsilon}{4}} &= \frac{1}{2} c_{M, \frac{\varepsilon}{4}} \rho c^2 U^2 dr
 \end{aligned} \tag{3.20}$$

Lifting force is perpendicular to the direction of inflow velocity and drag force vector is perpendicular to the vector of lift force. Local values of inflow angle and angle of attack have to be used to obtain forcing moments of the blade. Elementary rotor thrust and in-plane force (frequently called H-force) are defined by the following equations [7; 11; 27]

$$\begin{aligned}
 dT &= dL \cos \phi + dD \sin \phi \\
 dH &= dL \sin \phi - dD \cos \phi
 \end{aligned} \tag{3.21}$$

Numerical integration has to be used in an aerodynamic model based on the blade element method. This approach is both simple and accurate, especially if a high number of span-wise elements is used. Hence numerical integration is especially useful in computer-aided modelling of rotor aerodynamics. Arbitrary span-wise distributions of blade properties and flow conditions can be easily captured and the full form of blade aerodynamic equations can be used also.

$$\begin{aligned}
 M_{\psi, A} = Q &= \sum_{i=1}^{N_{elem}} r dH \\
 M_{\beta, A} &= \sum_{i=1}^{N_{elem}} r dT \\
 M_{\theta, A} &= \sum_{i=1}^{N_{elem}} \left[(dL \cos \alpha + dD \sin \alpha) \left(y_{EA} - \frac{c}{4} \right) + dM_{\frac{\varepsilon}{4}} \right]
 \end{aligned} \tag{3.22}$$

More detailed formulations of equations 3.22 can be found in Appendix A1 (equa-

tions A1-11 - A1-13).

3.2 Modelling of the Inflow of a Rotor in Autorotation

Many inflow models used for the modelling of helicopter aerodynamics are based on momentum theory. According to momentum theory (sometimes also called actuator disc theory), the speed of descent and the induced velocity are related and their relationship is based on the classical form of Bernoulli's equation [9; 25]. The theory predicts that the induced velocity of a rotor in hover is [9; 25; 40]

$$v_h = \sqrt{\frac{T}{2\rho A}} = \Omega R \sqrt{\frac{c_T}{2}} \quad (3.23)$$

Unfortunately, experimental measurements have shown that the momentum theory is invalid for the region of $-2 \leq \frac{V_c}{v_H} \leq 0$ [9; 12; 25]. Since this flight regime is typical for autorotating rotors (see Fig. 2.7), momentum theory can not be used for modelling of the inflow of autorotating rotors.

Glauert [28] showed in the beginning of the last century that a combination of the momentum theory, the blade element theory and an empirical method of induced velocity calculation can be used instead of pure momentum theory. Glauert's method was enhanced with the aid of experimental measurements twenty years later [9; 31]. It utilizes basic theory of rotor aerodynamics to calculate the inflow ratio of the rotor. This semi-empirical inflow model is described in more detail in Appendix A3.

Many different inflow models were developed during last sixty years. Leishman [12] gives a nice summary of inflow models developed to the date. Many of inflow models are based on the approximation of induced velocity distribution that was first proposed by Glauert [12; 28].

$$v_i = v_{i0} (1 + k_x x \cos \psi + k_y x \sin \psi) \quad (3.24)$$

Dynamic inflow models developed by Pitt and Peters, Gaonkar and Peters, Peters and HaQuang and Peters and He represent the most up-to-date inflow models. Modern three-state dynamic inflow models are defined in the following form [33; 40]

$$[\tau] \begin{bmatrix} \dot{v}_{i0} \\ \dot{v}_{is} \\ \dot{v}_{ic} \end{bmatrix} + \begin{bmatrix} v_{i0} \\ v_{is} \\ v_{ic} \end{bmatrix} = [\Lambda] \begin{bmatrix} T_{tot,1rav} \\ L_{tot,1rav} \\ M_{tot,1rav} \end{bmatrix} \quad (3.25)$$

Peters - HaQuang dynamic inflow model was modified by Houston and Brown [24] in order to capture the inflow of a rotor in autorotation. The model was used in the *AMRA* model and it is described in greater detail in Appendix A3. Although full 3-DoF dynamic model was incorporated into the *AMRA* code, in practice a simplified version was used. From the system of equations 3.25, only the first equation is used in the simulation as the remaining two components of the induced velocity can be neglected. This modification decreases computing time and reduces complexity of the model. The equation below shows formula for the rate of change of vertical component of induced velocity.

$$\dot{v}_{i0} = - \frac{3C_0 \left(2\pi\rho R^2 v_{i0} \sqrt{V_x^2 + V_y^2 + V_z^2} - \sqrt{2}V_z \sqrt{\frac{T}{\pi\rho R^2}} + \sqrt{\frac{T}{2\pi\rho R^2}} - T \right)}{8\rho R^3} \quad (3.26)$$

The equation 3.24 then becomes

$$v_i = \int \dot{v}_{i0} dt \quad (3.27)$$

There are several reasons for such simplification. First of all, results obtained with the aid of the full modified Peters-HaQuang model and its simplified version

are very similar. Hence reduction of the dynamic inflow model increases speed of simulations. Comparison of predicted values of induced velocity during low speed forward flight ($\mu=0.1$) is shown in figures 3.10 and comparison of other aeromechanical parameters can be found in table 3.1.

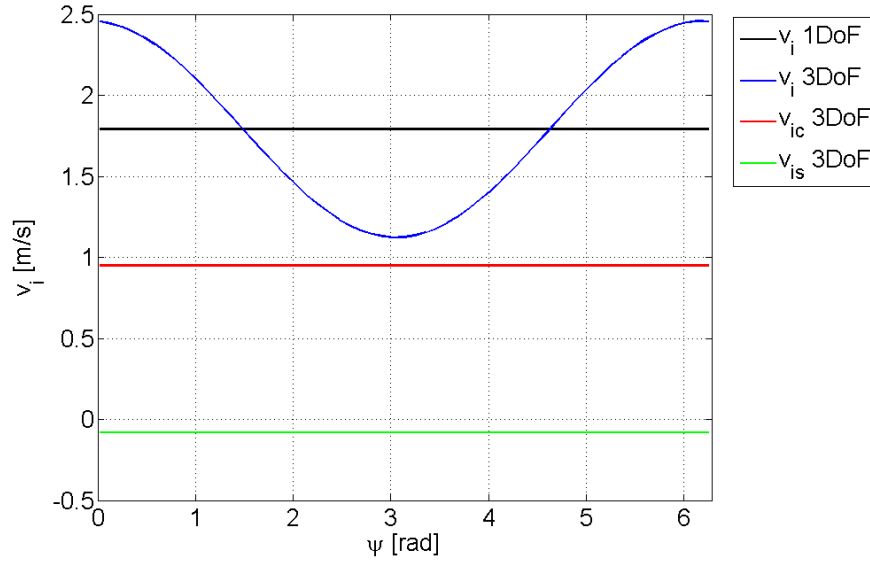


Figure 3.10: A comparison of the values of induced velocity obtained with the aid of full modified Peters-HaQuang dynamic inflow model and its simplified (1 DoF) version.

Table 3.1: Comparison of predictions of different versions of Peters-HaQuang dynamic inflow model

Model	V_D [m/s]	V_H [m/s]	Ω [rad/s]
1 DoF	5.09	20	53.2
3 DoF	5.846	20	53.05

Distribution of induced velocity over the rotor disc predicted by full version of the dynamic inflow model is depicted in figure 3.11.

The main reason for not using the full dynamic inflow model is the fact that high values of wake skew angle can result in singularity in both time matrix and static gain matrix if sine and cosine components of induced velocity are considered (see equation A3-9 and A3-10) [33]. It follows that high values of wake skew angle can

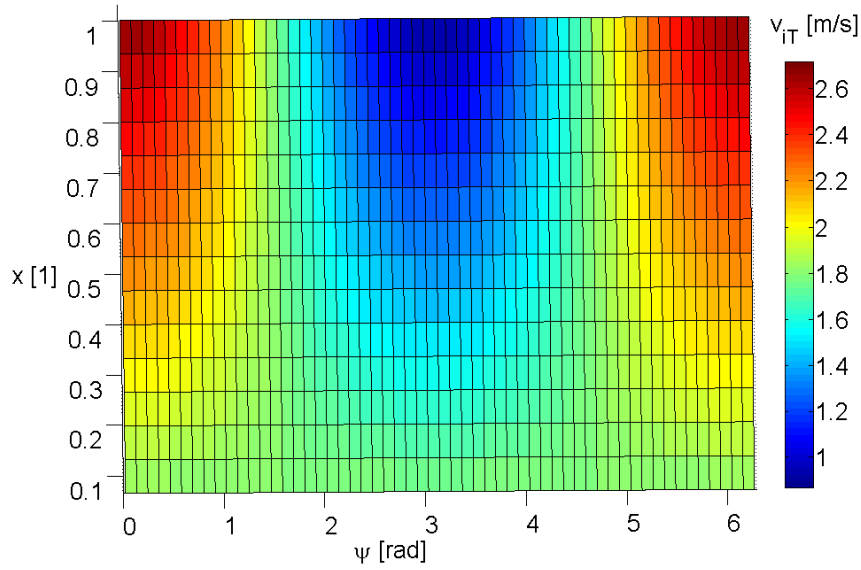


Figure 3.11: Distribution of induced velocity over the rotor disc during one revolution as predicted by full (3DoF) Peters-HaQuang model

result in unrealistically high values of v_{ic} and v_{is} . It is clear that high wake skew angles can easily occur during modelling of gyroplane rotor aeroelastics when the rotor might experience a wide range of values of thrust, forward speed and speed descent.

3.3 Modelling of Rotor Blade Structural Dynamics

A model of rotor blade dynamics is the key component of any model of rotorcraft aeroelastics. As it was shown in the introduction to this work, many different approaches can be used for development of structural dynamics model of a rotor blade. Lagrange's method of derivation of the equations of motion in combination with a simple finite element model of a slender beam was used in the *AMRA* model. This section describes the theoretical background and general arrangement of the *AMRA* blade dynamics model.

Since a typical modern gyroplane rotor uses teetering hinge instead of flap hinges and does not have any lag hinges, the equations of motion are simpler than for a conventional helicopter. On the other hand, rotor speed represents an additional

degree of freedom for autorotating rotors and hence one extra equation of motion is required. The results of the *AMRA* model are also fully applicable to teetering, hingeless or bearingless helicopter rotors in autorotation. The extended form of Euler's equations of motion (see equation A4-1) of a rigid blade can provide a good estimate of rotor blade dynamic behaviour [27].

3.3.1 Derivation of Full, Non-Linear Blade Equations of Motion

Lagrange's method is an elegant way of obtaining the equations of motion of complex physical systems and hence it is useful for the modelling of the dynamics of rotor blades. The method can be automated with the aid of a symbolic mathematical software, which results in a powerful and versatile tool. Depending on the type of generalized coordinate, corresponding generalized forcing is either a force or a moment. Lagrange's method was used in the *AMRA* code for derivation of full equations of rotor blade motion. While a slender beam FEM model was used for solution of equations of blade torsion and bending, simple equivalent spring stiffness models were used for simulation of rotor teeter, blade rotation and also for optional simplified models of 'rigid blade' torsion and flap. Lagrange's equations of motion of a rotor blade that has degrees of freedom in flap, torsion and rotation are shown below.

$$\begin{aligned}
 \frac{d}{dt} \left(\frac{\partial T}{\partial \dot{\beta}} \right) - \frac{\partial T}{\partial \beta} + \frac{\partial U}{\partial \beta} + \frac{\partial D}{\partial \dot{\beta}} &= M_{\beta,A} \\
 \frac{d}{dt} \left(\frac{\partial T}{\partial \dot{\theta}} \right) - \frac{\partial T}{\partial \theta} + \frac{\partial U}{\partial \theta} + \frac{\partial D}{\partial \dot{\theta}} &= M_{\theta,A} \\
 \frac{d}{dt} \left(\frac{\partial T}{\partial \dot{\Omega}} \right) - \frac{\partial T}{\partial \psi} + \frac{\partial U}{\partial \psi} + \frac{\partial D}{\partial \dot{\Omega}} &= M_{\psi,A}
 \end{aligned} \tag{3.28}$$

In Lagrange's method, the definition of kinetic and potential energies along with

external forcing is all that is needed for derivation of the equations of motion of any rigid body or multi-body system. This can be easily done in the case of lumped mass if the position vector of the mass is known. The position vector of an arbitrary point on a rotor blade in a non-rotating system of coordinates can be obtained by transformation of corresponding position vector in rotating frame of reference [11; 27]

$$\underline{r}_T = [T] \underline{r}_0 \quad (3.29)$$

Coordinate transformation has to be used for derivation of the equations of motion of rotating systems. Rotational speed is source of a significant amount of blade forcing that is dominant during rotor operation. Hence it is crucial to consider all rotational terms in correct form and get the transformation of coordinates right. Figure 3.12 shows centrifugal forces acting on a gyroplane rotor.

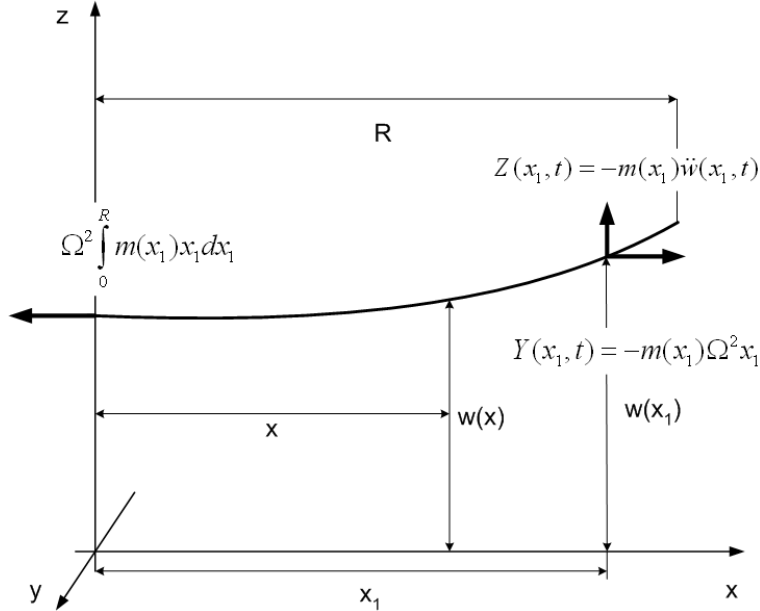


Figure 3.12: Centrifugal forces acting on a rotating slender beam

The coordinate transformation and derivation of rotor blade equations of motion are described in detail in Appendix A4. The transformation matrix is a function of the Euler angles that define mutual position of the rotating and the non-rotating frame of reference. In the case of a gyroplane rotor blade, coordinate transforma-

tion has to be done for flap, pitch and rotation, resulting in three transformation matrices. The final transformation matrix $[T]$ can be obtained by cascade multiplication of these matrices [11]. Figure 3.2 shows the coordinate system used in the *AMRA* model. The corresponding transformation matrix is shown in equation A4-6.

The time derivative of the blade position vector can be used for calculation of blade kinetic energy since

$$T = \frac{1}{2} m \dot{\underline{r}} \quad (3.30)$$

Since rotor speed of a rotor in autorotation can vary with time, Coriolis theorem has to be used for description of time derivative of blade position vector.

$$\dot{\underline{r}} = \dot{\underline{r}}_T + \Omega \times \underline{r}_T \quad (3.31)$$

Typical locations of blade centre of gravity, blade elastic axis and blade aerodynamic centre are shown in figure 3.13.

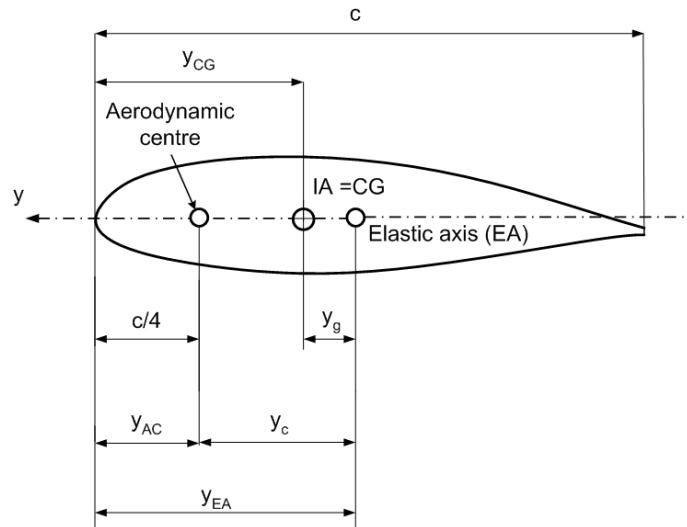


Figure 3.13: Positions of centre of gravity (CG), blade elastic axis (EA) and blade aerodynamic centre (AC) along the chord of a typical rotorcraft blade

The kinetic energy of a rotor blade can be expressed in terms of the time derivative of the position vector of the blade centre of gravity [11; 27]. Since gyroplane rotor blades do not have lag hinges and their chord-wise stiffness is relatively high, chord-wise bending of gyroplane rotor blades can be neglected [68]. Hence a model of blade chord-wise bending was included in *AMRA* model but it was not used during the research work. Following the equation A4-8, the kinetic energy of a blade element can be expressed as

$$\begin{aligned}
 T = \frac{m}{2} & \left[\dot{\beta}^2 r^2 - \dot{\beta}^2 y_g^2 + \Omega^2 y_g^2 + \Omega^2 \cos^2 \beta r^2 - \dot{\beta}^2 y_g^2 \cos^2 \theta + \dot{\theta}^2 y_g^2 \cos^2 \beta \right. \\
 & - \Omega^2 y_g^2 \cos^2 \beta + \Omega^2 y_g^2 \cos^2 \theta \cos^2 \beta + 2\dot{\beta}\dot{\theta} y_g r \cos \theta + 2\Omega \dot{\beta} y_g^2 \sin \theta \cos \theta \cos \beta \\
 & + 2\Omega \dot{\beta} y_g r \sin \beta \cos \theta - 2\Omega^2 y_g r \sin \beta \cos \beta \cos \theta - 2\Omega \dot{\theta} y_g r \sin \beta \cos \beta \\
 & \left. + 2\Omega \dot{\theta} y_g^2 \sin \beta \right] \quad (3.32)
 \end{aligned}$$

Substitution of the equation 3.32 into the first equation of the system of equations A4-3 results in the equation of motion of blade flapping. This equation is used in *AMRA* for modelling of blade flat-wise bending and in a modified form for simulation of rotor teeter.

$$\begin{aligned}
 m & \left[(r^2 + y_g^2 \sin^2 \theta) \ddot{\beta}^{B1} + r y_g \ddot{\theta} \cos \theta^{B2} - \Omega^2 r^2 \cos \beta \sin \beta^{B3} - \Omega^2 r y_g \sin \theta^{B4} \right. \\
 & + r y_g \dot{\Omega} \sin \beta \cos \theta^{B5} + y_g^2 \dot{\Omega} \sin \theta \cos \theta \cos \beta^{B6} + 2 y_g^2 \dot{\beta} \dot{\theta} \cos \theta \sin \theta^{B7} \\
 & - 2 r y_g \Omega \dot{\theta} \sin \beta \sin \theta^{B8} - 2 y_g^2 \Omega \dot{\theta} \sin^2 \theta \cos \beta^{B9} - r y_g \dot{\theta}^2 \sin \theta^{B11} \\
 & \left. - y_g^2 \Omega^2 \cos \beta \sin \beta \sin^2 \theta^{B12} + 2 r y_g \Omega^2 \sin \theta \cos^2 \beta^{B14} + r g \cos \beta^{B15} \right] \\
 & + k_\beta \beta^{B16} + c_\beta \dot{\beta}^{B17} = M_{\beta,A}^{B18} \quad (3.33)
 \end{aligned}$$

The term B3 in the equation above represents flat-wise stiffening due to the centrifugal force and the term B4 is the inertial force caused by the centrifugal force in presence of a torsional deflection θ [11].

The equation of blade torsion is

$$\begin{aligned}
 m & [(i_x^2 + y_g^2)\ddot{\theta}^{T1} + ry_g\ddot{\beta} \cos \theta^{T2} + \Omega^2 ry_g \cos \theta \cos \beta \sin \beta^{T3} + \Omega^2 y_g^2 \sin \theta \cos \theta \cos^2 \beta^{T4} \\
 & - ry_g \dot{\Omega} \cos \beta \sin \theta^{T5} + y_g^2 \dot{\Omega} \sin \beta^{T6} - y_g^2 \dot{\beta}^2 \cos \theta \sin \theta^{T7} + 2ry_g \Omega \dot{\beta} \sin \beta \sin \theta^{T8} \\
 & + 2y_g^2 \Omega \dot{\beta} \sin^2 \theta \cos \beta^{T9} + y_g g \cos \theta^{T10}] + k_\theta \theta^{T11} + c_\theta \dot{\theta}^{T12} - \sigma k_x^2 \theta^{T13} = M_{\theta,A}^{T13}
 \end{aligned}
 \tag{3.34}$$

The term T3 represents a torsional moment caused by flat-wise bending of the blade and corresponding inclination of elastic axis. Finally, the term T4 is stabilizing *propeller moment (tennis racquet effect)* resulting from a force couple that consists of two chord-wise components of radially aligned centrifugal forces [11]. Since Lagrangian derivation of blade equations of motion does not capture the effect of internal structure of blade on its dynamics, several terms were added to the equations.

For example, the term T13 in the equation 3.34 is *bifilar stiffening* that is caused by non-parallel alignment of tensile filaments of blade structure has to be included in the equations of motion [11]. Rotor blades are modeled as infinitely thin rods coincident with the axis of inertia and lie in distance y_g from elastic axis. Hence, a singularity can occur in the solution of blade torsional dynamics if the axis of inertia is located close to the elastic axis ($y_g \rightarrow 0$). In order to avoid this, the moment of inertia of blade cross-section about its centre of mass i_x was introduced into the equation 3.34.

Finally, the equation of blade rotation is

$$\begin{aligned}
& m[(r^2 \cos^2 \beta - y_g^2 \cos^2 \beta \sin^2 \theta - 2ry_g \sin \beta \cos \beta \sin \theta + y_g^2) \dot{\Omega}^{R1} \\
& + y_g^2 \ddot{\theta} \sin \beta^{R2} - ry_g \ddot{\theta} \cos \beta \sin \theta^{R3} + y_g^2 \ddot{\beta} \sin \theta \cos \theta \cos \beta^{R4} + ry_g \ddot{\beta} \sin \beta \cos \theta^{R5} \\
& - y_g^2 \dot{\beta}^2 \sin \theta \cos \theta \sin \beta^{R6} + y_g r \dot{\beta}^2 \cos \theta \cos \beta^{R7} - 2r^2 \Omega \dot{\beta} \sin \beta \cos \beta^{R8} \\
& + 2y_g^2 \Omega \dot{\beta} \sin^2 \theta \sin \beta \cos \beta^{R9} - 4y_g r \Omega \dot{\beta} \cos^2 \beta \sin \theta^{R11} + 2y_g r \Omega \dot{\beta} \sin \theta^{R12} \\
& + 2y_g^2 \dot{\beta} \dot{\theta} \cos \beta \cos^2 \theta^{R13} - y_g r \dot{\theta}^2 \cos \theta \cos \beta^{R14} - 2y_g^2 \Omega \dot{\theta} \sin \theta \cos \theta \cos^2 \beta^{R15} \\
& - 2y_g r \Omega \dot{\theta} \sin \beta \cos \beta \cos \theta^{R16}] = M_{\psi, A}^{R17}
\end{aligned} \tag{3.35}$$

The resulting non-linear system of equations describes dynamics of rotation, torsion and bending/flapping of a rotor blade. Linearized and simplified forms of the equations 3.33 and 3.34 were published in open literature [11].

Linearized forms of the coupled DEs of blade bending and torsion can also be found in open literature. Houbolt and Brooks [50] give derivations of the equations of motion of combined bending-torsion of a slender beam. Aeroelastic equations of a helicopter rotor undergoing torsion and both flap-wise and chord-wise bending can be found in Kaza and Kvaternik [39] and Bielawa [11].

3.3.2 Linearization of Equations of Motion of Autorotating Rotor Blade

The equations of rotor blade motion 3.33 - 3.35 can be linearized if flexural and torsional deflections of the blade are considered to be small. Derivation of linearized blade equations of motion can be found in Appendix A5. The final form of the linearized equations of motion is shown in equations A5-1 - A5-3. All terms in these equations are marked in the same manner as in the equations 3.33 - 3.35 in order to allow for comparison of linearized and full non-linear sets of equations of motion.

Aerodynamic forcing moments can be derived from the equations A1-16 - A1-18 and are given in equations A5-8 - A5-10. The equations of blade aerodynamic forcing have to be linearized. If the system of equations of motion is linearized around the rotor speed, the rotational equation of motion has to be dropped. This results in a system of two differential equations of motion that can be written in a matrix form.

$$[M]\{\ddot{q}\} + [C]\{\dot{q}\} + [K]\{q\} = [A]\{\dot{q}\} + [B]\{q\} \quad (3.36)$$

Since pitch-flap flutter is caused by destabilizing coupling between blade torsion and blade flap (teeter), these degrees of freedom are retained. Hence the generalized coordinates are

$$\{q\} = [\beta \quad \theta]^T \quad (3.37)$$

Linearization of the equations of motion for other combination of degrees of freedom (i.e. rotor speed - torsion or rotor speed - flap (teeter)) are not presented since investigation performed with the aid of the time-marching model did not reveal any instabilities for these sets of generalized coordinates.

Small terms are left out during the linearization process, which leads to further simplification of the equations. The inflow angle can also be neglected as the blade torsion θ represents a change of the angle of attack from the steady state [27]. A non-dimensional form of an analytical model of coupled flapping-torsion of a helicopter rotor blade can be found in Bramwell [27]. The aerodynamic forcing can be expressed in different form if Theodorsen's equations modified for use in frequency domain are used (see equations A1-9 - A1-10). This approach is used in the p-method and k-method of pitch-flap flutter analysis.

Aerodynamic forcing from the opposite rotor blade has to be included in the case of aerodynamic forcing in flap of a two-bladed teetering rotor. Hence, the forcing terms become

$$M_{A,\beta,T1} = M_{A,\beta,1} - M_{A,\beta,2} \quad (3.38)$$

The following assumptions can be made in order to develop an expression for aerodynamic forcing in teeter. Structural damping of flapping motion of a teetering rigid rotor can be neglected as aerodynamic damping of blade flapping motion is high. Torsional motion of each rotor blade is assumed to be unaffected by torsion of the opposite blade.

$$\begin{aligned} \dot{\beta}_2 &= -\dot{\beta}_1 \\ c_\beta &\approx 0 \end{aligned} \quad (3.39)$$

Resulting system of equations of motion of a single blade of a teetering rotor in autorotation can be written in the following form

$$[M_t] = \begin{bmatrix} 2r^2m^{B1E} & 2mry_g^{B2E} \\ mry_g^{T2E} & (my_g^2 + i_x^2)^{T1E} \end{bmatrix} \quad (3.40)$$

$$[K_t] = \begin{bmatrix} 2k_\beta^{B16E} - 2m\Omega^2r^{2,B3E} & m[-\Omega^2ry_g^{B4E} + 2r\Omega^2y_g^{B14E}] \\ m\Omega^2ry_g^{T3E} & k_\theta^{T11E} + m\Omega^2y_g^{2,T4E} \end{bmatrix} \quad (3.41)$$

$$[C_t] = \begin{bmatrix} 0 & 0 \\ 0 & c_\theta^{T12E} \end{bmatrix} \quad (3.42)$$

$$[A_t] = \frac{1}{6}\rho c\Omega R^3 \begin{bmatrix} -2c_{L\alpha} & 2c_{L\alpha} \left(\frac{3c}{4} - y_{EA} \right) \\ \frac{3c}{2R} \left(\frac{y_{EA}}{c} - \frac{1}{4} \right) c_{L\alpha} & \frac{3c}{2R} \left(\frac{y_{EA}}{c} - \frac{1}{4} \right) c_{L\alpha} \left(\frac{3c}{4} - y_{EA} \right) \end{bmatrix} \quad (3.43)$$

$$[B_t] = \frac{1}{8}\rho c\Omega^2 R^4 \begin{bmatrix} 0 & 2c_{L\alpha} \\ 0 & \frac{4c}{3R} \left(\frac{y_{EA}}{c} - \frac{1}{4} \right) (c_{L\alpha} + \delta_0) \end{bmatrix} \quad (3.44)$$

Linearized equations of motion of flapping and torsion of an isolated autorotating hingeless rotor blade are shown in Appendix A5.

3.3.3 Eigenvalue Analysis of Linearized Equations of Motion of Autorotating Rigid Rotor Blade

For the purpose of an eigenvalue analysis, following substitution has to be made [11]

$$\begin{aligned}\beta &= \bar{\beta}e^{\lambda t} \\ \theta &= \bar{\theta}e^{\lambda t}\end{aligned}\tag{3.45}$$

Substitution of the equation 3.45 into the linearized equations of motion results in following eigenvalue problem [11]

$$\det \begin{pmatrix} M_{\beta\beta}\lambda^2 + (C_{\beta\beta} - A_{\beta\beta})\lambda + (K_{\beta\beta} - B_{\beta\beta}) & M_{\beta\theta}\lambda^2 + (C_{\beta\theta} - A_{\beta\theta})\lambda + (K_{\eta\theta} - B_{\beta\theta}) \\ M_{\theta\beta}\lambda^2 + (C_{\theta\beta} - A_{\theta\beta})\lambda + (K_{\theta\beta} - B_{\theta\beta}) & M_{\theta\theta}\lambda^2 + (C_{\theta\theta} - A_{\theta\theta})\lambda + (K_{\theta\theta} - B_{\theta\theta}) \end{pmatrix} = 0 \tag{3.46}$$

The equation 3.46 can be expressed in the form of a polynomial of fourth order that represents the characteristic equation of the system

$$\bar{A}_4\lambda^4 + \bar{A}_3\lambda^3 + \bar{A}_2\lambda^2 + \bar{A}_1\lambda + \bar{A}_0 = 0 \tag{3.47}$$

Individual coefficients of the characteristic equation are derived in Appendix A5.

Conditions of stability of the systems are shown in the equation 3.48 [11]

$$\begin{aligned}\bar{A}_4, \bar{A}_3, \bar{A}_2, \bar{A}_1, \bar{A}_0 &> 0 \\ \text{or} & \\ \bar{A}_3\bar{A}_2\bar{A}_1 - \bar{A}_3^2\bar{A}_0 - \bar{A}_1^2\bar{A}_4 &> 0\end{aligned}\tag{3.48}$$

At the stability boundary, the real part of the root of the characteristic equation

is equal to zero and it holds that [11]

$$\lambda = i\omega \tag{3.49}$$

It follows from the equation 3.47 that

$$\omega^2 = \frac{\bar{A}_1}{\bar{A}_3} \tag{3.50}$$

3.3.4 Eigenvalue Analysis of Linearized Blade Equations Using FEM Formulation

This method of aeroelastic analysis is often referred to as *k-method* [75; 76]. In contrast to the eigenanalysis of linearized equations of motion of a rigid blade, eigenanalysis performed with the aid of FEM allows to compute high number of blade eigen-frequencies and mode shapes.

Assuming blade motion to be harmonic as in equation 3.45, blade natural frequencies $\{\omega\}$ and mode shapes $[\Phi]$ can be obtained by solving of the following eigenvalue problem [75; 76]

$$(-\omega^2 [M] + [K]) \{q\} = 0 \tag{3.51}$$

Once blade mode shapes are known, size of the system of equations of motion can be reduced significantly using principle of orthogonality of modes. Using a subset of shapes of the most significant modes of the blade $[\Phi_R]$, system matrices are modified as follows

$$\begin{aligned}
 [M_R] &= [\Phi_R]^T [M] [\Phi_R] \\
 [C_R] &= [\Phi_R]^T [C] [\Phi_R] \\
 [A_{GR}] &= [\Phi_R]^T [A_G] [\Phi_R] \\
 [K_R] &= [\Phi_R]^T [K] [\Phi_R]
 \end{aligned} \tag{3.52}$$

The system of blade equations of motion is simplified and hence easier to solve. It can be solved for the values of damping $\{g\}$ that has to be added to the system in order to make corresponding blade mode neutrally stable. If resulting values of this artificial damping are negative, the blade is stable for the given aerodynamic and inertial forcing. Using $\omega = \frac{2kV}{c}$ and re-multiplying reduced blade equations of motion by $\frac{1}{1+ig}$, the final form of blade equations of motion is [48; 75; 76]

$$\begin{aligned}
 \left(p^2 [\hat{M}_R] + [K_R] + [C_R] \right) \{\xi\} &= 0 \\
 [\hat{M}_R] &= \frac{k^2}{b^2} [M_R] + \frac{\rho}{2} [A_{GR}] \\
 p &= p_r + p_i i \\
 g &\approx p_i
 \end{aligned} \tag{3.53}$$

3.3.5 Solution of Differential Equations of Blade Motion with the Aid of Finite Element Method

The finite element method represents a numerical method that is by far most popular in the field of structural dynamics. The method of weighed residuals is one of the most convenient ways of solution of FEM problems. Using this method, a trial function that represents first approximation of the solution of the ODE has to be chosen. This approximate solution of the ODE can be either a function that is globally continuous in the domain (so-called strong formulation of the problem) or a function that is piece-wise continuous in the domain (weak formulation).

It can be very difficult to find approximations of an exact solution of an ODE that would be globally continuous and reasonably accurate at the same time. The weak formulation of the method of weighted residuals makes a selection of a trial function much easier since it uses piece-wise continuous trial functions. The trial function is defined by different functions on each sub-domain that are continuous on this sub-domain. The finite element method uses the weak formulation of the method of weighted residuals and finite elements are sub-domains on which individual components of the piece-wise continuous trial functions are defined.

The selected trial function is then substituted into the ODE and the residual is computed. The residual is not equal to zero for all coordinates within the domain since the trial function is not the exact solution of the ODE. In the next step, unknown constants of the trial function are determined. In order to achieve the best approximation of the exact solution, test functions (or weighting functions), are chosen and the weighted average of the residual over the domain of the problem is set to be zero. The number of test functions has to be equal to the number of unknown coefficients of the trial function [49].

The weak formulation of the differential equation of blade torsion can be written as [49]

$$\sum_{i=1}^{N_{elem}} \left(\int_{r_i}^{r_{i+1}} \left(\frac{\partial \hat{w}_i}{\partial r} G J_i \frac{\partial \theta_i}{\partial r} + \hat{w}_i i_{x,i} \ddot{\theta}_i - \hat{w}_i q_i \right) dr \right) = 0 \quad (3.54)$$

Unlike solution of DE of blade bending, the solution of DE of blade torsion does not necessarily require shape functions of higher order. Linear trial functions are sufficient for reasonably accurate solution of the problem. Hence, torsional deflection along i-th element of the blade can be expressed in the following manner [49]

$$\theta = S_1 \theta_i + S_2 \theta_{i+1} \quad (3.55)$$

where S_1 and S_2 are shape functions.

Using Galerkin method, the test function (weighting function) on i -th element of the blade is [49]

$$\begin{aligned}\hat{w}_i &= \frac{\partial \theta}{\partial \theta_i} = S_1 \\ \hat{w}_{i+1} &= \frac{\partial \theta}{\partial \theta_{i+1}} = S_2\end{aligned}\tag{3.56}$$

Use of Galerkin's formulation of finite element method for modelling of blade dynamics in torsion results in a system of differential equations that can be written in a matrix form [11; 27; 49]

$$[M]\{\ddot{\theta}\} + [C]\{\dot{\theta}\} + [K]\{\theta\} + \{f\} = 0\tag{3.57}$$

Mass matrix, damping matrix, stiffness matrix and forcing vector of i -th blade element $\{q\}$ are [49]

$$\begin{aligned}[M_i] &= \int_{r_i}^{r_{i+1}} \{S_i\}^T i_{x,i} \{S_i\} dr \\ [K_i] &= [C_i] = \int_{r_i}^{r_{i+1}} \{S'_i\}^T G J_i \{S'_i\} dr \\ \{f_i\} &= - \int_{r_i}^{r_{i+1}} q \{S_i\}^T dr\end{aligned}\tag{3.58}$$

Individual element matrices and the forcing vectors have to be assembled into the global matrices and the global forcing vector. This procedure is clearly described in Kwon and Bang [49]. If time-marching simulation is used, generalized coordinates and their first time derivatives (i.e. deflections and rates) that were computed in the previous time step are used for calculation of corresponding accelerations. Hence the matrix equation 3.57 reduces to

$$[M]\{\ddot{\theta}_i\} = -\{f_{F,j}\} \quad (3.59)$$

where $\{f_{F,i}\}$ is modified forcing vector of the system of equations at j-th time step

$$\begin{aligned} \{f_{F,j}\} &= \{f_j\} + \{c_j\} + \{k_j\} \\ \{c_j\} &= [C]\{\dot{\theta}_{j-1}\} \\ \{k_j\} &= [K]\{\theta_{j-1}\} \end{aligned} \quad (3.60)$$

In order to include the effects of blade rotation and couplings of rotor speed with the other blade degrees of freedom, additional terms have to be included in the differential equation of blade torsion. The corresponding DE is given by the equation 3.34. Since *AMRA* is a time-marching simulation, time derivatives of zeroth and first order of blade generalized coordinates have to be obtained from the previous time step. Hence the terms 3-6, 8 and 9 from the equation 3.34 are included in the forcing vector of the equation 3.59 [49]. Modified forcing vector is shown below.

$$\{f_{FA,j}\} = \{f_{F,j}\} + \{a_j\} \quad (3.61)$$

If a represents the sum of additional terms at i-th beam element, then the vector $\{a_i\}$ can be calculated as follows

$$\{a_j\} = \int_{r_i}^{r_{i+1}} a(t_j)\{H_i\}^T dr \quad (3.62)$$

Several different forms of shape functions can be used to solve the problem of blade torsion. Linear shape function is the most simple type of shape function that is applicable to the problem of torsional dynamics [49].

$$\begin{aligned} S_1 &= \frac{r_{i+1} - r}{r_{i+1} - r_i} = \frac{r_{i+1} - r}{l_i} \\ S_2 &= \frac{r - r_i}{r_{i+1} - r_i} = \frac{r - r_{i-1}}{l_i} \end{aligned} \quad (3.63)$$

Using equation 3.58, the stiffness matrix of i-th blade element is [49]

$$[K_i] = GJ \begin{bmatrix} \frac{1}{l_i} & \frac{-1}{l_i} \\ \frac{-1}{l_i} & \frac{1}{l_i} \end{bmatrix} \quad (3.64)$$

the element mass matrix is [49]

$$[M_i] = i_{x,i} \begin{bmatrix} \frac{l_i}{3} & \frac{l_i}{6} \\ \frac{l_i}{6} & \frac{l_i}{3} \end{bmatrix} \quad (3.65)$$

and the forcing vector of the i-th blade element is

$$\{f_i\} = f_i \left\{ \frac{l_i}{2} \quad \frac{l_i}{2} \right\}^T \quad (3.66)$$

The equation 3.65 shows so-called consistent form of the element mass matrix. Since solving of the matrix equation of blade motion requires inversion of the mass matrix, use of a consistent mass matrix decreases speed of computations. Hence the use of the diagonally lumped form of the mass matrix is more convenient

$$[M_i] = i_{x,i} \begin{bmatrix} \frac{l_i}{2} & 0 \\ 0 & \frac{l_i}{2} \end{bmatrix} \quad (3.67)$$

During the development of the *AMRA* model it was discovered that the dynamic FEM model of rotor blade torsion using linear shape functions could be less stable. Use of a FEM model with shape functions of higher order and diagonal (lumped) mass matrix removed this shortfall in the model. Other possible forms of shape functions are of higher order, cubic shape functions and square cosine shape functions being the simplest of them. Shape functions of higher order and corresponding finite element matrices are shown in Appendix A6.

Figure 3.14 shows comparison of different types of shape functions.

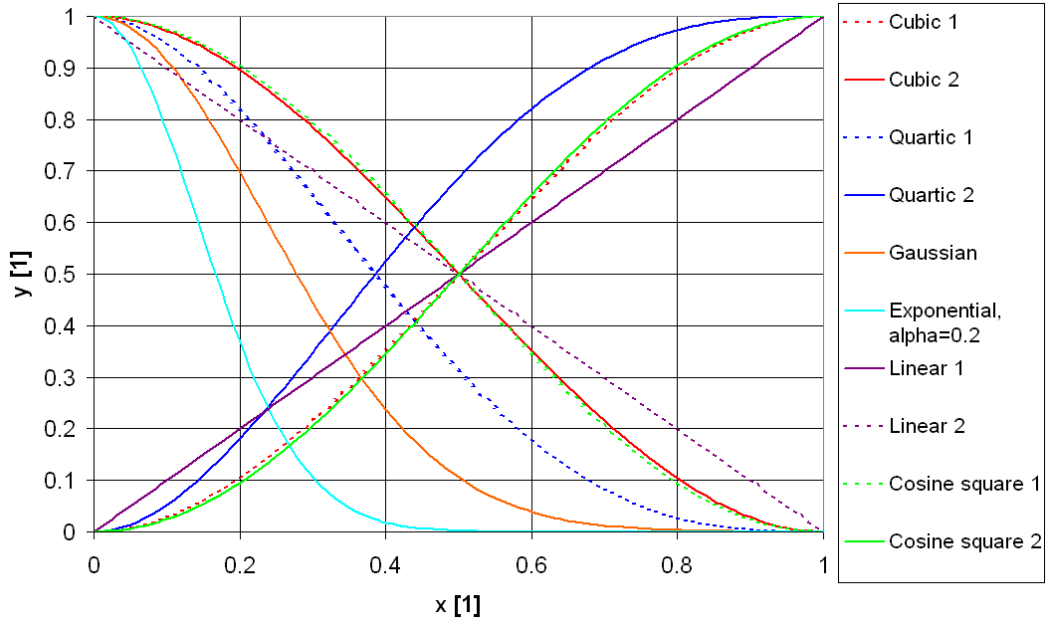


Figure 3.14: Comparison of different types of shape functions for FEM modeling of rotor blade torsion

The weak formulation of the differential equation of blade bending can be written as [49]

$$\sum_{i=1}^{N_{elem}} \left(\int_{r_i}^{r_{i+1}} \left(\frac{\partial^2 \hat{w}_i}{\partial r^2} EI_i \frac{\partial^2 w_i}{\partial r^2} + \hat{w}_i \hat{\mu}_i \ddot{w}_i - \hat{w}_i t_i \right) dr \right) = 0 \quad (3.68)$$

Unlike FEM modeling of rotor blade torsion, modeling of blade bending requires nodes with two degrees of freedom. The first degree of freedom represents blade vertical deflection and the second one is the slope of blade longitudinal axis. The vector of coordinates on i -th element of the blade is then

$$\{q_G\} = \{w_i \ \vartheta_i \ w_{i+1} \ \vartheta_{i+1}\}^T \quad (3.69)$$

Hence, more complex shape functions have to be used in order to describe the distribution of the two degrees of freedom over a blade element. Hamiltonian shape functions are mostly used in finite element models of beam bending (see equation 3.70). This form of shape functions is based on the cubic shape function de-

scribed in the previous section (see the equation A6-1) [49]. Other types of shape functions can be used too, for example Legendre shape functions [77].

$$\begin{aligned}
 H_1 &= 1 - 3\left(\frac{r - r_i}{l_i}\right)^2 + 2\left(\frac{r - r_i}{l_i}\right)^3 \\
 H_2 &= r - r_i - 2\left(\frac{(r - r_i)^2}{l_i}\right) + \left(\frac{(r - r_i)^3}{l_i^2}\right) \\
 H_3 &= 1 - H_1 = 3\left(\frac{r_{i+1} - r}{l_i}\right)^2 - 2\left(\frac{r_{i+1} - r}{l_i}\right)^3 \\
 H_4 &= -\frac{(r_{i+1} - r)^2}{l_i} + \frac{(r_{i+1} - r)^3}{l_i^2}
 \end{aligned} \tag{3.70}$$

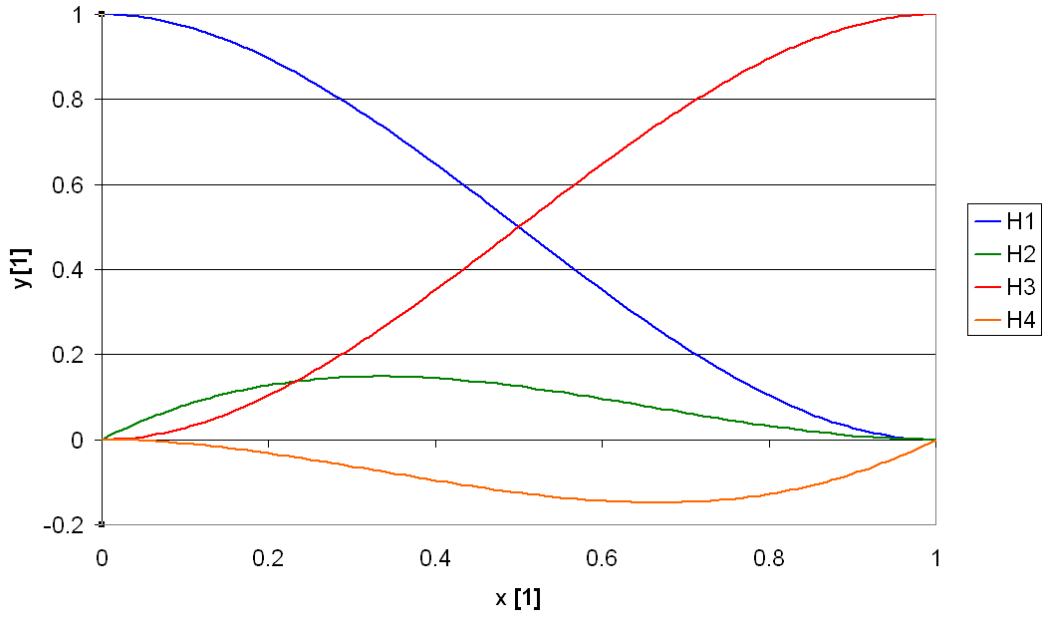


Figure 3.15: Hamiltonian shape functions for FEM modeling of blade bending

Application of Hamiltonian shape functions results in the following forms of stiffness matrix, damping matrix consistent mass matrix and forcing vector [49; 77]

$$\begin{aligned}
 [M_i] &= \int_{r_i}^{r_{i+1}} \{H_i\}^T i_{x,i} \{H_i\} dr \\
 [C_i] &= \int_{r_i}^{r_{i+1}} \{H'_i\}^T c_{\theta,i} \{H'_i\} dr \\
 [K_i] &= \int_{r_i}^{r_{i+1}} \{H''_i\}^T G J_i \{H''_i\} dr \\
 \{f_i\} &= - \int_{r_i}^{r_{i+1}} q \{H_i\}^T dr
 \end{aligned} \tag{3.71}$$

$$[K_i] = \frac{EI}{l_i^3} \begin{bmatrix} 12 & 6l_i & -12 & 6l_i \\ 6l_i & 4l_i^2 & -6l_i & 2l_i^2 \\ -12 & -6l_i & 12 & -6l_i \\ 6l_i & 2l_i^2 & -6l_i & 4l_i^2 \end{bmatrix} \tag{3.72}$$

$$[C_i] = \frac{c_\beta}{30l_i} \begin{bmatrix} 36 & 3l_i & -36 & 3l_i \\ 3l_i & 4l_i^2 & -3l_i & -l_i^2 \\ -36 & -3l_i & 36 & -3l_i \\ 3l_i & -l_i^2 & -3l_i & 4l_i^2 \end{bmatrix} \tag{3.73}$$

$$[M_i] = \mu_i \frac{l_i}{420} \begin{bmatrix} 156 & 22l_i & 54 & -13l_i \\ 22l_i & 4l_i^2 & 13l_i & -3l_i^2 \\ 54 & 13l_i & 156 & -22l_i \\ -13l_i & -3l_i^2 & -22l_i & 4l_i^2 \end{bmatrix} \tag{3.74}$$

$$\{f_i\} = \frac{f_i}{12} \{6l_i \quad l_i^2 \quad 6l_i \quad -l_i^2\}^T \tag{3.75}$$

Again, diagonal form of the mass matrix is more convenient for dynamic FEM analysis.

$$[M_i] = \mu_i l_i \begin{bmatrix} \frac{1}{2} & 0 & 0 & 0 \\ 0 & \hat{\alpha} l_i^2 & 0 & 0 \\ 0 & 0 & \frac{1}{2} & 0 \\ 0 & 0 & 0 & \hat{\alpha} l_i^2 \end{bmatrix} \quad (3.76)$$

The parameter $\hat{\alpha}$ has to be positive number smaller than $\frac{1}{50}$. Kwon and Bang [49] recommends $\hat{\alpha} = \frac{1}{78}$.

Mathematical models described within this chapter and in Appendices of this work were used in the *AMRA* model for modelling of aeroelastic behaviour of autorotating rotors and a major part of the work was focused on modelling of gyroplane rotors. Since the physical properties of light gyroplane rotor blades are not well documented and published, series of experimental measurements were carried out in order to obtain input parameters for the model of structural dynamics of a typical gyroplane rotor. An overview of these experiments and their results can be found in the following chapter (Chapter 4).

Individual components of *AMRA* model were verified and results of *AMRA* model were validated with the aid of both experimental results and prediction of validated analytical models. Validation and testing of the model and its components is shown in detail in the Chapter 5 of this work.

3.3.6 Capabilities of the *AMRA* Model

Since *AMRA* was designed with the open architecture approach in mind, it allows use of various combinations of different mathematical models (i.e. building blocks of the *AMRA* model). The model can perform computations in both time domain (time-marching simulations) and frequency domain (eigen-analysis).

The list of different models that are incorporated in *AMRA* is shown below.

A) Aerodynamics of the blade

- Quasi-steady model of rotor blade aerodynamics (can't predict compressibility effects) - time domain
- Unsteady model of rotor blade aerodynamics - Theodorsen's lift deficiency function with optional Wagner function - time domain (can't predict compressibility effects)
- Frequency domain formulation of Theodorsen's theory of unsteady aerodynamics (can't predict compressibility effects)
- Polynomial approximation of NACA 0012 aerodynamic characteristics (c_L , c_D and c_M) - includes both compressibility effects and non-linear aerodynamics
- Polynomial approximation of flat plate aerodynamic characteristics (c_L , c_D and c_M) - includes both compressibility effects and non-linear aerodynamics
- Different types of blade tip loss functions

B) Inflow modelling

- Semi-empirical inflow model of a rotor in autorotation - Glauert's model combined with several sets of experimental data (can't capture unsteady wake effects)
- Peters - HaQuang dynamic inflow model modified for autorotative flight - 1D (unsteady wake effects captured)
- Peters - HaQuang dynamic inflow model modified for autorotative flight - 3D (unsteady wake effects captured)

C) Structural dynamics

- FEM model of rotor blade coupled torsion/bending/chord-wise bending combined with 'rigid blade' models of blade teeter and rotation (chord-wise bending degree of freedom was locked)

- Equivalent spring stiffness model of rotor blade coupled torsion/bending/chord-wise bending combined with 'rigid blade' models of blade teeter and rotation (chord-wise bending degree of freedom was locked)
- Eigen-analysis of FEM model of coupled torsion/bending/chord-wise bending - classical k-method (chord-wise bending degree of freedom was locked)

D) Vehicle body dynamics

- A simple model of vehicle flight mechanics - prediction of speed of descent only (forward speed fixed)

Chapter 4

Estimation and Experimental Measurements of Blade Physical Properties

Since the majority of gyroplane rotor blades are manufactured by small private companies, it is relatively difficult to get any information on structural properties of these blades. A pair of blades from the Montgomerie-Parsons gyroplane were subjected to a series of experiments in order to assess their physical properties and mass distribution. Data gathered during the experiments were used as input values of the simulations and also for validation of the model of rotor blade dynamics.

4.1 Experimental Measurements of the Physical Properties of McCutcheon Rotor Blades

One of the two McCutcheon rotor blades was cut up into 20 sections and each was measured and weighed so as to ascertain span-wise mass distribution of the blade. Chord-wise position of centre of gravity was also estimated for each blade element from the arrangement of internal structure of blade cross-sections (i.e. position and size of the spar, thickness of the skin and distribution of potential filling material).

It was found that both mass distribution and chord-wise positions of CG are mainly given by span-wise distribution of the main blade spar. Span-wise distributions of blade mass per length that was obtained from the experiments is shown in the Fig. 4.1.

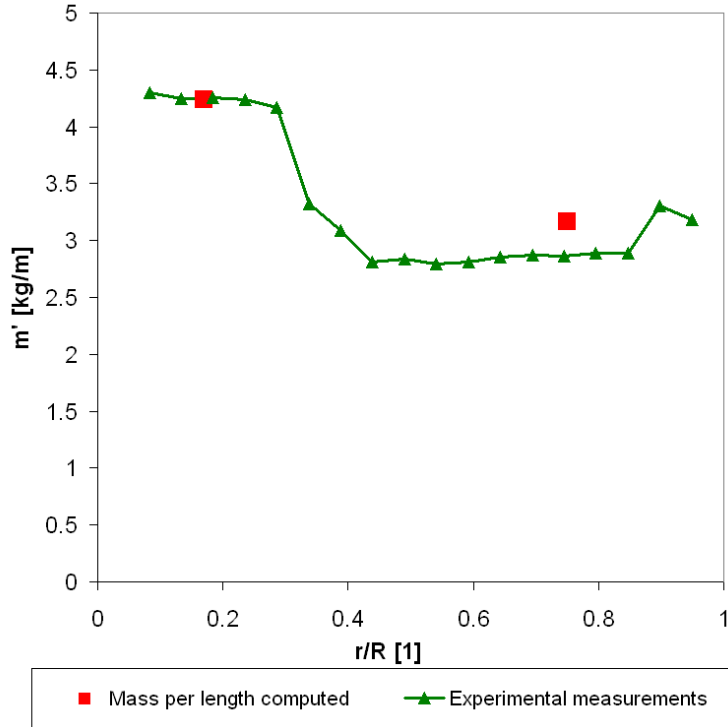


Figure 4.1: Span-wise distribution of mass of McCutcheon rotor blade

Experimental measurements accomplished with the aid of the second Montgomerie-Parsons gyroplane rotor blade were focused on structural properties of the blades. Torsional stiffness and chord-wise positions of elastic axis of the blade were measured at three span-wise stations. Span-wise positions of these stations were $x = 0.25$ (quarter-span), $x = 0.5$ (half-span) and $x = 0.75$. The rotor blade was firmly fixed at the root and an outboard clamp was attached at the appropriate span-wise station. The arrangement of the experiment is shown in the Fig. 4.2.

The outboard clamp was used for loading of the blade with a torsional moment. Constant weight was used and loading moment was altered by shifting of the weight along the clamp arm. Consequent measurements of blade angular deflections al-



Figure 4.2: Layout of the experiment aimed at measurements of blade stiffness and EA position

lowed calculation of corresponding torsional stiffness.

$$GJ = \frac{M_{\theta}}{\theta} r \quad (4.1)$$

Angular deflections of the blade in pitch were determined with the aid of a calibrated angle measuring instrument that was fixed to the upper surface of the clamp. Measurements were carried out for different values of torque at each span-wise station to increase higher accuracy of stiffness estimation. The method used for estimation of blade torsional stiffness of the blade is depicted in the Fig. 4.3.

Torsional stiffness was determined for each span-wise station of the blade (see the table 4.1).

Measurements of the first flexural natural frequency of the blade were used to estimate flexural stiffness of the blade. Using the slender beam theory, flexural stiffness can be calculated if a value of beam natural frequency, beam mass distribution and beam geometry are known [75].

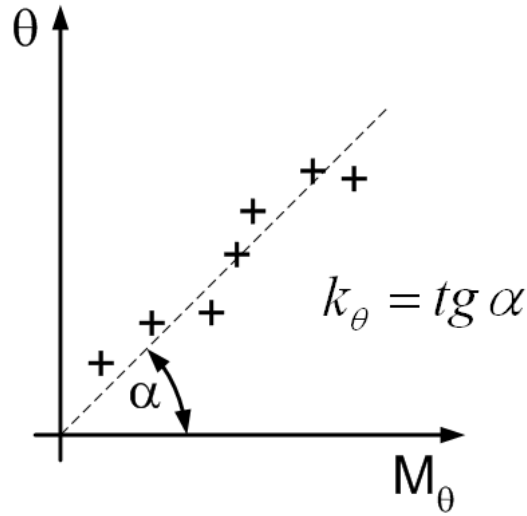


Figure 4.3: A sketch showing determination of blade stiffness from experimental data

Table 4.1: Results of experimental measurements of McCutcheon blade torsional stiffness and EA location

Span-wise station [1]	0.25	0.5	0.75
Location of EA [%c]	35.5	25.3	27.24
GJ [$N \cdot m^2/rad$]	1534	1443	1409

$$f = \frac{1}{T} = \frac{N_{cycles}}{t}$$

$$\omega = 2\pi f \tag{4.2}$$

$$EI \approx \frac{\omega_i^2}{\alpha_{il}} \sum_{j=1}^{N_{elem}} (m_j l_j^4)$$

Data gathered during the experiment are shown in the table below. The resulting estimated value of flexural stiffness is $EI = 1166.2N \cdot m^2$. The values of torsional and flexural stiffness obtained during the experimental measurements are of correct magnitude compared to data published in open literature [11; 78].

Figure 4.4 shows span-wise distributions of chord-wise positions of the elastic axis and the axis of inertia that were obtained experimentally. Note that blade elas-

Table 4.2: Results of experimental measurements of McCutcheon blade flexural natural frequency

N_{cycles} [1]	t [s]	T [s]	f [Hz]	ω [rad/s]
60	47.63	0.79383	1.2597	7.915
60	47.62	0.7937	1.2599	7.9167
60	47.67	0.7945	1.25865	7.9084

tic axis is located ahead of blade axis of inertia at the outboard part of the blade and hence pitch-flap flutter is possible. The rotor blade is not compliant with BCAR-T regulations that require blade centre of gravity ahead of its quarter-chord.

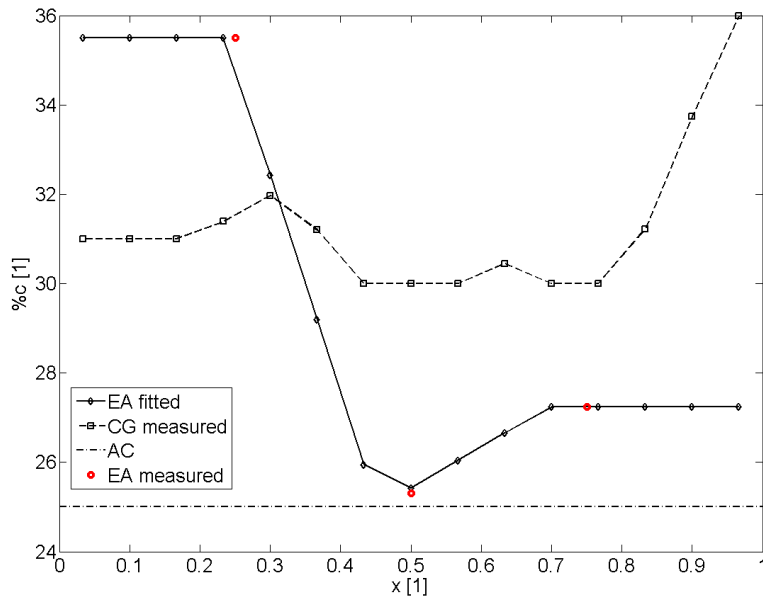


Figure 4.4: Span-wise distributions of EA, CG and AC of McCutcheon rotor blade

Span-wise distributions of torsional and flexural stiffness can be found in the Fig. 4.5.

The first natural frequency in torsion of the blade was determined experimentally as well. The blade was clamped at the root and forced to oscillate in torsion. The motion of the blade tip was recorded with the aid of high-speed camera; figure 4.6 shows layout of the experiment. The footage from the high-speed camera was trans-

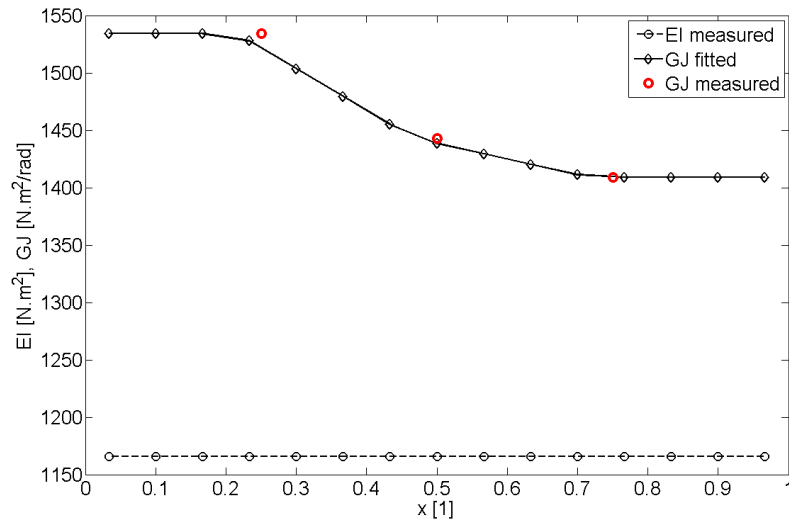


Figure 4.5: Span-wise distributions of torsional and flexural stiffness of McCutcheon rotor blade

formed into a time history of blade torsion. Resulting data were then processed with the aid of a spectral analysis tool, yielding estimation of frequency of the torsional oscillations. The first torsional frequency of McCutcheon rotor blade was estimated to be $f_{1T} = 34.8Hz$. This value agrees with torsional stiffness of the blade that was determined experimentally [75; 76].

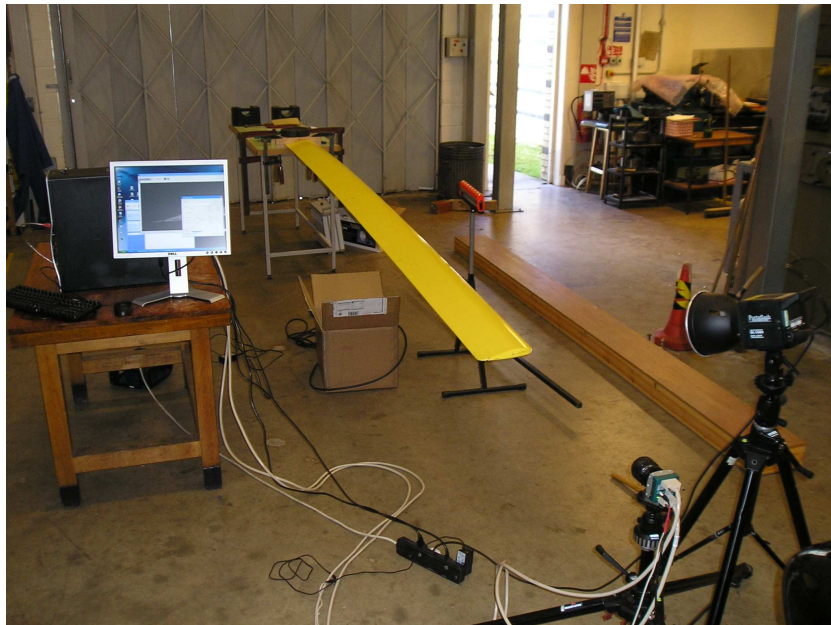


Figure 4.6: Experimental measurement of first natural frequency in torsion of McCutcheon rotor blade

4.2 Numerical Estimation of Moments of Inertia of McCutcheon Rotor Blade

A mathematical model of blade cross-section was created in order to estimate blade torsional mass moment of inertia and blade area moments of inertia. Torsional moment of inertia is an important input parameter of the model of blade dynamics. Since each blade element is modelled as a lumped mass, the model might exhibit singularities if the elastic axis is coincident with the centre of gravity. Addition of torsional mass moment of inertia into the equation of blade torsion solves this problem.

The structure of blade cross-section was discretized into a large number of elements and appropriate value of density was allocated to each of the elements. That allowed much more accurate estimation of blade mass moment of inertia in torsion and position of the centre of gravity than lumped mass approach and also made the inclusion of the contribution of blade skin possible. The figure 4.7 shows the values of blade mass moment of inertia per blade length for different positions of elastic axis as estimated by several different methods.

Results of the model were validated against experimental data. Both position of CG and mass per length of the blade are in good agreement with the values obtained during experimental measurements. Span-wise distribution of blade mass per length that was predicted by the model is compared with the results of experimental measurements in the Fig. 4.1. The figure 4.8 shows a comparison of the internal structure of the blade with the model of blade cross-section.

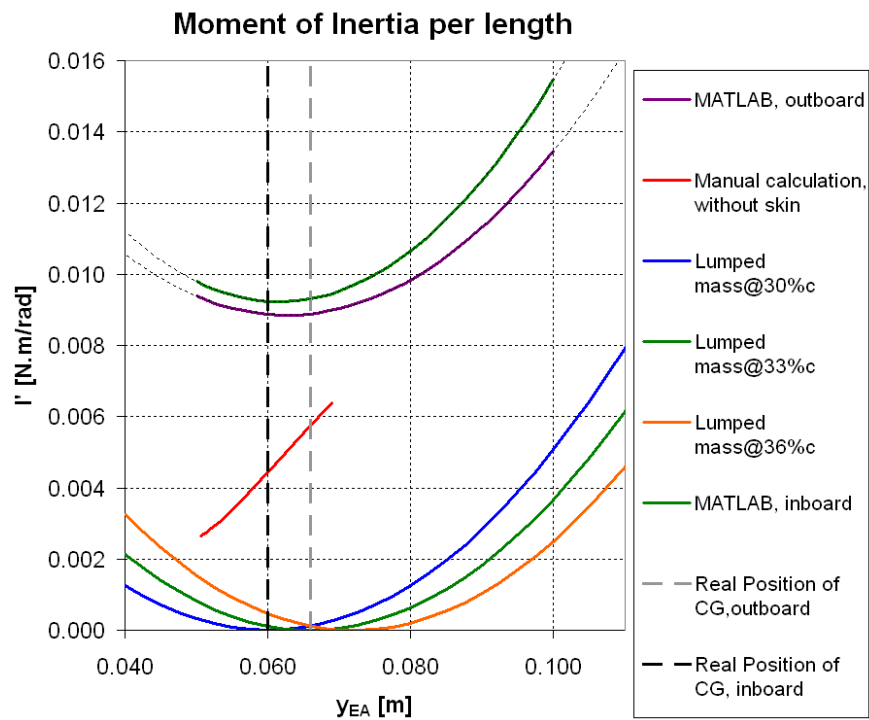


Figure 4.7: Values of mass moment of inertia in torsion of McCutcheon blade as estimated by several different methods

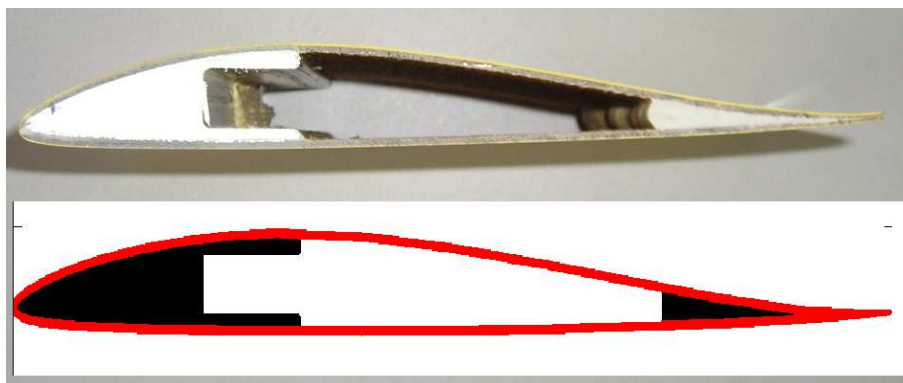


Figure 4.8: Comparison of a model of McCutcheon blade model with the real internal structure of the blade

Chapter 5

Verification and Validation of the *AMRA* Model

The main objective of the verification of the *AMRA* model was to make sure that all components of the model work correctly. The FEM model of blade dynamics represents the key block of *AMRA* and it is also by far the most complex component of the model. Hence extra care was taken during its testing and validation. Values of teetering angle predicted by the *AMRA* model were validated against G-UNIV flight data [74]. Predictions of the torsional and flexural frequencies were verified with the aid of results of several validated mathematical models.

Predictions of the torsional frequency of McCutcheon rotor blades were validated against the data gathered during experimental measurements of blade structural properties. Experimental data gathered during flight measurements of gyroplanes and published in the open literature were also used for validation of complete *AMRA* model [7].

5.1 Validation of the BEM Aerodynamic Model

Since the amended polynomial approximation of aerodynamic characteristics of NACA 0012 was developed specifically for the *AMRA* model, it had to be vali-

dated against experimental wind tunnel data. Figure 5.1 shows comparison of the values of lift coefficient as obtained with the aid of the improved Prouty’s method with experimental data from Carpenter [10] and outcomes of the original form of Prouty’s approximation. It can be seen that amended definition of coefficients C_5 and C_6 improves estimation of stall behaviour of the airfoil significantly for wide range of Mach numbers.

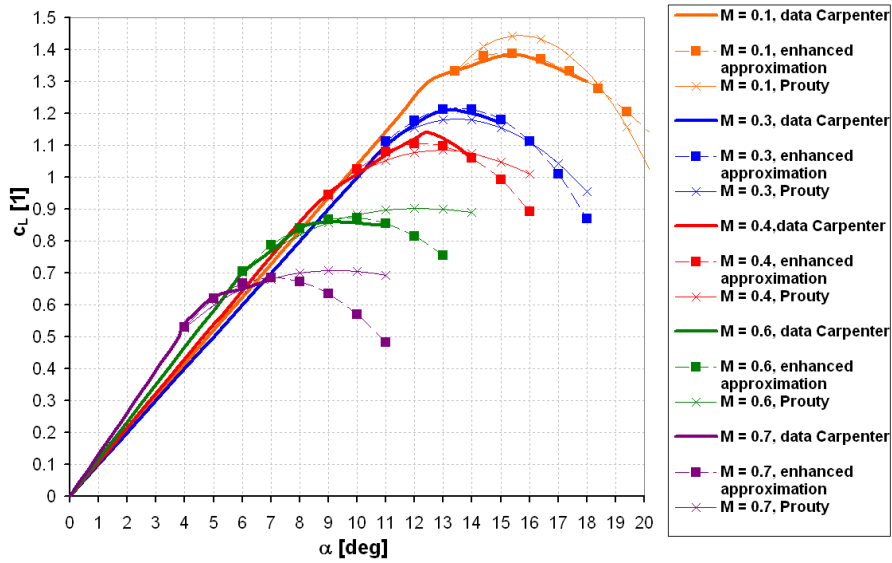


Figure 5.1: Comparison of the enhanced Prouty’s approximation of NACA 0012 lift curve with experimental data published by Carpenter [10] in the low angle-of-attack region

It was shown by the experimental measurements that the lift coefficient generated by an airfoil at high angles of attack ($\alpha \geq 20deg$) is a weak function of Mach number. Figure 5.2 depicts comparison of the values of NACA 0012 lift coefficient as obtained by polynomial approximation and data published in Sheldahl and Klimas [35]. Note that the behaviour of the airfoil during reverse flow is captured very well.

Figure 5.3 demonstrates that the values of NACA 0012 drag coefficient obtained with the aid of the Prouty’s method for low angles of attack are consistent with experimental data available in open literature.

Again, since drag coefficient of an airfoil at the angle of attack much higher than

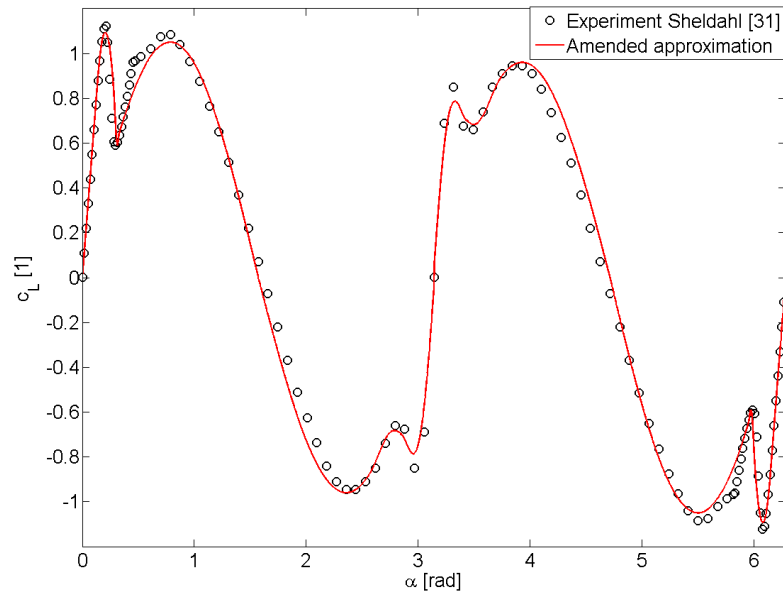


Figure 5.2: Comparison of the enhanced Prouty's approximation of NACA 0012 lift curve with experimental data published by Carpenter [10]

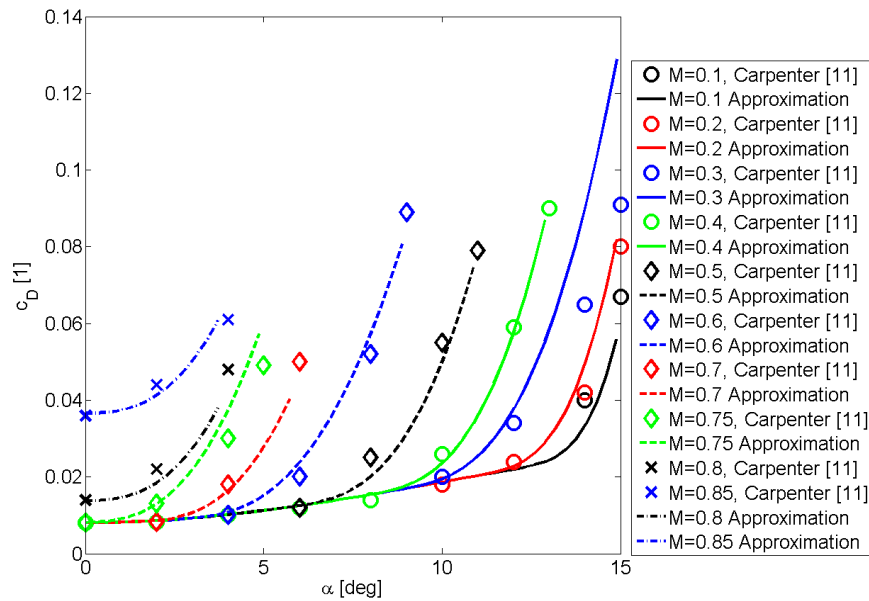


Figure 5.3: Comparison of the Prouty's approximation of NACA 0012 drag curve with experimental data published by Carpenter [10] in the low angle-of-attack region

the drag divergence angle does not depend on Mach number of the flow, figure 5.4 shows comparison of the polynomial fit and experimental data data for one Mach number only.

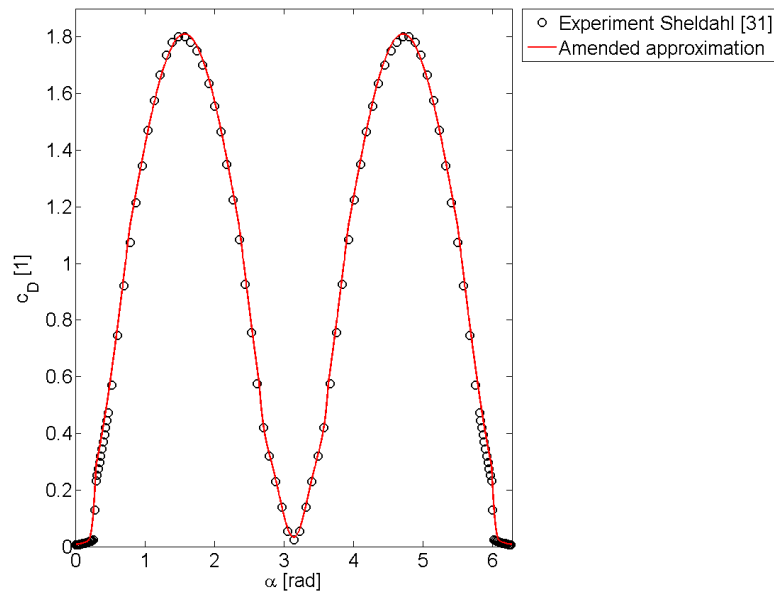


Figure 5.4: Comparison of the enhanced Prouty's approximation of NACA 0012 drag curve with experimental data published by Carpenter [10]

Figures 5.5 and 5.6 show comparison of the values of NACA 0012 moment coefficient obtained with the aid of the polynomial fit and corresponding experimental data for low angles of attack as published in Bielawa [11] and Leishman [12]. The data published in [12] originate from the wind tunnel research of Wood [79].

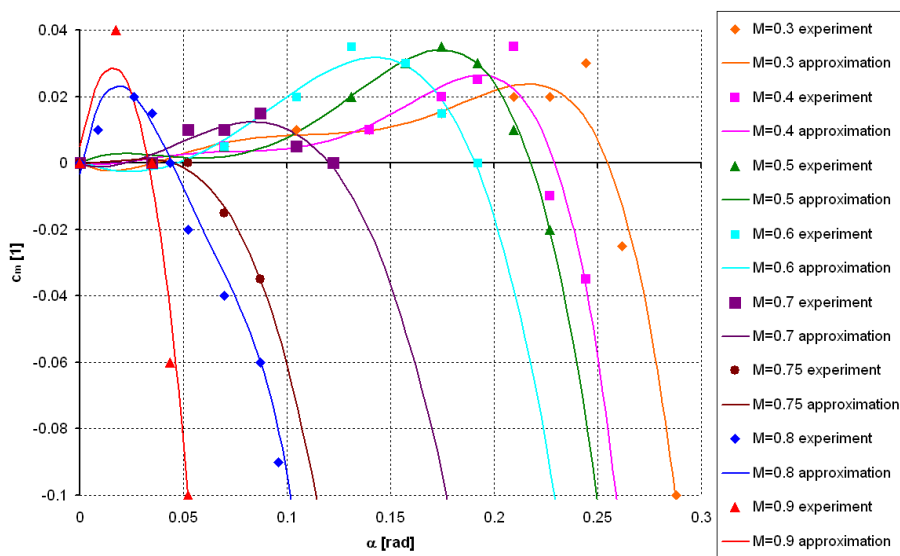


Figure 5.5: Comparison of polynomial fit of NACA 0012 moment curve with experimental data published by Bielawa [11] and Leishman [12]

Figure 5.6 depicts comparison of the values of polynomial approximation of NACA 0012 moment coefficient and data published in Sheldahl and Klimas [35].

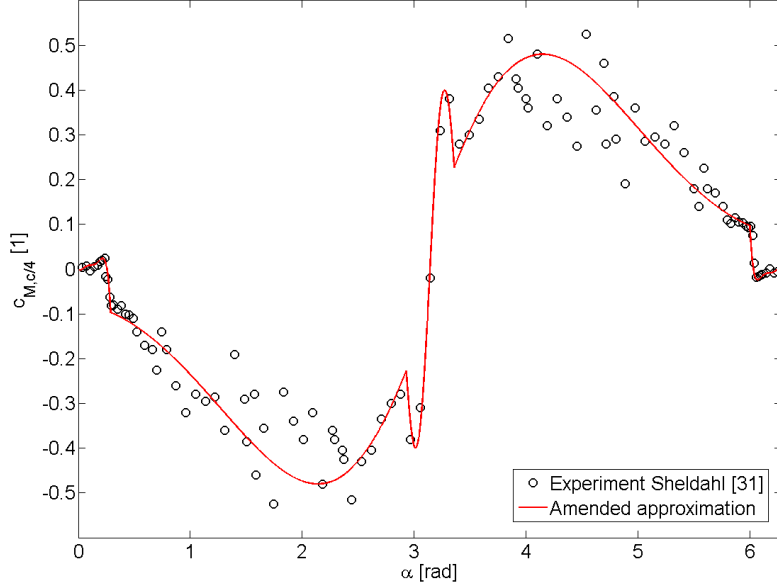


Figure 5.6: Comparison of newly formulated polynomial approximation of NACA 0012 moment curve with experimental data published by Carpenter [10] and [13]

5.2 Verification of the FEM Model of Blade Torsion

Predictions of static deflections in torsion made by the *AMRA* model were verified by analytical estimations of beam tip deflections. According to the St Venant theory of torsion, relationship between torsional deflection of a beam, torsional loading and beam torsional stiffness is

$$\begin{aligned} \frac{\partial \theta}{\partial L} &= \frac{M}{GJ} \\ \theta &= \frac{M}{GJ} L \end{aligned} \tag{5.1}$$

Beams of several different lengths and various values of torsional stiffness that were loaded statically by a torsional moment at the tip were computed by the *AMRA*

FEM model of blade torsion. The results were then compared with analytical estimations of beam tip deflections. As it can be seen from figure 5.7, predictions of the model are in agreement with theoretical results.

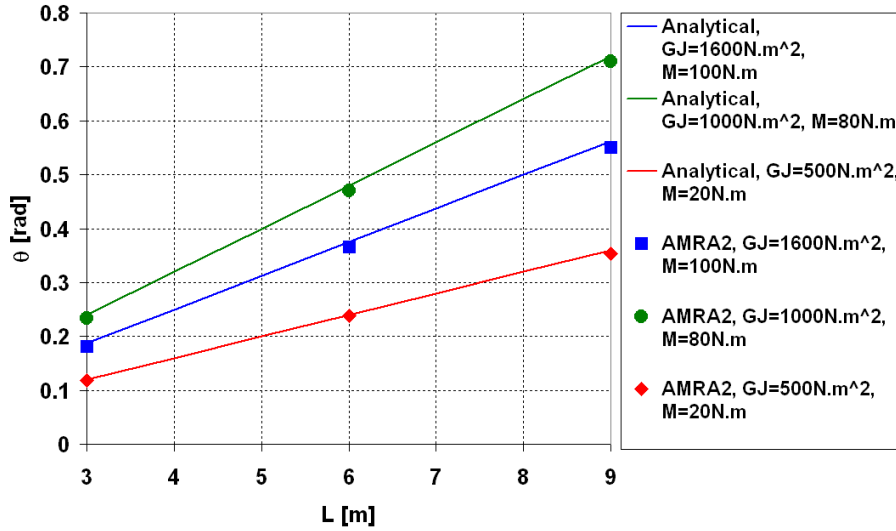


Figure 5.7: Comparison of estimations of torsional deformation of slender beam under static load of the FEM model of blade torsion with analytical results

The shape of the first torsional mode predicted by the FEM model was compared with the first torsional mode shape that was published in open literature [11] (see figure 5.8). The depicted mode is a rotating mode and the effect of the racquet moment can be observed towards the tip. The model gives very good agreement with the published data, especially in the case of an impulse load at the tip of a rotating blade and no aerodynamic loading. Span-wise distribution of blade torsion computed for forward flight (i.e. aerodynamic loading is present) is affected by span-wise distribution of blade aerodynamic loading and its harmonic character. Contributions of higher torsional modes are also more pronounced since tip impulse loading excites mainly the first torsional mode of the blade.

Figure 5.9 shows a comparison of the torsional mode shapes of the blade as predicted by *AMRA* with mode shapes obtained analytically [75].

Table 5.1 compares the values of non-rotating natural frequencies in torsion of

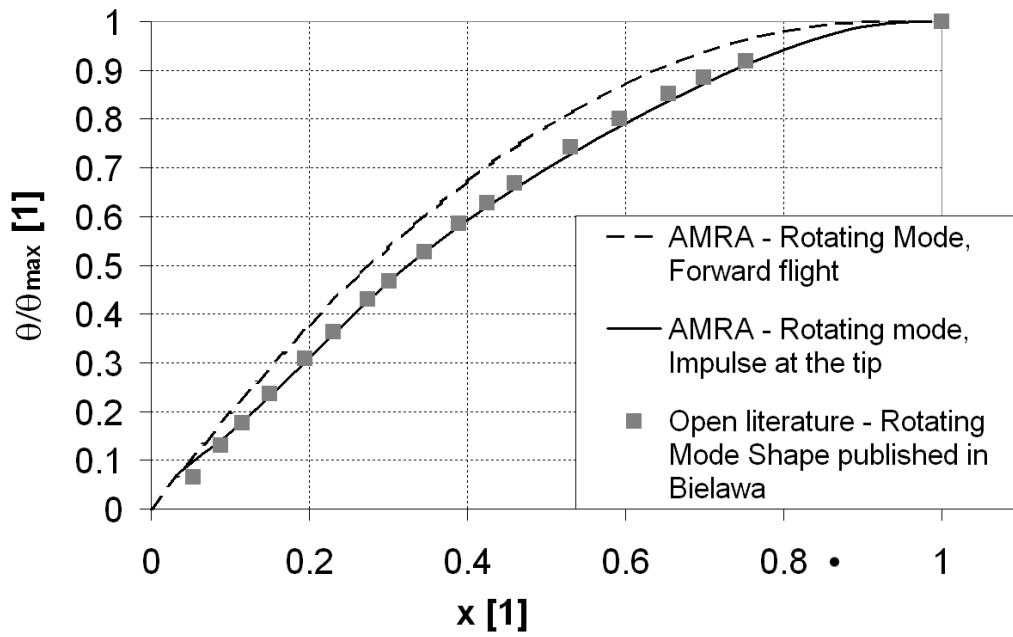


Figure 5.8: Comparison of the first torsional mode shape computed by *AMRA* and data from the open literature [11].

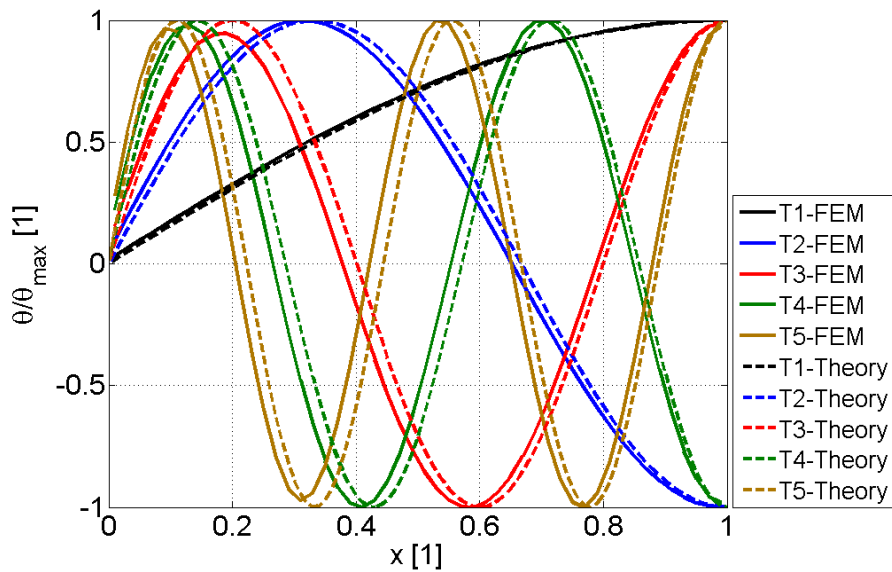


Figure 5.9: Comparison of the torsional mode shapes of McCutcheon blade computed by the *AMRA* and analytical results

McCutcheon rotor blades computed by *AMRA* with analytical results derived from the value of blade stiffness that was determined experimentally (see Chapter 4). Figure 5.10 shows a comparison of the first five non-rotating natural frequencies in torsion for different values of torsional stiffness as predicted by *AMRA* and by the theory [75].

Table 5.1: A comparison of the values of non-rotating torsional natural frequency of McCutcheon rotor blades as estimated by *AMRA* with analytical results

i	ω_{iT} [rad/s] AMRA	ω_{iT} [rad/s] Theory [75]	ω_{iT} [rad/s] Experiment
1	201.586	211.6	218.66
2	588.14	655.96	-
3	983.9	1093.28	-

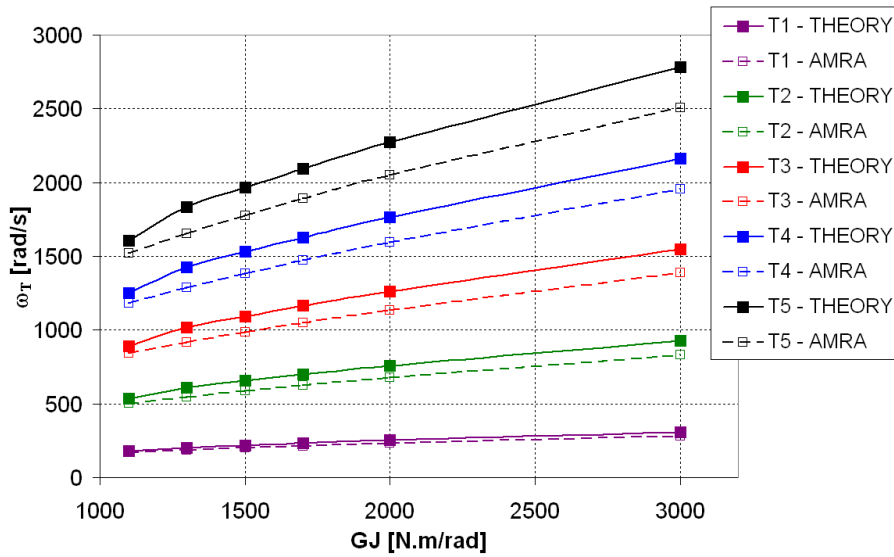


Figure 5.10: A comparison of torsional natural frequencies predicted by the *AMRA* with analytical results

Verification of predictions of the first torsional and flexural natural frequencies represented the next stage of *AMRA* testing. The data obtained during experimental measurements of physical properties of McCutcheon rotor blade were plotted in a Southwell plot along with corresponding values estimated by the model (see figure 5.11). As can be seen from the figure 5.11, the first natural frequency in torsion is under-predicted by *AMRA*. This discrepancy can be explained by low number of span-wise stations where the position of EA and torsional stiffness were measured. Errors in the measurements of blade physical properties together with the use of simplified slender beam FEM model of blade torsional dynamics might have caused less accurate prediction of the torsional natural frequency too.

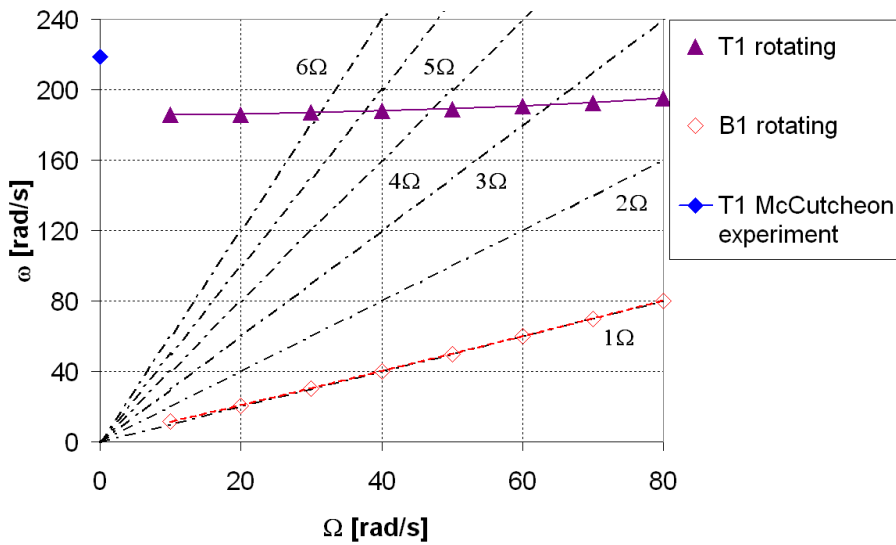


Figure 5.11: The Southwell plot of McCutcheon rotor blade showing the result of experimental measurements and predictions of *AMRA*

A comprehensive dataset of physical properties of Aérospatiale SA330 Puma helicopter rotor blades and results of several advanced mathematical models published in Bousman et al. [78] were also used for verification of the model of blade structural dynamics. A Southwell plot of the Puma helicopter rotor blade that includes comparison between results of the *AMRA* model and the aforementioned models for $\frac{\Omega}{\Omega_0} = 1$ can be found in figure 5.12.

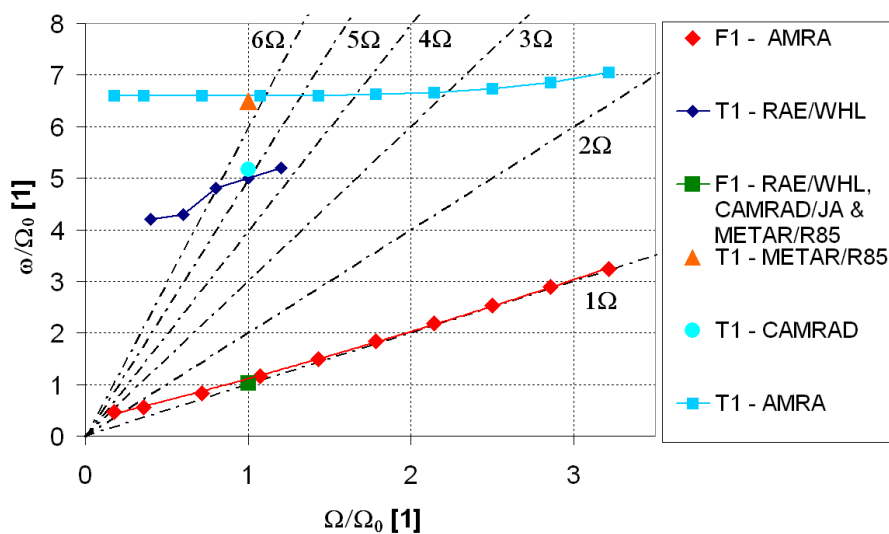


Figure 5.12: Southwell plot of the Aérospatiale SA330 Puma helicopter rotor blade

Estimation of the first natural frequency in torsion for a range of rotor speeds

are in very good agreement with results of *METAR/R85* model [78; 80]. Predictions of both *AMRA* and *METAR/R85* differ from the results of *CAMRAD* and *RAE/WHL* models [78; 81–83]. This is caused by the fact that both *CAMRAD* and *RAE/WHL* computations were carried out for finite values of control system stiffness, whereas *METAR/R85* and *AMRA* assume infinite stiffness of the control system. Taking these differences into account, Bousman et al. [78] describes predictions of modal frequencies obtained with the aid of *METAR/R85*, *CAMRAD* and *RAE/WHL* models as consistent. Hence predictions of the first natural frequency in torsion of the Puma rotor blades of the *AMRA* model can be considered to be in very good agreement with both published shake tests of similar rotor blades and results of other models of rotorcraft blade dynamics.

5.3 Verification of the FEM Model of Blade Bending

The coupled FEM model of blade torsion and bending was verified in a similar manner as the FEM model of blade torsion. Flexural deflections of rotor blades loaded both statically and dynamically were computed by *AMRA* and compared with analytical predictions, experimental measurements and the results of other mathematical models.

According to the classical theory of beam bending, blade vertical displacement and gradient of longitudinal blade axis can be calculated as shown in equation 5.2

$$\begin{aligned} w &= \frac{Fr^3}{3EI} \\ \frac{\partial w}{\partial x} &= \frac{Fr^2}{2EI} \end{aligned} \tag{5.2}$$

Beams of several different lengths and various values of flexural stiffness that

were loaded statically by a single force at the tip were considered in this verification exercise. Predictions of static bending as obtained from the *AMRA* model are in good agreement with analytical predictions. The values of blade vertical displacement obtained from the model are roughly 5% lower than the analytical predictions. Relative deviation of values of the blade gradient is roughly 6% and these values do not change with loading, blade flexural stiffness or blade length.

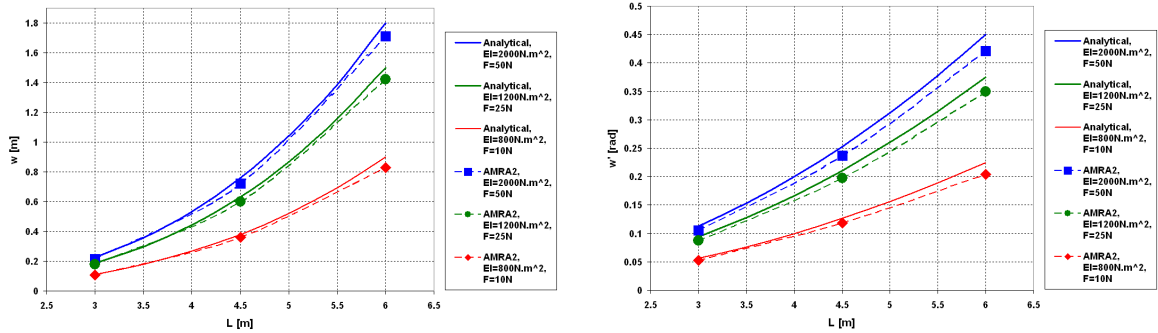


Figure 5.13: Comparison of the values of flexural vertical displacements and blade longitudinal gradients obtained from *AMRA* with corresponding analytical predictions

Figure 5.14 shows comparison of the bending mode shapes of a McCutcheon blade as predicted by *AMRA* with mode shapes obtained analytically [75].

Table 5.2 compares the values of non-rotating natural frequencies in bending of McCutcheon rotor blades computed by *AMRA* with analytical results based on the value of blade flexural stiffness that was determined experimentally (see Chapter 4). Figure 5.15 shows comparison of first five non-rotating natural frequencies in bending of homogeneous slender beams of different relative masses as predicted by *AMRA* and by the theory [75].

The ability of *AMRA* to predict rotor blade flexural dynamics was tested with the aid of the data published in Bousman et al. [78] and experimental measurements of McCutcheon rotor blade properties. It can be seen from figure 5.16 that there is a good agreement between the results of *AMRA* and the results of other models of

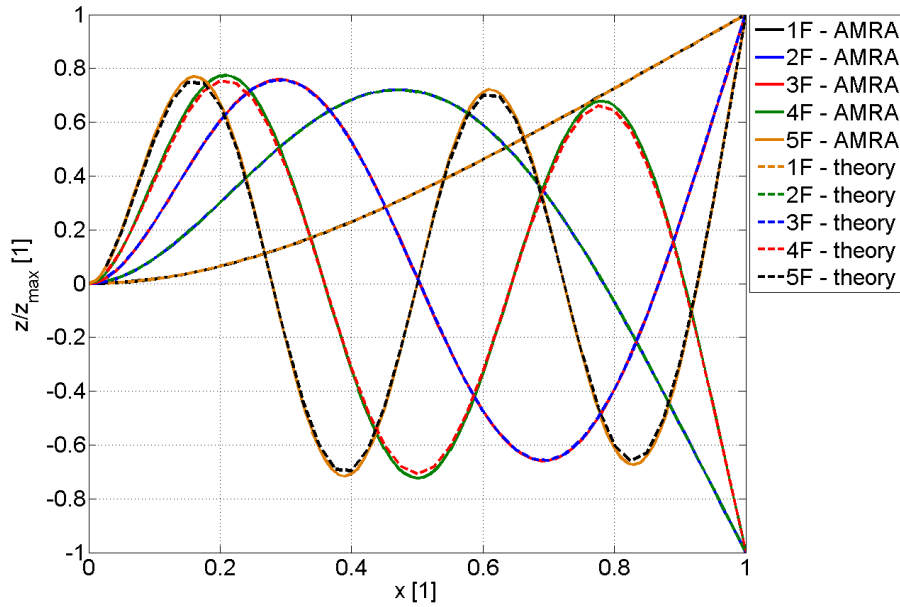


Figure 5.14: A comparison of bending mode shapes of McCutcheon blade computed by the *AMRA* with analytical results

Table 5.2: A comparison of the values of non-rotating flexural natural frequency of McCutcheon rotor blades as estimated by *AMRA* with analytical results

i	ω_{iF} [rad/s] AMRA	ω_{iF} [rad/s] Theory [75]	ω_{iF} [rad/s] Experiment
1	7.15	7.52	7.9
2	44.84	51.34	-
3	125.54	143.74	-

rotor blade structural dynamics.

The conclusion can be made that both static and dynamic behaviour of *AMRA* structural dynamics block was verified and that the model gives realistic estimations of both rotor blade torsion and bending.

5.4 Validation of Model of Rotor Teeter

Data gathered during CAA UK sponsored series of flight tests of the University of Glasgow Montgomerie-Parsons gyroplane (G-UNIV) (see Fig. 1.10) were used for

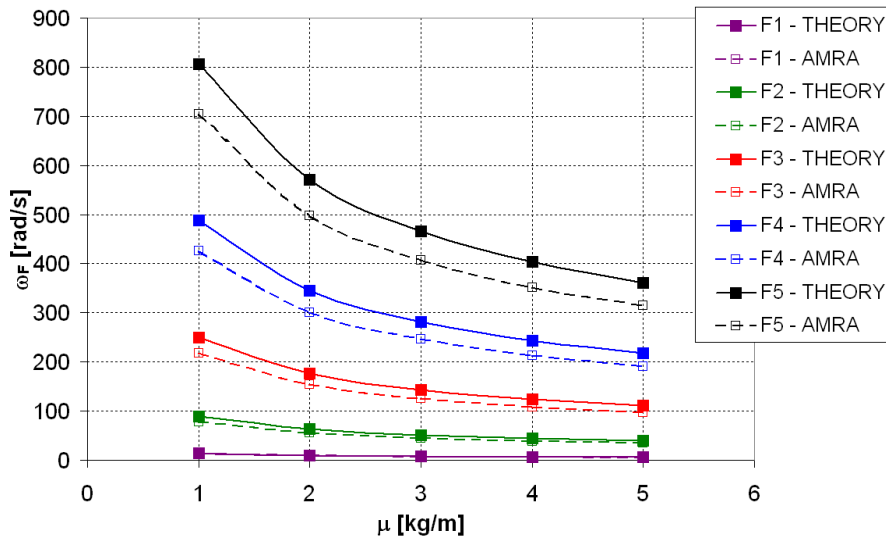


Figure 5.15: A comparison of bending natural frequencies predicted by the *AMRA* with analytical results

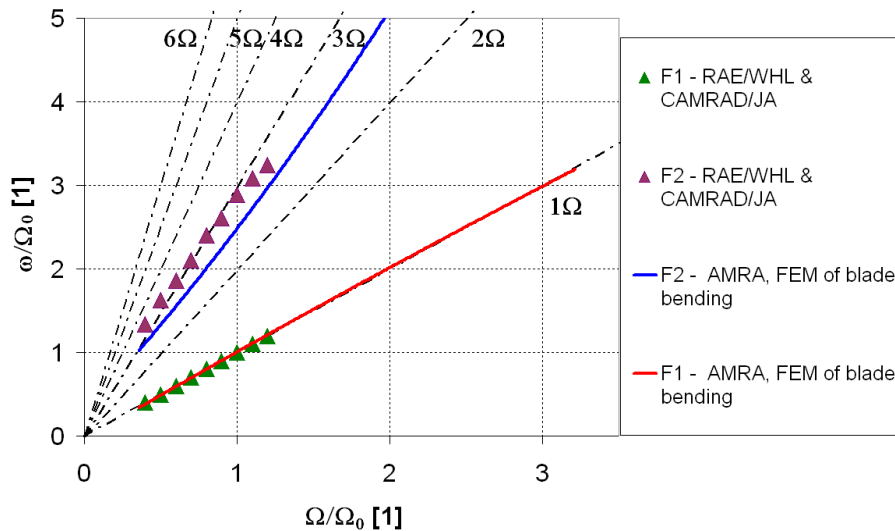


Figure 5.16: Comparison of the first two flapping natural frequencies of Aérospatiale SA330 Puma helicopter rotor blade computed by *AMRA* and other mathematical models

validation of the model of blade teeter that is included in *AMRA*.

AMRA uses NACA 0012 airfoil that has different aerodynamic characteristics in comparison with NACA 8-H-12 used in McCutcheon rotor blades. Since a database of non-linear aerodynamic characteristics of the latter was not available for a wide range of angles of attack, validation of the teeter model was performed for McCutcheon rotor blades with NACA 0012 sections. In order to reach similar flight

conditions during the simulations (especially rotor speed and speed of descent), rotor speed was set to mean value of rotor speed measured during the flight tests. Equilibrium rotor speed is higher if NACA 0012 is used instead of NACA 8-H-12 sections and hence predictions of the values of teeter angle would be affected by higher centrifugal stiffening. Two different regimes of steady level flight were chosen for the validation. Predictions of the model were found to be in a good agreement with the values of teeter angles measured during the flight trials. Table 5.3 and figures 5.17 and 5.18 show the results of validation of the model of rotor teeter.

Table 5.3: Comparison of predictions of rotor blade teeter and G-UNIV experimental data

CASE	V_H [m/s]	Ω [rad/s]	β G-UNIV [rad]	β AMRA [rad]
A	14	38	0.031	0.026
B	27	41	0.058	0.056

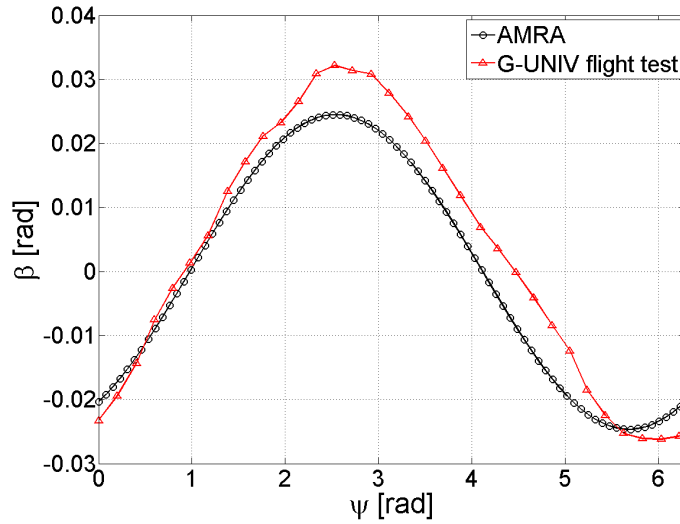


Figure 5.17: Comparison of predictions of rotor teeter and G-UNIV experimental data - case A

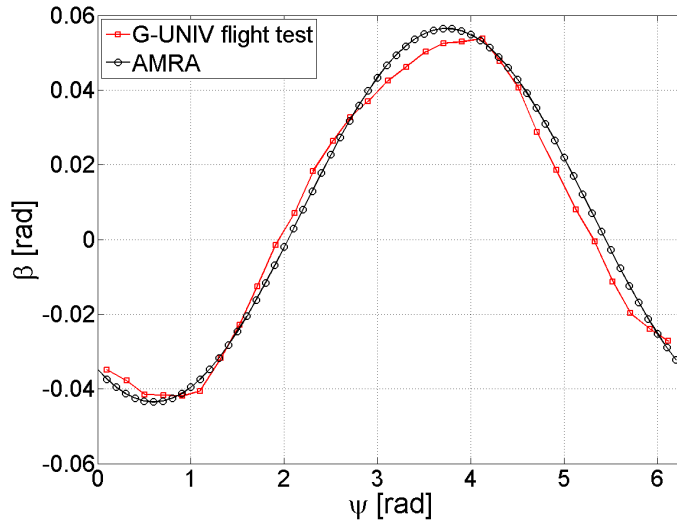


Figure 5.18: Comparison of predictions of rotor teeter and G-UNIV experimental data - case B

5.5 Verification of *AMRA* Predictions of Gyroplane Flight Mechanics and Performance

Once the model of blade structural dynamics that is used in *AMRA* model was validated, it was necessary to make sure that the complete model, i.e. the model of rotor aerodynamics coupled with the model of blade structural dynamics and the dynamic inflow model, works properly. This was done by comparison of *AMRA* results with the results of flight test measurements and wind tunnel data.

Steady axial flight in autorotation is characterized by torque equilibrium. The values of the horizontal component of lift at the inboard part of the blade are higher than the corresponding values of horizontal components of drag force during torque equilibrium. Hence positive torque generated by the inboard part of the rotor and it is in balance with negative torque generated by the outboard part of the rotor. This results in zero value of the total torque [7; 12]. Thrust-weight equilibrium represents the second essential condition of steady flight in autorotation. The total thrust of the rotor has to be in balance with the weight of the vehicle during steady autorotative vertical descent [7; 12]. The value of total rotor torque oscillates around the zero value during forward flight in autorotation due to harmonic variation of inflow

conditions. The total thrust is also a function of azimuth if forward speed of flight is not zero but the average value of rotor thrust is equal to the weight of the vehicle if steady flight is reached.

Both rotor thrust in axial flight and the average value of rotor thrust in the case of forward flight in autorotation converge towards the value of $M \cdot g$. Similarly, total rotor torque approaches zero value once steady flight in autorotation is achieved. Results of *AMRA* simulation of axial flight in autorotation of Montgomerie-Parsons gyroplane of weight $M=400\text{kg}$ (i.e. $M \cdot g= 3922.6 \text{ N}$, 1961.3N per blade) are shown in figure 5.19. It can be seen from the figure 5.19 that the model predicts the basic characteristics of a rotor in axial flight in autorotation correctly. Tests of the *AMRA* model confirmed that the value of total rotor aerodynamic torque converges towards zero and total rotor thrust converges towards $M \cdot g$ and the solution does not change with the length of time step.

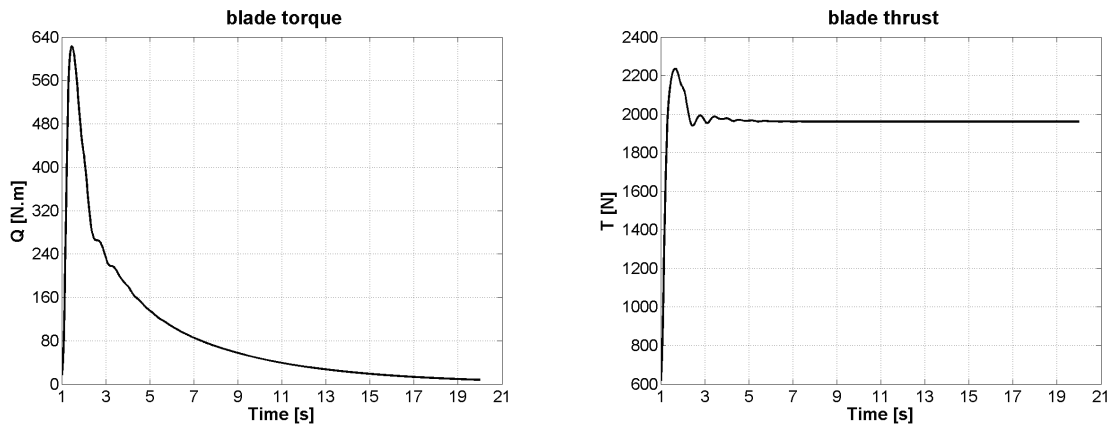


Figure 5.19: Results of *AMRA* simulation of axial flight in autorotation

A characteristic shape of the span-wise distribution of blade torque for a rotor in the autorotative regime is observed. The inboard part of the blade generates positive torque and the outboard part of the blade generates negative torque. In steady autorotation, the total value of torque generated by the blade is zero. Figure 5.20 shows span-wise distribution of torque obtained from the simulation. A sketch of torque distribution over the rotor disc as published in the open literature is depicted

in figure 2.5.

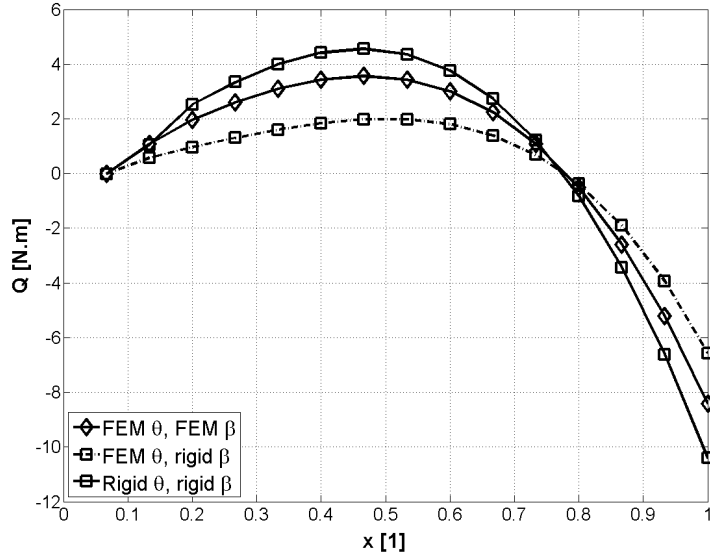


Figure 5.20: Span-wise distribution of rotor torque during autorotative vertical descent as predicted by *AMRA*

Since flow conditions of rotor blades vary with azimuth during autorotative forward flight, the torque generated by rotor blades changes with azimuth too. A rotor blade produces negative values of torque at the advancing side of the rotor disc and positive torque is generated at the retreating side of the rotor disc (but outside the reverse flow stall region). As it can be seen in figure 5.21, results of the *AMRA* model agrees with these findings.

In the case of vertical descent in autorotation, the value of rotor speed stabilizes when the torque equilibrium is reached. If the value of rotor speed is higher than the steady value for given rotor configuration, negative torque is produced by the rotor due to higher drag generated by the outboard parts of the rotor blades. This is caused by lower value of inflow angle at the blade tip region that causes small positive or negative values of the horizontal component of blade lift (see equation 3.21). Similarly, if the rotor speed is lower than the equilibrium value, the rotor is accelerated due to positive torque generated by the blades. The final value of the rotor speed during steady flight in autorotation (i.e. during torque equilibrium)

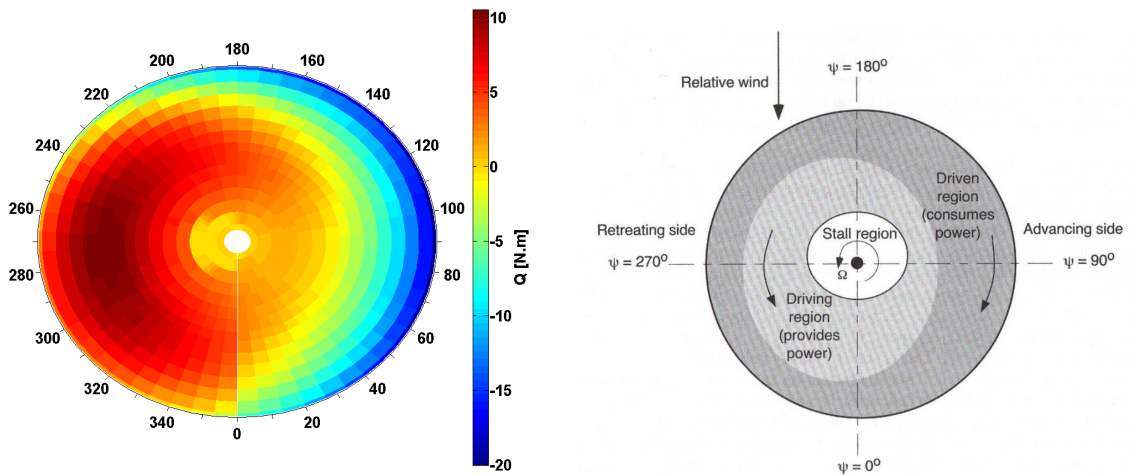


Figure 5.21: A qualitative comparison of distribution of torque generated by rotor blade over the rotor disc as predicted by the model and a qualitative sketch of torque distribution reproduced in open literature [12]

is not dependent upon the initial value of rotor speed, as long as it is higher than the critical value and the rotor is in the same, stable configuration. This behaviour can be observed in the results from the *AMRA* model. Figure 5.22 shows behaviour of gyroplane rotor pre-rotated to several different rotor speeds as predicted by the model. Again, the results of the model do not change with the length of time step.

The Vimperis diagram shown in figure 2.4 suggests that the range of blade fixed incidence in which a rotor can achieve steady autorotation is limited. The maximum value of aerodynamic angle of attack of a blade section is given by the value of angle of attack of the drag divergence. Figure 5.23 shows predictions of behaviour of an autorotating rotor in vertical descent for different values of fixed incidence. No experimental data are available but it can be seen from the figure that *AMRA* predicts reasonable trends.

Blade tip mass is commonly used in gyroplane design to increase rotor speed stability. Increased rotor moment of inertia leads to higher values of kinetic energy of the rotor during flight, which makes the rotor more resistant to destabilising effects of disturbances in rotor torque. Figure 5.24 depicts predictions of values of rotor speed during steady autorotative descent for different values of additional blade tip

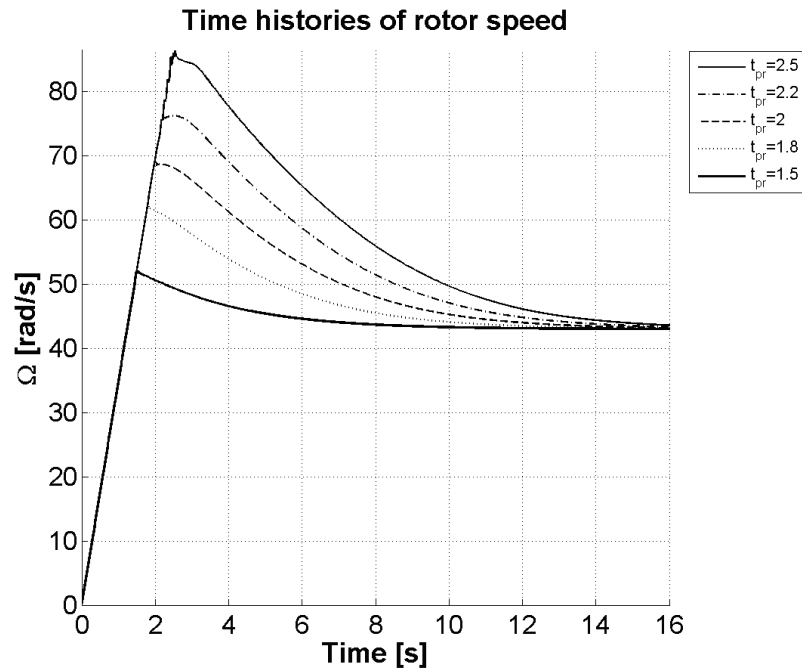


Figure 5.22: The effect of different initial values of rotor speed on the equilibrium value of rotor speed

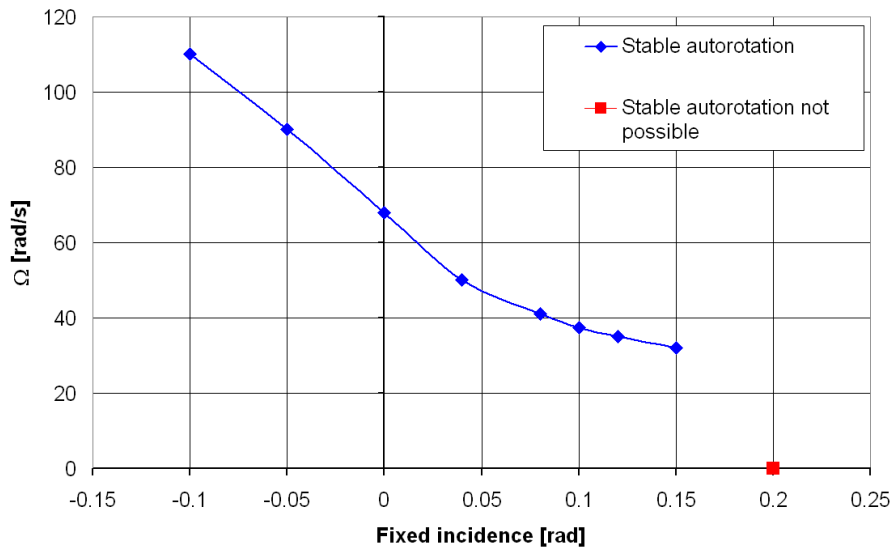


Figure 5.23: The effect of blade fixed angle of incidence on the steady value of rotor speed of a gyroplane rotor during axial autorotative flight as predicted by *AMRA*

mass. Again, no experimental data are available but the *AMRA* model gives a trend that agrees with real behaviour of gyroplane rotors.

Flight tests of rotors in autorotation showed that the value of flight speed of an autorotating rotor depends on the angle of attack of the rotor disc. It was also

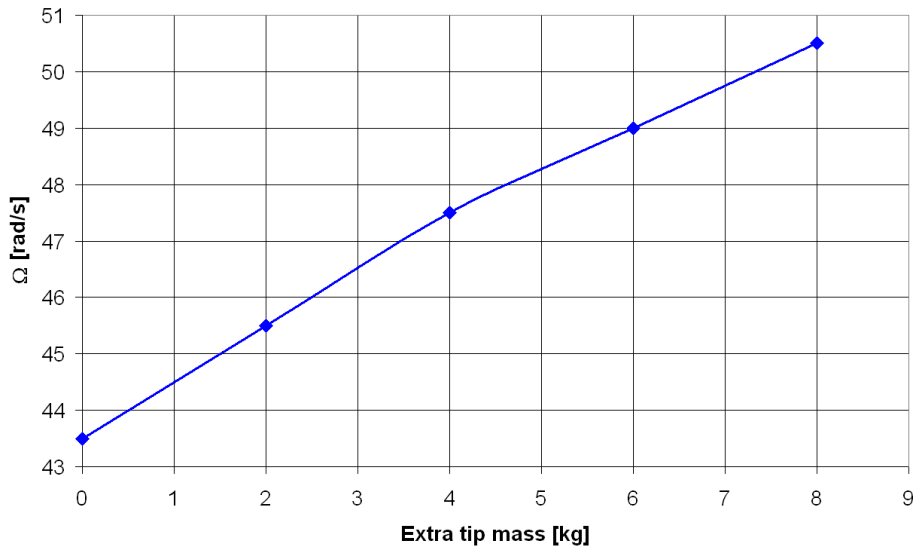


Figure 5.24: The effect of blade tip mass on the steady value of rotor speed of a gyroplane rotor during axial autorotative flight as predicted by *AMRA*

determined that speed of descent for $\alpha_D = 90deg$ (i.e. during axial flight in autorotation) lies between 10m/s and 12m/s. Values of speed of descent predicted by *AMRA* agree with the results of experimental flight measurements that were carried out by RAE and NACA [7; 23; 56]. Comparison of the results of the flight test and outcomes of the model are summarized in figure 5.25.

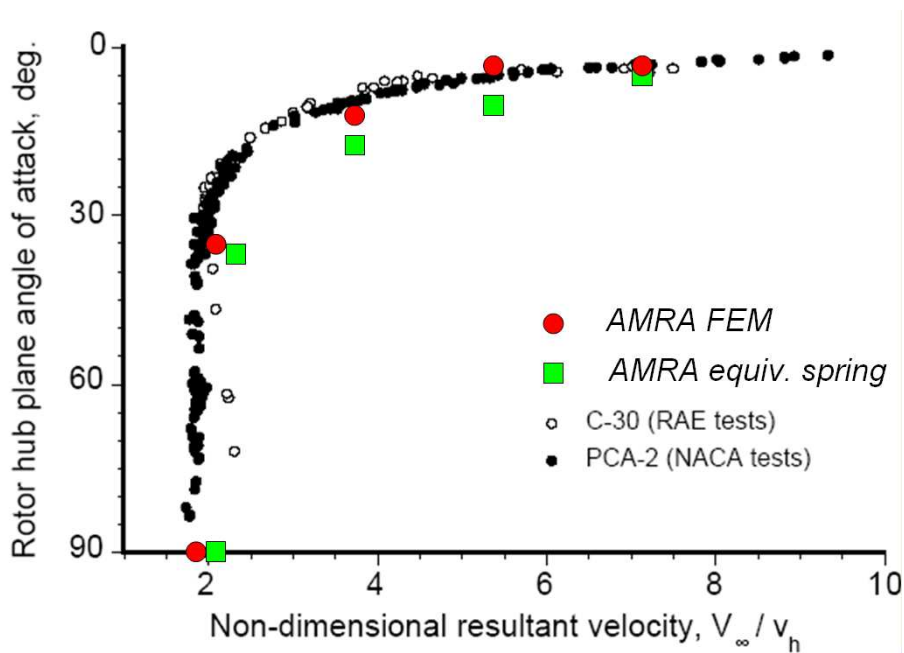


Figure 5.25: Comparison of values of dimensionless flight speed for a range of rotor disc angles of attack as determined during flight tests and predicted by *AMRA*

Experimental flight measurements also showed that resultant force coefficient c_R of a typical rotor during steady flight at large rotor disc angles of attack ($\alpha_D > 30deg$) is about 1.25 [7]. It is important to realize that the majority of gyroplane rotors have very small or zero fixed blade angle of incidence (i.e. collective pitch settings). The value of c_R is different for non-zero blade angles of incidence. Figure 5.26 shows the comparison of flight test data with the results of the *AMRA* simulation.

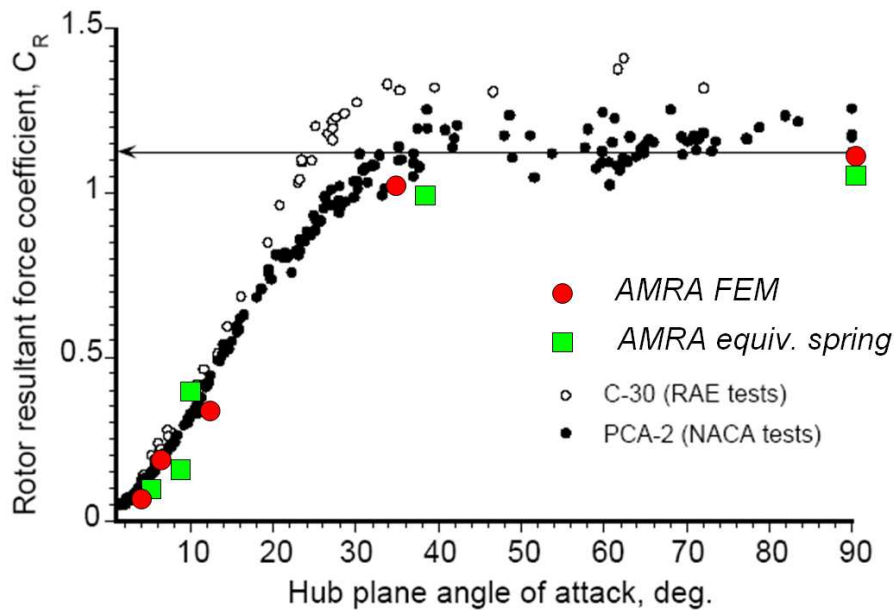


Figure 5.26: Comparison of values of resultant force coefficient for a range of rotor disc angles of attack as determined during flight tests and predicted by *AMRA*

The model also predicts correctly both speed of descent and forward flight speed for different flight regimes as it is shown in figure 5.27.

5.6 The Effect of Level of Complexity of the Blade Dynamic Model

Several different versions of the blade structural model were used for computation of the performance of the rotor. The aim of this study was to identify the configuration

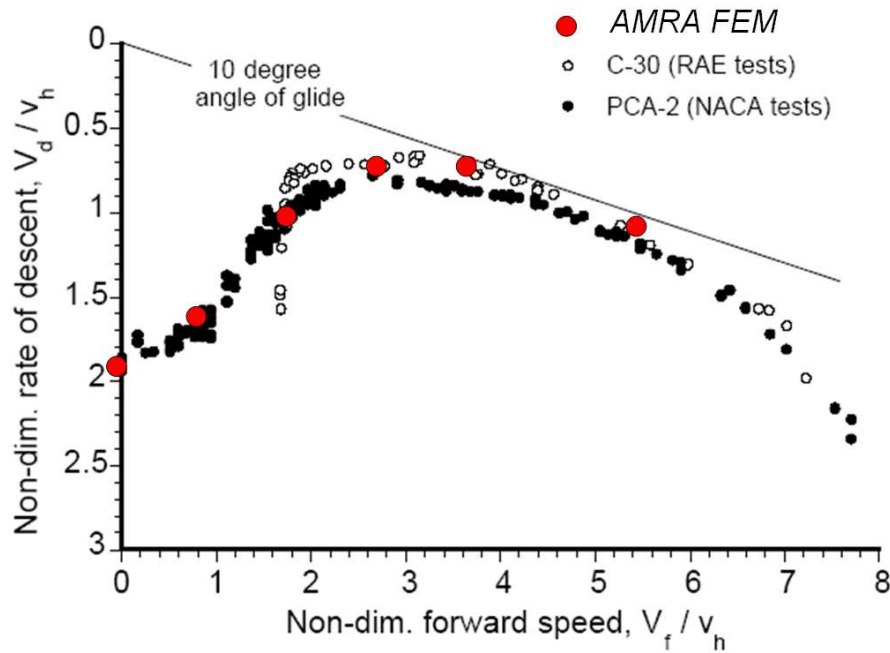


Figure 5.27: Comparison of the relationship between speed of descent and horizontal speed of a gyroplane as determined during flight tests and predicted by *AMRA*

of the model required for accurate prediction of rotor aeroelastic behaviour. The open architecture of the *AMRA* model allowed use of either a model of blade structural dynamics using equivalent spring stiffness ('rigid blade' models) or a model based on finite element method for modelling of rotor dynamics in torsion and bending. Alternatively, a combination of FEM model and simplified 'rigid blade' model could be used (e.g. equivalent spring stiffness model for blade bending and FEM for blade torsion etc.). All presented results were computed using FEM model of coupled torsion-bending of the rotor blades unless stated otherwise.

Results from the *AMRA* model show that the model is sensitive to the accuracy of modelling of blade torsional dynamics. Use of the equivalent spring stiffness model for modelling of blade torsional dynamics results in significantly different estimations of both blade deflections and rotor behaviour (see figure 5.28). Use of the simplified blade dynamic model results in 10% increment in the value of rotor speed during torque equilibrium since span-wise distribution of blade torsional deflection strongly affects prediction of blade aerodynamic loading. This significantly changes

the aeroelastic behaviour of the rotor as the increment of rotor speed leads to higher values of blade centrifugal stiffening.

On the other hand, differences in complexity of the model of blade bending/teeter seem to have only minor effect on predictions of performance of the rotor. Figure 5.28 shows a comparison of span-wise distributions of torsional deflections and vertical flexural displacements of a rotor blade in vertical autorotative descent computed for several different levels of complexity of rotor structural model.

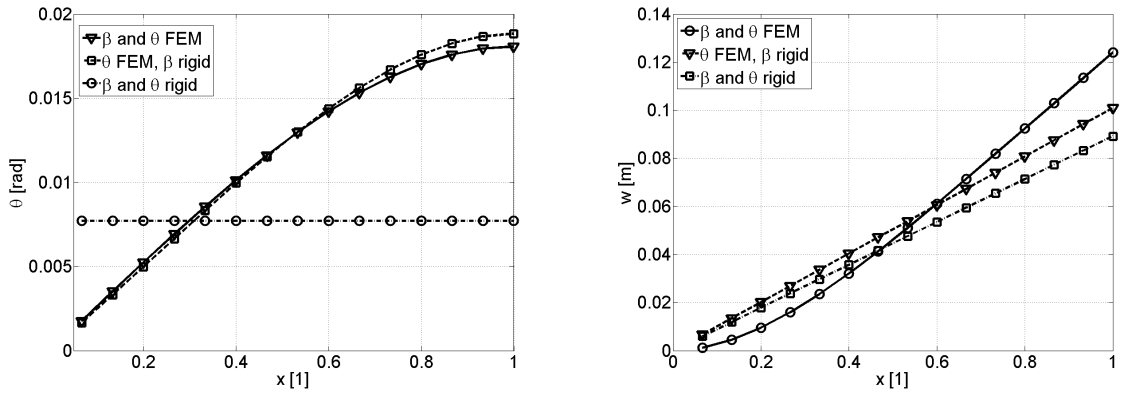


Figure 5.28: Results of *AMRA* simulation of axial flight in autorotation

It can be seen from figure 5.28 that the FEM dynamic model predicts that both the first bending (teeter) and first torsional modes are dominant during steady autorotative axial flight. Note that blade deflections in flap predicted by simplified rigid blade model represent very good approximation of the first teeter mode.

Since the inflow of rotors in steady axial autorotative flight is homogeneous, vibratory loading of rotor blades is not present or is negligible [7; 11; 27]. In contrast to axial flight regime, inflow velocity during forward flight reaches high values at the advancing side of the rotor disc and it drops significantly at the retreating side of the rotor. Hence the values of aerodynamic forces and moments generated by a rotor in steady autorotation oscillate around their equilibrium value (see Fig. 5.29). This results in a harmonic character of blade motion during steady forward flight in

autorotation. Fluctuation of rotor forcing occurs during forward autorotative flight and the performance of the rotor is also affected by compressibility effects and blade dynamic stall. These phenomena might have a de-stabilizing effect on aeroelastic behaviour of the rotor.

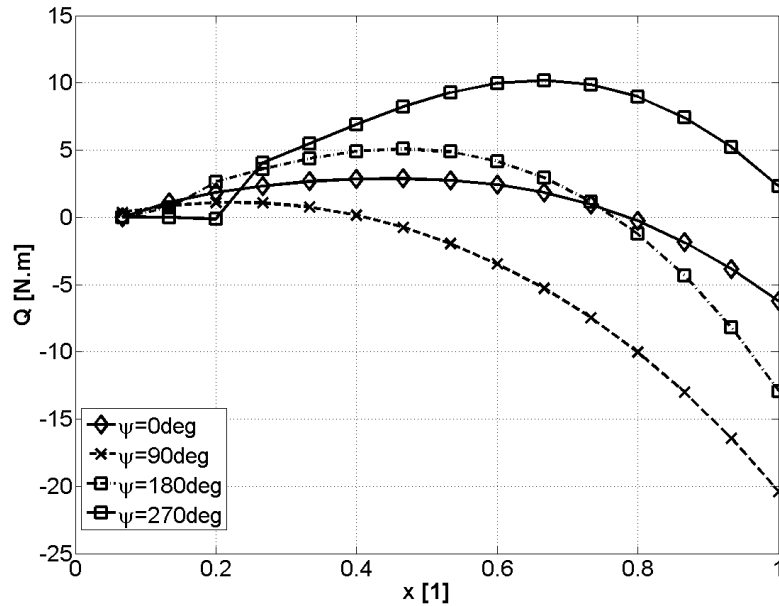


Figure 5.29: Span-wise distribution of blade torque during autorotative forward flight for different values of blade azimuth.

Comparisons of time histories of blade torsion and bending during one rotor revolution for different configurations of the blade structural dynamic model are depicted in figure 5.30.

Figure 5.30 shows that use of simplified model of blade torsional dynamics results in different predictions of amplitudes of blade torsion and that it also gives different trends of blade torsion during one revolution. This is given by the fact that the equivalent spring stiffness model can only capture the zero-th (rigid) mode of blade motion. It also can be seen from figure 5.30 that the amplitude of blade flapping motion predicted by the rigid blade torsional model is significantly lower. This is caused by higher rotor speed due to lower blade torsional deflections and corresponding higher centrifugal stiffening. However, the trend of blade flapping motion is very

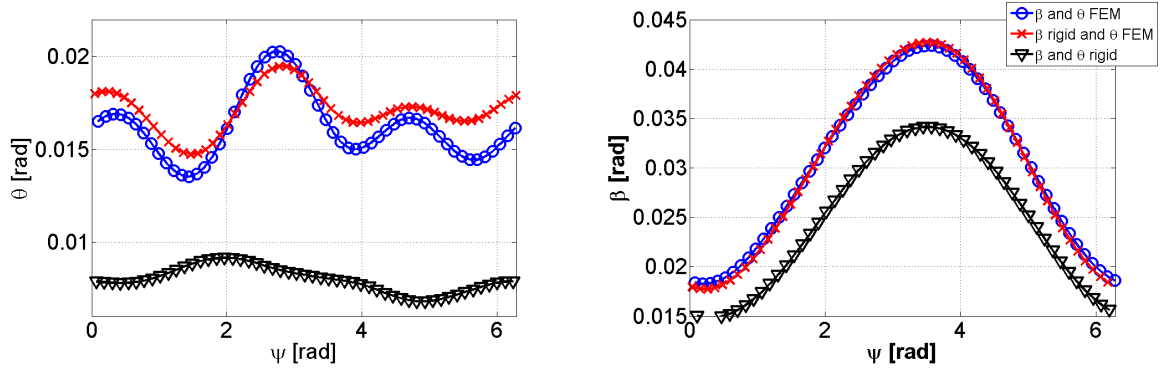


Figure 5.30: Rotor blade motion in flap and torsion in autorotative forward flight during one revolution

similar to the predictions of FEM model of blade structural dynamics if FEM model of blade torsion is used. This can be explained by dominance of the first flexural mode due to significant influence of centrifugal stiffening and aerodynamic damping on flapping motion of rotor blades. Aerodynamic damping of a rotor blade in flap (teeter) is proportional to $\dot{\beta}r$ and hence flapping and teetering motion is relatively highly damped. Aerodynamic damping and centrifugal stiffening of blade torsion are much lower since they are typically proportional to $\dot{\theta}y_g$ (and $y_g \ll r$ for major part of the rotor span) [11; 27].

Distributions of blade torsional deflections and vertical flexural displacements as predicted by *AMRA* for autorotative forward flight are depicted in figures 5.31 and 5.32.

It can be seen from figures 5.31 and 5.32 that *AMRA* predicts that the first modes are dominant in both torsion and flapping motion of a rotor blade during forward autorotative flight.

The results presented in this section demonstrate that accurate modelling of blade torsion is crucial for simulation of aeroelastics of autorotating rotors. Use of a FEM model of blade torsional dynamics is required for accurate estimation of blade span-wise distribution of angle of attack. Alternatively, an enhanced rigid blade model of blade torsion could be used, perhaps with the aid of prescribed mode

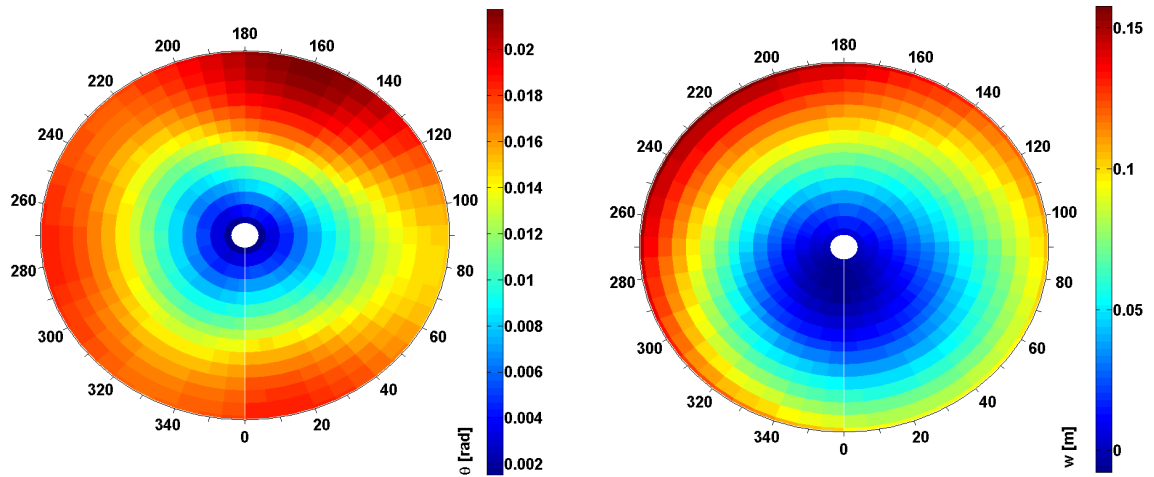


Figure 5.31: Distribution of blade torsional deflection and vertical displacement in bending obtained with the aid of *AMRA*

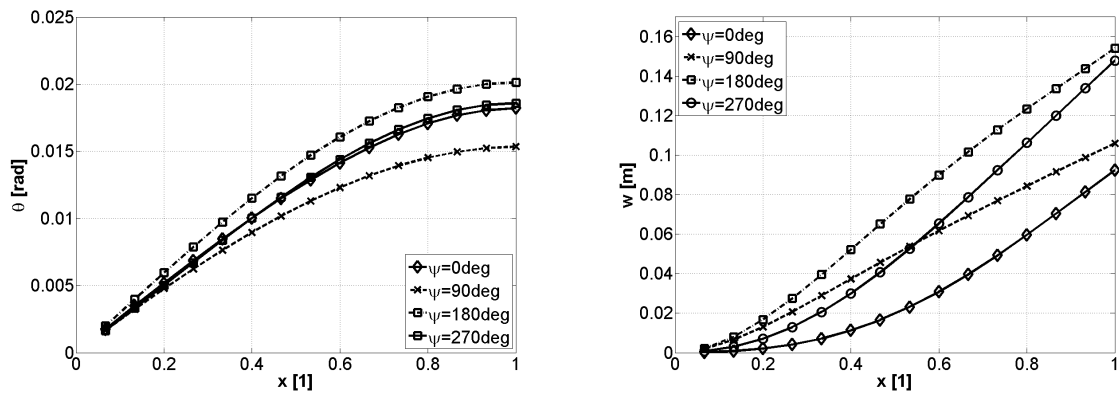


Figure 5.32: Span-wise distribution of blade torsional deflection and vertical flexural displacement in bending at four azimuthal stations as obtained with the aid of *AMRA*

shape. The resulting model would, however, be still able to capture only the first blade torsional mode, which would lead to inaccurate estimations of blade dynamics. As shown above, the use of a FEM model of blade bending further increases accuracy of the model but the difference is much smaller than in case of modelling of blade torsion.

The results of the *AMRA* model show that any future studies of aeromechanics of autorotating rotors should consider torsional degree of freedom and use at least simple FEM model of blade torsion. Some present studies dealing with performance and stability of rotors in autorotation could be extended in order to include blade

torsion [58; 59].

5.7 Summary

Verification of *AMRA* has shown that the model gives good predictions of aeromechanical behaviour of autorotating rotors. Although direct validation of the model was not possible (since no data describing aeroelastic behaviour of an autorotating rotor are available), verification of basic functionality of the model and its individual components was accomplished.

The model gives very good estimations of span-wise distributions of blade aerodynamic coefficients thanks to use of polynomial interpretation of aerodynamic wind tunnel data. *AMRA* can work across a full range of angles of attack and takes into account compressibility effects below stall. Accurate modelling of blade aerodynamics is, however, possible only for NACA 0012 airfoils and additional experimental data are required in order to switch to different type of blade section. It should also be noted that although the polynomial approximation of airfoil aerodynamic characteristics accounts for compressibility effects, both the theory quasi-steady aerodynamics and Theodorsen theory are inherently incompressible. Hence the model has limited capability to predict unsteady aerodynamic loading for high values of Mach number. The model is also not capable of modelling of stall flutter since it does not contain a dynamic stall model.

The model of blade structural dynamics included in *AMRA* is capable of prediction of rotor blade dynamics both in the time domain (time-marching model) and in the frequency domain (eigen-analysis). It was shown in this chapter that the model gives a good estimation of blade steady-state deflections and blade dynamics. However, capabilities of this block of the *AMRA* model are limited since it is based on 1D FEM model of a slender beam. Hence it is less accurate than more complex

mathematical models of blade structural dynamics (e.g. 3D FEM packages - ANSYS, PATRAN/NASTRAN, ABAQUS etc.) and its accuracy decreases for higher modes of blade motion. *AMRA* gives good predictions of both rotational speed and rotor teeter. Again, this applies only for rotor blades using NACA 0012 sections unless extra aerodynamic empirical data are added to the model.

Comparison of results from *AMRA* with data from experimental flight measurements showed that the model predicts overall flight performance and aerodynamics of rotors in autorotation well for a wide range of advance ratios. The *AMRA* model also exhibits basic qualitative features that were observed in autorotating rotors as torque equilibrium, weight-thrust equilibrium, a specific shape of span-wise distribution of aerodynamic torque and change of equilibrium rotor speed with blade tip mass.

The effect of different configurations of a model of blade structural dynamics on fidelity of the aeroelastic model of a rotor in autorotation was also investigated. The influence of accuracy of the model of rotor blade torsion on predictive performance of *AMRA* model was found to be strong. Configurations of the blade structural model that give unsatisfactory predictions of rotor behaviour during autorotation were identified. The results of *AMRA* simulations indicated what simplifications of the blade dynamic model are possible without significant degradation of its capabilities.

The comparison of the results obtained with the aid of different configurations of the model of blade structural dynamics show that

- Correct modelling of blade torsion during autorotation is absolutely essential
- Results of a model of a rotor in autorotation that does not contain an accurate model of blade torsion can be misleading thanks to coupling of blade torsion, flapping and rotor speed

- Finite element method model of blade torsion is required
- Fidelity of the model of blade flapping motion has much smaller effect on the results of the simulation
- Both FEM and equivalent spring stiffness model of blade flapping predict rotor behaviour well

Since a model of gyroplane flight dynamics is not included in *AMRA*, the model can be only used for modelling of steady axial or forward flight in autorotation (i.e. it is not capable of modelling of rotor aeroelastic behaviour during maneuvers).

Chapter 6

The Influence of Basic Design Parameters on the Stability of Rotors in Autorotation

A series of parametric studies was performed in order to investigate the influence of selected rotor blade design parameters on the performance of an autorotating rotor. Both axial descent in autorotation and autorotative forward flight were investigated. Author believes that a systematic study of the influence of blade design parameters on performance and aeroelastic stability of a rotor in autorotation has not been performed before. No relevant publications can be found in open literature. All presented results were computed using FEM model of coupled torsion-bending of the rotor blades unless stated otherwise.

The studies were focused on the following rotor blade design parameters:

- Blade fixed incidence angle
- Blade geometric twist
- Blade tip mass

The *AMRA* model was used to estimate aeroelastic behaviour of a rotor in autorotation for a range of values of these design parameters. Although blade torsional stiffness has also very strong influence on the behaviour of a rotor in autorotation, torsional and flexural stiffness of rotor blades are considered to be constant in this chapter and equal to the values determined experimentally (see Chapter 4). Blade axis of inertia was set to lie ahead of the blade elastic axis in order to avoid occurrence of pitch-flap flutter. The following chapter of this work (Chapter 7) is dedicated to a study of the influence of blade structural properties on aeroelastic stability of gyroplane rotors and an investigation of the rotor flutter boundary.

Since rotor torque during autorotation is generated solely by aerodynamic forces, the performance of an autorotating rotor is very sensitive to changes of blade span-wise distribution of angle of attack. If blade angles of attack are too high, torque equilibrium can not be achieved due to excessive values of the blade drag. Hence those of rotor design parameters that significantly affect span-wise distribution of blade angle of attack have a strong effect on the stability of flight in autorotation.

The same trend can be observed in the results from *AMRA*, which was as a lead during the selection of the blade design parameters that would be used in the study. Blade fixed incidence and geometric twist strongly affect blade aerodynamic angle of attack and hence have the most pronounced effect on the aeromechanical behaviour of autorotating rotors.

The last design parameter studied in this chapter, a blade tip mass, was chosen because it is frequently used in gyroplane rotor blade design to increase aeromechanic stability of the rotor. The concept of blade tip mass is straightforward - once the rotor is pre-rotated to certain rotational speed, the high moment of inertia of the rotor causes higher value of equilibrium rotor speed. Steady autorotative flight can not be achieved if rotor speed is too low - if rotor speed drops below the critical value, a positive value of total rotor aerodynamic torque is not reached. Hence

higher value of equilibrium rotor speed increases the stability of the rotor since more severe reduction of rotor speed would be needed in order to reach its critical value. Due to higher blade moment of inertia, more energy has to be extracted from the airflow in order to reach dangerously low values of rotor speed.

This behaviour of autorotating rotors imposes some limitations on the flight envelopes of rotors in autorotation since reduction of rotor speed below the critical value would have catastrophic consequences. Severe restrictions on negative load factor manoeuvres are required to prevent such decrease of rotor speed. Significant drop of rotor speed caused by negative inflow into the rotor disc could make steady flight impossible. Influence of manoeuvres on the stability of gyroplane rotors was not investigated in this work and simulations were focused on the relationship between the critical rotor speed and rotor blade design parameters.

6.1 Blade Fixed Incidence Angle

Theoretical works on aerodynamics of autorotating rotors and experimental measurements during flight in autorotation reveal that the range of incidence angle of a rotor blade section for which steady autorotation can be achieved is limited [7; 12]. A parametric study investigating the effect of fixed incidence angle on aeroelastic behaviour of rotors in autorotation was performed with the aid of the *AMRA* model. Very little relevant information is available in open literature. The outcomes of the study can be used as a basic lead during rotor blade design or preparation of emergency landing procedures of helicopters.

The results obtained from the *AMRA* model correlate with conclusions of experimental measurements. Magnitude of the critical value of fixed incidence angle agrees with the critical value of local incidence angle of a blade section in autorotation as obtained from Vimperis diagram - see figure 2.4. Figure 6.1 shows change of

the equilibrium rotor speed of a typical light gyroplane with fixed incidence of the rotor blades.

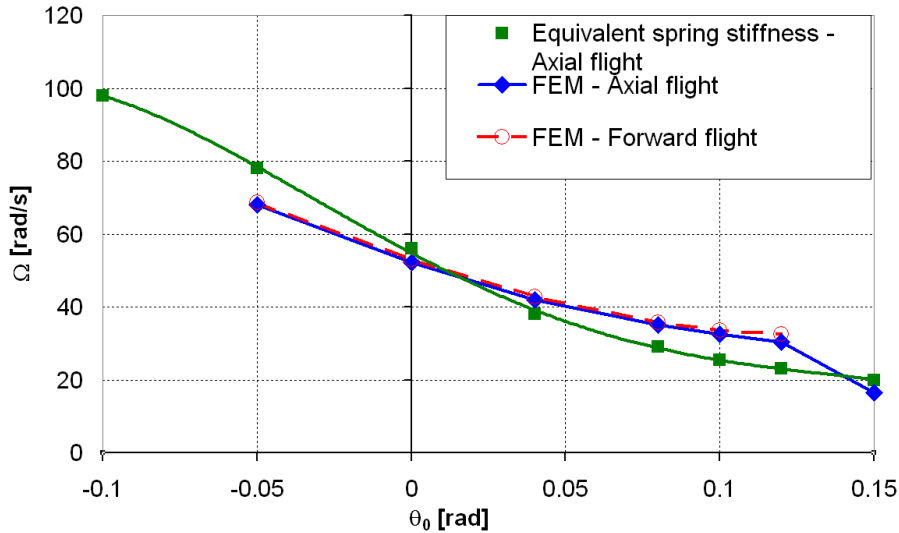


Figure 6.1: The effect of blade fixed angle of incidence on rotor speed of a rotor in autorotative flight as predicted by *AMRA*

Figure 6.1 also shows that use of simplified rigid blade dynamic model of rotor blades results in different predictions of equilibrium rotor speed. As it was shown in Chapter 5, use of equivalent spring stiffness causes under-prediction of the torsional deformations of the outboard part of the blade. Hence the critical value of fixed incidence angle is over-predicted.

Figure 6.2 shows the effect of fixed incidence angle on resultant force coefficient of a typical gyroplane rotor as predicted by *AMRA*. It can be seen from the figure that maximum c_R is about 1.25, which correlates with results of experimental flight measurements - see Chapter 5. It can also be seen from figure 6.2 that the use of an equivalent spring stiffness model of a rotor in autorotation results in prediction of significantly higher values of c_R for high values of blade fixed angle of incidence.

The simulations have shown that blade fixed incidence angle has significant effect on the value of rotor induced velocity. Figure 6.3 shows that the effect is especially pronounced during axial flight in autorotation.

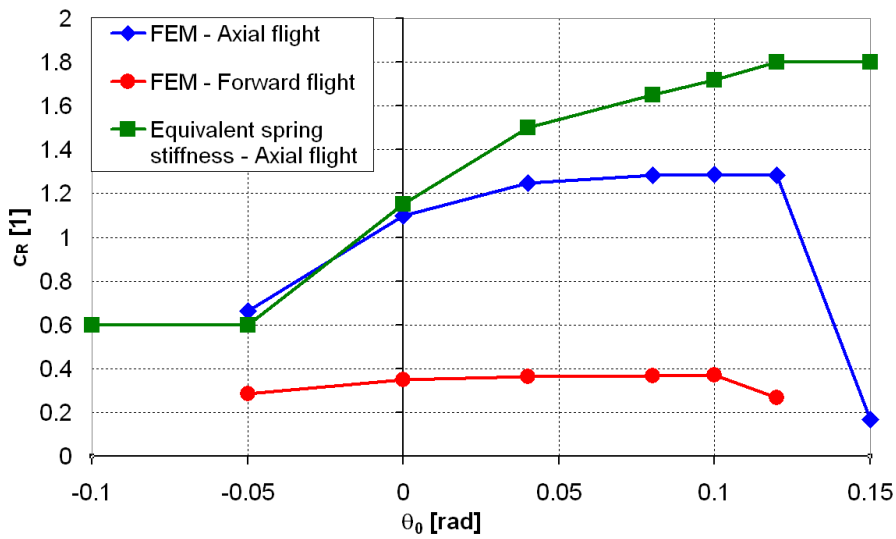


Figure 6.2: The effect of blade fixed angle of incidence on rotor resultant force coefficient during autorotative flight

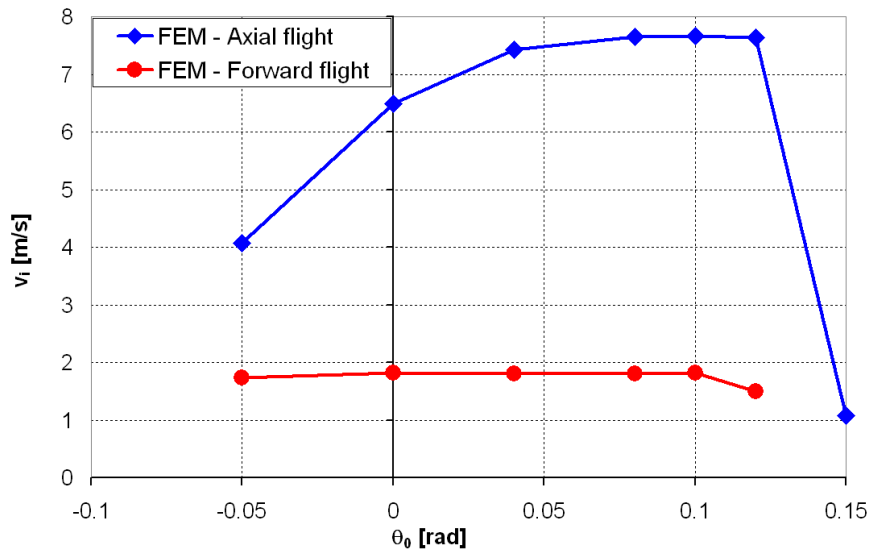


Figure 6.3: The effect of blade fixed angle of incidence on rotor induced velocity during autorotative flight

Since high fixed incidence angles cause increase of blade drag, the inboard (driving) region of the blade has to produce higher aerodynamic torque to keep up with the outer (driven) part of the blade - see figure 6.4.

The inboard part of the blade becomes partially stalled if blade fixed angle is high, while drag produced by the tip region of the blade would still increase with

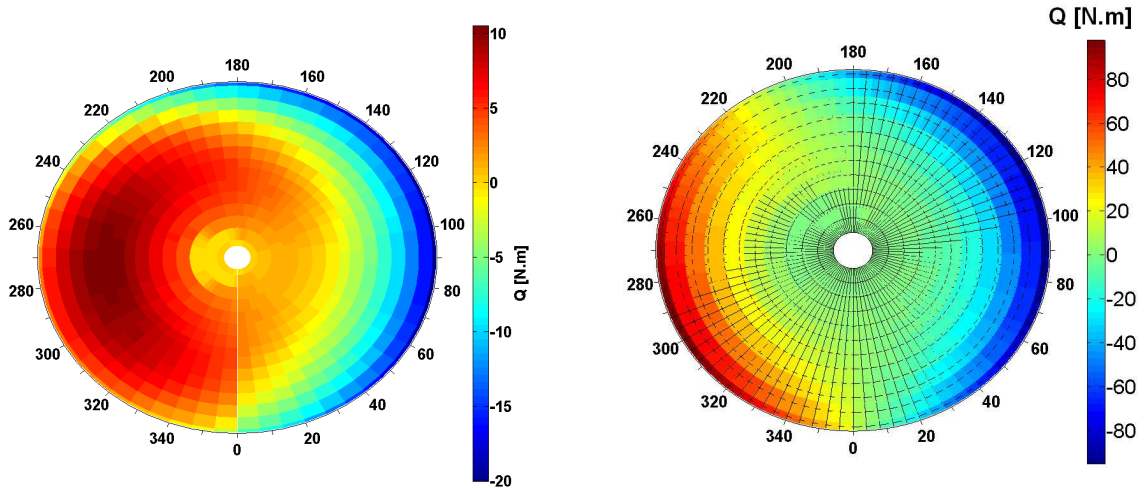


Figure 6.4: A comparison of distribution of aerodynamic torque over the rotor disc during forward flight in autorotation as predicted by the model for zero fixed angle of incidence (left) and fixed angle of incidence approaching the critical value

fixed angle of incidence (see figure 6.5). It can be seen in figure 6.5 that a small increment of blade drag at the tip region results in significant drop in aerodynamic torque due to much higher values of inflow speed in the outboard part of the blade.

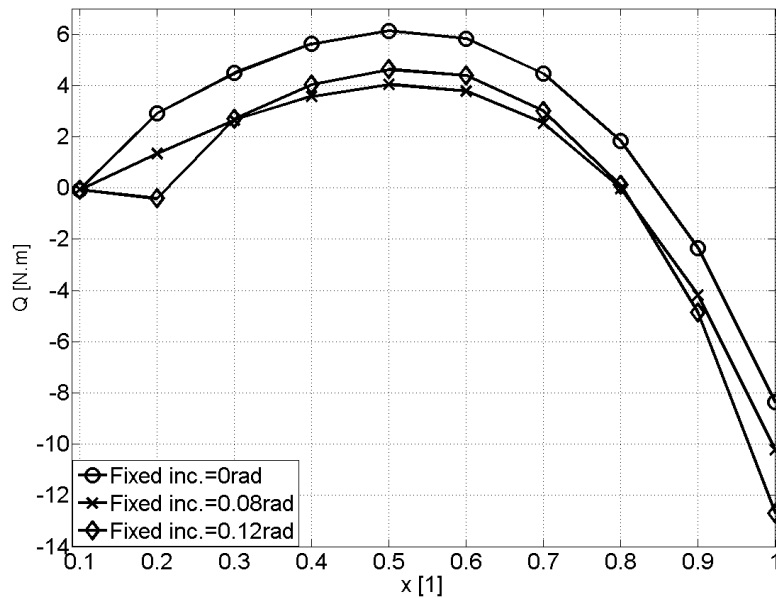


Figure 6.5: The effect of blade fixed angle of incidence on span-wise distribution of blade aerodynamic torque during axial autorotative flight

Exceeding of the critical value of fixed incidence angle in both forward and axial

flight results in a rapid drop in rotor speed and increase in speed of descent. The results of the simulations suggest that high values of blade fixed incidence angle would have catastrophic consequences. Figure 6.6 shows a comparison of rotor instability caused by excessive blade fixed angle of incidence as it occurs during vertical descent and forward flight in autorotation. It can be seen from the figure that a critical value of blade fixed incidence during axial flight results in an aeroelastic instability that resembles aeroelastic divergence and does not include blade torsional oscillations.

This type of aeroelastic instability is similar to stall flutter of rotorcraft blades and it is also predicted by the model for blades with a single degree of freedom in torsion (i.e. degrees of freedom in bending and teeter are locked). The instability is primarily caused by nonlinearity of rotor blade stall and does not require de-stabilizing coupling of blade torsion and flap. Hence it can't be avoided by mass-balancing of the rotor blades. A similar aeroelastic behaviour of rotor blades might be observed in case of incorrect collective pitch settings or failure of the pitch change mechanism of a helicopter rotor during emergency landing in autorotation.

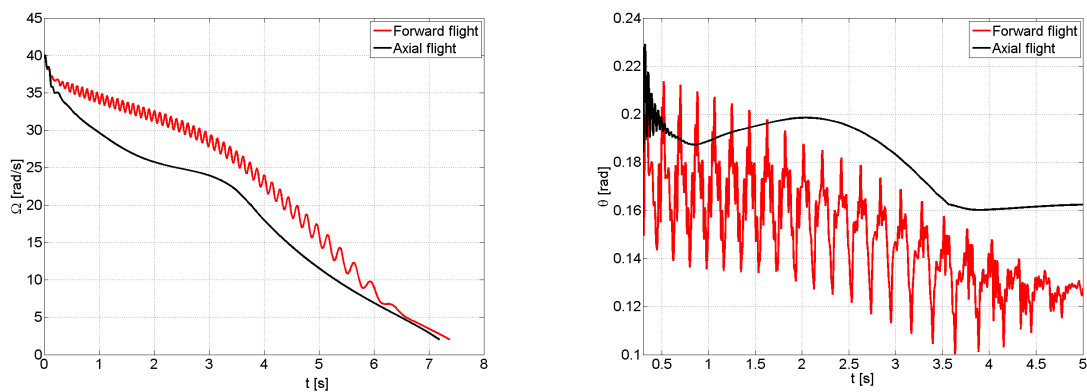


Figure 6.6: Example of an aeroelastic instability during flight in autorotation caused by high blade fixed incidence angle as predicted by *AMRA*

While the critical value of blade fixed incidence during forward flight was estimated to be lower than 0.15rad, the *AMRA* model predicted that steady autorotative axial flight would be still possible for fixed incidence angles up to 0.2rad. This can be explained by unsteady rotor inflow that occurs during forward flight. It can be

seen from figure 6.7 that fluctuation of blade angle of attack that occurs if blade fixed angle of incidence is high causes high aerodynamic loading of the blade. That results in increased blade oscillations in torsion that leads to increased blade drag and negative mean value of blade aerodynamic torque.

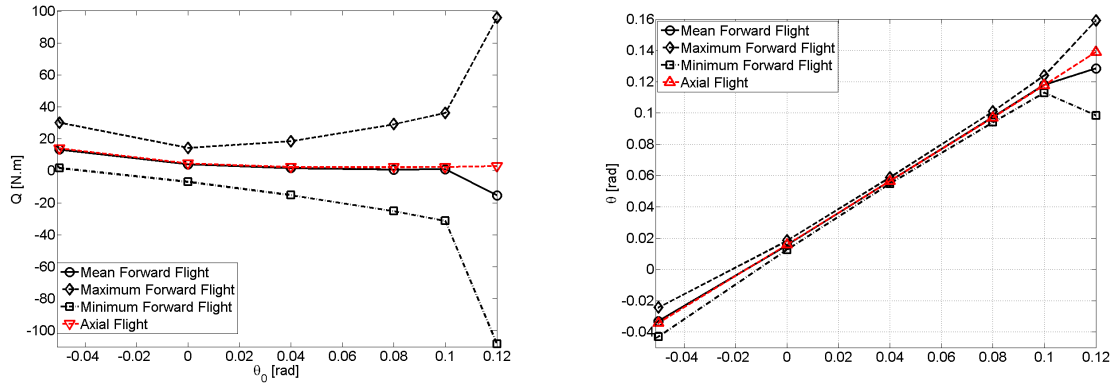


Figure 6.7: Values of aerodynamic torque and blade torsional deflections of a gyroplane blade estimated by *AMRA* for different values of fixed incidence angle

The simulations showed that the rotor over-speeds, if blade fixed incidence angle is negative and torque equilibrium is established. However, the speed of descent of an autorotating rotor with negative blade fixed incidence angle is very high due to insufficient rotor thrust (see figure 6.8).

If blade fixed incidence is too low, the outer blade region produces less thrust due to low local values of inflow angle. Hence equilibrium between gravitational force and rotor thrust is established after speed of descent and rotor speed are increased. As a consequence, the inboard part of rotor blades produces significantly higher portion of total rotor thrust and torque (see figure 6.9).

An increase in speed of descent and rotor speed causes incremental changes of values of blade inflow speed and blade drag coefficient and thus help to compensate for loss of blade lift coefficient due to negative blade fixed incidence (see 6.10).

Hence practical use of negative fixed incidence angle is limited as it would re-

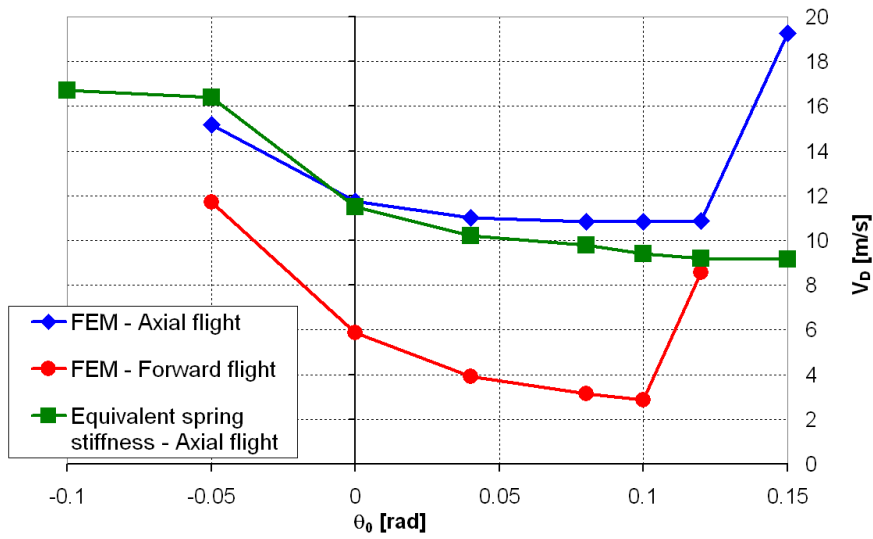


Figure 6.8: The effect of blade fixed angle of incidence on speed of descent during autorotative flight

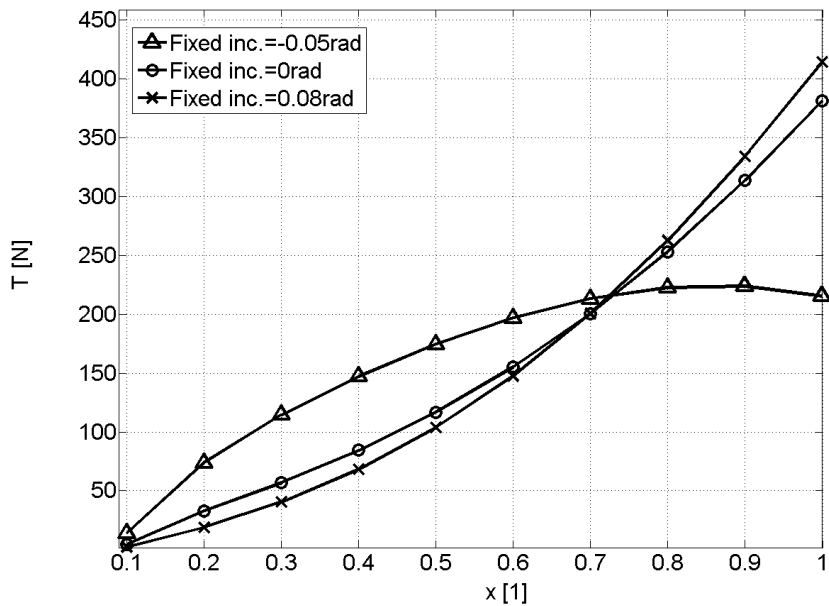


Figure 6.9: The effect of blade fixed angle of incidence on span-wise thrust distribution during autorotative axial flight

quire higher longitudinal rotor tilt (backward tilt of the rotor hub) in forward flight in order to keep speed of descent of the vehicle low. This would increase required thrust of the engine and specific fuel consumption of the vehicle.

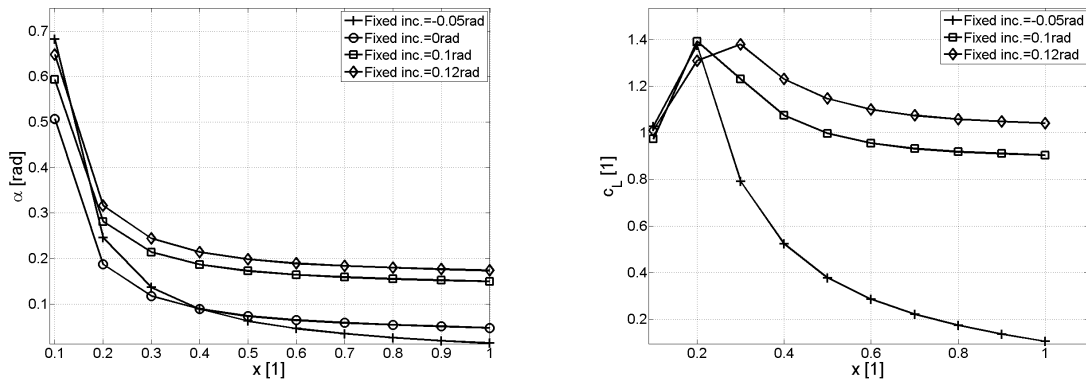


Figure 6.10: Change of rotor blade span-wise distributions of angle of attack and lift coefficient

6.2 Blade Geometric Twist

Another parametric study performed with the aid of the *AMRA* model was focused on the effect of linear span-wise distribution of blade geometric twist on performance and stability of rotors in autorotation. Geometric twist is widely used both in fixed wing and rotary wing aircraft - it helps to avoid stall of wing tips and consequent loss of lateral control at high angles of attack (especially in wings with high taper ratio or high sweep). High values of geometric twist (values higher than 60 degrees are not unusual) are used in aircraft propellers in order to obtain ideal flow conditions at all propeller span-wise stations. This is also the reason why moderate geometric twist (up to 20 degrees) is often used in helicopter rotor design.

Only little information is available on the effect of rotor blade geometric twist on behaviour of autorotating rotors. In contrast to helicopter rotor blades, blades of modern gyroplanes have usually no geometric twist. Two different types of blade twist distribution were used; one with zero twist at the blade root and maximum value of twist at the blade tip and another with zero twist at the blade tip and maximum value of twist at the root. The former type of blade twist distribution will be further referred to as 'tip twist' while the latter will be called simply 'root twist'.

Computations carried out with the aid of the *AMRA* model have shown that the tip twist has similar effect as blade fixed incidence. Figure 6.11 shows that the critical value of tip twist roughly agrees with the critical value of fixed incidence angle.

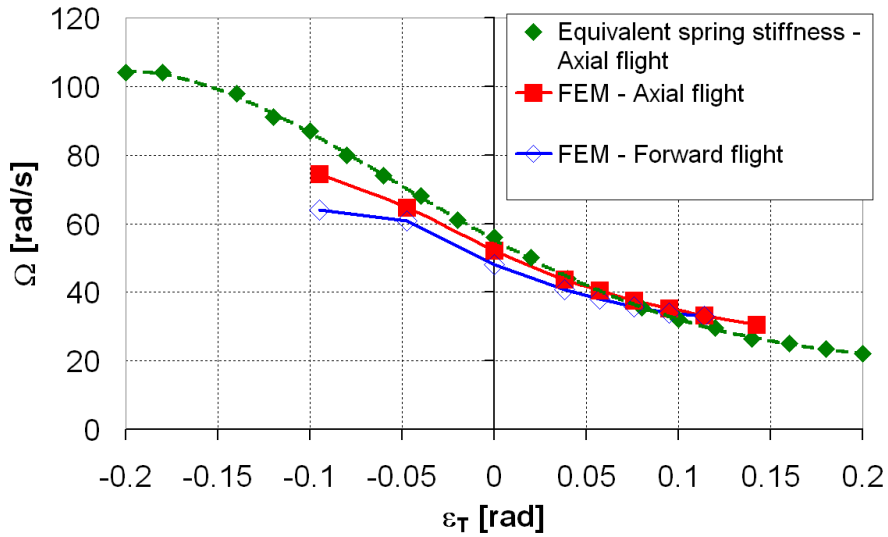


Figure 6.11: The effect of blade geometric twist at the tip region on rotor equilibrium rotor speed during autorotative flight

Again, the highest value of rotor resultant force coefficient and hence lower speed of descent is achieved for values of the tip twist just below the critical value. Negative values of tip twist result in higher rotor speed but lower resultant force coefficient and higher speed of descent.

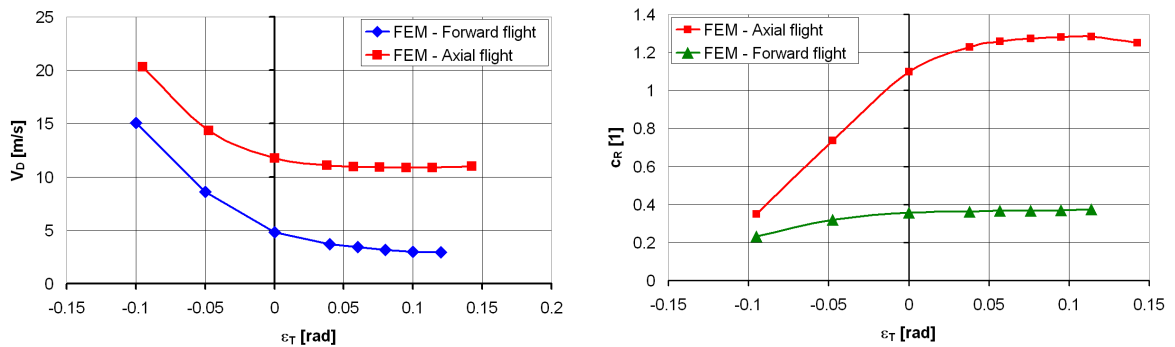


Figure 6.12: Change of speed of descent and rotor resultant force coefficient with the value of blade geometric twist at the tip

Positive values of tip twist increase rotor resultant force coefficient but decrease equilibrium rotor speed, decreasing the stability of autorotation. Stability of autorotation is increased if the value of tip twist is negative at the price of rise of speed of descent. The tip blade region is characterised by high values of inflow speed and hence it generates the majority of blade aerodynamic forcing. Hence the changing of blade incidence in the tip region causes significant increase of blade drag, which makes reaching torque equilibrium more difficult. Aeroelastic instability predicted for very high values of tip geometric twist is very similar to the instability described in the section dedicated to fixed incidence angle.

Parametric studies carried out for geometric twist applied to the inboard region of a rotor blade have shown that it has much less drastic effect on rotor performance than both blade fixed angle of incidence and tip geometric twist. As it can be seen from figure 6.13 steady autorotation was predicted for a wide range of values of root geometric twist - in fact no aeroelastic instability was observed.

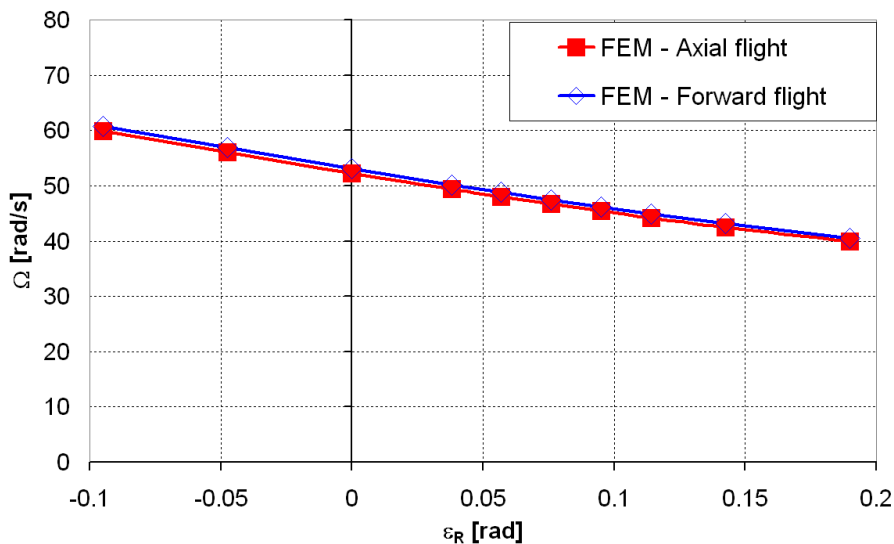


Figure 6.13: The effect of blade geometric twist at the root region on rotor equilibrium rotor speed during autorotative flight

Figure 6.14 shows that the application of negative root geometric twist can increase the equilibrium rotor speed without causing significant drop in the resultant force coefficient. This can be used for the improvement of the stability of rotors

during autorotative flight regime since higher rotor speed makes the rotor stiffer and less prone to the destabilizing effects of uneven inflow (i.e. gusts, turbulent flow or maneuvers). Similarly, use of positive geometric twist at the blade root allows reasonable increment of rotor c_R (i.e. reduction of speed of descent) without significant reduction of the value of the equilibrium rotor speed below the safe level.

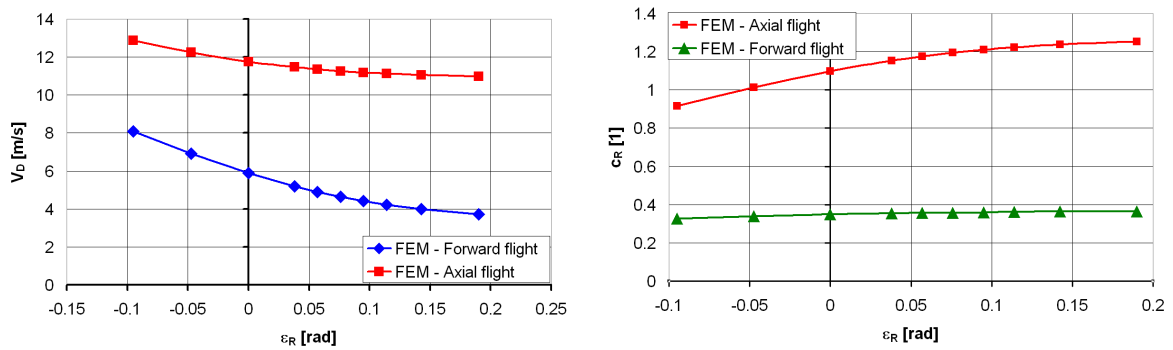


Figure 6.14: Change of speed of descent and rotor resultant force coefficient with the value of blade geometric twist at the root

Values of inflow speed in the inboard region of a rotor blade are lower and therefore it generates smaller portion of aerodynamic forces than the outboard part. Hence the effect of change of blade root twist on magnitudes of aerodynamic forces and moments generated by the rotor is much smaller than in case of fixed blade incidence or tip geometric twist. A change of angle of attack at the blade root also causes a much lower increment of overall blade drag than an equivalent change of angle of attack at the tip region. This can be seen from figure 6.15 - change of blade root twist results in a moderate change of induced velocity that is strongly dependent on the value of rotor thrust.

Since the inboard part of the blade is the 'driving' region producing positive aerodynamic torque necessary for rotor equilibrium and it works at high angles of attack, application of negative root geometric twist can have positive effect as it would reduce or entirely avoid stall in this blade region [7; 12].

It can be concluded that negative values of geometric twist applied to the in-

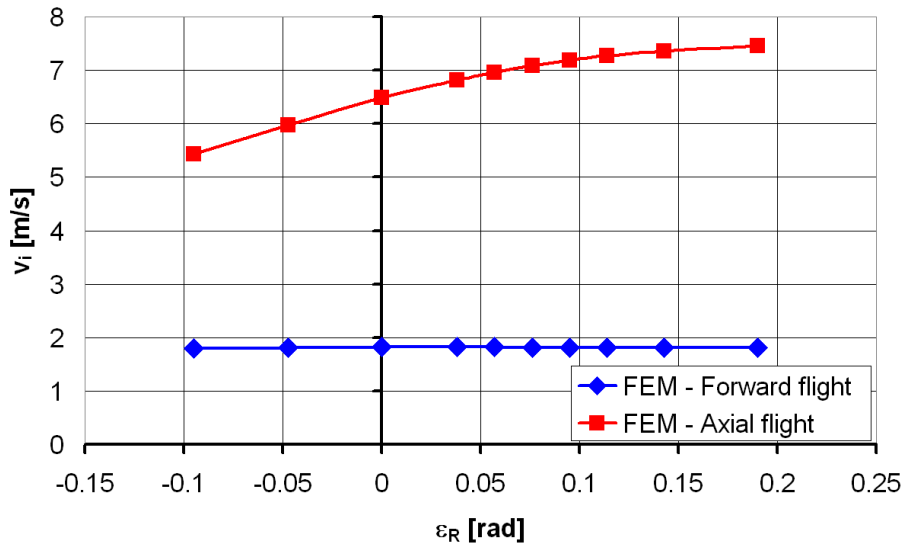


Figure 6.15: The effect of blade root geometric twist on rotor induced velocity during autorotative flight

board parts of gyroplane blades can positively affect stability of autorotation in both axial and forward flight (see figure 6.16). This design solution can be conveniently combined with a moderate value of blade tip mass that would further increase equilibrium rotor speed and also make rotor speed less sensitive to disturbances in rotor inflow.

Performance and stability of rotors in autorotation might be also improved with the aid of control devices, e.g. trailing edge flaps. Trailing edge flaps can be used in helicopter rotor design and many research studies dealing with flapped rotor blades can be found in open literature. Majority of studies focus on application of trailing edge flaps in the outboard blade region. Helicopter rotor blade design equipped with inboard flaps was suggested by Gagliardi [84]. This rotor design could use inboard trailing edge flaps for enhancement of rotor stability during autorotative flight instead of the inboard geometric twist of the rotor blades.

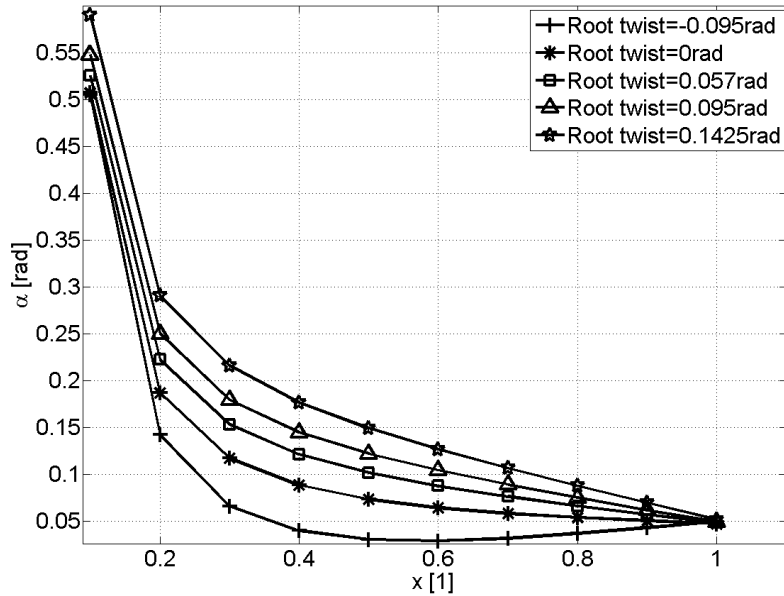


Figure 6.16: The effect of blade geometric twist at the root region on blade span-wise distribution of aerodynamic angle of attack during autorotative flight

6.3 The Critical Rotor Speed and Blade Tip Mass

Simulations carried out with the aid of *AMRA* showed that autorotation has a self-stabilizing character provided that rotor speed is high enough and the rotor is in a stable configuration. The computations were carried out for several different magnitudes of disturbance in blade torsional deflection to study the ability of a rotor in autorotation to recover from sudden drop of rotor speed. A decrease of rotor speed during flight in autorotation can be caused by change of rotor disc inflow, e.g. gust, blade-vortex interaction, turbulent flow or manoeuvres (especially manoeuvres leading to negative rotor inflow). The increment of geometric twist at the blade tip was used for the simulation of disturbances in blade torsional deflection. A linear change of geometric twist along the blade span was used. Both negative and positive change of blade geometric twist angle were studied. Figure 6.17 shows a basic shape of the geometric twist input used in the study. It can be seen from the figure that the length of fixed incidence angle inputs was exaggerated in order to reach the critical value of rotor speed (i.e. minimum value of rotor speed at which steady autorotative flight is possible in given flight conditions).

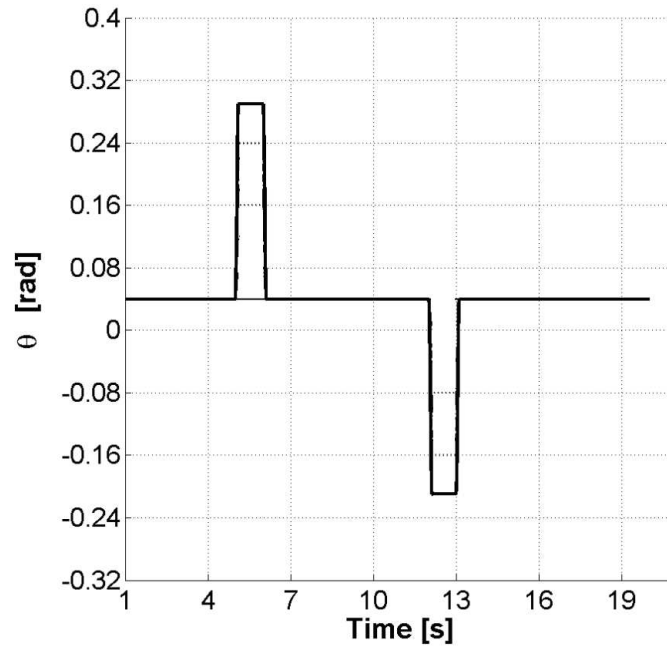


Figure 6.17: The shape of step increment of blade twist used to study the effect of step change of rotor blade torsional deflection

Figure 6.18 depicts clearly auto-stabilizing capability of rotors in autorotative flight. Steady autorotation is recovered even if the magnitude of torsional disturbance is relatively high.

The results show that the rotor is not able to reach steady autorotation if the value of the rotor speed drops below a limit value (see figure 6.18). Flow conditions along the blade do not allow generation of positive torque if the rotor speed is too low. This is why the majority of modern gyroplane designs use pre-rotation of the rotor. High torsional deflection of rotor blades leads to significant decrease of rotor speed that results in stall of a large part of the blade. Steady autorotation is not re-established since the lift drops and drag increases considerably behind the stall point, resulting in decrease of rotor thrust and increment of speed of descent. That leads to further increase of inflow angle and expansion of the stalled area of the blade. Hence the conditions needed for recovery of stable autorotation (i.e. positive aerodynamic torque generated by the blade) cannot be established and the speed of descent will reach values that would have catastrophic consequences in operation.

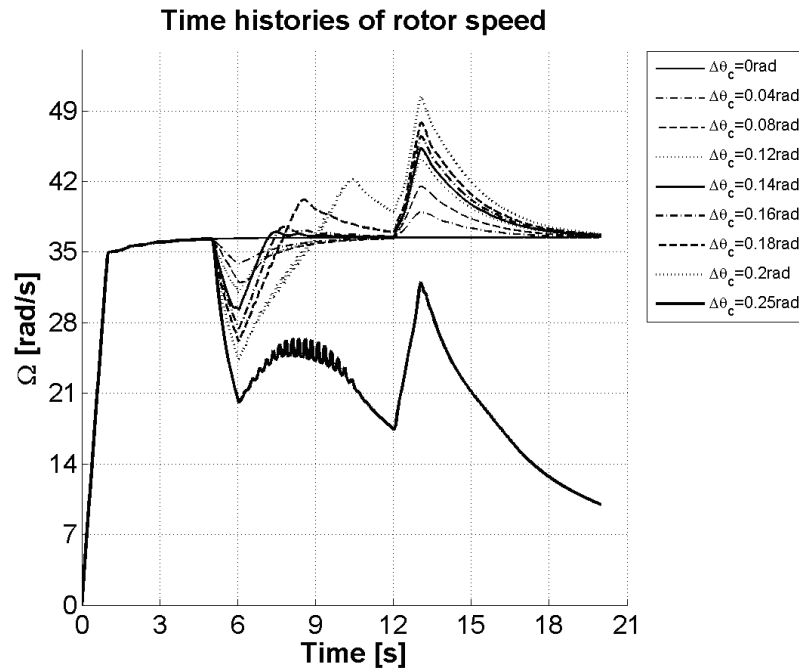


Figure 6.18: The effect of step increment of blade twist on rotor speed of a gyroplane rotor

Since the critical value of rotor speed depends on flow conditions along the blade span, it does not remain constant for a given rotor design and changes with flight conditions and weight of the vehicle. The critical value of rotor speed is around 15 rad/s for a light gyroplane in a configuration similar to Montgomerie-Parsons gyroplane equipped with McCutcheon rotor blades during steady vertical descent (i.e. $V_D \approx 12m/s$). The simulations have suggested that the value of critical rotor speed is a weak function of horizontal speed of the vehicle and that it is strongly affected by the value of speed of descent of the vehicle. In order to assure the highest possible stability during autorotation, the critical rotor speed during a typical flight regime should be as low as possible. The equilibrium rotor speed in steady flight should not approach the critical value.

Blade tip mass is used to avoid low values of the rotor speed. The addition of the tip mass also increases centrifugal stiffening of the blade and hence increases the effective blade stiffness. Modelling of rotor performance for several different values of blade tip mass was undertaken to establish sensitivity of the autorotative state to

changes in blade moment of inertia. A concentrated mass representing the blade tip mass was placed at blade tip local elastic axis in order not to affect blade aeroelastic stability. The outcome of the simulations is shown in figure 6.19. It can be seen that the *AMRA* model predicts that the tip mass would increase rotor speed as expected. The computations also showed that the addition of the tip mass causes only a small increase of equilibrium speed of descent; an extra 8kg of tip mass (i.e. increment of blade mass by 61%) changes equilibrium speed of descent by 1m/s during axial descent (i.e. increase of V_D by approximately 7%).

However, further computations carried out with the aid of *AMRA* show that the addition of blade tip mass not only increases the equilibrium rotor speed but also increases the value of the critical rotor speed. This is a logical consequence of higher rotor moment of inertia (higher change of aerodynamic torque is needed to increase of rotor speed from a given value) and also the result of a slight change of equilibrium speed of descent. As can be seen from figure 6.19, the gradient of change of critical rotor speed with blade tip mass is lower than in case of equilibrium rotor speed.

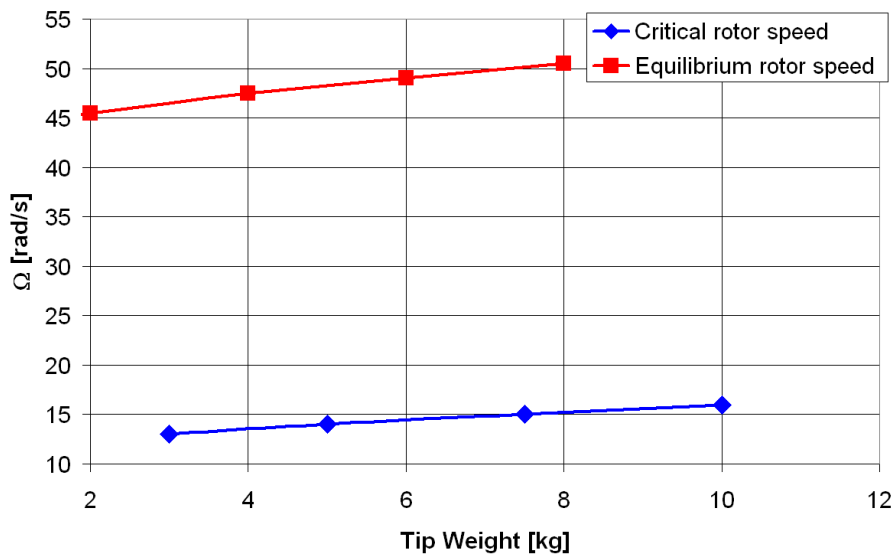


Figure 6.19: The effect of blade tip mass on rotor speed of a rotor in autorotation

Hence use of excessive values of blade tip mass does not seem to be convenient

as it might increase the value of critical rotor speed. Significant increment of rotor moment of inertia might also increase the time needed for recovery of rotor speed in case it decreases during flight. Results from *AMRA* suggest that the use of moderate values of blade tip mass in combination with negative geometric twist in blade inboard sections should keep the value of critical rotor speed constant and increase equilibrium rotor speed.

6.4 Concluding Remarks

The parametric studies carried out with the aid of the *AMRA* model showed the influence of selected rotor blade design parameters on performance and stability of autorotating rotors. The results demonstrate the key role of blade incidence in aerodynamics of rotors in autorotation. Although the rotor blades used in the studies were mass balanced (i.e. torsion-flap flutter was not possible), some geometries resulted in an aeroelastic instability. This instability is similar to divergence in vertical descent and has oscillatory character in forward flight (and resembles stall flutter).

The study of the effect of blade fixed angle of attack lead to the following conclusions

- Excessive values of blade fixed angle of incidence results in an aeroelastic instability in blade torsion
- Rotor speed decreases and rotor resultant force coefficient grows with increasing blade fixed angle of incidence until the critical value is reached
- Negative values of fixed of angle of incidence result in an increment of rotor speed but also in significant increment speed of descent

The main findings that resulted from the simulations of the effect of a linear variation of blade geometric twist are

- Geometric twist applied to the outboard region of the blade has very similar effect to blade fixed angle of incidence (including appearance of an aeroelastic instability in blade torsion)
- Geometric twist applied to the inboard region of the blade causes smaller change of rotor speed and speed of descent
- Negative values of inboard geometric twist can increase rotor stability by moderation of blade stall

Investigation of the value of the critical rotor speed and the effect of blade tip mass have shown that

- Steady autorotation is not possible if the value of rotor speed is lower than the critical value
- The critical value of rotor speed depends on the properties of the rotor and also on rotor flow conditions and configuration of the vehicle
- The value of critical rotor speed at typical flight conditions should not approach the value of equilibrium rotor speed
- The use of blade tip mass increases equilibrium rotor speed and hence improves the stability of a rotor in autorotation
- Application of tip mass also causes moderate increment of the critical rotor speed

Chapter 7

Aeroelastic Stability of Rotors in Autorotation

According to the theory of aeroelasticity, classical pitch-flap flutter of a rotor blade section will occur when the blade centre of gravity is located aft of pitch axis of the section and the torsional stiffness, or blade pitch stiffness, is low enough. If blade CG is located aft of EA, an acceleration of the blade in flap will lead to acceleration in torsion in the same direction, i.e positive (upwards) blade flap would result in blade nose-up motion and negative blade flap leads to nose-down torsion. This is obviously destabilizing the blade dynamics since higher blade incidence results in higher aerodynamic loading and thus flapping acceleration is further increased [11; 48; 75; 76]. In helicopter rotors, a lag degree of freedom can also be involved in this rotor blade instability, leading to rotor pitch-flap-lag instability. This is caused by higher blade drag due to high values of blade torsional deflection and also by low aerodynamic damping of lag motion [47].

Unlike helicopter rotors in powered flight, rotors in autorotation can experience significant variations in rotor speed due to changing flow conditions of the rotor blades. A decrease of rotor speed causes a drop in centrifugal stiffness of the rotor blades and the resulting higher deflections in flap and twist generate more drag. This cause further reduction in rotor speed. It is clear that the thrust and torque of

the rotor are functions of rotor speed and the distribution of local values of angle of attack along the blade span. The results of the model have shown that blade torsion has dominant influence on aeromechanical behaviour of a rotor in autorotation. The *AMRA* model has also shown that the extra degree of freedom in rotor speed has significant effect on the character of an aeroelastic instability of an autorotating rotor, although it does not change the point of its onset. Predicted behaviour of autorotating rotors during aeroelastic instability is unique thanks to variable rotor speed. A series of parametric studies were carried out with the aid of the model and published in open literature [85; 86] - see the previous chapter of this work. To the knowledge of the author, a similar research was not undertaken and published to date.

Pitch-flap flutter and pitch-flap-lag instability were investigated extensively in the field of helicopter rotor aeroelasticity and aeroelastic behaviour of helicopter rotors in powered flight is well understood [26; 47]. However, little is known about behaviour of autorotating rotors during an aeroelastic instability. It was noted in Chapter 2 that virtually no publications can be found dealing with modelling of coupled pitch-flap motion of rotors in autorotation. However, several publications provide experimental data on rotor blade motion during autorotative flight.

Hence a major part of the research work was dedicated to investigation of rotor stability in coupled bending-torsion-rotation motion. Experimental flight measurements showed that the influence of blade flat-wise bending on dynamics of gyroplane rotor is negligible [68]. Since rotor speed of autorotating rotors is not fixed and it can *adjust* to the aerodynamic forcing acting on the blades, the influence of lag degree of freedom is not so strong and can be neglected [68]. Gyroplane rotors do not use lag hinges and flat-wise bending stiffness of gyroplane rotor blades is very high due to their lower aspect ratio and high thickness. Hence degree of freedom in flat-wise bending was not considered in this study. Influence of flexibility of the hub control bars on aeroelastic stability of a rotor was not considered due to time

constraints of this dissertation. This feature is typical for gyroplane rotors and it can affect rotor aeroelastic behaviour if stiffness of the control bars is low enough. *AMRA* simulations were carried out for various values of blade stiffness, chord-wise positions of centre of gravity and elastic axis.

Both time-marching aeroelastic simulations and eigenanalysis of gyroplane rotors (i.e. modelling in the frequency domain) were performed. Although aeroelastic computations in the frequency domain are much faster than time-marching simulations, they require significant simplification of both blade equations of motion and aerodynamic forcing terms (see Chapter 3). Analysis in the time domain allows using full non-linear equations of motion and inclusion of both non-linear aerodynamics and compressibility effects. Hence it is convenient to compare and possibly cross-validate the results of time-marching simulations and eigenanalysis. The results of time marching *AMRA* simulations were compared with the results of eigenanalysis of linearized blade equations of motion that was also carried out with the aid of the *AMRA* model.

7.1 Torsional Aeroelastic Stability Boundary of an Autorotating Rotor

As was shown in the previous chapters of this work, the axial flight in autorotation is characteristic by steady values of blade states and aerodynamic loading if torsional equilibrium is achieved and the rotor inflow is homogeneous. Blade motion becomes oscillatory with increasing value of forward speed. It was shown in the chapter dedicated to model validation (Chapter 5) that the *AMRA* model describes well all major features of aerodynamics of a rotor in both autorotative axial and forward flight [85; 86].

According to the classical theory of aeroelasticity, pitch-flap flutter stability

boundaries of rotor blades have a hyperbolic shape. Same results were obtained during eigenanalysis of autorotating rotors. Two different types of eigenanalysis were performed and comparison of their results is given in figure 7.1. Eigenanalysis of the equivalent spring stiffness model of a rotor blade is less complex of the two since it assumes rigid rotor blades and a uniform span-wise distribution of blade properties. Dimensionless form of the analysis is given in Bramwell [27] and identical results were obtained for its dimensional form given in Chapter 3. Eigenanalysis of the FEM model of a rotor blade included in *AMRA* was also carried out. It allows non-uniform span-wise distribution of rotor blade properties and is capable of capturing higher modes of blade motion. It can be seen from the figure that 'stiffer' model (i.e. eigenanalysis of the rigid blade equations of motion) predicts higher aeroelastic stability, which is quite an intuitive outcome. Note that variable blade rotational speed was not included in the models since the blade equations of motion were linearized around rotor speed.

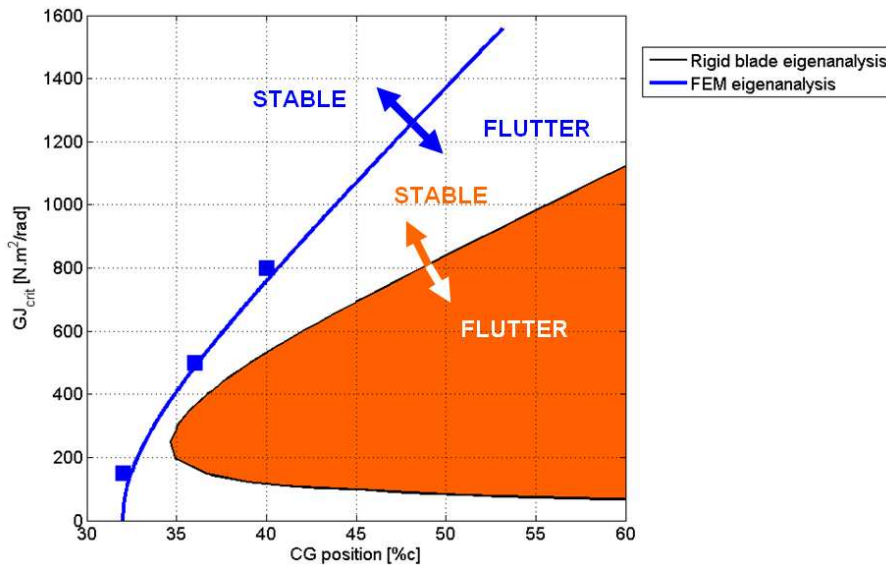


Figure 7.1: Comparison of aeroelastic stability boundaries obtained from two different frequency domain models of an autorotating rotor. Elastic axis of the rotor blades lies at 32% chord.

In order to include variable rotor speed into modelling of aeroelastic stability of an autorotating rotor, time-marching *AMRA* simulations were carried out for EA at 32%*c*, different chord-wise locations of CG and various values of torsional stiffness.

Blade fixed angle of incidence was set to 0.04rad for simulations of both axial flight and forward flight unless stated otherwise.

The results of the simulations have revealed that low torsional stiffness of the blade leads to an aeroelastic instability that comes through as coupled rotor speed-pitch-flap flutter oscillations. These oscillations result in catastrophic decrease of rotor speed. This is a demonstration of strong rotor speed-pitch-flap coupling that exists only during autorotation. Decrease of the rotor speed reduces centrifugal stiffness of the rotor and the resulting higher deflections in flap and twist generate more drag and cause further drop in rotor speed and increment of speed of descent. It is shown in figure 7.2 that a general trend of decreasing rotor speed can be visible from time history of both blade flap and torsion.

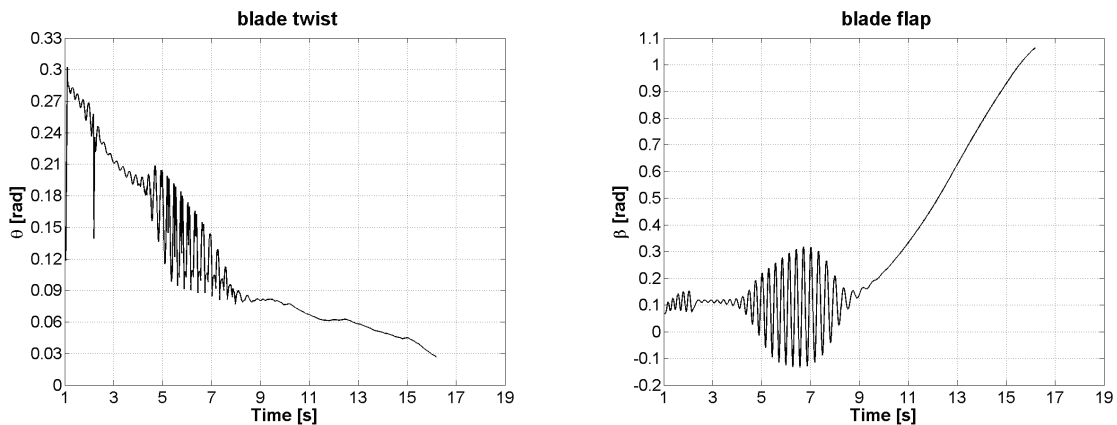


Figure 7.2: Aeroelastic instability during axial flight in autorotation

These oscillations result in catastrophic decrease of rotor speed as it is shown in figure 7.3. As can be seen in figure 7.3, the reduction of rotor speed from a steady value to zero takes only few seconds. Speed of descent increases to an unacceptable value during this time since low rotor speed leads to reduction of rotor thrust.

This type of flutter time history seems to be unique for rotors in autorotation since it differs from both helicopter rotor flutter and flutter of a fixed wing. This is the first time this type of aerolastic stability has been identified. Pitch-flap flutter

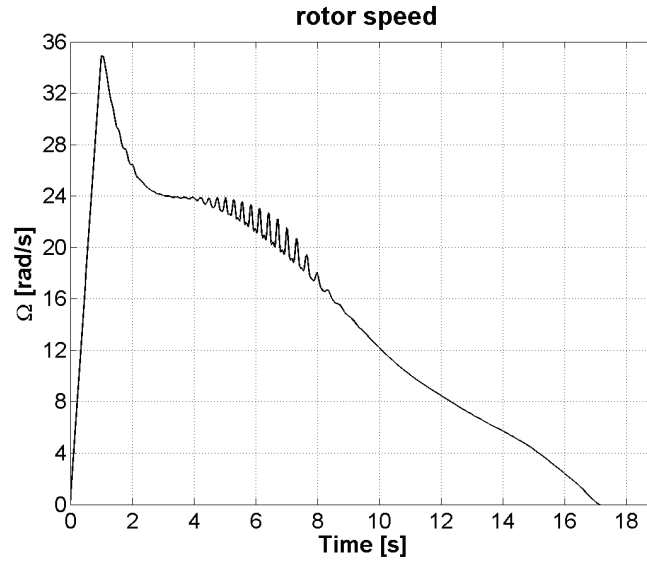


Figure 7.3: Catastrophic decrease of rotor speed during aeroelastic instability during autorotative vertical descent

of a rotor in autorotation has not been previously modelled and no similar results are published in open literature, to the knowledge of the author.

Although rotor oscillations die out with decreasing rotor speed, the high value of speed of descent of the vehicle caused by low thrust generated by the rotor does not allow re-establishing of rotor torque equilibrium. High values of speed of descent simply result in stall of rotor blades due to dramatic increase of inflow angles. Similar instability can be observed if speed of descent is kept constant; the rotor is able to recover just to enter another round out of pitch-flap oscillations. This scenario is, however, purely theoretical since the rotor is the only lifting surface of a gyroplane.

Figure 7.4 shows aeroelastic stability boundary of an autorotating rotor as predicted by *AMRA*.

The fact that *the character* of the aeroelastic instability during autorotation seems to be unique does not necessarily mean that the resulting aeroelastic stability boundary will significantly differ from stability boundary of identical rotor for constant value of rotor speed. Hence the values of critical torsional stiffness obtained

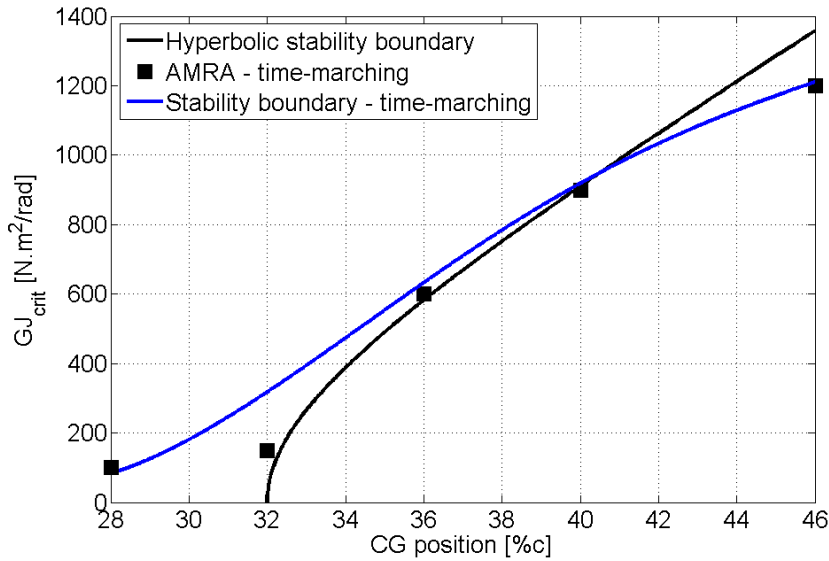


Figure 7.4: Torsional stability boundary of an autorotating rotor in axial flight as predicted by the *AMRA* model

for variable rotor speed had to be compared with the values computed for constant rotational speed.

The *AMRA* model was used to compute the values of the critical torsional stiffness of a typical gyroplane rotor with degrees of freedom in torsion and flap. The value of rotational speed was fixed at the equilibrium values that were computed by the model for variable rotor speed. The results of the study suggest that the effect of degree of freedom in rotation on the shape of rotor aeroelastic stability boundary is not significant and hence the instability represents a special case of pitch-flap flutter. The values of the critical torsional stiffness are virtually identical to the values obtained from eigenanalysis of the *AMRA* FEM model (see above). The aeroelastic stability boundary predicted by *AMRA* is very similar to pitch-flap flutter boundaries of helicopter rotors that have hyperbolic shape if small oscillations are assumed. Figure 7.5 shows that the values of critical torsional stiffness predicted for fixed rotor speed are very similar to the values obtained for variable rotor speed.

Hence blade equations of motion linearized around rotor speed or modelling in

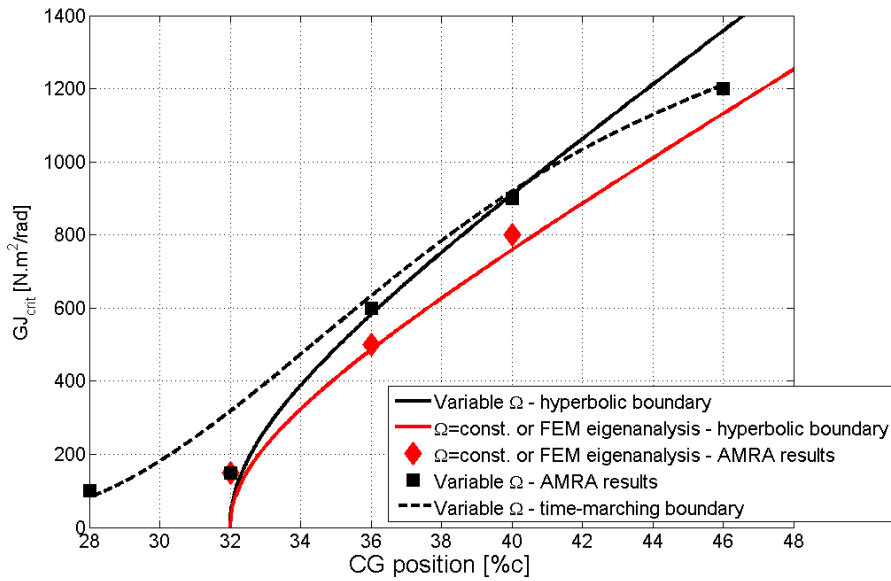


Figure 7.5: The effect of degree of freedom in rotation on the shape of blade torsional stability boundary.

the frequency domain (eigen-analysis) can be used for prediction of the aeroelastic stability of autorotating rotors. Degrees of freedom of torsion and flap seem to affect the shape of the aeroelastic stability boundary of rotors in autorotation more significantly (see figure 7.28). Although the degree of freedom in rotation does not have a strong effect on the *onset* of the aeroelastic instability in autorotation, it strongly affects aeromechanical behaviour of the rotor *during* this instability. Couplings of the rotor speed with the other blade degrees of freedom and vehicle speed of descent have auto-stabilizing character for stable rotor configuration but they lead to a catastrophic increase of speed of descent during aeroelastic instability.

Lower values of blade torsional stiffness lead to higher torsional and flexural deflections even if the blade is in a stable configuration. The resulting higher values of blade drag cause a drop in rotor speed - see figures 7.6 and 7.7. This can lead to an aeroelastic instability even if the rotor blades are well balanced (i.e. CG is ahead of EA) since it increases the possibility of reaching the critical rotor speed for which torque equilibrium is not possible (see Chapter 6).

Predictions of aeroelastic behaviour of the rotor remain similar if different levels

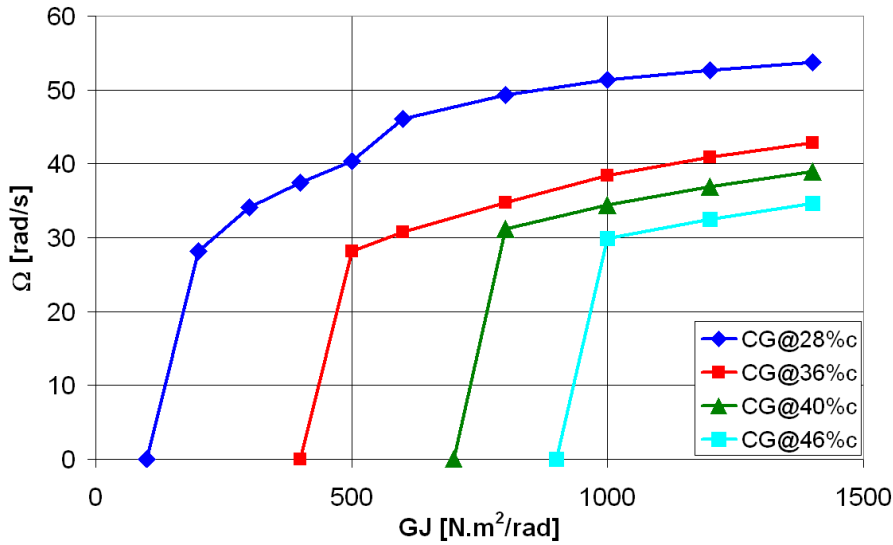


Figure 7.6: A comparison of the values of equilibrium rotor speed during autorotative vertical descent; computed for different span-wise positions of blade CG and varying blade torsional stiffness

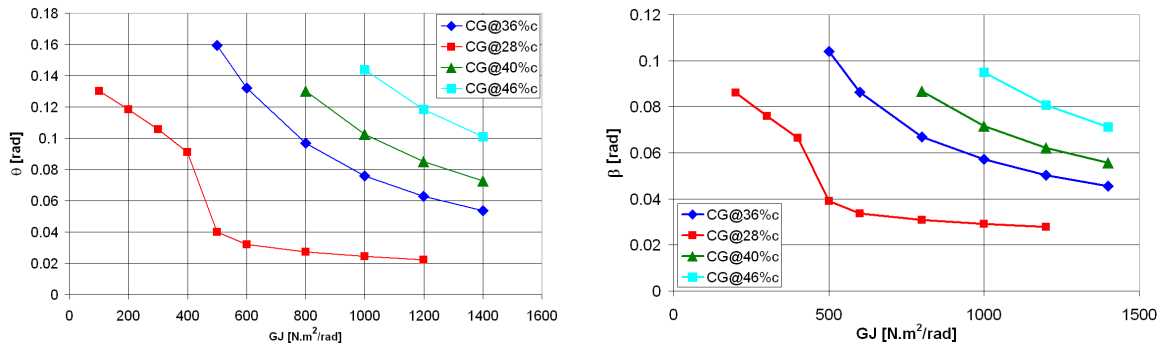


Figure 7.7: A comparison of the values of equilibrium blade torsional and flapping deflections during autorotative vertical descent; computed for different span-wise positions of blade CG and varying blade torsional stiffness

of complexity of the model of blade structural dynamics are used. It is shown in figure 7.8 that the aeroelastic instability predicted by the model using equivalent spring stiffness approach has very similar character to the instability predicted with the aid of full FEM model.

Simulations for various values of torsional stiffness, chord-wise positions of centre of gravity (CG) and chord-wise positions of elastic axis (EA) of a gyroplane rotor in forward flight were also performed. Computations carried out with the aid of the *AMRA* model have shown that the rotor suffers of aeroelastic instability if CG lies aft EA and the value of blade torsional stiffness is lower than the critical value.

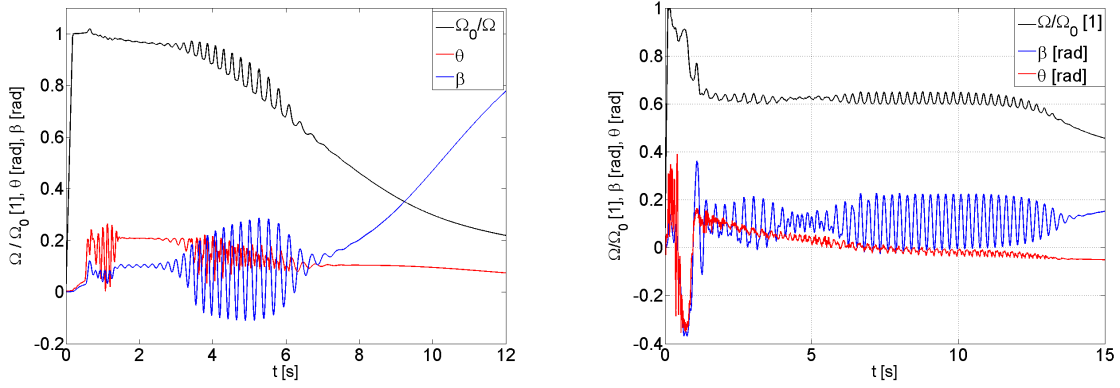


Figure 7.8: Comparison of an aeroelastic instability during axial flight in autorotation as predicted by the *AMRA* using equivalent spring stiffness (left) and coupled torsion-bending FEM model of blade dynamics.

As it can be seen from figure 7.9, the main features of the aeroelastic instability remained the same - excessive torsional deflections lead to significant reduction of rotor speed from a steady value that takes only few seconds. Speed of descent increases dramatically during this time as rotor thrust is significantly reduced due to reduction of rotor speed and the presence of blade oscillations. Stall of rotor blades caused by very high values of inflow angle makes recovery without pre-rotation impossible.

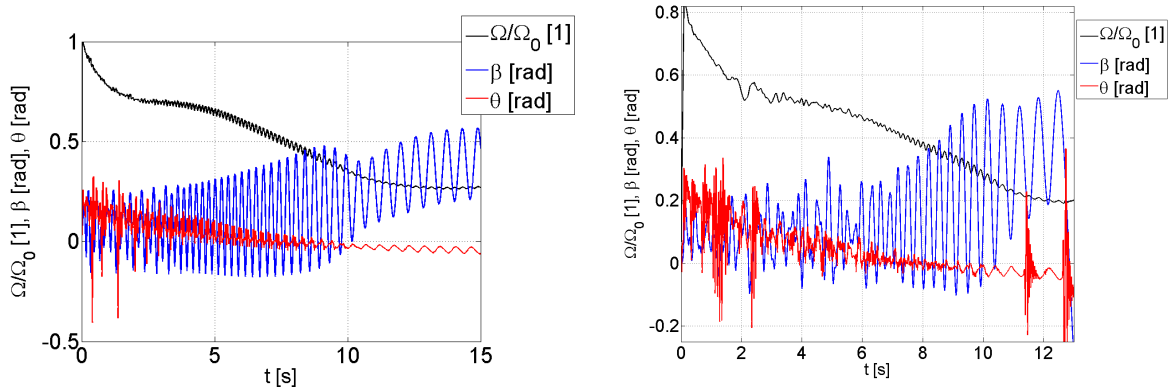


Figure 7.9: Comparison of an aeroelastic instability during forward flight in autorotation as predicted by the *AMRA* using equivalent spring stiffness (left) and coupled torsion-bending FEM model of blade dynamics.

Since the majority of rotor parameters in forward autorotative flight have har-

monic behaviour, some of the results are presented in the form of boundaries of their trends. This approach allows comparison of multiple data sets in one plot.

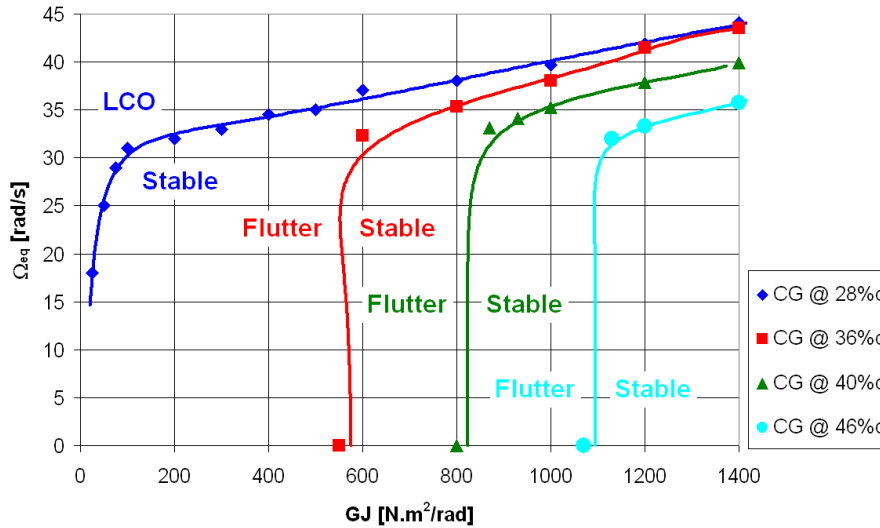


Figure 7.10: A comparison of the values of equilibrium rotor speed during autorotative forward flight; computed for different span-wise positions of blade CG and varying blade torsional stiffness

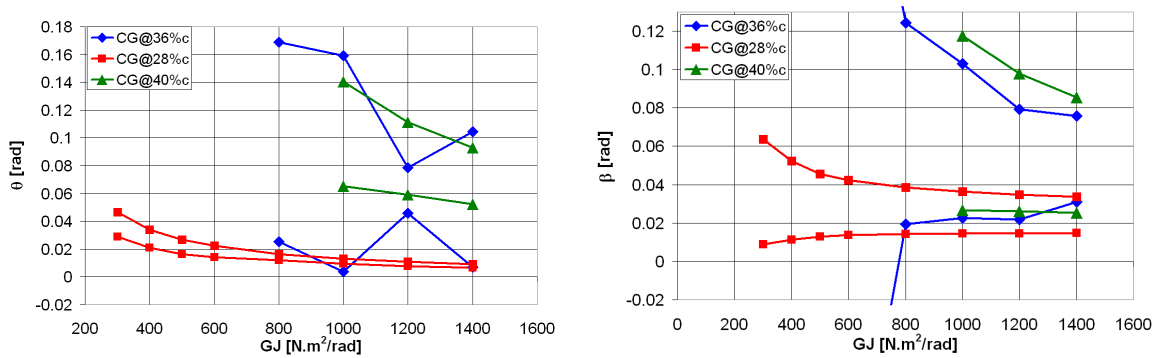


Figure 7.11: A comparison of the values of equilibrium blade torsional and flapping deflections during autorotative forward flight; computed for different span-wise positions of blade CG and varying blade torsional stiffness

Results of the *AMRA* simulations obtained for different levels of complexity of the model of blade structural dynamics are showed in figure 7.9. Again, comparison of predictions obtained with different blade structural models is given to demonstrate that the character of the instability does not change with fidelity of the model. The results of computations executed with the aid of FEM model of coupled bending-torsion of rotor blades are consistent with the results obtained from the blade model

using equivalent spring stiffness approach. Both configurations of the model predict very similar aeroelastic instability that takes place if torsional stiffness of the blade is lower than the critical value.

However, lower values of both blade torsion and bending are predicted if the spring stiffness approach is used instead of FE analysis. While simplification of the model of blade bending have only a minor effect on the results of the simulation, use of equivalent spring stiffness instead of FEA for the modelling of blade torsion seems to have a more pronounced effect. Application of FEM model of blade torsional dynamics results in a more realistic estimation of span-wise distribution of blade torsion that is characterised by higher tip deflections than is predicted by the equivalent spring stiffness model. The FEM approach also allows the capture of higher modes of blade motion.

The comparison of resulting stability boundaries given in figure 7.12 shows that fidelity of the model of blade torsional dynamics has a major effect on the shape of the aeroelastic stability boundary.

Although the simplified version of the *AMRA* model predicts different stability boundary for axial and forward flight, identical values of the critical blade torsional stiffness were obtained with the aid of full FEM model of blade dynamics. The resulting aeroelastic stability boundary can be found in figure 7.13.

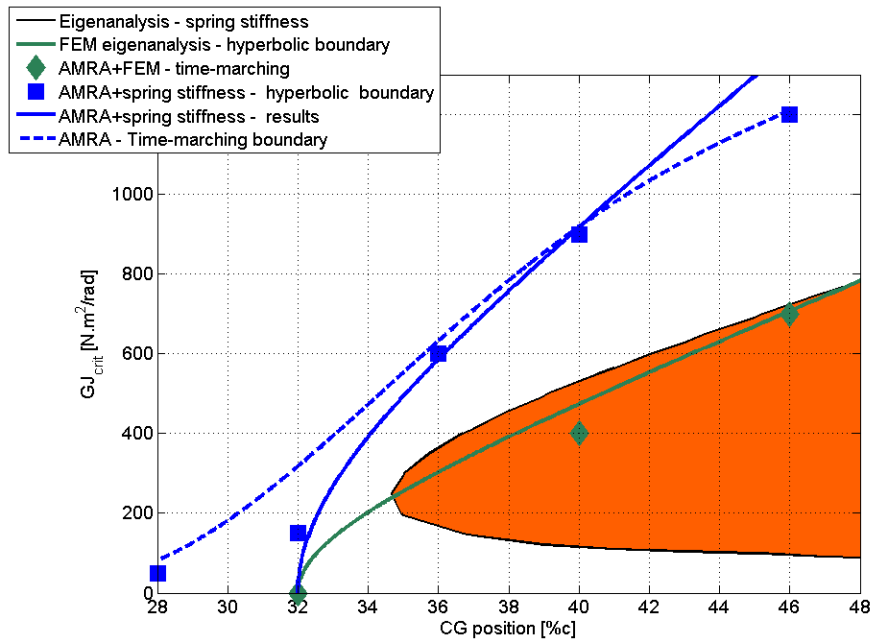


Figure 7.12: Torsional stability boundaries of gyroplane rotor in forward flight as predicted by different versions of *AMRA*

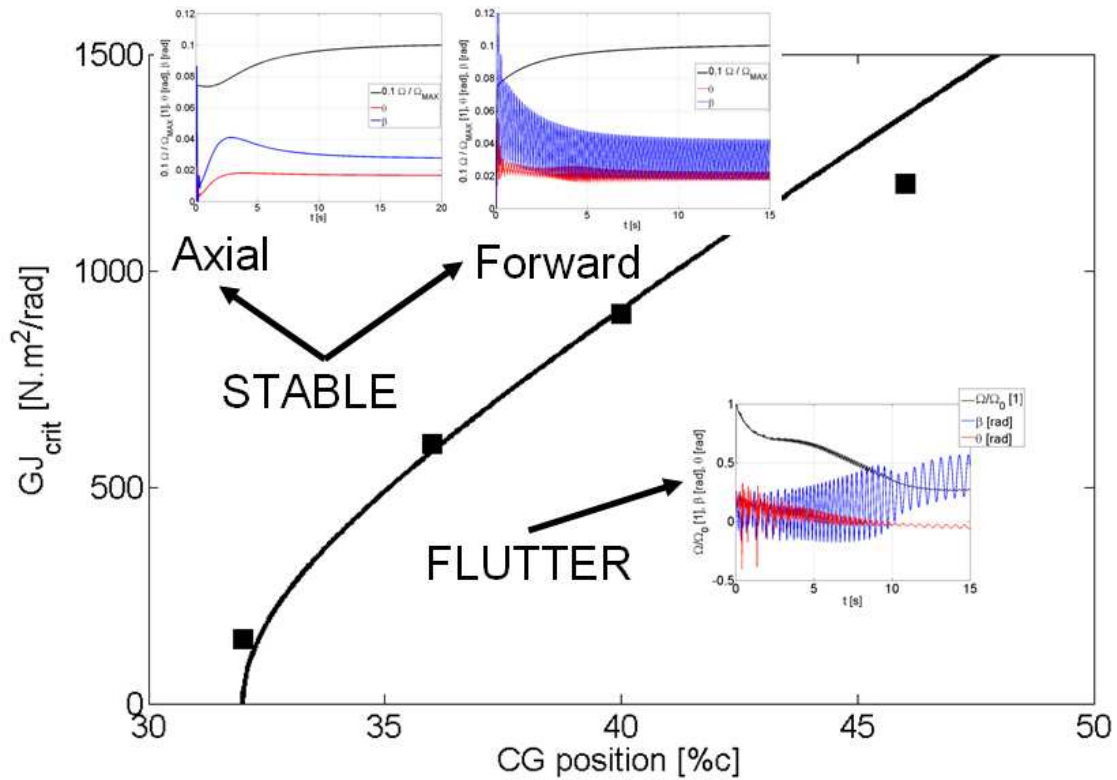


Figure 7.13: Stability boundary of a rotor in autorotation

7.2 The Effect of Blade Fixed Angle of Incidence on Rotor Aeroelastic Stability

It was shown in the previous chapters of this work that blade fixed incidence angle has a major effect on stability of rotors in autorotation. Hence a study was carried out in order to investigate the influence of blade fixed angle of incidence on the shape of aeroelastic stability boundary of an autorotating rotor.

A comparison of torsional stability boundaries computed for two different values of fixed angle of incidence of the rotor blades is shown in figure 7.14.

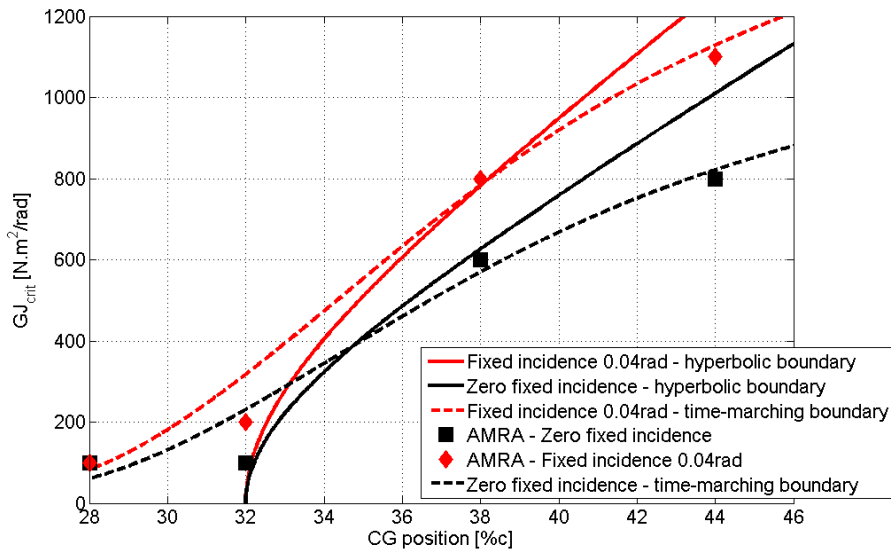


Figure 7.14: A comparison of torsional stability boundaries for two different values of blade fixed angle of incidence.

It can be seen from the figure that even relatively small increments of blade fixed angle of incidence affect the values of the critical blade torsional stiffness. The out-of-plane bending stiffness of the blade is increased by the higher blade fixed incidence angle but flexural motion of the blade is strongly affected by centrifugal forcing that provides additional stiffening regardless the value of fixed angle of incidence. Blade torsional stiffness, however, is not affected by the change of blade fixed angle of incidence and the effect of centrifugal loading on blade torsional dynamics

is much smaller too.

As was shown in Chapter 6 of this work, an increment of blade fixed angle of incidence leads to lower equilibrium rotor speed. This has a negative effect on rotor stability since effective stiffness of rotor blades is decreased. This effect is demonstrated in figure 7.15.

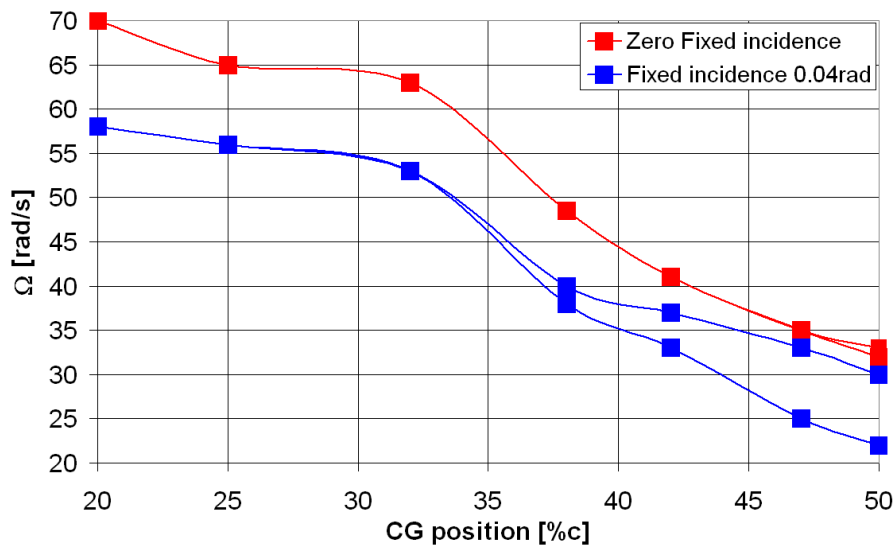


Figure 7.15: A comparison of the values of equilibrium rotor speed for two different values of blade fixed angle of incidence, varying chord-wise positions of CG and typical values of torsional stiffness ($GJ=1500\text{N.m/rad}$)

Results of another parametric study carried out with the aid of *AMRA* suggests that increased value of blade fixed angle of incidence might cause higher blade vibratory loading during forward flight in autorotation as it results in lower equilibrium rotor speed and higher inflow angles. Hence a larger portion of the blade span passes through the stall each rotor revolution, which results in more profound harmonic vibrations of the blade.

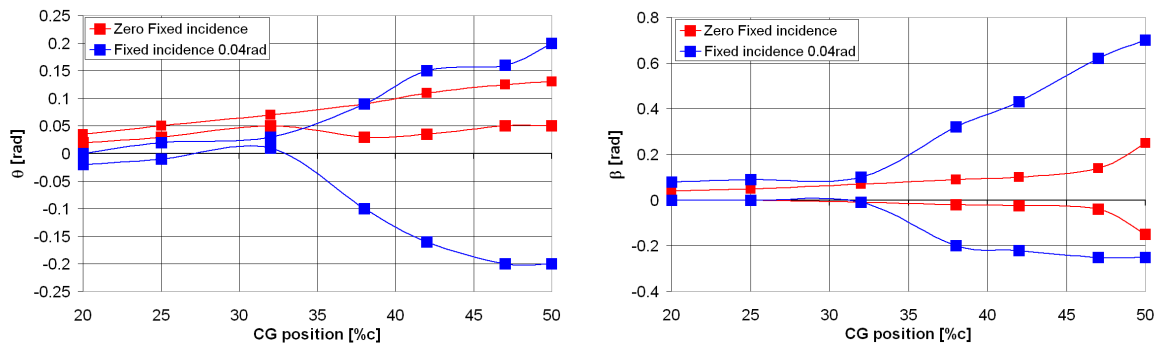


Figure 7.16: A comparison of the values of equilibrium blade torsional and flapping deflections for two different values of blade fixed angle of incidence, varying chord-wise positions of CG and typical values of torsional stiffness ($GJ=1500\text{N.m/rad}$)

7.3 The Effect of Chord-Wise Position of Blade Elastic Axis on Rotor Aeroelastic Stability

An extensive study on aeroelastic stability of a gyroplane rotor for various span-wise positions of blade CG and EA and different values of blade torsional rigidity was carried out. Since a high number of individual simulations was required, a simplified model of blade structural dynamics using equivalent spring stiffness was used. The results of parametric studies have shown that the chord-wise position of CG has much stronger effect on stability of autorotation than chord-wise position of EA. The aeroelastic stability boundaries that were computed for different chord-wise locations of CG and EA of a rotor in autorotation can be found in figure 7.17.

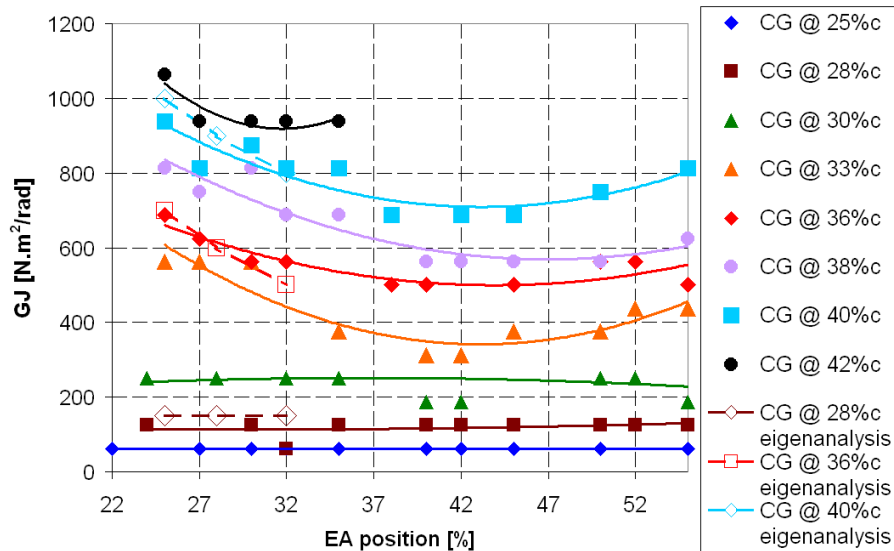


Figure 7.17: The effect of elastic axis position on stability of a rotor in autorotative flight.

The results of the simulations have shown that although aeroelastic stability is driven mainly by the value of CG-EA offset and blade torsional stiffness, it is also affected by the offset of aerodynamic centre (AC) from blade elastic axis. It can be seen in figure 7.17 that increase of this offset is de-stabilizing. This behaviour can be explained by the fact that the AC-EA offset represents the arm of aerodynamic torsional moment.

The figure also shows that the results of the time-marching configuration of *AMRA* model are in a good agreement with predictions of eigen-analysis carried out with the aid of the model in frequency domain.

7.4 The Effect of the Value of Blade Zero-Lift Pitching Moment Coefficient on Rotor Aeroelastic Stability

The majority of modern light gyroplanes use rotor blade airfoils with reflex camber. Reflex camber airfoils generate positive pitching moment (nose-up) for low angles of attack. This feature is unique for this type of airfoil - symmetrical airfoils do not generate any pitching moment if not stalled and classical cambered airfoils generate negative values of pitching moment. Reflex camber airfoils are often used in tail-less aircraft design due to their auto-stabilizing properties.

Positive values of blade pitching moment that are achieved for a wide range of angles of attack below stall can be used in gyroplane design to avoid over-speeding of the rotor and the rise of speed of descent. This can be deduced from the results presented in the Chapter 6 of this work. Parametric studies carried out with the aid of *AMRA* showed that a negative blade twist applied to the outboard blade region causes significant increase of rotor speed and speed of descent.

Rotor over-speed is dangerous due to possible occurrence of vehicle control problems and excessive centrifugal loading. Since the effect of different values of zero-lift pitch moment coefficient (c_{m0}) on stability of rotors in autorotation was not clear, the *AMRA* model was used for prediction of stability of rotor blades with different values of c_{m0} .

Figures 7.18 and 7.19 show that the use of reflex camber airfoils (i.e. positive values of blade pitching moment) have de-stabilizing character. The results show that stability of the rotor is reduced even if the blades are in a stable configuration (i.e. CG ahead of EA; all results are computed for EA at 32% chord). Negative values of c_{m0} , on the other hand, have a stabilizing character. Higher values of equilibrium rotor speed lead to high centrifugal loading and thus to higher effective stiffness of the blade.

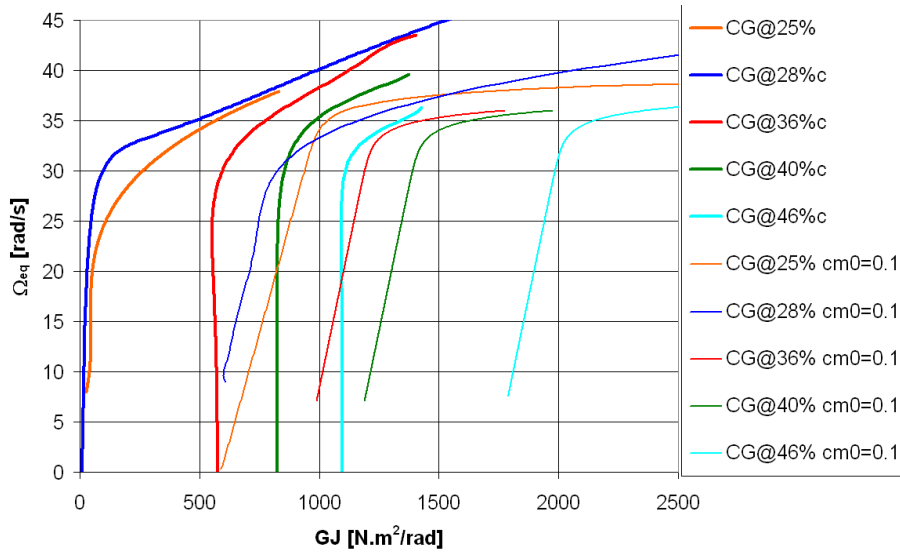


Figure 7.18: The effect of positive values of c_{m0} on the values of equilibrium rotor speed for different positions of blade CG.

Figure 7.20 gives a comparison of aeroelastic stability boundaries of gyroplane rotor blades that use symmetrical, cambered and reflex-camber airfoils.

It is apparent that positive values of c_{m0} increase the probability of loss of aerodynamic torque equilibrium. It can be seen from figure 7.20 that the *AMRA* model predicts that use of reflex camber airfoils increases the values of critical torsional stiffness significantly. The figure also shows that the new values of critical torsional stiffness are relatively close to the values obtained during experimental measurements of physical properties of McCutcheon gyroplane blades (see Chapter 4). Rotor blades for light gyroplanes are being manufactured in modest conditions, which

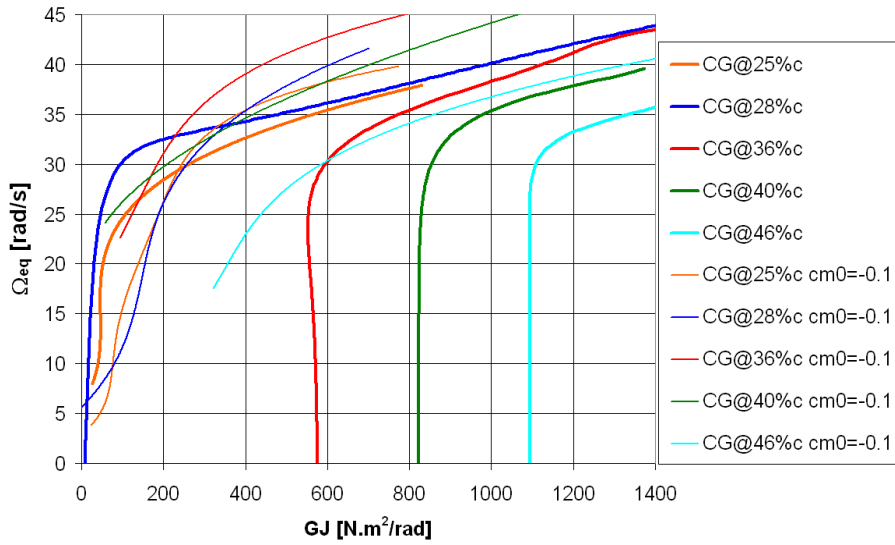


Figure 7.19: The effect of negative values of c_{m0} on the values of equilibrium rotor speed for different positions of blade CG.

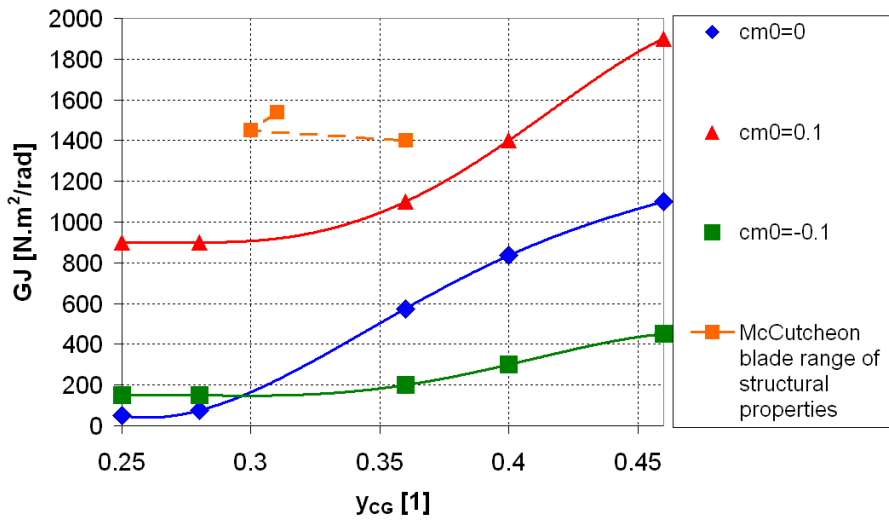


Figure 7.20: The effect of different values of c_{m0} on the shape of blade torsional stability boundary.

leads to a high scatter of blade properties. The majority if not all of them also use rotor blades equipped with reflex-camber airfoils.

The UK Civil Aviation Authority has identified loss of rotor speed and excessive values of control forces as the key factors in some of gyroplane accidents. The results presented above suggest that these accidents might be caused by combination of rotor blades with unsuitable structural properties (e.g. low torsional stiffness or EA ahead of CG) and use of reflex camber airfoils.

7.5 The Effect of Rotor Disc Tilt Hinge Offset on Rotor Aeroelastic Stability

An offset of rotor longitudinal tilt hinge and rotor disc centre of rotation (that is usually coincident with rotor teeter hinge) is often used in rotor hub design of modern light gyroplanes. Figure 7.21 shows layout of such hub design, namely the hub of the Montgomerie-Parson light gyroplane.

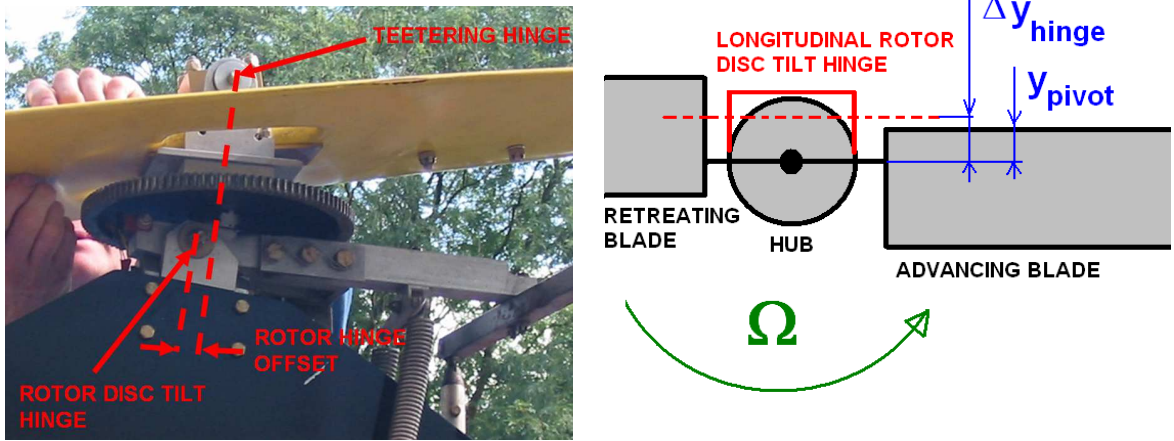


Figure 7.21: Rotor hinge offset in a typical modern light gyroplane rotor design

This arrangement results in harmonic change of EA-CG offset if blade pitch around the point of its root attachment and finite stiffness of gyroplane controls are assumed. The change of CG-EA offset length with blade azimuth is then

$$y_g = y_{EA,h} - y_{CG} = y_{pivot} + \Delta y_{hinge} \sin \psi - y_{CG} \quad (7.1)$$

Alternatively, a linear variation of the chord-wise position of blade elastic axis from the blade root attachment position at the blade root to the 'natural' position of EA given by the blade structure at the blade tip can be assumed. Equation 7.1 then changes to

$$y_g = y_{EA,h} - y_{CG} = y_{EA} \frac{r}{R} + (y_{pivot} + \Delta y_{hinge} \sin \psi) \left(1 - \frac{r}{R}\right) - y_{CG} \quad (7.2)$$

Figure 7.22 shows that a rotor hub with hinge offset can potentially decrease aeroelastic stability of the rotor since it causes change of the position of blade EA with blade azimuth. Hence the aeroelastic stability boundary of each rotor blade also changes shape with azimuthal position.

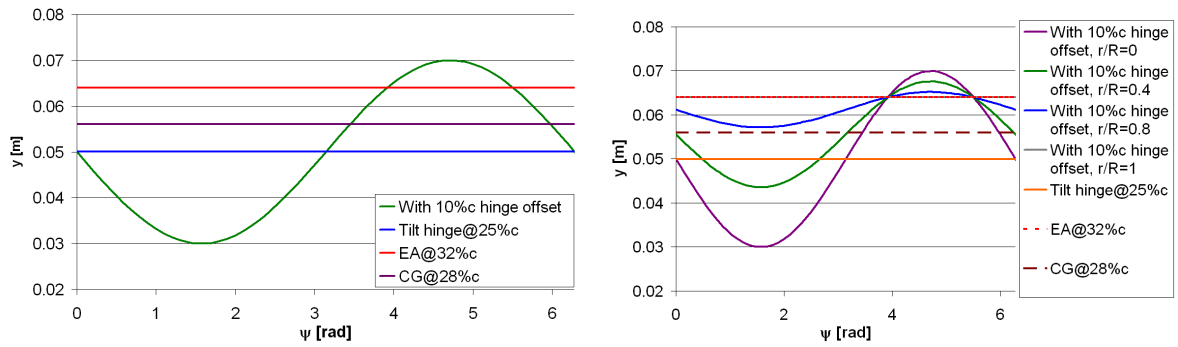


Figure 7.22: Change of CG-EA offset of a gyroplane rotor with non-zero hinge offset. In the figure on the left, the blades are assumed to pitch around the root attachment only. Linear change of elastic axis between root attachment at the root and natural elastic axis is assumed in the right-hand side figure.

The effect of rotor hinge offset on the aeroelastic stability of a gyroplane rotor was investigated with the aid of the *AMRA* model. Since *AMRA* did not contain a model of the dynamics of the vehicle control system, an assumption was made that the effective value of control system stiffness is similar to the torsional stiffness of the blades. Results of the simulations suggest that harmonic changes of EA position alone does not have any major effect on aeroelastic stability of the rotor. It can be seen from figure 7.23 that the equilibrium values of rotor speed are not affected by rotor hinge offset.

Figure 7.24 compares aeroelastic stability boundary of gyroplane rotors with zero hinge offset and with negative hinge offset (i.e. rotor longitudinal tilt hinge is ahead of rotor pivot point).

One possible explanation of this is that the aeroelastic instability does not have enough time to develop since the blade enters more stable configuration every revolution, after having gone through a region of lower aeroelastic stability (see figure 7.22).

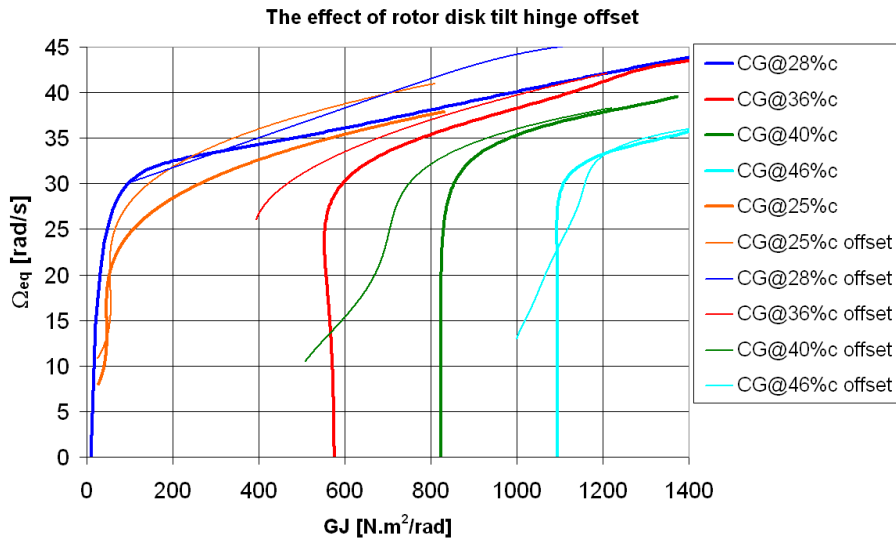


Figure 7.23: The effect of rotor hinge offset on the values of equilibrium rotor speed for different positions of blade CG. Computed for $\Delta y_h = -0.1c$.

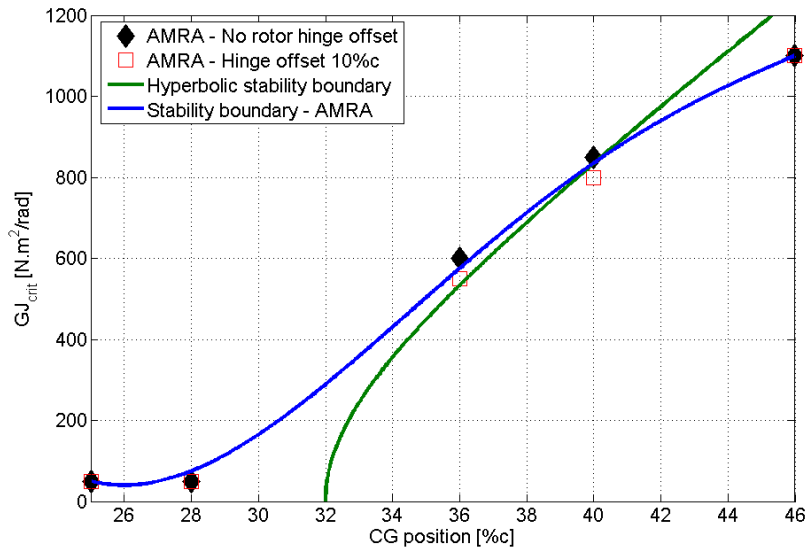


Figure 7.24: The effect of rotor hinge offset on the shape of blade torsional stability boundary. Computed for $\Delta y_h = -0.1c$.

A conclusion can be made that the hinge offset alone does not cause significant change of rotor stability. However, it is likely that the control system stiffness of a typical light gyroplane has a major effect on aeroelastic stability of the rotor. Low control system stiffness might decrease rotor stability even if the rotor has no hinge offset since the root attachment of many of modern gyroplanes is located at blade quarter-chord. As was shown in this work, it is likely that chord-wise position of

centre of gravity of many gyroplane blades lies aft 25% chord. It is recommended that control system stiffness should be determined and included in future models of gyroplane rotor aeroelastics.

7.6 The Effect of Flexural Stiffness on Rotor Aeroelastic Stability

The results obtained with the aid of *AMRA* suggest that variation of blade flexural stiffness within a realistic and practical range of values has a minor effect on rotor aeroelastic stability. Figure 7.25 shows the variation of the equilibrium rotational speed and critical torsional stiffness with blade flexural stiffness as predicted by *AMRA* time-marching and frequency domain models. Results of the parametric study confirm that lower fidelity of the model of blade flap does not have significant significant effect on predictions of the aeroelastic model.

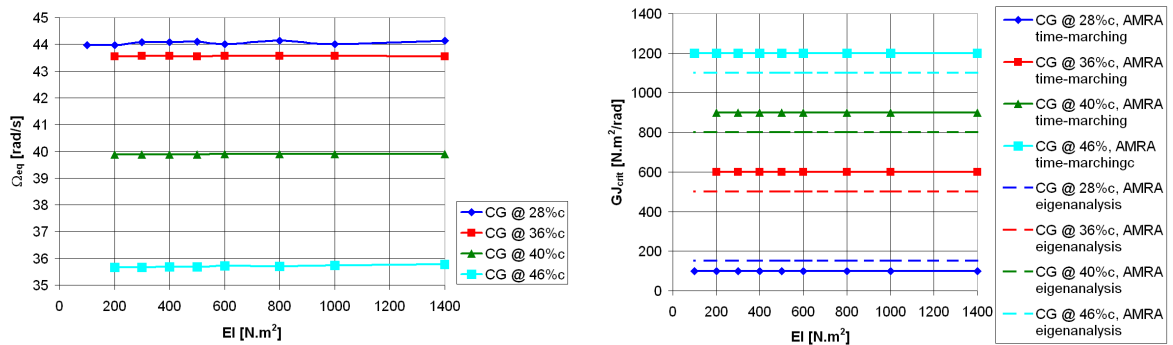


Figure 7.25: Dependence of the value of equilibrium rotor speed and critical torsional stiffness upon blade flexural stiffness of an autorotating rotor.

The simulations also showed that a change of blade flexural stiffness does not affect the shape of blade torsional stability boundary even if blade flexural stiffness is very low (see figure 7.26). This can be explained by high centrifugal stiffening present during rotor operation and high aerodynamic damping of the blade teetering motion. The magnitude of the additional blade stiffening due to centrifugal forces is usually much higher than structural stiffness alone and hence even very low blade

flexural stiffness does not have significant effect on rotor stability during operation at nominal rotor speed. However, the values of blade flexural stiffness have to be kept within a practical range of values since very flexible rotor blades would make operation of the vehicle impossible.

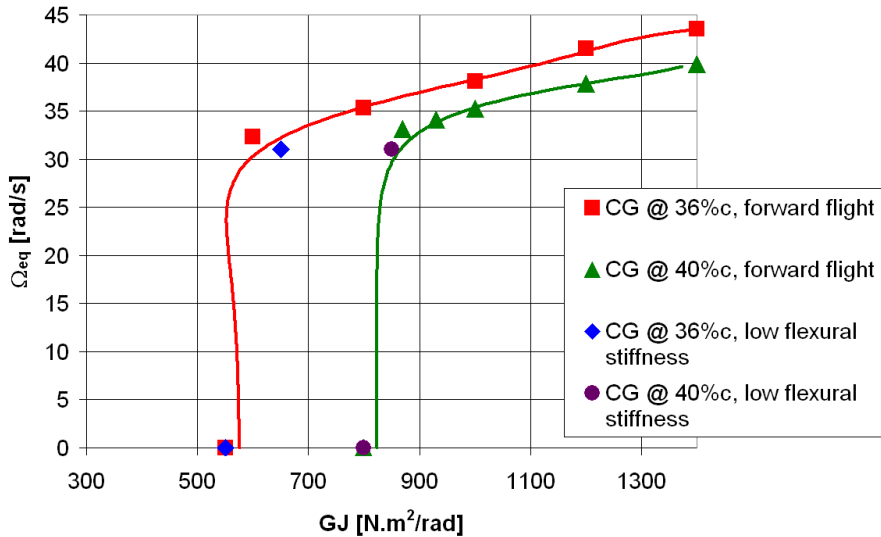


Figure 7.26: Single degree of freedom aeroelastic instability in torsion of a rotor in vertical descent in autorotation.

The simulations carried out with the aid of the *AMRA* model indicated that a single degree of freedom instability can be encountered if blade flexural stiffness is very high and the torsional stiffness is low. Figure 7.27 shows that the instability is very similar to pure divergence if the rotor is in axial autorotative flight (i.e. if the inflow speed into the rotor disc does not change with blade azimuth).

Although the values of the critical torsional stiffness are much lower than in the case of torsion-flap flutter, the reduction of rotor speed is slower. The figure also shows that a steady value of rotor speed seems to be maintained in the forward flight regime. This stabilising effect of the forward flight regime might be caused by a combination of stall of the blades at the retreating side of the rotor disc and aerodynamic coupling between the rotor speed and blade torsion. Contrary to axial flight in autorotation, the forward flight regime might allow reaching of torque equilibrium thanks to varying flow conditions across the rotor disc.

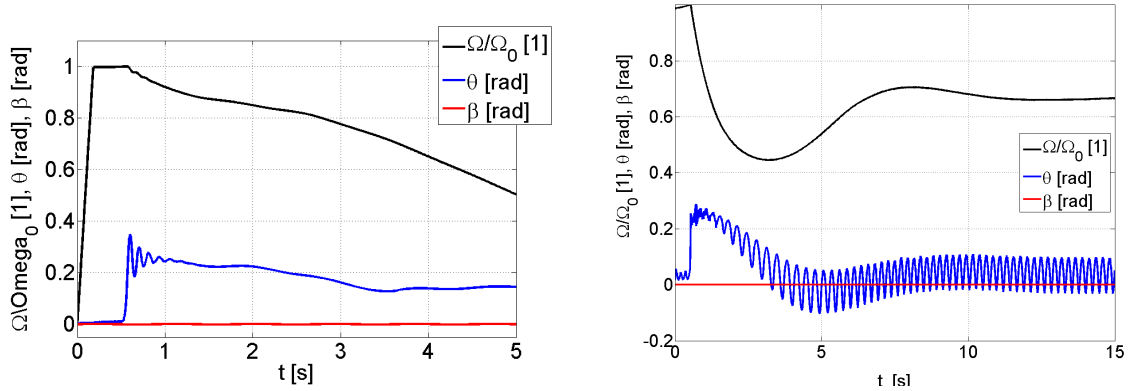


Figure 7.27: Single degree of freedom aeroelastic instability in torsion of a rotor in vertical descent in autorotation and autorotative forward flight.

Since the value of the critical torsional stiffness of blade divergence is much lower than in the case of torsion-flap flutter, very high values of blade flexural stiffness would have stabilizing character. Figure 7.28 shows that very high blade flexural stiffness increases the equilibrium rotor speed during autorotation. However, this approach is not practically applicable since it would result in excessive weight of the blade structure and also the use of extremely expensive materials and manufacturing techniques. It can also be seen from the figure that the value of the equilibrium rotor speed during autorotation remains constant if blade torsional stiffness is very high. This is given by the fact that flapping motion has much smaller effect on the local values of blade angle of attack than torsion and that it is strongly damped by aerodynamic forces.

7.7 Summary

A new form of pitch-flap flutter was predicted to occur in autorotating rotors by the *AMRA* model. This aeroelastic instability is characterized by coupled oscillations in torsion, teeter and rotor speed and results in catastrophic reduction of rotor speed. Further investigation revealed that the point of onset of the flutter of rotors in autorotation is not significantly affected by extra degree of freedom in rotation. The

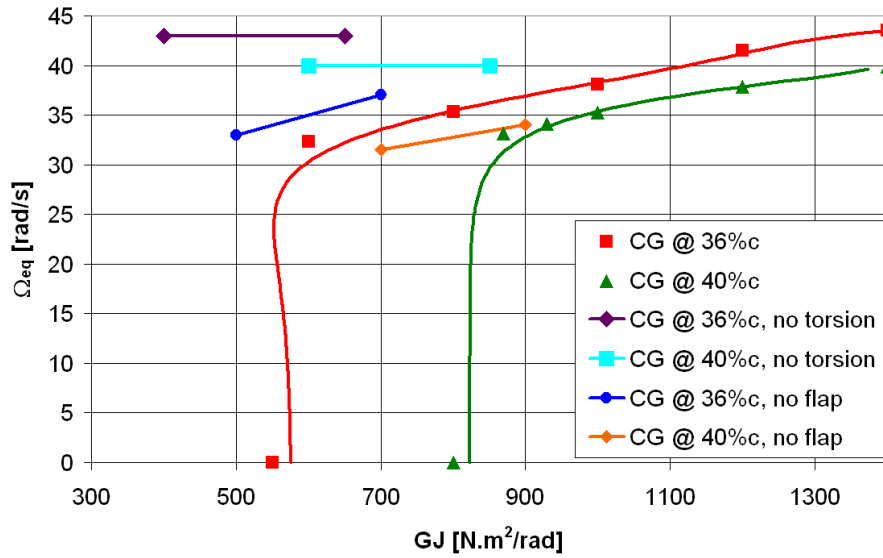


Figure 7.28: The change of the equilibrium rotor speed with blade torsional stiffness of a typical gyroplane rotor, a gyroplane rotor with infinitely high torsional stiffness and a gyroplane rotor with infinitely high flexural stiffness.

shape of torsional stability boundary of autorotating rotors is hence similar to that of helicopter rotors.

However, variable rotor speed has strong effect on the character and time history of the instability. Especially coupling of rotor speed with blade torsion is significant, resulting in change of the values of blade critical torsional stiffness with fixed angle of incidence of the rotor blades. A similar form of aeroelastic instability of rotors in autorotation was also predicted for mass balanced rotors with excessive blade fixed incidence (see Chapter 6) and it was shown that a single-degree of freedom instability in torsion might occur for very low values of torsional stiffness.

Simulations performed with the aid of *AMRA* identified rotor blade design parameters that are critical for aeroelastic stability of rotors in autorotation. These parameters and their effects are

- Torsional stiffness of rotor blades - higher stiffness delays flutter onset (i.e. it is stabilizing)

- The offset of blade elastic axis from blade axis of inertia - elastic axis ahead of centre of gravity is stabilizing
- The value of moment coefficient generated by rotor blade sections at moderate angles of incidence - positive values are destabilizing
- Blade fixed angle of incidence - positive values are destabilizing, negative values cause increase of speed of vertical component of flight speed

A large positive value of aerodynamic pitching moment coefficient generated by rotor blades that is typical for modern gyroplane rotors was found to be destabilizing. Similarly, positive values of blade fixed incidence angle increase the value of blade critical torsional stiffness. Hence pitch-flap flutter is unlikely to occur as long as the values of these two design parameters are kept low and blade axis of inertia lies ahead of blade elastic axis.

Some other rotor blade design parameters influence rotor stability but their effect is not significant for realistic values of these parameters (see below).

- The offset of the elastic axis from blade aerodynamic centre
- The offset of rotor disc longitudinal hinge (pitch control hinge) from the axis of rotation of the rotor
- Blade flexural stiffness

Chapter 8

Conclusions

Gyroplane accidents that occurred during last few decades have drawn attention to gyroplane aeromechanics and handling qualities. The aeroelastic behaviour of autorotating rotors is relatively unexplored and only few publications on the topic are available in open literature. No research studies focused on coupled pitch-flap-rotor speed dynamics of autorotating rotors and determination of their flutter stability boundary are available in open literature. Similarly, analysis of the effect of different rotor blade design parameters on performance of autorotating rotors can't be found in open literature. Hence an original research work had to be carried out in order to assess the role that rotor design and aeroelastic behaviour might play in recent gyroplane accidents.

The aim of this research work was to investigate aeroelastic behaviour of gyroplane rotors and identify possible hazardous rotor configurations or modes of operation. An aeromechanical model of a rotor in autorotation *AMRA* was developed and used for prediction of rotor aerodynamic performance and aeroelastic behaviour. The model was successfully implemented in MATLAB, making it easy to use and portable. The *AMRA* model is based on a combination of blade element theory with unsteady aerodynamics, a dynamic inflow model, a dynamic finite element model of blade coupled torsion-bending and a 'rigid' blade structural model of blade teeter and rotation. A frequency domain model was also developed, allowing prediction

of blade natural frequencies and mode shapes. Hence *AMRA* represents relatively versatile tool for modelling of aerodynamics and aeroelasticity of autorotating rotors.

In order to obtain input parameters for the structural model of the blade, a series of experimental measurements were carried out to determine the physical properties of a typical gyroplane blade. All input data required for the model were obtained from the experiments, i.e. blade mass distribution, position of elastic axis, spanwise distribution of CG locations and the values of torsional and flexural stiffness were measured. Resulting data are relatively rare since no information on physical properties of gyroplane rotors can be found in open literature. The results of the experimental measurements confirmed that the physical properties of gyroplane rotors can vary widely along the blade span. This is given by the fact that many gyroplane rotor blades are manufactured by small companies in relatively modest conditions and variation of blade physical properties is not always checked. Blade centre of gravity laying aft of blade elastic axis along a major part of the blade was perhaps the most surprising outcome of the experiments. McCutcheon rotor blades were found to be relatively stiff in torsion and flat-wise bending but very flexible in flap-wise bending.

The fidelity of the *AMRA* model was assessed with the aid of both the theory of aeroelasticity, experimental measurements and results of other validated predictive tools. Verification of basic functionality and accuracy of all model components for modelling of both axial descent and forward flight in autorotation was performed, despite limited amount of available data. More comprehensive verification of the model would require additional experimental measurements that would be relatively complex and expensive. Predictions of the model were found to be in a good agreement with the data used during the verification, although capabilities of the structural blade model are limited as it is based on a simplified FEM model using slender beam theory. It is likely that fidelity of the model, and especially modelling of blade torsional dynamics, would be further improved if a 2D (flat plate) FEM model of rotor

blade was used. Aerodynamic characteristics of a reflex camber airfoil (preferably the NACA 8-H-12) for a full range of angles of attack and Mach numbers should be added to the aerodynamic once available. A comprehensive database of airfoil aerodynamic properties is used in the model that takes into account both compressibility effects and non-linear character of blade aerodynamic properties at higher angles of attack. However, predictive capabilities of the model at higher Mach numbers is limited since neither the theory of quazi-steady aerodynamics, nor Theodorsen's theory can capture compressibility effects.

Once verified, the *AMRA* model was used for modelling of performance and aeroelastic stability of autorotating rotors. The simulations have shown that autorotation is a complex aeromechanical process with an auto-stabilizing character. Coupling of blade torsional and flapping motion with the rotor speed drives the rotor toward torque equilibrium. This equilibrium is reached on condition that the rotor speed is higher than the critical value of rotor speed. Critical rotor speed in autorotation depends not only upon the configuration of the rotor and the vehicle but also on its flight regime and flight conditions. This is given by strong coupling between the rotor speed and vehicle flight mechanics. The concept of critical rotor speed is one of the most important features of this work. Virtually no published work is dealing with this problem, although the approach becomes clear once a mathematical model of an autorotating rotor is coupled with a model of vehicle flight mechanics. The coupling between rotor performance and vehicle flight states is unique for autorotative flight in autorotation since the pilot is not able to control rotor speed directly. Once the rotor speed drops below the critical value, torque equilibrium cannot be reached without change of vehicle flight conditions or rotor pre-rotation as growing speed of descent causes rotor blade stall. The author believes that a similar study has not been published in open literature.

A series of parametric studies were performed to investigate the effect of variation of selected rotor blade design parameters on performance and stability of a rotor

during autorotation. The results of the studies have shown that the parameters that affect span-wise distribution of blade angle of attack have by far the strongest influence on the performance of rotors in autorotation. This is caused by a strong aerodynamic coupling between blade torsion and rotor speed and thus blade torsional dynamics plays the key role during flight in autorotation. Analysis of this kind is unique and no comparable publications can be found in open literature.

The outcomes of *AMRA* model suggest that positive values of blade fixed incidence angle and blade geometric twist has adverse effect on performance of a rotor during autorotative flight, especially if applied to the outboard portion of the rotor blades. Excessive values of these design parameters cause generation of high amounts of blade drag at the outboard part of the blade and reduction of aerodynamic torque generated by the inboard region of the blade due to blade stall.

Very low positive or zero fixed blade incidence angle and moderate amount of blade tip mass seem to be beneficial for performance of a rotor in autorotation. The results of the model confirmed that addition of a blade tip mass increases equilibrium rotor speed and hence improves stability of autorotation. Application of rotor blade tip mass is often used within amateur gyroplane pilots to increase rotor stability. The blade tip mass can be also used for mass balancing of the rotor blades (i.e. moving blade CG ahead of its elastic axis). However, increase of the value of equilibrium rotor speed with increasing blade tip mass was found to be rather low. Moreover, it was predicted by the model that the critical value of rotor speed increases with growing blade tip mass. Hence it can be concluded that only moderate amounts of blade tip mass should be used.

The model showed that negative values of blade outboard twist lead to rotor over-speed, loss of thrust and hence cause lower aerodynamic efficiency (gliding ratio) of the rotor. Moderate values of negative blade geometric twist applied to the blade inboard region, however, seem to improve rotor behaviour as they lead to

lower values of angle of attack of the inboard part of the blade. Hence stall of inboard blade sections is postponed and the ability of rotor blades to generate positive aerodynamic torque is improved. It can be concluded that zero value of blade fixed incidence together with moderate negative geometric twist in the inboard part of the blade and sensible application of blade tip mass will result in high stability and good performance of a rotor in autorotation. Since rotor blades of modern gyroplanes are not twisted, use of negative geometric twist of the rotor blade inboard region represents a novel design solution.

A study of the effect of the level of complexity of the blade structural model on predictions of the aeroelastic model (a sensitivity analysis) was carried out. Results of the *AMRA* simulations have shown that modelling of rotor blade torsion has a major effect on the fidelity of an aeroelastic model of a rotor in autorotation. The use of an equivalent spring stiffness model for the simulation of blade flexural dynamics was found sufficient to achieve fidelity comparable to a full coupled FEM model.

Modelling of blade torsional dynamics was found to be the key element of the model and it was shown that incorrect or misleading results will be obtained if an accurate model of blade torsion is not used. Hence the FEM model of blade dynamics should be used *at least* for modelling of blade torsional dynamics during autorotative flight. A simplified model of blade flexural dynamics can be used. This feature of an aeroelastic model of a rotor in autorotation seems to be unique since the effect of accuracy of prediction of blade torsion is not so significant in helicopter aeroelasticity. Again, this is caused by the fact that blade torsion has strong effect on the value of rotor speed during autorotation and hence strongly affects the amount of centrifugal forcing present. Hence the outcomes of the study are compatible with findings gathered during the parametric studies of autorotating rotors. Similar fidelity study focused on gyroplane aeroelasticity is not available in open literature and the influence of blade torsion on performance of autorotating rotors is clearly

not appreciated enough. This is demonstrated by the fact that the torsional degree of freedom of the rotor blades is ignored in a number of research works dealing with stability of autorotating rotors.

An aeroelastic instability in coupled blade *pitch-bending-rotation* was predicted for blade axis of inertia located aft of the blade elastic axis and low values of blade torsional stiffness. Occurrence of a type of flutter that is unique for autorotating rotors was predicted by the model both during axial descent in autorotation and during autorotative forward flight. This aeroelastic instability is driven by blade *pitch-bending-rotor speed coupling* and differs from both flutter of a helicopter rotor and flutter of a fixed wing. The instability results in catastrophic decrease of the rotor speed and significant increase of speed of descent. It is likely that this the first time that this unique flutter phenomenon has been identified and explained since no relevant information can be found in open literature.

The simulations have shown that the additional degree of freedom in rotation does not have a strong effect on the shape of the aeroelastic stability boundary. Hence the shape of stability boundary predicted using full, non-linear form of blade equations of motion is essentially identical to the stability boundary predicted by eigenanalysis of equations of motion linearized around rotor speed. However, the coupling of rotor speed with other degrees of freedom of the rotor blades and vehicle flight mechanics strongly affects the character of the aeroelastic instability. Removing of a blade degree of freedom in either torsion or teeter leads to a significant increment in rotor stability since pitch-flap coupling is not present. The same result is obtained if flight mechanics of the vehicle are ignored (i.e. if horizontal speed and especially speed of descent are kept constant). However, a single degree of freedom instability in torsion can be encountered if blade torsional stiffness is very low. This instability is very similar to aeroelastic divergence if forward speed is low. If not coupled with rotor torsion, blade flexural dynamics proved to have a minor effect on aerodynamics and aeroelastic stability of autorotating rotors.

The effect of the use of cambered and reflex camber airfoils in gyroplane rotor design was also investigated. Although a comparison of aerodynamics of reflex camber airfoils with other types of airfoils was carried out and published in the past, no publications are available comparing performance and stability of autorotating rotors equipped with different types of airfoils. The model predicted that the values of critical torsional stiffness are increased significantly if reflex camber airfoils are used. This outcome is given by the fact that positive values of pitching moment generated by reflex camber airfoils are destabilizing due to excessive nose-up torsion of the rotor blades. Higher torsional deflections of the rotor blades result in lower equilibrium rotor speed and hence reduce centrifugal stiffening of the blades. Reflex camber airfoils are used in rotor blade design of majority of modern light gyroplanes. Since use of cambered airfoils might lead to rotor over-speed, high-performance symmetrical airfoils or amended reflex camber airfoils generating lower pitching moments should be used in gyroplane rotor design.

The influence of rotor disc tilt hinge offset from the rotor pivot point on rotor aeroelastic stability was also studied. This design feature is present in a number of light gyroplane designs. Although the hinge offset causes variation of blade elastic axis position with azimuth, the model did not predict any significant effect on the shape of rotor stability boundary. However, further research is required in order to fully understand the effect of the design feature on rotor stability since a model of flexible gyroplane control system was not included in the study.

The author is not aware of any published research work that would provide detailed performance analysis of rotors in autorotation. No publications on modelling of pitch-flap-rotor speed dynamics are available and a number of phenomena predicted by the *AMRA* model were not previously described in any open literature entry. Apart from identifying the unique flutter phenomenon caused by extra degree of freedom in rotation, the strong aeromechanic coupling between blade torsion and

rotor speed was studied in detail for the first time. Hence the present work represents a novel contribution to the field of rotorcraft aeroelasticity.

A detailed description of the influence of various design parameters on stability of autorotating rotors given in this work can be used in preliminary rotor design or as a guidance during rotor blade modifications. Information on the character of the aeroelastic instability in autorotation can help to enhance existing airworthiness regulations (e.g. BCAR-T).

The author also hopes that this thesis will trigger further investigation of aerodynamics and aeroelastic behaviour of autorotating rotors. Study of the effects of aeroelastic instability of a rotor in autorotation on flight dynamics of a light gyroplane, research of rotor aeroelastics using more comprehensive aerodynamic model (dynamic stall model and reflex camber airfoil aerodynamic data) or investigation of functionality of rotor blade trailing edge flaps during autorotative flight can be used as an example.

References

- [1] D. Cameron and D.G. Thomson. Scottish Contribution to Rotary Wing Flight. In *Proceedings of the 64th AHS Annual Forum, April-May 2008, Montreal, Canada*, 2008.
- [2] D.G. Thomson and S. Houston. Advances in Understanding Autogyro Flight Dynamics. In *Proceedings of the 64th AHS Annual Forum, April-May 2008, Montreal, Canada*, 2008.
- [3] B.H. Charnov. *From Autogiro to Gyroplane: The Amazing Survival of an Aviation Technology*. Praeger Publishers, Westport, Connecticut, USA, ISBN 978-1567205039, 2003.
- [4] R. Anderson. Updated: CarterCopter and Its Legacy. *Contact Magazine*, 2006. Issue 84, July 2006.
- [5] Hawk 4 on Winter Olympic Duty. *Flight International Magazine*, Issue 8-14 January 2002, 2002.
- [6] G. Warwick. Unmanned Deliveries. *Aviation Week & Space Technology Magazine*, 2009. Issue 6 July 2009.
- [7] J.G. Leishman. The Development of the Autogiro: A Technical Perspective. *Journal of Aircraft*, 41(2):765–781, 2004.
- [8] R. W. Prouty. *Helicopter Performance, Stability and Control*. Robert E. Krieger Publishing Co., Malabar, FA, USA, 1990.

- [9] A. Gessow. Review of Information on Induced Flow of a Lifting Rotor. NACA Technical Note, *National Advisory Committee for Aeronautics*, Langley Aeronautical Laboratory, VA, USA, 1954. TN 3238.
- [10] P.J. Carpenter. Lift and Profile-drag Characteristics of an NACA 0012 Airfoil Section as Derived from Measured Helicopter-rotor Hovering Performance. NACA Technical Note, *National Advisory Committee for Aeronautics*, Langley Memorial Aeronautical Laboratory, VA, USA, 1958. TN 4357.
- [11] R. L. Bielawa. *Rotary Wing Structural Dynamics and Aeroelasticity, Second edition*. AIAA Education series, 2006. 1-56347-698-3.
- [12] J.G. Leishman. *Principles of Helicopter Aerodynamics, Second edition*. Cambridge University Press, Cambridge, UK, 2006. ISBN 0-521-85860-7.
- [13] Synthetized Aerodynamic Data of NACA0012, 0015, 0018 and 0021 Airfoils. L.Lazaukas, Aerospace Consultant, Cyberiad, 25/65 William St., Adelaide 5000, Australia, 2005.
- [14] G. Warwick. Gyro revival. *Flight International Magazine*, 2006. Issue 21-27 February 2006.
- [15] G. Norris. Carter Claims Mu Record, But Suffers Another Crash. *Flight International Magazine*, 2005. Issue 12-18 July 2005.
- [16] I. Hancock. *The Lives of Ken Wallis - Engineer and Aviator Extraordinaire*. Ian Hancock, ISBN 978-0-9541239, 2005.
- [17] Magni Gyro. Vittorio Magni, Magni Gyro s.r.l., Via Volpina, I-21010 Besnate (VA), Italy, 2005.
- [18] D.G. Thomson, S.S. Houston, and V. M. Spathopoulos. Experiments in Autogiro Airworthiness for Improved Handling Qualities. *Journal of American Helicopter Society*, 50(4):295, October 2005.
- [19] Air Accidents Investigation Branch (AAIB). AAIB, Berkshire Copse Rd., Aldershot, Hampshire, GU11 2HH, UK, 2008.

-
- [20] S. S. Houston. Longitudinal Stability of Gyroplanes. *The Aeronautical Journal*, 100(991):1–6, October 1996.
- [21] S. S. Houston. Identification of Autogiro Longitudinal Stability and Control Characteristics. *Control and Dynamics*, 21(3):391–399, 1998.
- [22] F. Coton, Smrcek, L., and Z. Patek. Aerodynamic Characteristics of a Gyroplane Configuration. *Journal of Aircraft*, 35(2):274–279, 1998.
- [23] P. A. Hufton, A. E. Woodward Nutt, F. J. Bigg, and J.A. Beavan. General Investigation into the Characteristics of the C.30 Autogiro. R.A.E. Reports and Memoranda, *Royal Aircraft Establishment*, 1939. No. 1859.
- [24] S. S. Houston and R. E. Brown. Rotor Wake Modelling for Simulation of Helicopters Flight Mechanics in Autorotation. *Journal of Aircraft*, 40(5), 2003.
- [25] W. Castles and R.B. Gray. Empirical Relation Between Induced Velocity, Thrust and Rate of Descent of a Helicopter Rotor as Determined by Wind-Tunnel Tests on Four Model Rotors. NACA Technical Note, *National Advisory Committee for Aeronautics*, Washington, USA, 1951. TN 2474.
- [26] P. P. Friedmann and D.H. Hodges. Rotary Wing Aeroelasticity - A Historical Perspective. *Journal of Aircraft*, 40(6), 2003.
- [27] A. R. S. Bramwell. *Bramwell's Helicopter Dynamics, Second edition*. Butterworth-Heinemann, 2001. ISBN 0-7506-5075-3.
- [28] H. Glauert. A General Theory of the Autogyro. Reports and Memoranda, *Aeronautical Research Council*, 1926. R&M 1111.
- [29] H. Glauert. *The Elements of Aerofoil and Airscrew Theory*. Cambridge Science Classics. Cambridge University Press, UK, 1983. ISBN 0-521-27494-X.
- [30] J. B. Wheatley and C. Bioletti. Wind-Tunnel Tests of a 10-foot-diameter Gyroplane Rotor. NACA Technical Report, *National Advisory Committee for Aeronautics*, 1936. TR 536.
-

- [31] A.A. Nikolsky and E. Seckel. An Analytical Study of the Steady Vertical Descent in Autorotation of Single-Rotor Helicopters. NACA Technical Note, *National Advisory Committee for Aeronautics*, 1949. TN 1906.
- [32] R.E. Brown. Rotor Wake Modeling for Flight Dynamic Simulation of Helicopters. *AIAA Journal*, 38(1), 2000.
- [33] S. S. Houston. Modelling and Analysis of Helicopter Flight Mechanics in Autorotation. *Journal of Aircraft*, 40(4), 2003.
- [34] S. F. Racisz. Effects of Independent Variations of Mach Number and Reynolds Number on the Maximum Lift Coefficients of Four NACA 6-series Airfoil Sections. NACA Technical Note, *National Advisory Committee for Aeronautics*, Langley Memorial Aeronautical Laboratory, VA, USA, 1952. TN 2824.
- [35] R. E. Sheldahl and P. C. Klimas. Aerodynamic Characteristics of Seven Aerofoil Sections Through 180 Degrees Angle of Attack for Use in Aerodynamic Analysis of Vertical Axis Wind Turbines. Technical Report SAND80-2114, *Sandia National Laboratories*, Albuquerque, New Mexico, USA, 1981.
- [36] L. K. Loftin. Airfoil Section Characteristics at High Angles of Attack. NACA Technical Note, *National Advisory Committee for Aeronautics*, Langley Field, VA, USA, 1954. TN 3241.
- [37] L.S. Stivers and F. J. Rice. Aerodynamic Characteristics of Four NACA Airfoil Sections Designed for Helicopter Rotor Blades. NACA Technical Note, *National Advisory Committee for Aeronautics*, Langley Field, VA, USA, 1946. RB L5K02.
- [38] T. Theodorsen. General Theory of Aerodynamic Instability and the Mechanism of Flutter. NACA Technical Report, *National Advisory Committee for Aeronautics*, USA, 1935. TR 496.
- [39] K.R.V. Kaza and R.G. Kvaternik. Nonlinear Aeroelastic Equations for Combined Flapwise Bending, Chordwise Bending, Torsion and Extension of Twisted

- Nonuniform Rotor Blades in Forward Flight. NASA Technical Memoranda, *National Aeronautics and Space Administration*, Ames Research Centre, Berkeley, California, USA, 1977. TM 74059.
- [40] R. T. N. Chen. A Survey of Nonuniform Inflow Models for Rotorcraft Flight Dynamics and Control Applications. NASA Technical Memoranda, *National Aeronautics and Space Administration*, Ames Research Centre, Berkeley, California, USA, 1989. TM 102219.
- [41] R. P. Coleman, A. M. Feingold, and C. W. Stempin. Evaluation of the Induced Velocity Fields of an Idealized Helicopter Rotor. NACA ARR, *National Advisory Committee for Aeronautics*, Washington, USA, 1945. L5E10.
- [42] J. M. Drees. A Theory of Airflow Through Rotors and Its Application to Some Helicopter Problems. *Journal of the Helicopter Association of Great Britain*, 3 (2), 1949.
- [43] P. R. Payne. *Helicopter Dynamics and Aerodynamics*. Pittman and Sons, London, 1959.
- [44] D. M. Pitt and D. A. Peters. Theoretical Prediction of Dynamic Inflow Derivatives. *Vertica*, 1981(5), 1981.
- [45] J. Zhao. *Dynamic Wake Distortion Model for Helicopter Maneuvering Flight*. PhD. Thesis, School of Aerospace Engineering, Georgia Institute of Technology, USA, 2005.
- [46] D. Lee. *Simulation and Control of a Helicopter Operating in a Ship Air-wake*. PhD. Thesis, The Graduate School, Department of Aerospace Engineering, The Pennsylvania State University, USA, 2005.
- [47] P. P. Friedmann. Rotary-Wing Aeroelasticity: Current Status and Future Trends. *AIAA Journal*, 42(10), 2004.
- [48] R. L. Bisplinghoff, H. Ashley, and R. L. Halfman. *Aeroelasticity*. Dover Publications Inc., NY, USA, 1996. 0-486-69189-6.

- [49] Y. W. Kwon and H. Bang. *The Finite Element Method Using MATLAB, Second Edition*. CRC Press, 2000. 0-8493-0096-7.
- [50] C. H. Houbolt and G. W. Brooks. Differential Equations of Motion for Combined Flapwise Bending, and Torsion of Twisted Nonuniform Rotor Blades. NACA Technical Report, *National Advisory Committee for Aeronautics*, USA, 1958. TR 1346.
- [51] R. Courant. Variational Methods for the Solution of Problems of Equilibrium and Vibration. Bulletin of American Mathematical Society, American Mathematical Society, 1943.
- [52] I. Babuska. *Courant element: before and after*, volume 164 of *Lecture Notes in Pure and Applied Mathematics*. Marcel Dekker, NY, USA, 1994.
- [53] L. Cermak, J. Nedoma, and A. Zenisek. In Memoriam Professor Milos Zlamal. *Application of Mathematics*, 43(1), 1998.
- [54] A. Gessow. Flight Investigation of Effects of Rotor-Blade Twist on Helicopter Performance in the High-Speed and Vertical-Autorotative-Descent Conditions. NACA Technical Note, *National Advisory Committee for Aeronautics*, Langley Aeronautical Laboratory, VA, USA, 1948. TN 1666.
- [55] J.B. Wheatley. The Aerodynamic Analysis of the Gyroplane Rotating-Wing System. NACA Technical Note, *National Advisory Committee for Aeronautics*, Langley Memorial Aeronautical Laboratory, VA, USA, 1934. TN 492.
- [56] J.B. Wheatley. An Aerodynamic Analysis of the Autogiro Rotor with a Comparison between Calculated and Experimental Results. NACA Technical Report, *National Advisory Committee for Aeronautics*, Washington, USA, 1934. TR 487.
- [57] G. Sissingh. Contribution to the Aerodynamics of Rotating-Wing Aircraft. NACA Technical Memoranda, *National Advisory Committee for Aeronautics*, Washington, USA, 1939. TM 921.

- [58] Y.I. Somov and O.Y. Polyntsev. Nonlinear Dynamics and Control of a Windmilling Gyroplane Rotor. In *Proceedings of the Physics and Control International Conference, St. Petersburg, Russia*, volume 1, 2003.
- [59] D. Rezgui, P.C. Bunniss, and M.H. Lowenberg. The Stability of Rotor Blade Flapping Motion in Autorotation Using Bifurcation and Continuation Analysis. In *Proceedings of the 32nd European Rotorcraft Forum, Maastricht, Netherlands*, 2006.
- [60] J.B. Wheatley. An Analytical and Experimental Study of the Effect of Periodic Blade Twist on the Thrust, Torque, and Flapping Motion of an Autogiro Rotor. NACA Technical Report, *National Advisory Committee for Aeronautics*, Langley Memorial Aeronautical Laboratory, Langley Field, VA, USA, 1938. TR 591.
- [61] J.B. Wheatley. Wing Pressure Distribution and Rotor-Blade Motion of an Autogiro as Determined in Flight. NACA Technical Report, *National Advisory Committee for Aeronautics*, Langley Memorial Aeronautical Laboratory, Langley Field, VA, USA, 1937. TR 475.
- [62] F.J. Bailey Jr. and F.B. Gustafson. Observations in Flight of the Region of Stalled Flow Over the Blades of an Autogiro Rotor. NACA Technical Report, *National Advisory Committee for Aeronautics*, Langley Memorial Aeronautical Laboratory, Langley Field, VA, USA, 1939. TR 741.
- [63] J. A. J. Bennett. Vertical Descent of the Autogiro. NACA Technical Memorandum, *National Advisory Committee for Aeronautics*, Langley Memorial Aeronautical Laboratory, Langley Field, VA, USA, 1932. TM 673.
- [64] J. A. J. Bennett. The Flight of an Autogiro at High Speed. NACA Technical Memorandum, *National Advisory Committee for Aeronautics*, Langley Memorial Aeronautical Laboratory, Langley Field, VA, USA, 1933. TM 729.
- [65] W.C. Peck. Landing Characteristics of an Autogiro. NACA Technical Note,

- National Advisory Committee for Aeronautics*, Langley Memorial Aeronautical Laboratory, Langley Field, VA, USA, 1934. TN 508.
- [66] J.B. Wheatley. Analysis and Model Tests of Autogiro Jump Take-off. NACA Technical Note, *National Advisory Committee for Aeronautics*, Langley Memorial Aeronautical Laboratory, Langley Field, VA, USA, 1936. TN 582.
- [67] F.J. Bailey Jr. A Study of the Torque Equilibrium of an Autogiro Rotor. NACA Technical Report, *National Advisory Committee for Aeronautics*, Langley Memorial Aeronautical Laboratory, Langley Field, VA, USA, 1938. TR 623.
- [68] J.B. Wheatley. A Study of Autogiro Rotor-Blade Oscillations in the Plane of the Rotor Disk. NACA Technical Report, *National Advisory Committee for Aeronautics*, Langley Memorial Aeronautical Laboratory, Langley Field, VA, USA, 1939. TR 581.
- [69] J. B. Wheatley and M. J. Hood. Full-Scale Wind-Tunnel Tests of a PCA-2 Autogiro Rotor. NACA Technical Report, *National Advisory Committee for Aeronautics*, 1936. TR 515.
- [70] J. B. Wheatley and C. Bioletti. Wind-Tunnel Tests of a 10-foot-diameter Autogiro Rotors. NACA Technical Report, *National Advisory Committee for Aeronautics*, 1936. TR 552.
- [71] J.B. Wheatley. An Analysis of the Factors That Determine the Periodic Twist of an Autogiro Rotor Blade, with a Comparison of Predicted and Measured Results. NACA Technical Report, *National Advisory Committee for Aeronautics*, Langley Memorial Aeronautical Laboratory, Langley Field, VA, USA, 1938. TR 600.
- [72] F.J. Bailey Jr. Flight Investigation of Control-Stick Vibration of the YG-1B Autogiro. NACA Technical Report, *National Advisory Committee for Aeronautics*, Langley Memorial Aeronautical Laboratory, Langley Field, VA, USA, 1940. TR 764.

- [73] M. Bagiev, D. G. Thomson, and S. S. Houston. Autogyro Inverse Simulation for Handling Qualities Assessment. In *Proceedings of the 29th European Rotorcraft Forum, Friedrichshafen, Germany, 2003*.
- [74] M. Bagiev. *Autogyro Handling Qualities Assessment Using Flight Testing and Simulation Techniques*. PhD. Thesis, Department of Aerospace Engineering, University of Glasgow, Scotland, UK, 2005.
- [75] D. H. Hodges and G. A. Pierce. *Introduction to Structural Dynamics and Aeroelasticity*. Cambridge University Press, 2002. ISBN-13: 978-0521806985.
- [76] E.H. Dowell et al. *A Modern Course in Aeroelasticity*. Kluwer Academic Publishers, 2008. ISBN-13: 978-1402027116.
- [77] C.A. Felippa. Customizing the Mass and Geometric Stiffness of Plane Thin Beam Elements by Fourier Methods. NACA Technical Note, *Centre for Aerospace Structures*, University of Colorado, Boulder, CO, USA, 2000. Report No. CU-CAS-00-19.
- [78] W.G. Bousman, C. Young, F. Toulmany, N.E. Gilbert, R.C. Strawn, J.V. Miller, T.H. Maier, and M. Costes. A Comparison of Lifting-Line and CFD Methods with Flight Test Data from a Research Puma Helicopter. NASA Technical Memoranda, *National Aeronautics and Space Administration*, Ames Research Centre, Berkeley, California, USA, 1996. TM 110421.
- [79] M.E. Wood. Results from Oscillatory Pitch Tests on the NACA 0012 Blade Section. ARA Memo 220, Aircraft Research Association, Bedford, UK, 1979.
- [80] G. Arnaud and P. Beaumier. Validation of R85/METAR on the Puma RAE Flight Tests. In *Proceedings of the 18th European Rotorcraft Forum, 1992*.
- [81] W. Johnson. Development of a Comprehensive Analysis for Rotorcraft - I. Rotor Model and Wake Analysis. *Vertica*, 5(1981).
- [82] W. Johnson. *CAMRAD/JA: A Comprehensive Analytical Model of Rotorcraft*

- Aerodynamics and Dynamics; Johnson Aeronautics Version; Volume 1, Theory Manual.* Johnson Aeronautics, Palo Alto, California, 1988.
- [83] J.G. Leishman and T.S. Beddoes. A Second Generation Model for Airfoil Unsteady Aerodynamics Behaviour and Dynamic Stall. WHL Research Paper No. 704, Westland Helicopters Ltd., 1986.
- [84] A. Gagliardi. *CFD Analysis and Design of a Low-Twist, Hovering Rotor Equipped with Trailing-Edge Flaps.* PhD. Thesis, Department of Aerospace Engineering, University of Glasgow, Scotland, UK, 2007.
- [85] J. Trchalík, E.A. Gillies, and D.G. Thomson. Aeroelastic Behaviour of a Gyroplane Rotor in Axial Descent and Forward Flight. In *Proceedings of the 32nd European Rotorcraft Forum, Maastricht, Netherlands, 2006.*
- [86] J. Trchalík, E.A. Gillies, and D.G. Thomson. Development of an Aeroelastic Stability Boundary for a Rotor in Autorotation. In *Proceedings of the AHS Specialist's Conference on Aeromechanics, Fisherman's Wharf, San Francisco, CA, USA, 2008.*

A P P E N D I C E S

APPENDIX A1. Quasi-steady and Unsteady Aerodynamics of a Rotor Blade

Quasi-steady Aerodynamics

A classical formulations of quasi-steady lift and moment coefficient as given in Leishman [7] are

$$c_L = 2\pi \left[\alpha + \frac{\dot{h}}{V} + b \left(\frac{1}{2} - a \right) \frac{\dot{\alpha}}{V} \right] \quad (\text{A1-1})$$

$$c_{M, \frac{c}{4}} = -\frac{\pi \dot{\alpha} b}{4 V} \quad (\text{A1-2})$$

Unsteady Aerodynamics

Theodorsen's lift deficiency function $C(k)$ is defined with the aid of Bessel functions

$$C(k) = \frac{H_1^{(2)}(k)}{H_1^{(2)}(k) + iH_0^{(2)}(k)} \quad (\text{A1-3})$$

Alternatively, Theodorsen's function can be approximated by a simple polynomial

$$C(k) \approx 1 - \frac{0.165}{1 - \frac{0.0455i}{k}} - \frac{0.335}{1 - \frac{0.3i}{k}} \quad (\text{A1-4})$$

In the time domain, Theodorsen's theory gives following formulations of lift and moment coefficient of an oscillating airfoil

$$c_L = 2\pi C(k) \left[\alpha + \frac{\dot{h}}{V} + b \left(\frac{1}{2} - a \right) \frac{\dot{\alpha}}{V} \right] + \pi b \left[\frac{\dot{\alpha}}{V} + \frac{\ddot{h}}{V^2} - \frac{ab\ddot{\alpha}}{V^2} \right] \quad (\text{A1-5})$$

$$\begin{aligned}
c_{M,\frac{\varepsilon}{2}} = & \pi C(k) \left(\frac{1}{2} + a \right) \left[\alpha + \frac{\dot{h}}{V} + b \left(\frac{1}{2} - a \right) \frac{\dot{\alpha}}{V} \right] + \frac{\pi}{2} \left[\frac{ab\ddot{h}}{V^2} - \frac{b^2}{V^2} \left(\frac{1}{8} + a^2 \right) \ddot{\alpha} \right] \\
& - \frac{\pi}{2} \left[\left(\frac{1}{2} - a \right) \frac{b\dot{\alpha}}{V} \right]
\end{aligned} \tag{A1-6}$$

Since the equations A1-5 and A1-6 still contain the quasi-steady terms, they can be written in a simplified form

$$c_L = 2\pi \left(C(k) (\alpha + \alpha_q) + \frac{\alpha_u}{2} \right) \tag{A1-7}$$

$$c_{M,\frac{\varepsilon}{2}} = \pi C(k) \left(\frac{1}{2} - a \right) (\alpha + \alpha_q) + c_{M,u} - c_{M,c} \tag{A1-8}$$

Use of Theodorsen's theory is especially convenient in the frequency domain. Assuming harmonic motion of an airfoil in pitch and plunge $h = h_0 e^{i\omega t}$ and $\alpha = \alpha_0 e^{i\omega t}$ and using substitution $\omega = \frac{2kV}{c}$, equations A1-7 and A1-8 become

$$c_L = 2\pi C(k) \left[\alpha + \frac{hik}{b} + \left(\frac{1}{2} - a \right) \alpha ik \right] + \pi \left[ik\alpha - \frac{hk^2}{b} + \alpha ak^2 \right] \tag{A1-9}$$

$$\begin{aligned}
c_{M,\frac{\varepsilon}{2}} = & \pi C(k) \left(\frac{1}{2} + a \right) \left[\alpha + \frac{hik}{b} + \left(\frac{1}{2} - a \right) \alpha ik \right] + \frac{\pi}{2} \left[-\frac{hak^2}{b} + \left(\frac{1}{8} + a^2 \right) \alpha k^2 \right] \\
& - \frac{\pi}{2} \left(\frac{1}{2} - a \right) \alpha ik
\end{aligned} \tag{A1-10}$$

Blade Aerodynamic Forcing

Using numerical integration, aerodynamic forcing moments can be expressed in a form that can be used for a blade element model of an autorotating rotor

$$M_{\psi,A} = \sum_{i=1}^{N_{elem}} \left[\frac{1}{2} \rho c_i \Omega^2 r_i^3 [c_{L\alpha,i} \sin \phi_i (\alpha_i + \alpha_{q,i}) - c_{D,i} \cos \phi_i] \Delta r_i \right] \quad (A1-11)$$

$$M_{\beta,A} = \sum_{i=1}^{N_{elem}} \left[\frac{1}{2} \rho c_i \Omega^2 r_i^3 [c_{L\alpha,i} (\alpha_i + \alpha_{q,i}) \cos \phi_i + c_{D,i} \sin \phi_i] \Delta r_i \right] \quad (A1-12)$$

$$M_{\theta,A} = \sum_{i=1}^{N_{elem}} \left[\frac{1}{2} \rho c_i^2 \Omega^2 r_i^2 \left[\left(\frac{y_{EA,i}}{c_i} - \frac{1}{4} \right) (c_{L\alpha,i} (\alpha_i + \alpha_{q,i}) \cos \alpha_i + c_D \sin \alpha_i) + c_{M,i} \right] \Delta r_i \right] \quad (A1-13)$$

Rotor pitching moment and rotor rolling moment are defined as follows [27]

$$L_R = \sum_1^{N_b} \left\{ \int_0^R r \sin \psi dT \right\} \quad (A1-14)$$

$$M_R = \sum_1^{N_b} \left\{ \int_0^R -r \cos \psi dT \right\} \quad (A1-15)$$

Blade aerodynamic forcing moments derived with the aid of analytical integration (i.e. homogeneous span-wise distributions of blade geometry and aerodynamic properties are assumed) are [7; 27]

$$M_{\psi,A} = \frac{1}{8} \rho c \Omega^2 R^4 \left[c_{L\alpha} \phi \left(\alpha + \frac{4}{3} \alpha_q \right) - c_D \right] \quad (A1-16)$$

$$M_{\beta,A} = \frac{1}{8} \rho c \Omega^2 R^4 \left[c_{L\alpha} \left(\alpha + \frac{4}{3} \alpha_q \right) + \phi c_D \right] \quad (A1-17)$$

$$M_{\theta,A} = \frac{1}{6} \rho c^2 \Omega^2 R^3 \left[\left(\frac{y_{EA}}{c} - \frac{1}{4} \right) \left(c_{L\alpha} \left(\alpha + \frac{3}{2} \alpha_q \right) \cos \alpha + c_D \sin \alpha \right) + c_M \right] \quad (A1-18)$$

The equations can be used in a simplified analytical model of autorotating rotor

blade aerodynamics and are also essential for linear stability analysis of rotor blades.

APPENDIX A2. Polynomial Approximation of Rotor Blade Aerodynamic Characteristics

Prouty's polynomial approximation of NACA 0012 lift curve

Prouty's amended compressibility correction

$$c_{L\alpha} = \frac{C_1}{\sqrt{1-M^2}} + C_2M \quad (\text{A2-1})$$

For NACA 0012, $C_1 = 0.1deg^{-1}$ and $C_2 = -0.01deg^{-1}$. Prouty assumes that for a low speed airflow, the slope of linear part of NACA 0012 lift curve is $c_{L\alpha} = 5.73rad^{-1}$.

$$\alpha_L = C_3 + C_4M \quad (\text{A2-2})$$

For NACA 0012, $C_3 = 15deg$ and $C_4 = -16deg$.

Hence, for values of angle of attack lower than α_L (linear part of lift-curve) and above α_L , values of lift coefficient of the airfoil can be estimated as follows

$$\begin{aligned} c_L &= c_{L\alpha}\alpha \\ c_L &= c_{L\alpha}\alpha - C_5(\alpha - \alpha_L)^{C_6} \end{aligned} \quad (\text{A2-3})$$

Prouty [8] suggests that dependence of the coefficient C_6 on Mach number is linear (see equation 3.15) and that for NACA 0012, the values of coefficients of the linear equation are $C_7 = 2.05$ and $C_8 = -0.95$. Further, the coefficient C_5 can be calculated with the aid of equation 3.14.

Exponent C_6 can be obtained by plotting the difference between the linear values of the lift coefficient and measured non-linear lift coefficient ($c_{L\alpha0}\alpha - c_L$) against the

difference of the actual angle of attack and α_L with both axis in logarithmic scale (see the figure A2-1). The slope of linear interpolation of points plotted for certain Mach number is the desired coefficient C_6 [8].

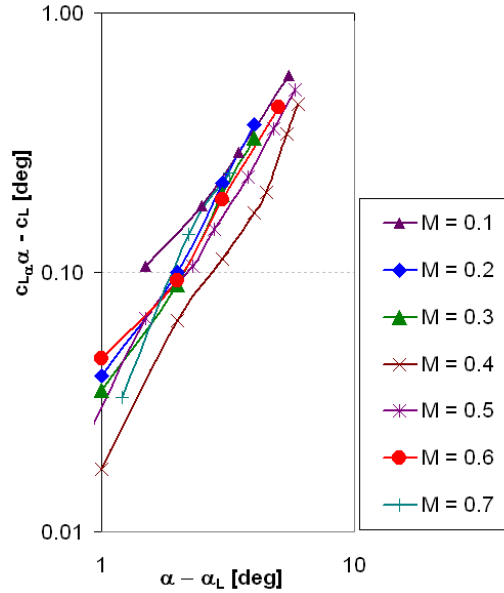


Figure A2-1: The difference between linear lift-curve lift coefficient and measured non-linear lift coefficient plotted against $\alpha - \alpha_L$. The plot uses logarithmic scale.

Prouty's polynomial approximation of NACA 0012 drag curve

Angle of attack of drag divergence can be computed as

$$\alpha_{div} = D_1 + D_2 M \quad (A2-4)$$

For NACA 0012 airfoil, angle of attack of the drag divergence is $\alpha_{div} = 17 - 23.4M$ [8]. For Mach numbers lower than $M=0.1$, Prouty [8] gives following form of the polynomial (values of α are in degrees)

$$c_{D,inc} = 0.081 + (-350\alpha + 369\alpha^2 - 63.3\alpha^3 + 3.66\alpha^4) 10^{-6} \quad (A2-5)$$

Wind tunnel data published at [13] and by Carpenter [10] were used for refinement of this polynomial. The resulting enhanced approximation of drag coefficient

is shown below.

$$c_{D,inc} = 0.081 - 6.03688 \cdot 10^{-5}\alpha + 1.64211 \cdot 10^{-4}\alpha^2 - 5.21562 \cdot 10^{-6}\alpha^3 \quad (\text{A2-6})$$

If Mach number is higher than 0.1 and $\alpha < \alpha_D$ (i.e. airfoil is below drag divergence), additional terms have to be used in order to capture the effects of compressibility

$$c_{D,comp} = c_{D,inc} + D_3(\alpha - \alpha_D)^{D_4} \quad (\text{A2-7})$$

Values of the coefficients D_3 and D_4 that were obtained from experimental measurements of NACA 0012 are dependent upon Mach number [8]. Using average values of these coefficients, the equation A2-7 has following form

$$c_{D,comp} = c_{D,inc} + 0.00066(\alpha - (17 - 23.4M))^{2.54} \quad (\text{A2-8})$$

Prouty [8] uses a single form of fitting curve for the rest of range of angles of attack (i.e. for $\alpha > 20deg$) and assumes that drag coefficient of the airfoil during reverse flow is not significantly different from drag coefficient for $\alpha \approx 0$

$$c_{D,\alpha>20deg} = 1.03 - 1.02\cos(2\alpha) \quad (\text{A2-9})$$

Polynomial approximation of NACA 0012 moment curve

Tabulated coefficients of polynomial approximation of pitching moment curve of the NACA 0012 airfoil

Table A2-1: Values of coefficients of polynomial approximation of NACA 0012 moment curve

M	0th order	1st order [rad ⁻¹]	2nd order [rad ⁻²]
0.3	$-5.319 \cdot 10^{-5}$	$-3.425 \cdot 10^{-1}$	$1.5213 \cdot 10^1$
0.4	$-3.434 \cdot 10^{-4}$	$-6.751 \cdot 10^{-2}$	6.622
0.5	$-3.414 \cdot 10^{-4}$	$2.759 \cdot 10^{-1}$	-9.262
0.6	$5.178 \cdot 10^{-4}$	$-2.515 \cdot 10^{-1}$	4.961
0.7	$-4.5 \cdot 10^{-4}$	$-1.438 \cdot 10^{-1}$	8.832
0.75	$-1.146 \cdot 10^{-4}$	$-1.667 \cdot 10^{-2}$	5.486
0.8	$-3.335 \cdot 10^{-3}$	3.307	$-1.309 \cdot 10^2$
0.9	$5.056 \cdot 10^{-3}$	3.073	$-9.636 \cdot 10^1$
M	3rd order [rad ⁻³]	4th order [rad ⁻⁴]	5th order [rad ⁻⁵]
0.3	$-1.875 \cdot 10^2$	$9.468 \cdot 10^2$	$-1.666 \cdot 10^3$
0.4	$-1.195 \cdot 10^2$	$8.375 \cdot 10^2$	$-1.904 \cdot 10^3$
0.5	$9.859 \cdot 10^1$	$-2.442 \cdot 10^2$	$-1.843 \cdot 10^2$
0.6	$1.065 \cdot 10^1$	$-1.564 \cdot 10^2$	0
0.7	$-6.319 \cdot 10^1$	0	0
0.75	$-1.139 \cdot 10^2$	0	0
0.8	$1.59 \cdot 10^3$	$-7.082 \cdot 10^3$	0
0.9	0	0	0

APPENDIX A3. Inflow Modelling in Autorotating Rotors

Modified Glauert's Semi-empirical Inflow Model

Two main conditions have to be fulfilled during a steady axial flight in autorotation - rotor thrust has to be in balance with the weight of the vehicle and the overall torque generated by the flow through the rotor disc has to be zero [31; 55].

$$\begin{aligned}
 T &= Mg \\
 Q &= 0
 \end{aligned}
 \tag{A3-1}$$

The thrust equation can be consequently used for calculation of rotor speed. The inflow ratio can be computed once rotor speed is calculated with the aid of the zero aerodynamic torque condition. An analytical or empirical relation between

the vertical component of inflow velocity U_p and the speed of descent V_d can be used to estimate the rate of descent of a rotor in autorotation. This is equivalent to the relationship of thrust coefficient based on resultant air velocity F and thrust coefficient based on descending velocity f [31].

$$\begin{aligned}
 F &= \frac{T}{2\pi R^2 \rho U_p^2} \\
 f &= \frac{T}{2\pi R^2 \rho V_d^2} \\
 \frac{f}{F} &= \left(\frac{U_p}{V_d} \right)^2
 \end{aligned}
 \tag{A3-2}$$

Several experimental measurements were carried out to determine the relationship between $\frac{1}{f}$ and $\frac{1}{F}$ [31; 55] and some of them are summarised in figure A3-1

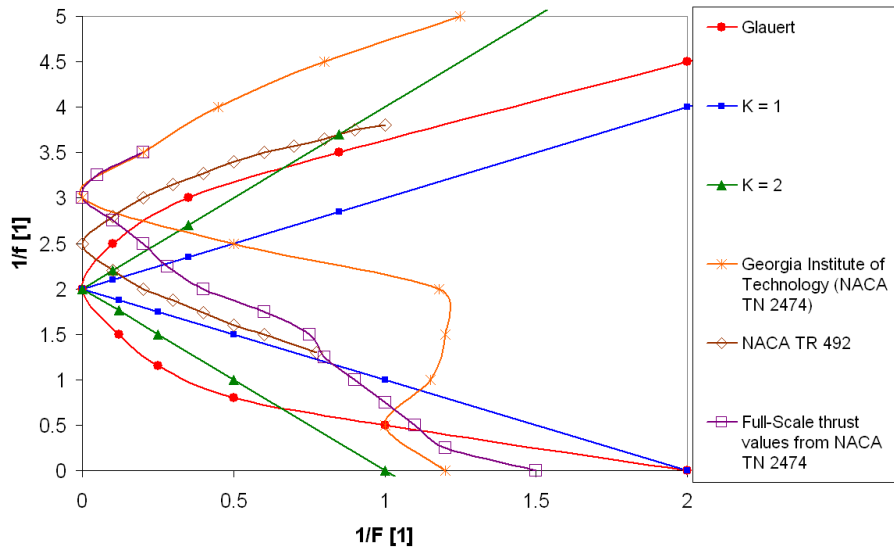


Figure A3-1: Different versions of the F-curve, graphical interpretation of the relationship between vertical component of inflow velocity and speed of descent

Nikolsky and Seckel [31] also gives an analytical approximation of relationship between $\frac{1}{f}$ and $\frac{1}{F}$ (see figure A3-1).

$$\frac{1}{f} = 2 \pm K \frac{1}{F}
 \tag{A3-3}$$

$$|K| \in \langle 1, 2 \rangle
 \tag{A3-4}$$

A positive value of K corresponds to the windmill brake-state (i.e. the upper branch of F-curve) and a negative K indicates that the rotor is in the vortex ring state (VRS; the lower branch of F-curve) [31].

Rotor inflow ratio can be calculated as

$$\lambda = \frac{\frac{-c_{L\alpha E}\theta}{4} + \sqrt{\left(\frac{c_{L\alpha E}\theta}{4}\right)^2 + 4\left(\frac{c_{L\alpha E}}{3} - \frac{c_{DE}}{2}\right)\left(\frac{c_{DE}}{4} + \frac{2Q}{N_B\rho\Omega^2 R^4 c_E}\right)}}{\frac{2c_{L\alpha E}}{3} - c_{DE}} \quad (\text{A3-5})$$

Once the inflow ratio is calculated, the inflow speed can be obtained with the help of the following equations

$$\lambda_D = \sqrt{\frac{1}{f} \frac{T}{2\pi\rho\Omega^2 R^4}} \quad (\text{A3-6})$$

$$v_i = \Omega R (\lambda_D - \lambda)$$

Some of the data sets obtained during the experimental measurements of a rotor in autorotative flight suggest that Glauert's linear approximation of the F-curve can be improved or replaced with a more accurate approximation. The lower branch of full-scale thrust experimental measurements that were published by Castles and Gray [25] can be approximated with the aid of a linear function

$$\left(\frac{1}{f}\right)_L = 3 - \frac{2}{F} \quad (\text{A3-7})$$

Polynomial fits of both the upper and the lower branches of the F-curve are

$$\begin{aligned}\left(\frac{1}{f}\right)_U &= \left(2.2\frac{1}{F}\right)^{0.7} + 3 \\ \left(\frac{1}{f}\right)_L &= -0.3207\left(\frac{1}{F}\right)^4 - 1.846\left(\frac{1}{F}\right)^3 - 2.5336\left(\frac{1}{F}\right)^2 - 1.1336\left(\frac{1}{F}\right) + 2.8834\end{aligned}\tag{A3-8}$$

Table A3-1 shows predictions of rotor induced velocity and vehicle speed of descent in axial flight obtained with the help of different empirical F-curves (see figure A3-1).

Table A3-1: Comparison of outcomes of the semi-empirical inflow model for three different versions of the F-curve

F-Curve	V_D [m/s]	v_i [m/s]	Ω [rad/s]
Glauert	10.5	8.25	48.15
Georgia Institute of Technology	12	8.65	48.15
NACA TN 942	11.0	9.64	48.15

Modified Peters-HaQuang Dynamic Inflow Model

Time matrix and dynamic inflow static gain matrix can be written in the following forms

$$[\tau] = \begin{bmatrix} \frac{4R}{3\pi v_t C_0} & 0 & \frac{-R \tan \frac{\chi}{2}}{12u_m} \\ 0 & \frac{64R}{45u_m(1 + \cos \chi)} & 0 \\ \frac{5R \tan \frac{\chi}{2}}{8v_t} & 0 & \frac{64R \cos \chi}{45u_m(1 + \cos \chi)} \end{bmatrix}\tag{A3-9}$$

$$[\Lambda] = \frac{1}{\rho\pi R^3} \begin{bmatrix} \frac{R}{2v_t} & 0 & \frac{15\pi \tan \frac{\chi}{2}}{64u_m} \\ 0 & \frac{-4}{u_m(1 + \cos \chi)} & 0 \\ \frac{15\pi \tan \frac{\chi}{2}}{64v_t} & 0 & \frac{-4 \cos \chi}{u_m(1 + \cos \chi)} \end{bmatrix}\tag{A3-10}$$

Total velocity at the rotor disc centre is [24]

$$v_t = \sqrt{V_x^2 + V_y^2 + (V_z - v_h)^2} \quad (\text{A3-11})$$

The mass flow parameter is defined as [24]

$$u_m = \frac{V_x^2 + V_y^2 + (2v_h - V_z)(v_h - V_z)}{v_t} \quad (\text{A3-12})$$

$$v_h = \sqrt{\frac{T}{2\rho A}}$$

The wake skew angle can be calculated with the aid of the following equation [24]

$$\chi = \tan^{-1}\left(\frac{\sqrt{V_x^2 + V_y^2}}{v_h - V_z}\right) \quad (\text{A3-13})$$

Total induced velocity at azimuth angle ψ and radial station x is then [24]

$$v_i = v_{i0} + v_{ic}x \cos \psi + v_{is}x \sin \psi \quad (\text{A3-14})$$

APPENDIX A4. Rotor Blade Structural Dynamics

Euler equations of motion

$$i_x \ddot{\theta} - (J_y - J_z) \dot{\beta} \Omega = M_{\theta,A}$$

$$J_y \ddot{\beta} - (J_z - i_x) \dot{\theta} \Omega + M_b y_{CG} a_z = M_{\beta,A} \quad (\text{A4-1})$$

$$J_z \dot{\Omega} - (i_x - J_y) \dot{\beta} \dot{\theta} - M_b y_{CG} a_y = M_{\psi,A}$$

Lagrange's Method

In general, Lagrange's equation has the following form [11; 27]

$$\frac{d}{dt} \left(\frac{\partial T}{\partial \dot{q}_G} \right) - \frac{\partial T}{\partial q_G} + \frac{\partial U}{\partial q_G} + \frac{\partial D}{\partial \dot{q}_G} = F_G \quad (\text{A4-2})$$

For one degree of freedom problem, differential equation of motion can be written in the following form [11; 27]

$$m\ddot{q}_G + c\dot{q}_G + kq_G = F_G \quad (\text{A4-3})$$

The above equation can be modified in order to obtain more useful form of the equation above [11]

$$\begin{aligned} \ddot{q}_G + 2\zeta\omega_N\dot{q}_G + \omega_N^2q_G &= \frac{F_G}{m} \\ \zeta &= \frac{c}{c_{crit}} \\ \omega_N &= \sqrt{\frac{k}{m}} \end{aligned} \quad (\text{A4-4})$$

The figure A4-1 depicts the principle of coordinate transformation. Coordinate system $x_1y_1z_1$ was created by rotation of the original system $x_0y_0z_0$ around z axis.

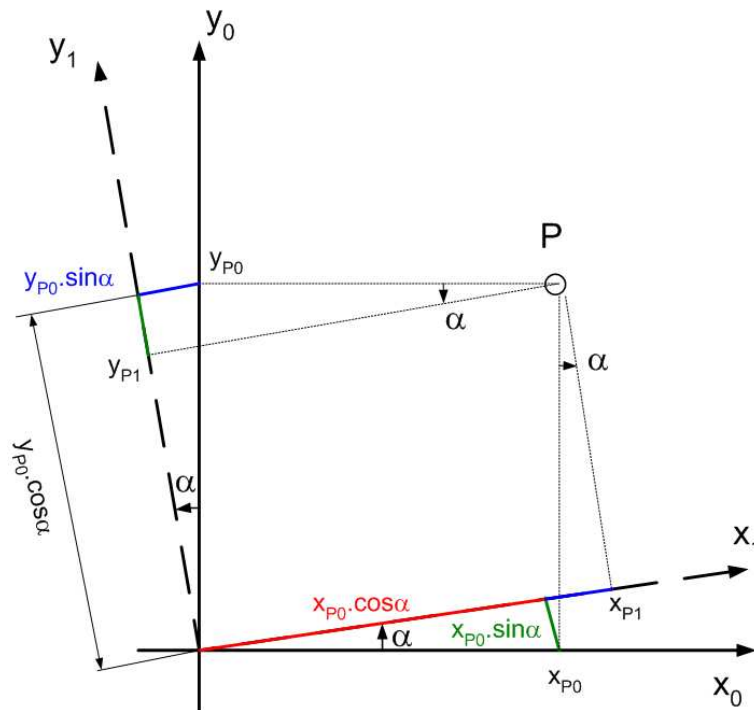


Figure A4-1: An example of transformation of coordinates from rotating frame of reference to non-rotating one

As the figure A4-1 shows, the relation between new and old coordinates of point P are given by [11]

$$\begin{aligned}
 x_{P1} &= x_{P0} \cos \alpha + y_{P0} \sin \alpha \\
 y_{P1} &= y_{P0} \cos \alpha - x_{P0} \sin \alpha \\
 z_{P1} &= z_{P0}
 \end{aligned} \tag{A4-5}$$

Resulting transformation matrix is

$$[T] = \begin{bmatrix} \cos(\psi+\xi) \cos \beta & -\cos(\psi+\xi) \sin \theta \sin \beta - \sin(\psi+\xi) \cos \theta & -\cos(\psi+\xi) \cos \theta \sin \beta + \sin(\psi+\xi) \sin \theta \\ \sin(\psi+\xi) \cos \beta & -\sin(\psi+\xi) \sin \theta \sin \beta + \cos(\psi+\xi) \cos \theta & -\sin(\psi+\xi) \cos \theta \sin \beta - \cos(\psi+\xi) \sin \theta \\ \sin \beta & \sin \theta \cos \beta & \cos \theta \cos \beta \end{bmatrix} \tag{A4-6}$$

If all blade hinge offsets are considered to be negligible, position vector of an arbitrary point of blade axis of inertia is

$$\begin{aligned}
 \underline{r}_0 &= [r \quad y_g \quad 0] \\
 y_g &= y_{EA} - y_{CG}
 \end{aligned} \tag{A4-7}$$

If the blade element method is used for calculation of blade aerodynamic forcing, it is convenient to calculate blade kinetic energy by summation of kinetic energies of individual blade elements. Blade elements can be modeled as uniform, infinitely thin beams or lumped masses and an assumption can be made that blade physical properties are constant along each blade element.

$$T = \sum_{i=1}^{N_{elem}} \left\{ \frac{1}{2} m_i (\dot{\underline{r}}_i \cdot \dot{\underline{r}}_i) \right\} \tag{A4-8}$$

The potential energy of a rotor blade consists of an elastic component and a gravitational component.

$$U = U_e + U_g \quad (\text{A4-9})$$

Elastic component of potential energy represents the strain energy due to a deformation of blade structure.

$$U_e = \frac{1}{2} (k_\beta \beta^2 + k_\theta \theta^2 + k_\xi \xi^2) \quad (\text{A4-10})$$

The effect of gravitational forces on rotor blade dynamics is usually neglected since centrifugal forces acting on a blade are much bigger. Gravitational component of potential energy of i-th blade element can be expressed as follows

$$U_g = mg (r + r \sin \beta + (y_g + r \sin \xi) \sin \theta) \quad (\text{A4-11})$$

Figure A4-2 shows the way gravitational component of rotor blade potential energy can be calculated.

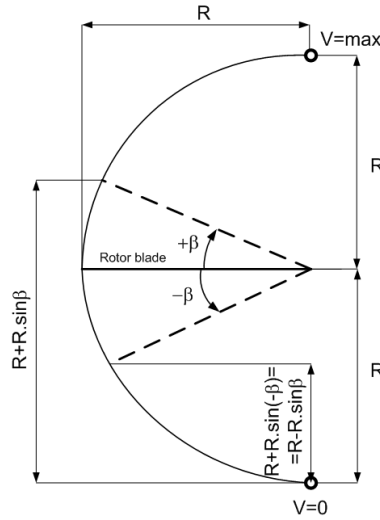


Figure A4-2: Potential energy of a rotor blade due to gravitational force

A dissipation function can be understood as a measure of amount of damping that is present in a physical system. For a rotor blade, the dissipation function can be written in the following form

$$D = \frac{1}{2} (c_\beta \dot{\beta}^2 + c_\theta \dot{\theta}^2 + c_\xi \dot{\xi}^2) \quad (\text{A4-12})$$

APPENDIX A5. Linearization of Blade Equations of Motion and Eigenvalue Analysis

Neglecting small terms, the final form of the linearized equations of blade motion is

$$m[r^2\ddot{\beta}^{B1} + ry_g\ddot{\theta}^{B2} - \Omega^2 r^2\beta^{B3} - \Omega^2 ry_g\theta^{B4} + ry_g\dot{\Omega}\beta^{B5} + y_g^2\dot{\Omega}\theta^{B6} + 2ry_g\Omega^2\theta^{B14} + rg^{B15}] + k_\beta\beta^{B16} + c_\beta\dot{\beta}^{B17} = M_{\beta,A}^{B18} \quad (\text{A5-1})$$

$$m[y_g^2\ddot{\theta}^{T1} + ry_g\ddot{\beta}^{T2} + \Omega^2 ry_g\beta^{T3} + \Omega^2 y_g^2\theta^{T4} - ry_g\dot{\Omega}\theta^{T5} + y_g^2\dot{\Omega}\beta^{T6} + y_g g^{T10}] + k_\theta\theta^{T11} + c_\theta\dot{\theta}^{T12} = M_{\theta,A}^{T13} \quad (\text{A5-2})$$

$$m(r^2 + y_g^2)\dot{\Omega}^{R1} = M_{\psi,A}^{R17} \quad (\text{A5-3})$$

Aerodynamic forcing moments can be derived from the equations A1-16 - A1-18. Blade torsional deflection, the inflow angle and the angle of attack were assumed to be small.

$$M_{\psi,A} = \frac{1}{8}\rho c\Omega^2 R^4 \left[c_{L\alpha}\phi \left(\alpha + \frac{4}{3}\alpha_q \right) - c_D \right] \quad (\text{A5-4})$$

$$M_{\beta,A} = \frac{1}{8}\rho c\Omega^2 R^4 \left[c_{L\alpha} \left(\alpha + \frac{4}{3}\alpha_q \right) + \phi c_D \right] \quad (\text{A5-5})$$

$$M_{\theta,A} = \frac{1}{6}\rho c^2\Omega^2 R^3 \left[\left(\frac{y_{EA}}{c} - \frac{1}{4} \right) \left(c_{L\alpha} \left(\alpha + \frac{3}{2}\alpha_q \right) + c_D\alpha \right) + c_M \right] \quad (\text{A5-6})$$

The following simplified expression of the blade drag coefficient can be adopted

$$c_D \approx \delta_0 + \delta_1\alpha + \delta_2\alpha^2 \quad (\text{A5-7})$$

The equations of aerodynamic forcing then become

$$M_{\psi,A} = \frac{1}{8}\rho c\Omega^2 R^4 c_{L\alpha}\phi\alpha + \frac{1}{6}\rho c\Omega R^3 c_{L\alpha}\phi \left(-\dot{\beta} + \left(\frac{3c}{4} - y_{EA} \right) \dot{\theta} \right) - \frac{1}{8}\rho c\Omega^2 R^4 (\delta_0 + \delta_1\alpha + \delta_2\alpha^2) \quad (\text{A5-8})$$

$$M_{\beta,A} = \frac{1}{8}\rho c\Omega^2 R^4 c_{L\alpha}\alpha + \frac{1}{6}\rho c\Omega R^3 c_{L\alpha} \left(-\dot{\beta} + \left(\frac{3c}{4} - y_{EA} \right) \dot{\theta} \right) + \frac{1}{8}\rho c\Omega^2 R^4 \phi (\delta_0 + \delta_1\alpha + \delta_2\alpha^2) \quad (\text{A5-9})$$

$$M_{\theta,A} = \frac{1}{6}\rho c^2\Omega^2 R^3 \left(\frac{y_{EA}}{c} - \frac{1}{4} \right) c_{L\alpha}\alpha + \frac{1}{4}\rho c^2\Omega R^2 \left(\frac{y_{EA}}{c} - \frac{1}{4} \right) c_{L\alpha} \left(-\dot{\beta} + \left(\frac{3c}{4} - y_{EA} \right) \dot{\theta} \right) + \frac{1}{6}\rho c^2\Omega^2 R^3 \left(\frac{y_{EA}}{c} - \frac{1}{4} \right) (\delta_0 + \delta_1\alpha + \delta_2\alpha^2) \alpha + \frac{1}{6}\rho c^2\Omega^2 R^3 c_M \quad (\text{A5-10})$$

Resulting system of equations of motion of a single cantilever blade of a rotor in autorotation can be written in the following form

$$[M] = \begin{bmatrix} r^2 m^{B1E} & m r y_g^{B2E} \\ m r y_g^{T2E} & (m y_g^2 + i_x)^{T1E} \end{bmatrix} \quad (\text{A5-11})$$

$$[K] = \begin{bmatrix} k_\beta^{B16E} - m\Omega^2 r^2, B3E & m[-\Omega^2 r y_g^{B4E} + 2r\Omega^2 y_g^{B14E}] \\ m\Omega^2 r y_g^{T3E} & k_\theta^{T11E} + m\Omega^2 y_g^2, T4E \end{bmatrix} \quad (\text{A5-12})$$

$$[C] = \begin{bmatrix} c_\beta^{B17E} & 0 \\ 0 & c_\theta^{T12E} \end{bmatrix} \quad (\text{A5-13})$$

$$[A] = \frac{1}{6} \rho c \Omega R^3 \left[\begin{array}{cc} -c_{L\alpha} & c_{L\alpha} \left(\frac{3c}{4} - y_{EA} \right) \\ \frac{3c}{2R} \left(\frac{y_{EA}}{c} - \frac{1}{4} \right) c_{L\alpha} & \frac{3c}{2R} \left(\frac{y_{EA}}{c} - \frac{1}{4} \right) c_{L\alpha} \left(\frac{3c}{4} - y_{EA} \right) \end{array} \right] \quad (\text{A5-14})$$

$$[B] = \frac{1}{8} \rho c \Omega^2 R^4 \left[\begin{array}{cc} 0 & c_{L\alpha} \\ 0 & \frac{4c}{3R} \left(\frac{y_{EA}}{c} - \frac{1}{4} \right) (c_{L\alpha} + \delta_0) \end{array} \right] \quad (\text{A5-15})$$

Following equation 3.46, individual coefficients of the characteristic equation of the blade are

$$\bar{A}_4 = M_{\beta\beta} M_{\theta\theta} - M_{\theta\beta} M_{\beta\theta} \quad (\text{A5-16})$$

$$\bar{A}_3 = M_{\beta\beta} (C_{\theta\theta} - A_{\theta\theta}) + M_{\theta\theta} (C_{\beta\beta} - A_{\beta\beta}) - M_{\beta\theta} (C_{\theta\beta} - A_{\theta\beta}) - M_{\theta\beta} (C_{\beta\theta} - A_{\beta\theta}) \quad (\text{A5-17})$$

$$\begin{aligned} \bar{A}_2 = & M_{\beta\beta} (K_{\theta\theta} - B_{\theta\theta}) + (C_{\beta\beta} - A_{\beta\beta}) (C_{\theta\theta} - A_{\theta\theta}) + M_{\theta\theta} (K_{\beta\beta} - B_{\beta\beta}) \\ & - M_{\beta\theta} (K_{\theta\beta} - B_{\theta\beta}) - (C_{\beta\theta} - A_{\beta\theta}) (C_{\theta\beta} - A_{\theta\beta}) - M_{\theta\beta} (K_{\beta\theta} - B_{\beta\theta}) \end{aligned} \quad (\text{A5-18})$$

$$\begin{aligned} \bar{A}_1 = & (C_{\beta\beta} - A_{\beta\beta}) (K_{\theta\theta} - B_{\theta\theta}) + (K_{\beta\beta} - B_{\beta\beta}) (C_{\theta\theta} - A_{\theta\theta}) \\ & - (C_{\beta\theta} - A_{\beta\theta}) (K_{\theta\beta} - B_{\theta\beta}) - (K_{\beta\theta} - B_{\beta\theta}) (C_{\theta\beta} - A_{\theta\beta}) \end{aligned} \quad (\text{A5-19})$$

$$\bar{A}_0 = (K_{\beta\beta} - B_{\beta\beta}) (K_{\theta\theta} - B_{\theta\theta}) - (K_{\beta\theta} - B_{\beta\theta}) (K_{\theta\beta} - B_{\theta\beta}) \quad (\text{A5-20})$$

APPENDIX A6. Application of the Finite Element method

Cubic shape function is defined as follows [49].

$$\begin{aligned} S_1 &= 3\left(\frac{r_{i+1} - r}{l_i}\right)^2 - 2\left(\frac{r_{i+1} - r}{l_i}\right)^3 \\ S_2 &= 1 - S_1 = 3\left(\frac{r - r_i}{l_i}\right)^2 - 2\left(\frac{r - r_i}{l_i}\right)^3 \end{aligned} \quad (\text{A6-1})$$

Corresponding mass and stiffness matrices and the forcing vector are

$$[K_i] = GJ \begin{bmatrix} 6 & -6 \\ \frac{5l_i}{-6} & \frac{5l_i}{6} \\ \frac{5l_i}{-6} & \frac{5l_i}{6} \end{bmatrix} \quad (\text{A6-2})$$

$$[M_i] = i_{x,i} \begin{bmatrix} \frac{13l_i}{35} & \frac{9l_i}{70} \\ \frac{9l_i}{70} & \frac{13l_i}{35} \end{bmatrix} \quad (\text{A6-3})$$

$$\{f_i\} = f_i \left\{ \begin{array}{c} \frac{l_i}{2} \\ \frac{l_i}{2} \end{array} \right\} \quad (\text{A6-4})$$

Behaviour of the cubic shape function is very similar to behaviour of square cosine shape function (see figure 3.14).

$$\begin{aligned} S_1 &= \cos^2\left(\frac{\pi}{2}\frac{(r_{i+1} - r)}{l_i}\right) \\ S_2 &= 1 - S_1 = \cos^2\left(\frac{\pi}{2}\frac{(r - r_i)}{l_i}\right) \end{aligned} \quad (\text{A6-5})$$

Corresponding mass and stiffness matrices and forcing vector are

$$[K_i] = GJ \begin{bmatrix} \frac{\pi^2}{8l_i} & \frac{-\pi^2}{8l_i} \\ \frac{-\pi^2}{8l_i} & \frac{\pi^2}{8l_i} \end{bmatrix} \quad (\text{A6-6})$$

$$[M_i] = i_{x,i} \begin{bmatrix} \frac{3l_i}{8} & \frac{l_i}{8} \\ \frac{l_i}{8} & \frac{3l_i}{8} \end{bmatrix} \quad (\text{A6-7})$$

$$\{f_i\} = f_i \left\{ \begin{array}{c} \frac{l_i}{2} \\ \frac{l_i}{2} \end{array} \right\} \quad (\text{A6-8})$$

The quartic shape function is defined as follows.

$$S_1 = 6 \left(\frac{r_{i+1} - r}{l_i} \right)^2 - 8 \left(\frac{r_{i+1} - r}{l_i} \right)^3 + 3 \left(\frac{r_{i+1} - r}{l_i} \right)^4 \quad (\text{A6-9})$$

$$S_2 = 1 - S_1$$

Application of the quartic shape functions leads to

$$[K_i] = GJ \begin{bmatrix} \frac{48}{35l_i} & \frac{-36}{35l_i} \\ \frac{-36}{35l_i} & \frac{48}{35l_i} \end{bmatrix} \quad (\text{A6-10})$$

$$[M_i] = i_{x,i} \begin{bmatrix} \frac{17l_i}{35} & \frac{17l_i}{70} \\ \frac{17l_i}{70} & \frac{17l_i}{35} \end{bmatrix} \quad (\text{A6-11})$$

$$\{f_i\} = f_i \left\{ \begin{array}{c} \frac{3l_i}{5} \\ \frac{3l_i}{5} \end{array} \right\} \quad (\text{A6-12})$$

Gaussian shape function is another type of shape function and its definition can be found below.

$$S_1 = \frac{e^{-9 \left(\frac{r_{i+1} - r}{l_i} \right)} - e^{-9}}{1 - e^{-9}} \quad (\text{A6-13})$$

$$S_2 = 1 - S_1$$

The exponential shape function is similar to the Gaussian type of shape function but it is more generic. It is identical with Gaussian shape function for $\alpha_x \rightarrow \frac{1}{3}$.

$$S_1 = e^{-\left(\frac{r_{i+1} - r}{l_i}\right)/\alpha_x} \tag{A6-14}$$
$$S_2 = 1 - S_1$$